DOT/FAA/AR-10/34

Federal Aviation Administration
William J. Hughes Technical Center
Aviation Research Division
Atlantic City International Airport
New Jersey 08405

Development of Computational Models for Simulating Full-Scale Crash Tests of Aircraft Fuselage and Components

January 2012

Final Report

U.S. Department of Transportation
Federal Aviation Administration

NOTICE

Technical Report Documentation Page

1. Report No.	2. Government Accession No.	3. Recipient's Catalog No.
DOT/FAA/AR-10/34		

4. Title and Subtitle	5. Report Date
DEVELOPMENT OF COMPUTATIONAL MODELS FOR SIMULATING FULL-SCALE CRASH TESTS OF AIRCRAFT FUSELAGE AND COMPONENTS	January 2012
	6. Performing Organization Code

7. Author(s)	8. Performing Organization Report No.
Tein-Min Tan, Jonathan Awerbuch, Alan C.W. Lau, and Alan D. Byar	

9. Performing Organization Name and Address	10. Work Unit No. (TRAIS)
Drexel University University City Main Campus 3141 Chestnut Street Philadelphia, PA 19104	
	11. Contract or Grant No. FAA Grant 99-G-046

12. Sponsoring Agency Name and Address	13. Type of Report and Period Covered
U.S. Department of Transportation Federal Aviation Administration William J. Hughes Technical Center Aviation Research Division Aircraft Systems & Structures Branch Atlantic City International Airport, NJ 08405	Final Report
	14. Sponsoring Agency Code ANM-115

15. Supplementary Notes

The Federal Aviation Administration Airport and Aircraft Safety R&D Division Technical Monitor was Allan Abramowitz.

16. Abstract

In November 2000, a vertical drop test of a Boeing 737 airplane fuselage section was conducted at the Federal Aviation Administration (FAA) William J. Hughes Technical Center, Atlantic City International Airport, New Jersey. The intent was to determine the impact response of a narrow-body airplane fuselage section, including the response of the airframe structure and cabin items of mass. The purpose of this study was to develop a finite element model to simulate the vertical drop test of that fuselage section. The 10-foot-long test section included 18 seats occupied by dummy passengers, luggage stowed in the cargo compartment beneath the floor, and two different FAA-certified overhead stowage bins. The test article was dropped from a 14-foot height, resulting in a vertical impact velocity of 30 ft/sec. The primary goal of this drop test was to characterize the behavior of the two overhead bins under a severe, but survivable, impact condition.

17. Key Words	18. Distribution Statement
Boeing 737, Modeling, Simulation, Drop test, Aircraft fuselage, Overhead stowage bins	This document is available to the U.S. public through the National Technical Information Service (NTIS), Springfield, Virginia 22161. This document is also available from the Federal Aviation Administration William J. Hughes Technical Center at actlibrary.tc.faa.gov.

19. Security Classif. (of this report)	20. Security Classif. (of this page)	21. No. of Pages	22. Price
Unclassified	Unclassified	174	

TABLE OF CONTENTS

LIST OF FIGURES

LIST OF TABLES

LIST OF ACRONYMS

AAIT	Air Accident Investigation Tool
ATD	Anthropomorphic test dummy
FAA	Federal Aviation Administration
FE	Finite element
FS	Fuselage station
g	Acceleration of gravity
ms	Millisecond
t = 0	Contact and simulation begins
μs	Microsecond

EXECUTIVE SUMMARY

In November 2000, a vertical drop test of a Boeing 737 airplane fuselage section was conducted at the Federal Aviation Administration (FAA) William J. Hughes Technical Center, Atlantic City International Airport, New Jersey. The intent was to determine the impact response of a narrow-body airplane fuselage section, including the response of the airframe structure and cabin items of mass. The purpose of the current study was to develop a finite element model to simulate the vertical drop test of that fuselage section. The 10-foot-long test section included 18 seats occupied by 6 anthropomorphic test dummies, 12 mannequins, luggage stowed in the cargo compartment beneath the floor, and two different FAA-certified overhead stowage bins. The test article was dropped from a 14-foot height, resulting in a vertical impact velocity of 30 ft/sec. The primary goal of this drop test was to characterize the behavior of the two overhead bins under a severe, but survivable, impact condition.

The simulation was evaluated through a series of comparisons with experimental data. For the overhead stowage bins, which were the primary items of interest, the simulation results showed typical peak accelerations ranging from 11 to 14 g's. This compares very well with the experimental results, which showed nearly identical peak acceleration responses ranging from 10 to 14 g's. However, a shift in peak value timing is found on the right-side overhead bin, with the simulation showing an earlier peak. Peak loads in the simulated structural supports of the overhead bins also matched extremely well with the experimental data. A key variable in the simulation was the luggage, whose properties, under dynamic loading, were unknown. The luggage was modeled as viscous foam, and validation of the luggage model comes largely from a comparison of under-floor crushing with experimental data, both in terms of timing and magnitude of vertical displacement. Simulation results showed the luggage dissipates approximately 35% of the impact energy. Under-floor luggage or the lack thereof, is therefore a significant factor in the crashworthiness of large transport aircraft. Simulation results also indicated that the frames dissipate 33% of the impact energy, with the balance of energy dissipated throughout the remainder of the airframe.

Other impact conditions were also studied through simulations. The effect of roll angle at impact, the effect of removing the luggage from the under-floor compartment, and the effect of combined longitudinal and vertical loading were all studied.

Overall, the simulation results compared extremely well with those of the experimental drop test in terms of peak acceleration values and crushing patterns. A detailed study of the simulation results provided an increased understanding of the impact event and permitted the correlation of acceleration pulses with the observed buckling and crushing of the under-floor structure. The analysis of energy dissipation for individual structures, only possible through simulation, provided guidance for future energy-absorbing configurations. Finally, the current study provides the basis for a method of analyzing an aircraft impact event, including fuselage structure, cabin items, luggage, and seats. Acceleration profiles from the simulated seats may be used as input to occupant injury models, or alternatively, anthropomorphic test dummy models may be incorporated in the current simulation directly.

1. INTRODUCTION.

While the history of aviation crashworthiness dates back to the earliest days of powered flight, modern systematic studies of survivability arose in large part from the experience of the U.S. Army in the 1960s. It was observed that numerous army helicopter crashes had resulted in serious injuries or fatalities, even in cases where the velocity at impact was relatively low. A series of studies were initiated to determine such basic issues as the causes of these fatalities, and subsequently, the range of impact conditions for which fatalities could be prevented. As expected, it was determined that the vertical force experienced by the occupant during impact was a key factor in many fatalities [1]. The military has since been deeply involved in developing crashworthiness standards.

The same impetus exists behind crashworthiness studies for commercial aircraft. Although crashworthiness features have been incorporated into many new designs, primarily in helicopters, and while certification requirements continue to evolve to push for greater survivability, there is still potential for improvement.

Current crashworthiness research focuses experimentally on issues such as component testing of seats and energy-absorbing under-floor structures, and on assessing occupant injury with test dummies. Numerical analysis is also used to study these issues. However, impact testing of completely instrumented air vehicles is extremely expensive and time consuming, and such studies are not frequently conducted. Partly because of this, a detailed numerical simulation of an aircraft impact has yet to be performed.

In the automotive industry, however, crashworthiness testing is an important and highly visible component in any new design. Complete vehicle testing is routine, and now is coupled with numerical simulations of the full vehicle, including occupants, in a number of different impact conditions. Simulations permit a significant reduction in the number of required experimental tests, as the simulation may be used to study a variety of designs and impact variables.

In the aviation industry, there is a relative lack of basic experimental data on the impact response of transport aircraft under survivable crash conditions. This has been addressed by the Federal Aviation Administration (FAA), which has initiated a series of crashworthiness tests at the FAA William J. Hughes Technical Center, Atlantic City International Airport, New Jersey. These tests involve vertical impacts of commuter airframes, regional transports, and fuselage sections of large transport aircraft. The objective of these tests is to characterize the impact response of these airframe structures and their associated cabin components.

Parallel to the test program is an effort to develop a finite element (FE)-based crashworthiness modeling and analysis procedure for the pre- and posttest analyses. Such a modeling and analysis procedure should provide additional insight into the detailed acceleration time histories of the fuselage structures. It should also show the overall pattern of deformation as a function of time, highlight potential failure sites, and provide a more detailed understanding of the dynamic response of large, complex, airframe structures subjected to impact loading.

Crashworthiness modeling is intended to complement experimental impact testing. Crashworthiness models, once validated, can be used to study other impact conditions, thus reducing the need for extensive experimental testing. Such models can also be used to provide guidance for future testing conditions or configurations. Furthermore, a validated modeling methodology can be used as a basis for simulating other airframes that are of interest. The FE simulation approach is also well suited for studying a variety of crashworthiness-related issues and a range of design options. Simulations can be used to study the effects of individual components on the dynamic structural responses of the fuselage, such as cargo door reinforcements, the content of the cargo, the type of overhead bins used, seat configurations, or gross weight. The effect of varying either geometry or structural materials can be readily analyzed by observing the impact response of the fuselage, cabin components, and occupants.

The first objective of the current study was to develop an FE model to simulate a 30-ft/sec vertical drop test of a 10-foot-long Boeing 737 fuselage section containing two different overhead stowage bins. The drop test was conducted in November 2000 at the vertical drop test facility located at the FAA William J. Hughes Technical Center. Acceleration time histories were calculated at selected locations on the floor, frames, and overhead stowage bins, corresponding to sensor locations in the test article. These results were compared with the data recorded in the actual drop test to validate the performance of the simulation.

The validation itself is a major objective, as there is still a very small body of dynamic impact simulations that have been studied in detail, compared to experimental testing. Validation of the current study will not only incrementally increase confidence in aviation crashworthiness simulations, but will also assist in guiding future studies, even in such basic issues as mesh density. Kindervater [2] writes that it is not practical at present to conduct a detailed simulation of a complete aircraft. This is true, using the mesh density currently employed by the automotive industry. While guidelines do exist for modeling automotive structures for impact analysis, strict use of these guidelines in aircraft will lead to unrealistic model sizes. However, by focusing attention on critical structural supports, those members most responsible for energy dissipation and for transmitting impulses to the occupants and cabin, it may be possible to reduce the model size to a level manageable with current computing resources.

The goal in the present case was not to attain a fully convergent simulation, but to adopt a level of detail needed to capture the basic buckling and crushing behavior of the fuselage structure and to capture the basic acceleration pulse experienced by critical cabin items and occupants. In this regard, the goal was to employ a level of detail that could realistically be extended to a complete aircraft simulation.

The second objective was to study a selected set of key simulation parameters, to determine basic guidelines for performing future crashworthiness simulations of air vehicles. Issues studied included friction between the fuselage and impact surface, modeling of luggage, possible degradation of material yield strength due to corrosion and fatigue, and the use of an element failure criterion.

The third objective was to use the validated simulation to study a range of impact conditions. Experimental tests provide valuable data for a given impact condition and test configuration, but are not practical for studying a variety of conditions. Numerical methods, however, are ideally suited for analyzing issues such as changing roll angles, effect of luggage, and combining longitudinal and vertical impact conditions.

Future efforts could employ the present methodology to perform an aircraft impact simulation, including not only the fuselage and cabin items, but also the occupants. With such a simulation, the methodology would be in place to perform complete vehicle crashworthiness design studies and to analyze and select the best possible designs for optimizing occupant survivability.

2. REVIEW OF CURRENT RESEARCH.

2.1 PURPOSE OF CRASHWORTHINESS STUDIES.

The interest in aviation crashworthiness extends to the earliest period of flight. This interest was initially motivated by the simple observation that pilots occasionally survive impacts that have proven fatal to others, and that the velocity at impact is not the only factor to explain this difference in outcomes. An excellent review of crashworthiness history, beginning with the pioneering days of aviation, is provided by Waldock [3]. He notes that the first systematic statement of crashworthiness principles is attributed to Hugh DeHaven, who may be considered the father of aircraft crashworthiness. DeHaven's own interest in survivability arose from his crash following a midair collision, an event in which the other pilot was killed. Waldcock cites DeHaven's four basic principles, which are modeled on observations of the freight and packing industry. The four principles are quoted below:

> "1) The package should not open up and spill its contents, and should not collapse under expected conditions of force.
>
> 2) The packaging structures which shield the inner container must not be made of brittle or frail materials; they should resist force by yielding and absorbing energy.
>
> 3) Articles contained in the package should be held and immobilized. This interior packaging is an extremely important part of the overall design, for it prevents movement and the resultant damage from impact against the inside of the package itself.
>
> 4) The means for holding an object inside a shipping container must transmit the forces applied to the container to the strongest parts of the contained objects."

As noted by Waldcock, the container in this case is the fuselage, the interior packaging is the seat and restraint system, and the objects inside the container are the occupants.

Modern crashworthiness studies seek to implement these same basic principles. Initial studies relied on experimental methods, while current studies frequently employ numerical methods in conjunction with testing. A summary of recent analytical studies in crashworthiness, while focused more on composite structures, is provided by Kindervater [2]. He offers a clear evaluation of the state of the art in numerical modeling and of current designs for crashworthy composite structures. With new materials and analytical tools, it is now possible to design lightweight, energy-absorbing composite structures.

2.2 BASIC APPROACHES TO NUMERICAL ANALYSIS.

Two distinct numerical approaches have been used in modern crashworthiness studies. The first is termed a hybrid FE code and is based on modeling an airframe with a lumped-mass spring damper system. The term hybrid arises from the fact that this code requires experimental or otherwise derived data to describe the impact response of the fuselage structure as it contacts the ground. Spring elements with load deflection curves are used to simulate crushing, and the fuselage is generally modeled very simply, with several hundred elements at most. An example of such a hybrid code is KRASH. Cranfield Impact Center used KRASH to develop the Air Accident Investigation Tool (AAIT). The advantages of codes such as AAIT are that they are relatively easy to use and simulations require little computational time, typically a matter of minutes. The disadvantage of such codes is that they require either substantial effort to accurately determine the spring parameters or the necessary experience and judgment to reasonably estimate these parameters.

The second approach is that of explicit FE codes, such as Pam-Crash, MSC Dytran, and LS-DYNA. These codes are based on fundamental engineering principles, and given correct material properties and geometry, require no prior experimental testing. In practice, however, it is frequently noted that experimental verification remains an important requirement [4]. In fact, validation of numerical analyses continues to be a critical concern, particularly for transient dynamic simulations.

2.3 COMPARISON OF AUTOMOTIVE AND AIRCRAFT CRASHWORTHINESS STUDIES.

While crashworthiness research has evolved a substantial body of knowledge in recent years, limited efforts have been directed at conducting detailed impact simulations of large transport aircraft. In contrast, the automotive industry now routinely includes numerical simulations of impacts as an integrated tool in the design process. In fact, fabrication of early test articles does not begin until crashworthiness simulations have been conducted. Volkswagen, for example, discusses their 10 years of experience with crash impact analysis in a paper published in 1994 [5]. Even at that time, with more limited computational abilities, Volkswagen was routinely employing FE methods and occupant injury models to simulate a variety of impacts with existing and proposed designs. Other manufacturers now also engage in numerical simulations of vehicle impacts on a regular basis. This integrated experimental and analytical approach reduces development time, and also permits study of a much wider variety of designs and impact conditions compared to experimental testing alone.

The situation in the aircraft industry is very different, in that no detailed and complete simulations are generally conducted of either large or regional transport air vehicles. This is not to suggest that no crashworthiness studies are underway in aviation. Rather, such studies are typically directed toward understanding specific issues or toward modeling of relatively small structures. Examples of these studies include a detailed simulation of crushing small riveted structures, impact response of small under-floor assemblies, dynamic buckling of beams, using energy-absorbing boxes or foam-filled structures, and designing energy-absorbing composite structures for use in general aviation aircraft. Also, the helicopter industry is heavily involved in crashworthiness research, both analytically and experimentally. Finally, extensive experimental studies and dynamic certification tests are performed with seats, while statically equivalent analysis is typically used to satisfy crash requirements for other assemblies or components within large transport aircraft.

While complete vehicle crash simulations for automobiles are now standard practice, Kindervater, among others, has noted that "rather surprisingly, much less attention has been paid to the development of FE simulation of aircraft structures under dynamic crash conditions, despite the extremely high cost of aircraft crash tests" [2]. Several reasons can be given for this situation. First, there is the acknowledged and very real need to better understand the details of impact modeling and component behavior, prior to conducting more comprehensive simulations. A sampling of such issues recently being studied include joint failure modeling [6]; design of foam-filled, energy-absorbing tubes and boxes [7], rate-sensitive material properties during inelastic failure during impact [8]; effect of damping on explicit dynamic computations [9]; impact failure of beams [10], dynamic buckling of beams [11], buckling of plates during medium-velocity impact [12], and dynamic failure criteria [13], among others.

Second, modeling full-size airframes, or even large sections of transport aircraft, presents noteworthy difficulties, such as limitations in model size and a general lack of access to detailed geometric information. In the early 1990s, a full automotive vehicle simulation involved 30,000 to 40,000 elements [5]. Ten years later, full simulations typically involve from 300,000 to 400,000 elements, possibly more. Even with this more generous limit, it is not generally considered feasible to model a full-size airframe to a similar level of detail. Thus, simplifications are required, such as not explicitly modeling rivets, substituting beam elements in place of frames, or stringers modeled with shell elements. Access to geometry is also crucial. For in-house studies, the automotive industry can access their own geometry and material database for use in FE models. Outside automotive research groups can and do fully disassemble an automobile, scan each part, and use the digitized data to construct a model. No one, however, has attempted to do this with a B-737, for good reason. While the required database for an aircraft model resides in The Boeing Company, such FE models for use in impact studies have not as yet been constructed.

Another possible reason for the lack of aircraft simulations is the more urgent need to study smaller general aviation and small regional transports, as these are typically lacking in crashworthy abilities. This poor crashworthy performance is due to the lack of available crushing stroke and, in many general aviation aircraft, to the limited ability of basic composite structures to absorb impact energy. Large transport aircraft perform rather well in attenuating

impact energy, at least in the vertical direction, as they possess substantial margins for crushing, coupled with the more generous ability of aluminum frames to dissipate impact energy.

Numerous studies, such as those of Jackson and Fasanella [14, 15, and 16], have been undertaken to address crashworthiness in smaller or composite airframes. These studies combine testing and simulation of composite structures to develop and verify new crashworthy design concepts. The combination of simulation and testing is an important part of the process. Simulations can assist in selecting, or possibly ruling out, proposed designs, and testing provides a point for validation of the modeling approach. The proposed design concept in this case was a partially foam-filled under-floor, though the exact geometry of the foam-filled section is a crucial variable.

A final difficulty in performing crashworthiness simulations of large airframes is the relative lack of experimental data with which to validate the model. There are noteworthy exceptions to this, one being the Crashworthiness Test Program being conducted at the FAA William J. Hughes Technical Center. This program has conducted fully instrumented tests of general aviation aircraft, regional transports, and sections of large transport aircraft. This provides an invaluable database for assessing crashworthiness simulations.

This database has been used, again by Jackson and Fasanella [17], in cooperation with the FAA. A vertical drop test was conducted of a 10-foot-long section of a B-737 fuselage section, with a conformal fuel tank attached under-floor. This drop test was simulated in detail, and the results were compared with experimental test data. The overall comparison of simulation and test results was generally good, with the simulation capturing many of the buckling details seen in the actual test. Some features of the test event were difficult to capture, such as the fracture of under-floor beams in contact with the fuel tank and the failure of the tank supports early in the impact event. This test and simulation represented a significant milestone in the path to a comprehensive and integrated study of crashworthiness of large transport aircraft.

Other models of transport aircraft have been constructed, but for the purpose of assessing the interaction of the aircraft and various ground structures that could be impacted. One such study was performed by Lawver [18], using beam and shell elements in complete models of a C-130 and C-141. This study focused on impacts into reinforced concrete and steel structures. Even with a somewhat less detailed model, the need to save computational time resulted in the use of half symmetry for the C-141 impact simulation. Further, the wings and engines were represented by adding weights in the wing box area. Although the effect of impact on aircraft cargo was evaluated, the primary focus was to assess the force-time history on the ground structure and to determine the degree of damage to be expected under different impact conditions.

2.4 EFFECT OF RIVETS ON CRUSHING OF UNDER-FLOOR STRUCTURES.

Numerous studies have been conducted addressing specific issues in crashworthiness, some of which are relevant to simulations of aircraft. The question of modeling joints and connections in an airframe structure has been discussed in detail by Marzenmiller [6], who notes that several options are available for modeling these joints. Nodal constraints and tied nodes are used to simulate spot welds, as typically found in automotive applications. Discrete beam elements may

be used to simulate rivets or bolts. The beam connects two adjacent structures, such as an angle and frame or frame and skin. Beam elements, representing rivets, may be given nonlinear plastic properties, along with a failure criterion. While Marzenmiller shows significant differences in loads transferred with the different joint modeling options, his study was conducted with a simulation of a small sample lap test.

Whether this level of detail is required for impact simulations is still an open question. A study by Bisagni investigated the impact response of a helicopter under-floor structure [19]. Bisagni constructed an FE model of the under-floor region of a new AGUSTA helicopter design, and subjected it to simulated impacts. The model included rivets modeled as beam elements, and included a failure criterion. Significantly, however, he studied the impact response both with and without rivet failure, and found that the peak and average crushing loads changed very little. He concluded that "rivet failure is not critical for the prediction of total crash response of the considered intersection," that is, an approximately square tube with riveted edges. Both simulated cases compared well with experimental data.

Vignjevic and Meo simulated an under-floor structure of a helicopter in a water impact [20]. The structure was a slightly simplified version of the Lynx helicopter. In this simulation, rivets were ignored, and beams and bulkheads were joined directly, on an element by element basis. While the focus of their study was the effect of water on impact response, the results showed reasonable behavior and good agreement with the available experimental data. In the conclusions from this paper, Vignjevic proposes adding rivets to a more detailed version of his model to assess the effect of including rivets with a failure criterion. The final results from this work are not yet available.

2.5 ANALYSIS OF ENERGY ABSORPTION.

A significant advantage of FE impact simulations, in comparison to testing, is that it is possible to identify and optimize energy absorption of individual components within a structure. In a study of an energy-absorbing guardrail, Reid [21] employs an explicit FE approach to determine exactly where and how the impact energy is absorbed and dissipated. Subcomponents of the guardrail system were modeled first and impacted with a simulated moving deformable barrier and simplified vehicle model. The complete sequentially kinking terminal was then modeled, and an impact simulation was conducted with an existing pickup truck model from the National Crash Analysis Center. A small car model was also used in a simulated impact. After validating the simulation through comparisons with experimental data, the results were analyzed to determine which components were most responsible for energy absorption. Energy dissipation comes from the guardrail, the sequentially kinking terminal head, wooden posts, and the impacting vehicle, as well as friction. By carefully assessing the energy dissipated for each component, it was possible to identify critical design features and to focus efficiently on optimizing the most important design components. This is a key advantage of the FE method. It is very difficult to determine experimentally the conversion of kinetic energy to internal energy for individual components of a structure during impact.

In a similar study, Altenhof investigated the energy absorption characteristics of a steering wheel armature during impact [22]. Altenhof also noted that "experimental methods do not provide a method of determining the energy absorbed by any single entity" in the case of impact involving deformable bodies. Numerical methods, however, are well suited to quantifying energy absorption of individual components involved in an impact. Using these methods permits crashworthy evaluation and improvements in steering wheels early in the design phase. This study simulated the impact between a deformable body and a steering wheel and was validated with comparisons to experimental data. The simulation results were analyzed to determine the critical components in dissipating energy during impact. Again, this permits designers to focus on these critical components and to efficiently optimize their designs for energy absorption.

2.6 SEATS.

While this report does not address the issue of energy-absorbing seats, it must be noted that seats are a critical component of any crashworthy design. Accordingly, extensive dynamic seat testing is conducted by the FAA, as well as other groups. These tests include seat certification tests, as well as testing novel energy-absorbing seat designs [22-25].

Hooper and Ellis summarize the crashworthiness issues and regulatory requirements for seats in both small and large aircraft [26]. These requirements include two dynamic test conditions for seats with dummy occupants. The first test condition employs combined vertical and longitudinal loads, and the second test condition employs combined longitudinal and lateral loads. A peak acceleration of gravity (g) level and pulse duration is specified for each test, depending on the aircraft type, and maximum permissible injury criteria are specified.

While seat testing is currently the only available method of certifying seat performance during impact, numerical methods are also used to study occupant response in order to predict injuries. MADYMO is a common analytical tool used for occupant modeling [27]. MADYMO uses rigid-body ellipsoids to model test dummies, and currently has a library of validated models to represent numerous test dummies. Interaction between the rigid bodies and the surrounding FE structure is given by predefined, experimentally derived contact parameters. MADYMO excels in duplicating the kinematic behavior of test dummies by accurately representing the joints and relative motions of body segments. MADYMO is also used to predict potential injuries by calculating, for example, lumbar or femur loads during impact.

The primary drawback of MADYMO is that the program is based on rigid, nondeformable bodies, and therefore cannot accurately simulate the interaction between deformable bodies. While MADYMO can use LS-DYNA as a subroutine, the interaction between the FEs and the rigid occupant model must be specified with known parameters. To alleviate this problem, work was initiated on an FE dummy model, and a series of such models are now available. There are two primary drawbacks in the adoption of FE occupant models. First, the joint descriptions and resulting kinematic motion are more difficult to capture with an FE model. Second, the use of a complete and detailed FE dummy model is computationally intensive. This is a reasonable concern, as the FE dummy model must be included in an already large and detailed vehicle model. It is likely that both of these difficulties with FE dummy models will be overcome with continuing advances in computing capabilities.

In summary, one of the clear advantages of numerical studies is noted by Bisagni, who writes that "finite element analysis can be used to aid the designers in evaluating the crashworthiness of different structural concepts, and can therefore be an important means of reducing development costs" [19]. However, this is from a paper published in 2002, and illustrates the degree to which the aviation industry lags in adopting more widespread use of numerical simulations. Kindervater, in 1999, also notes that FE codes, "although well accepted in the automotive industry, are not yet established in the aircraft industry" [2]. Furthermore, despite the fact that calls are widespread for an integrated systems approach to crashworthiness, tests are still conducted on a component basis, with limited efforts to evaluate complete designs, from airframe to occupants. Static testing or hand analysis is used to satisfy the crashworthiness requirements for individual cabin items to remain adequately fixed during impact. Current crashworthiness certification of seats is done exclusively with experimental tests, though efforts are underway to employ numerical methods in conjunction with testing. Thus, a complete and predictive vehicle impact simulation, including accurate modeling of the airframe, cabin components, seats, and occupants, remains a goal in aviation crashworthiness studies.

3. DESCRIPTION OF THE TEST ARTICLE.

Figure 1 shows the vertical drop tower test facility. The 10-foot-long B-737 test section is also shown in the figure. The test section dropped from a 14-foot height, resulted in a 30-ft/sec initial impact velocity. The test section includes seven frames that are spaced 20 inches apart. The location of each frame is identified by a fuselage station (FS) number, which indicates the distance in inches from a forward reference point. A higher station number indicates a position closer to the rear of the aircraft. The frames in this test article range from FS 380 to FS 500.

Figure 1. Vertical Drop Tower Test Facility at the FAA William J. Hughes Technical Center

Figures 2 and 3 show the front and aft views, respectively, of the test article before the drop test. The test article includes a floor in the passenger compartment supported by seven under-floor beams that are attached to the seven frames. When preparing the test section, the adjacent fuselage structures in front of FS 380 and aft of FS 500 were removed, resulting in a loss of structural stiffness of the test section. To compensate for the missing stiffness, and reduced structural support, a second under-floor beam was added under the beam at each end of the fuselage section, at FS 380 and FS 500, respectively. These two beams served to compensate for end effects.

Figure 2. Front View of the B-737 Fuselage Section Before Drop Test

Figure 3. Aft View of the B-737 Fuselage Section Before Drop Test

Three rows of triple seats were installed on each side of the test section in the passenger compartment, with twelve mannequins and six anthropomorphic test dummies (ATD) occupying the seats. The seats were anchored to four longitudinal floor tracks, two on each side, that are part of the floor. A close-up end view of a floor track is shown in figure 4. The luggage compartment beneath the floor was completely filled with luggage, as shown in figures 2 and 3.

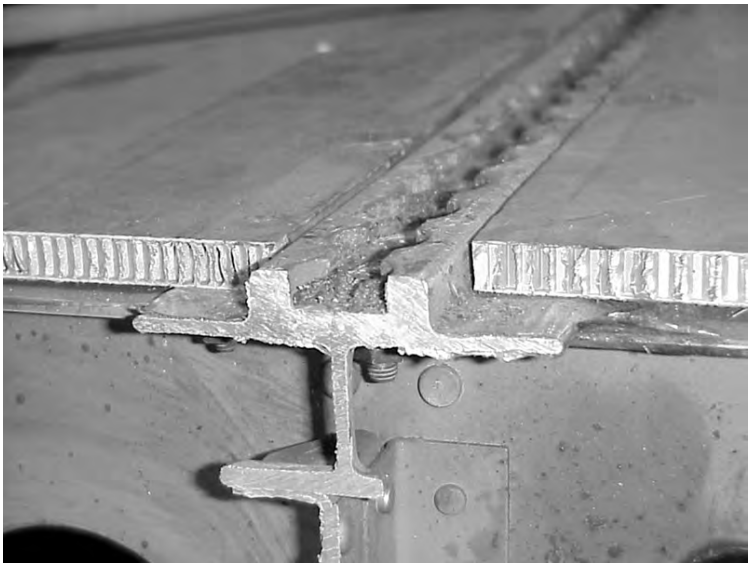

Figure 4. End View of One of the Four Floor Tracks

A significant feature of the fuselage section is a cargo door located on the lower right side. Figure 5 shows an interior view of the cargo door. The cargo doorframe is heavily reinforced, making the structure on the lower right side of the fuselage section much stiffer than the lower left side. This stiff cargo doorframe has a significant effect on the deformation and acceleration of the fuselage structure and its components, as observed during the actual drop test.

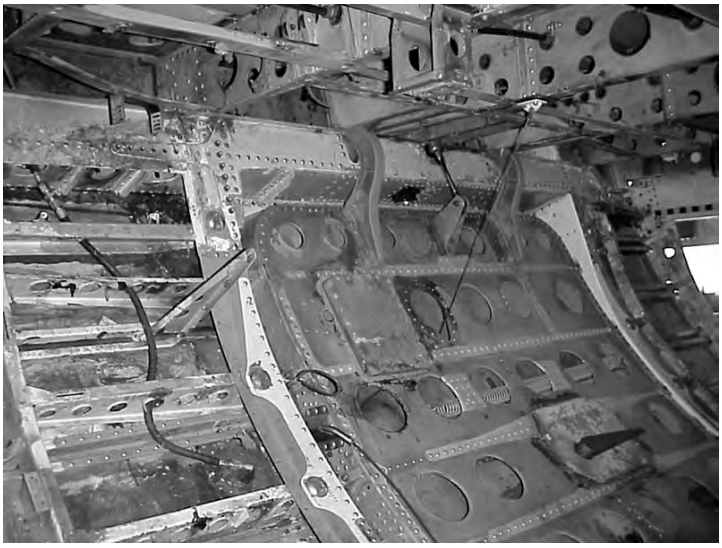

Figure 5. Internal View of the Cargo Door

Two different overhead stowage bins were installed in the fuselage section. A Hitco bin is on the upper left side, and a Heath Tecna bin is on the upper right side, as shown in figures 6 and 7, respectively. These two bin designs are currently approved and certified by the FAA. The major goal of this drop test was to determine the reaction of these two bins to a severe, but survivable, impact condition. This impact condition was well in excess of the bin certification requirement, which is based on withstanding an equivalent static load of 5 g's. Therefore, the bins and their supporting structures had to be modeled carefully. Both bins were approximately 60 inches long, extending from FS 410 to FS 470.

Figure 6. Hitco Bin Installed on the Left-Hand Side of the Fuselage

Figure 7. Heath Tecna Bin Installed on the Right-Hand Side of the Fuselage

The primary vertical support for the Hitco bin was provided by two vertical tie rods located at the forward and aft ends of the bin. The top end of each tie rod was connected to a horizontal cylindrical rod, which was then mounted to the frames. Outboard support of the Hitco bin consisted of a pair of short beams that were connected to the forward and aft outboard edges of the bin, and vertical and horizontal links at each end of the beams that were connected to the frames. The vertical links provided additional vertical support, while the horizontal links provided the inboard/outboard supports for the bin. Figure 8 shows the supporting structures at the forward end of the Hitco bin. A drag strut, which is not shown in the figure, provided the longitudinal support for the bin.

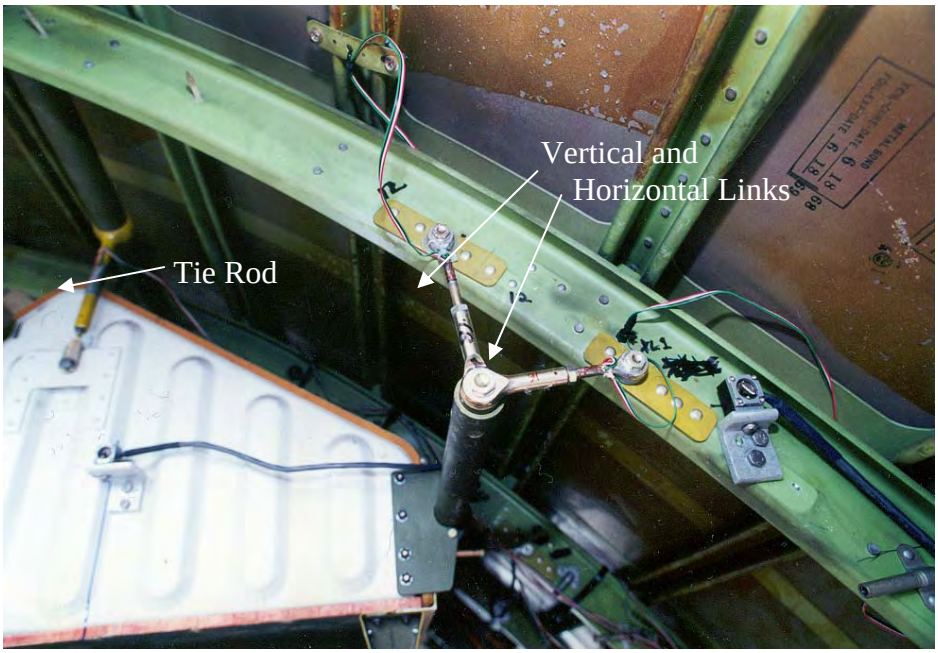

Figure 8. Hitco Bin Supporting Structure With a Tie Rod on the Left and Links on the Right

The primary vertical support for the Heath Tecna bin was provided by two vertical struts located at the forward and aft ends of the bin. Each vertical strut was attached to an overhead C-channel that was fixed to the frames. Outboard support of the bin was provided by a longitudinal channel that was fastened to the outboard edge of the bin. The channel extended from FS 400 to FS 480 and was attached to the frames with five L brackets, each consisted of an inclined A leg and a horizontal B leg. The B legs provided inboard/outboard support, while the A legs provided both inboard/outboard and additional vertical support for the bin. Figure 9 shows the supporting structures at the forward end of the Heath Tecna bin.

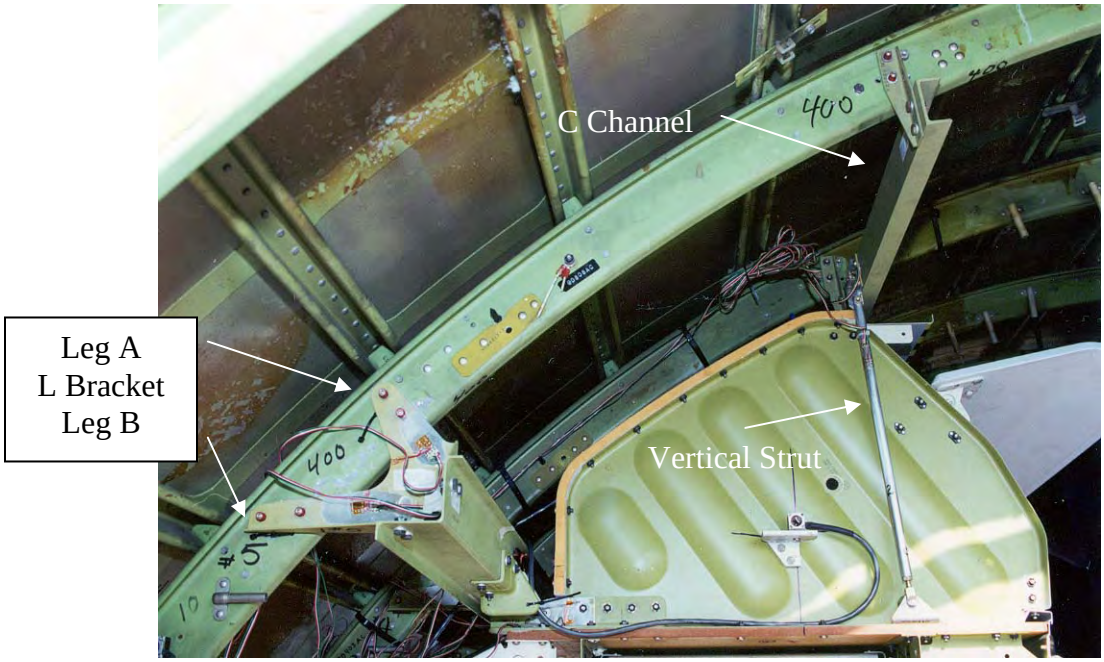

Figure 9. Heath Tecna Bin Supporting Structure With an L Bracket on the Left

Each bin was loaded with wooden blocks to simulate luggage. The Hitco bin weighed 57 lb and was loaded with 200 lb of wood blocks, as shown in figure 10. The Heath Tecna bin weighed 56 lb and was loaded with 120 lb of wood blocks, as shown in figure 11.

Figure 10. Wood Blocks Stowed in Hitco Bin

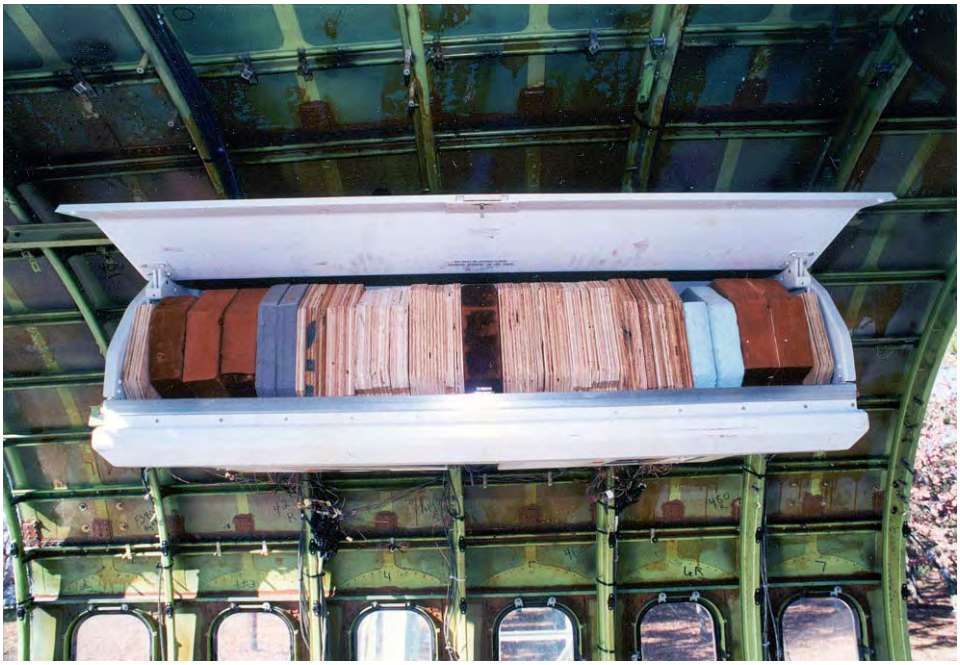

Figure 11. Wood Blocks Stowed in Heath Tecna Bin

Two cameras were installed on two overhead camera mounts. One was attached to frames at FS 380 and FS 400, and the other to frames at FS 480 and FS 500. The cameras were used to record the fuselage interior responses during the drop test. It was noticed after the drop test that the heavy cameras and the camera mounts caused considerable plastic deformation in the frames. It is therefore important to include the cameras and the mounts in the FE model to account for their effect on the responses of the neighboring structure and components, such as the overhead stowage bins.

The test article was instrumented at various locations with strain gages and accelerometers to record the strain and acceleration histories during the drop test. In the simulation, accelerations and forces were calculated at the same locations for comparison with the recorded data.

4. DESCRIPTION OF EXPERIMENTAL PROCEDURE.

The experimental procedure and choice of instrumentation for the drop test was determined by the FAA Crashworthiness Research Group. The test plan was based on their substantial experience in crashworthiness testing of commuter, regional, and large transport aircraft. Following is a summary of the instrumentation and data acquisition tools employed in the current test. This summary is based largely on information supplied by the FAA in a report on the vertical drop test of a B-737 narrow-body fuselage section [28].

Instrumentation for this test included 32 Endevco model 7231C-750 accelerometers mounted on the overhead stowage bins, floor tracks, and frames. Six ATDs were also instrumented with accelerometers located on the pelvis to record vertical acceleration pulses on the occupants. Six 50^{th}-percentile Hybrid II ATDs were used, one in each of the center seats. The ATD response,

however, was not the primary focus of this test. The seats used in the test were 9-g static certified.

Three contact switches were used to provide timing of the drop and impact initiation. One contact switch was mounted on the release hook, which held the fuselage prior to drop. Two contact switches were mounted on the bottom of the fuselage to determine the time of contact with the platform.

Strain gages were mounted on all supporting struts, links, and brackets for each of the two overhead stowage bins. Strain gages were mounted to capture axial loads only for each of the supporting members. A full Wheatstone bridge configuration was used.

Calibrations were conducted individually for each support and in a static testing condition. Individual calibrations served to determine the sensitivity of each support to use in programming the data acquisition system. The recorded test data were therefore reported as load data, rather than analog voltage.

Static tests of the assembled bins were used to determine the expected load distribution and perform a three-dimensional force balance to ensure that the previous sensitivity studies were accurate. Static bin tests were used to determine an influence coefficient for each supporting element. The influence coefficient represents the percentage of total load reacted by an individual support. These influence coefficients were later used to compare the difference in load distribution between static and dynamic loading conditions.

The drop test platform was also instrumented with 12 load cells and 12 accelerometers. This was done to determine if the platform response itself had an influence on the fuselage accelerometer results.

Two data acquisition systems were used to collect data from the test. An NEFF 490 was used to collect 77 channels of data, using a 10-kHz sampling frequency. A prefiltered cutoff frequency of 1 kHz was employed.

An EME DAS-48S was used to acquire 48 channels of analog data and 3 channels of digital data. A sampling frequency of 7500 samples per second was employed, due to software limitations. Again, all channels were prefiltered with a cutoff frequency of 1 kHz.

Timing of data acquisition was controlled and coordinated by an IRIG satellite-based time code receiver, which generated a pulse that was used to synchronize the two data acquisition systems. A pretrigger sampling mode was used to collect data beginning 2 seconds prior to hook separation. A Bowen 10-channel sequencer was used to initiate hook release and to coordinate all video and camera recording. Careful posttest comparisons of video and recorded test data confirmed the exact timing of impact.

With the exception of the ATD load cells, all test data were initially filtered with an SAE Class 60 (100-Hz) filter. The results from this filter, however, did not clearly delineate an acceleration pulse. The resulting acceleration time histories showed significant fluctuations, making it

difficult to determine the underlying acceleration pulse. Consequently, a 20-Hz filter, following the guidelines of SAE J211, was used to filter all test data. In this report, the 20-Hz filter is used for all accelerometer data.

5. DESCRIPTION OF THE FE MODEL.

An FE model for the 10-foot-long fuselage section of a B-737 airframe was developed using the PATRAN computer software code. Figure 12 shows the model from two different views. The model was constructed based on detailed hand measurements of the actual test article. It is noted that the current FE model does not include a detailed model of the luggage in the overhead stowage bins. Rather, the total mass of the wood blocks is distributed on a shelf inside the bins. Also, the camera masses are lumped onto the platforms of the camera mounts.

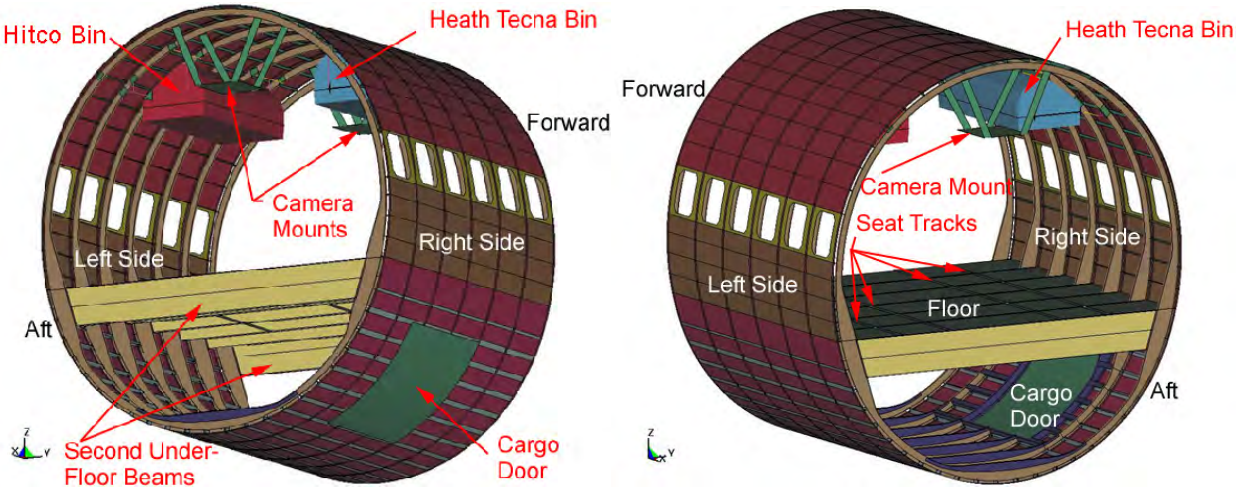

Figure 12. Test Section FE Model

The under-floor luggage was modeled as viscous foam. This model included nonlinear elastic stiffness coupled with a viscous damper.

The viscous foam equations used are:

$$E_t = E_0(V^{n1}) \tag{1}$$

$$vt = v_0(abs(1\text{-}V))^{n2} \tag{2}$$

Where E_t is the time-dependent value of E, v_t is the time-dependent value of the viscosity coefficient; E_0 = 0.6 lb/in^2 is the initial value for E (Young's Modulus); v_0 = 0.218 is the initial viscosity coefficient; V is relative volume, defined as ratio of current to initial volume; $n1$ = 4.0 is the exponent in power law for Young's Modulus; and $n2$ = 0.2 is the exponent in power law for viscosity.

The elastic stiffness limits total deformation, while the viscosity serves to absorb energy. The stiffness and damping are calculated at each time step, based on the current relative volume of the element and on the selected power law coefficients. Two different values for Young's Modulus (E) were tested, the results for which will be shown. The final selected value of E_0 in section 7 was 0.6 lb/in^2 (1.2 lb/in^2 was also studied). The initial viscous coefficient was 0.218, and Poisson's Ratio was 0.001.

Limited experimental data concerning luggage stiffness was obtained by Jackson and Fasanella [29]. Their original data is presented in the form of a load deflection curve (figure 13), which has been roughly translated into a representation of E (Young's Modulus) as a function of volumetric strain. Unfortunately, their experimental data end at 0.35, while the range of primary interest is from 0.4 to 0.6, with some elements reaching up to 0.7. Also, it must be noted that the experimental results drop off significantly at 0.35, showing highly nonlinear behavior.

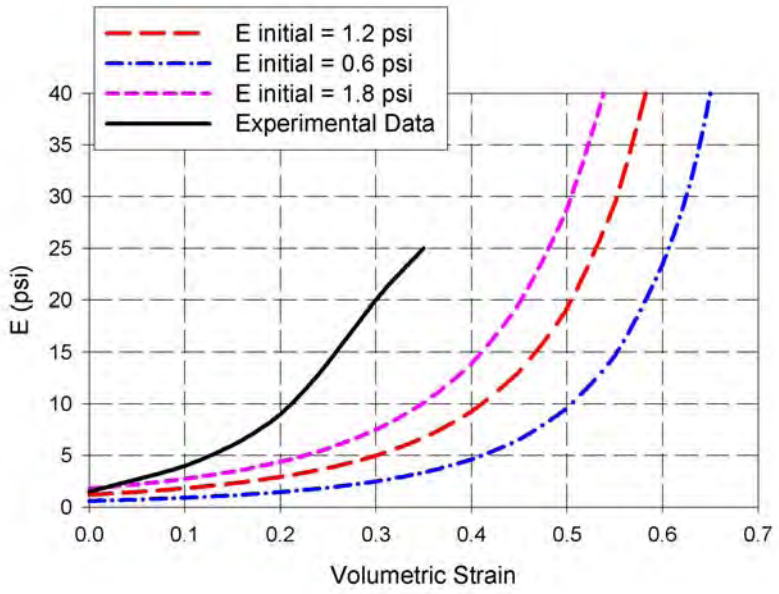

Figure 13. Luggage Stiffness as a Function of Volumetric Strain

The simulated under-floor luggage does not extend all the way out to the corners of the luggage compartment, as shown in figure 14. It was assumed that the corner portions of the luggage would not contribute significantly to energy absorption during impact. This assumption was based on the relative volume of the empty region, which was 18% of the total under-floor region, and on the observation that crushing at the corners is less significant than crushing in the center section. Also, modeling the luggage in these corner regions proved to be computationally very time-consuming. It is possible that including the luggage in these regions could have had a local effect on the pattern of bucking in the frames.

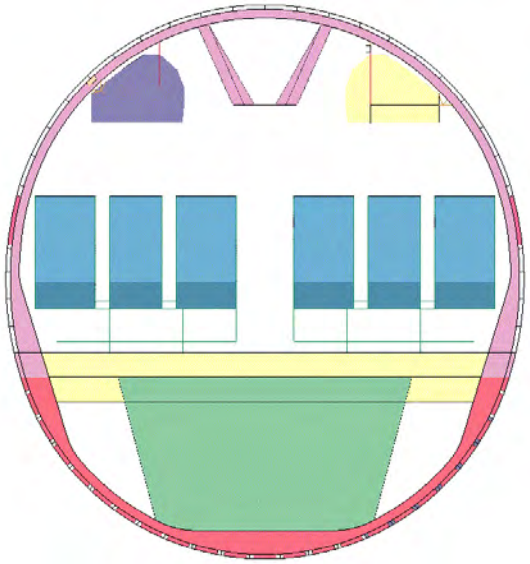

Figure 14. Front View With Simulated Luggage

The seat frames and surfaces were modeled with beam and shell elements. The masses of the ATDs and mannequins were distributed on the lower seat surfaces to approximate loading of occupants on seat cushions. This was done to simulate the delay that occurs in transferring inertial forces from the occupants to the floor tracks. Still, additional damping occurs with the seat cushions, but this effect was not included in the simulation. Material properties for seat bottoms and seat backs were estimated. Also, severe deformation, or collapse, of the seat structure will significantly affect the response of the frames and the floor. Figure 15 shows the seats in an angled view of the test article without luggage.

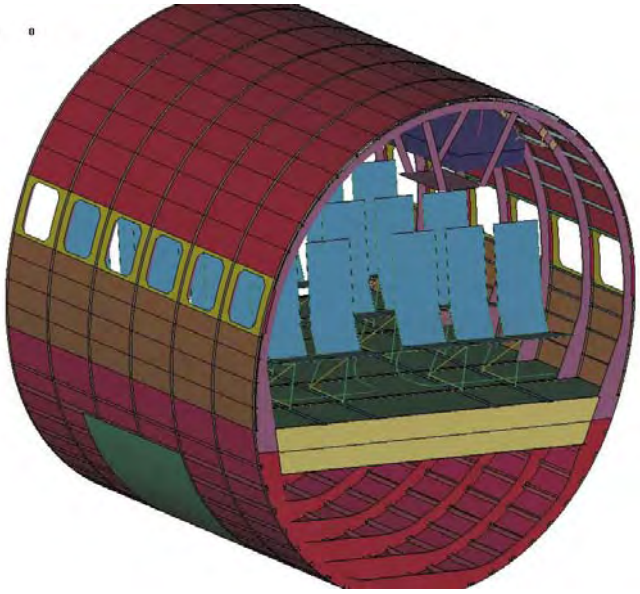

Figure 15. Front Angled View Without Luggage

An important area of the model was the cutout for the cargo door. The structure surrounding the cargo door was reinforced considerably. As shown in figure 16, areas of reinforcement included the upper and lower doorframes and the forward and aft edges of the door. These edges were reinforced with short beams, linking the door reinforcement with the closest frame. The forward edge of the cargo door aligns with the frame at FS 420. The aft edge of the door is located between frames at FS 460 and FS 480 and the short beams connecting the aft doorframe with the frame at FS 480. The short frame sections between the upper edge of the door and the floor were also reinforced at FS 420, FS 440, and FS 460, in the region directly above the upper door edge. The added stiffness on the right-hand side of the frames had a major effect on the overall response of the fuselage structure to the impact loading. Furthermore, as previously noted, the front edge of the cargo door coincides with the frame at FS 420, while the aft edge of the cargo door ends between the frames at FS 460 and FS 480. These two door edge support structures result in different load paths and considerably influence how impact energy is transmitted from the lower frames to the upper frames. The effect of the cargo door cutout, and of the reinforcing structure, is evident in both the actual and simulated impact results, as will be shown in section 7.

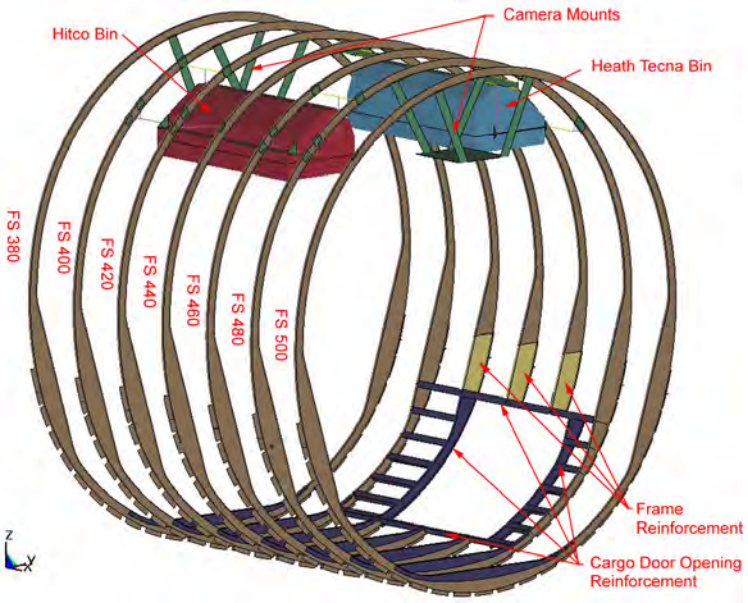

Figure 16. The FE Model Showing Frames, Cargo Door Reinforcement, Overhead Bins, and Camera Mounts

Shell elements were used to model the fuselage section, including the fuselage skin, the frames, the floor and its supporting beams, the cargo door, and the camera mounts. Using shell elements has the advantage of being able to more accurately simulate flange buckling and crippling during impact, as well as more accurately calculating the internal energy absorption.

Shell elements were also used to model the two overhead stowage bins and the C-channels that attach the struts of the Heath Tecna bin to the frames. All the other supporting structural members were modeled with beam elements. For the Heath Tecna stowage bin, these included the forward and aft struts, the longitudinal channel, and the two legs of each of the five L

brackets. For the Hitco bin, beam elements were used for the tie rods, the cylindrical rods, the short beams, the vertical links, and the horizontal links. Details of the modeling for the bins and their supporting structure are shown in figures 17 and 18.

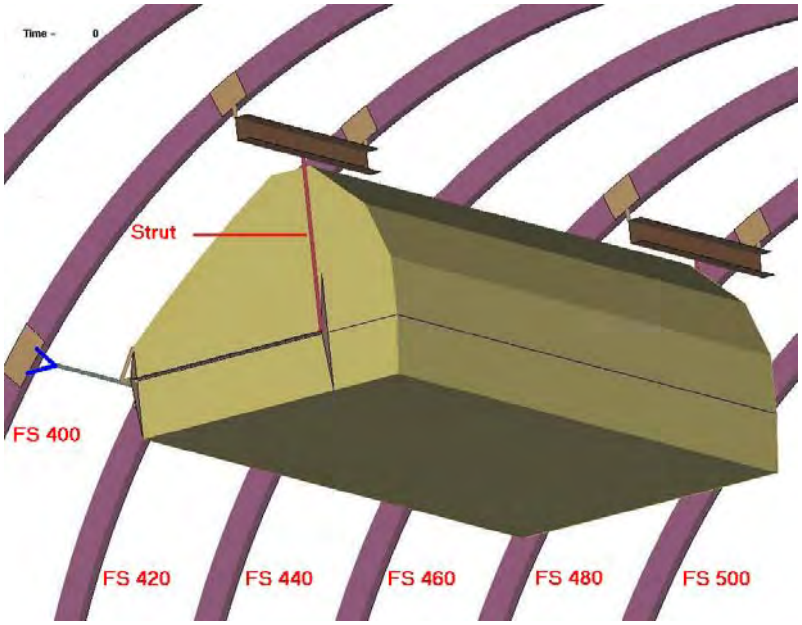

(a) View Looking Outboard

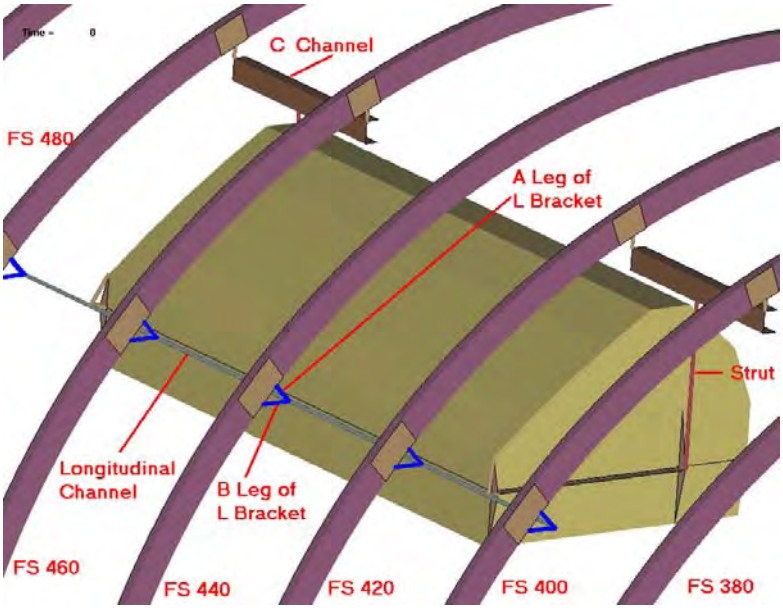

(b) View Looking Inboard

Figure 17. Heath Tecna Bin and Supporting Structure

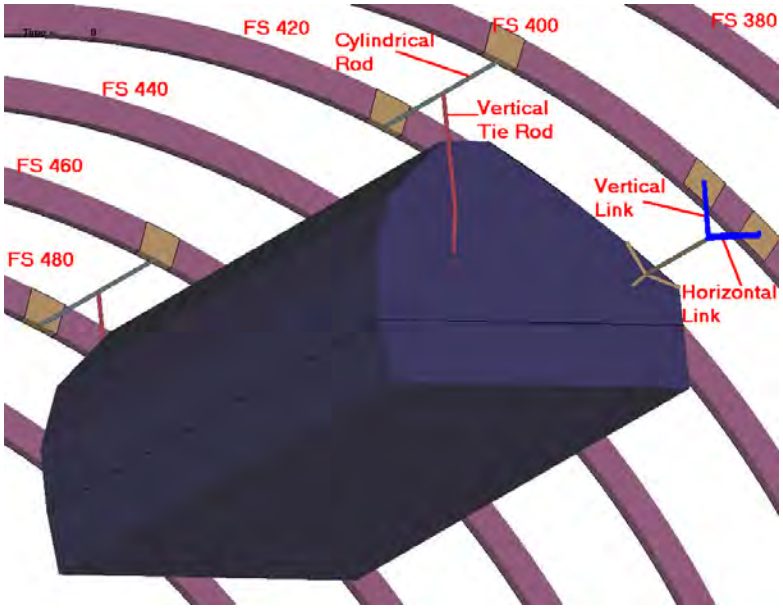

(a) View Looking Outboard

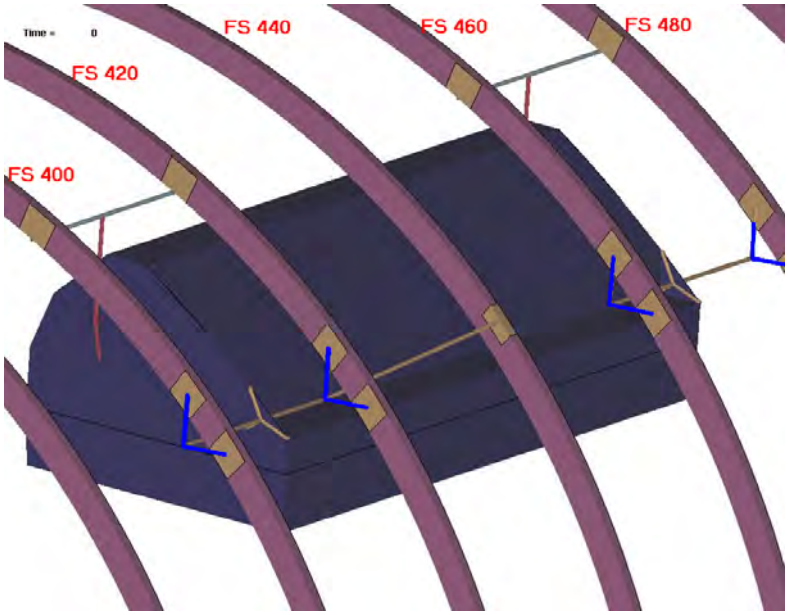

(b) View Looking Inboard

Figure 18. Hitco Bin and Supporting Structure

The overall FE model consisted of 68,007 nodes, 53,407 shell elements, 13,824 solid elements, and 691 beam elements. Shell elements employ a reduced-integration scheme in calculating element stiffness to enhance solution efficiency. As a routine procedure in this type of impact analysis, the viscous hourglass damping option was activated to prevent any potential spurious deformation modes. To accurately capture plastic deformation, five integration points through the element thickness were used.

The material properties used in the FE model are based on typical materials used in the construction of the B-737 fuselage. Aluminum 2024-T3, which possesses superior fatigue characteristics, was used for the skin panels. Aluminum 7075-T6, which is a high-strength alloy, was used for all other structural members. Material properties were taken from a standard aviation textbook. A point-by-point curve with 100 data points was used to represent the actual stress-strain curves of both aluminum alloys.

The total weight of the FE model is 8974 lb, and the total weight of the test article was 8870 lb. The weights of the significant mass items are listed in table 1.

Table 1. Weights of Key Items in Test Article and Simulation

Item	Test Article Weight (lb)	Simulation Weight (lb)
Fuselage section	1360	1355
Stowed luggage	3229	3300
Passengers, seats, and miscellaneous	3550	3596
Overhead bins and luggage	433	433
Cameras and mounts	298	290
Total weight	8870	8974

6. DESCRIPTION OF DROP TEST SIMULATION.

The simulation was performed with LS-DYNA, and the results were viewed in LS-POST. LS-DYNA is an explicit nonlinear FE code developed specifically for modeling impact and contact events. This code has been used extensively in the automotive industry for crashworthiness studies, resulting in a substantial body of knowledge of modeling techniques for crash and impact events.

One of the key parameters in performing the explicit time integration for the transient responses of a dynamic equation is the value of the integration time step, Δt. Based on the Courant-Friedrichs-Lewy condition [8], convergence of the solution can be achieved if Δt is set to be smaller than the time required for an acoustic wave to travel through the smallest element in the mesh, i.e.,

$$\Delta t \le L_c / C \tag{3}$$

$$C = \sqrt{E/\rho} \tag{4}$$

where L_c is the shortest dimension of the smallest element in the mesh, C is the speed of the acoustic wave in a material having Young's modulus E, and ρ is the mass density.

The initial value for Δt can be specified based on the length of the smallest side of any element. As the simulation proceeds, the value of Δt will be adjusted and updated based on the dimensions of the deformed elements. For this simulation, the initial Δt used was

4 microseconds (μs), which was adjusted by the program throughout the analysis. The final time step was 1 μs as the result of extensive element distortion. The simulations were carried out up to 500 milliseconds (ms), approximately the same duration as the actual drop test.

The initial velocity used in the simulation was 30 ft/sec. However, the contact algorithm in the FE code does not allow for the impacting surfaces to be in contact at time zero. For this reason, the fuselage section was placed at 0.1 inch above the impact surface at time zero. Consequently, the actual impact between the fuselage section and the impact surface occurred at approximately 0.28 ms. The effect of this 0.28-ms time delay is quite small, and it was therefore assumed that contact in the simulation begins with time = 0 (t = 0).

In the experimental drop test, the test article was dropped onto a wooden platform. In the simulation, the model was dropped onto a rigid floor to simplify the solution process. While small errors may occur in local stress distributions as a result of this approximation, its effect on the overall response and the acceleration time histories of primary structure should be negligible.

7. RESULTS.

7.1 ENERGY CONVERSION.

The test section consisted of several substructures, including the fuselage skin, frames, floor, under-floor beams, overhead stowage bins, and seats, as well as the luggage stowed in the cargo compartment. During the drop test, each component absorbs a portion of the kinetic energy and converts it to internal energy. More accurately, these structures dissipate, rather than store, the converted internal energy. By analyzing the percentage of kinetic energy that is transferred to individual structural components, it is possible to determine which components play the most significant role in absorbing and dissipating energy during the impact event.

Figure 19 shows the conversion of kinetic energy to internal energy, as calculated by LS-DYNA. It is shown that during the first 2 ms, no energy conversion has occurred, indicating that the structure is still deforming elastically. In fact, kinetic energy increases slightly, as the structure continues to accelerate under the effect of gravity. During the first 2 ms, the downward velocity of the test section is not affected by impact. Once the energy conversion begins to take place at approximately 3.0 ms, the total kinetic energy begins to decrease slightly as a result of energy dissipation through structural damping, but eventually approaches a value near zero at approximately 125 ms. At this moment, more than 95% of the impact energy has been converted to the internal energy. Therefore, even though the FE simulation has been carried out up to 500 ms, approximately the same duration as the actual drop test, most of the results will be presented up to 250 ms only, as all major deformation would have been completed by that stage in the impact event.

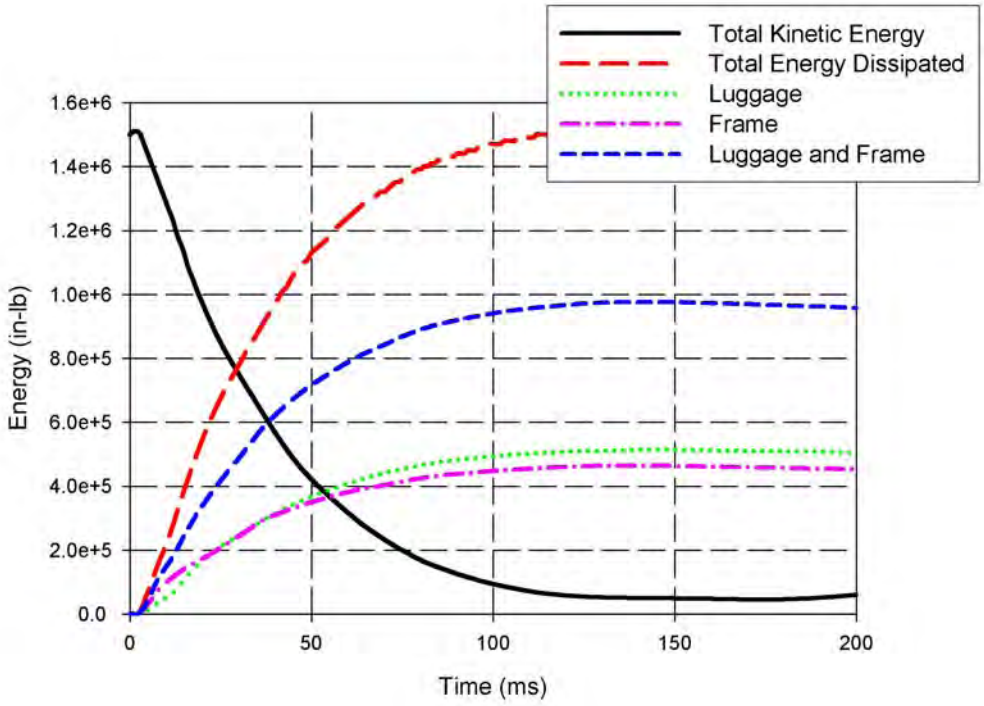

Figure 19. Dissipation of Kinetic Energy During Impact

Figure 19 also shows the amount of internal energy absorbed by the frames and luggage compared to the total internal energy. The frames alone dissipate approximately 33% of the total internal energy, making them the single most important structural component. The frames, therefore, have a dominant effect on the overall response of the fuselage section. Because of this, a careful examination of the deformation histories of the frames during the impact event can provide vital information for a better understanding of how other structural components respond. The simulation shows that an additional 35% of the impact energy was absorbed by the luggage, meaning that the luggage and frames combined account for 68% of the energy dissipation during impact. This indicates that the luggage is an extremely important factor in the energy absorption process in both the experimental and simulated drop test.

7.2 DEFORMATION HISTORY OF FUSELAGE FRAMES.

Figure 20 shows the deformation histories of the overall frames and the cargo doorframe region obtained from the FE simulation at selected time steps up to 140 ms. Also shown, at each time step, is the contour of effective plastic strain. The early time steps coincide with some of the key events that occurred to the frames during impact.

No plastic deformation was observed during the first 2.5 ms of impact, which agrees with the result of energy conversion, as shown in figure 19. At 3 ms, the bottom of the frame, which comes in contact with the rigid floor at t = 0, begins to deform plastically, as shown in figure 20(a). The plastic zone propagates upward along the frame as the impact event progresses. At 7 ms, the flanges of the lower frame section begin to yield due to the force of the luggage and the excessive deformation of the frames, as shown in figure 20(b).

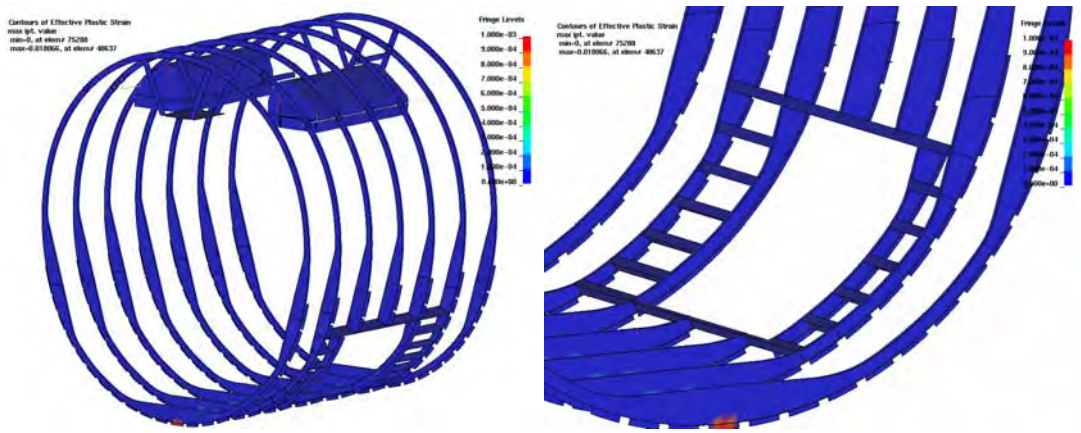

(a) Effective Plastic Strain at t = 3 ms

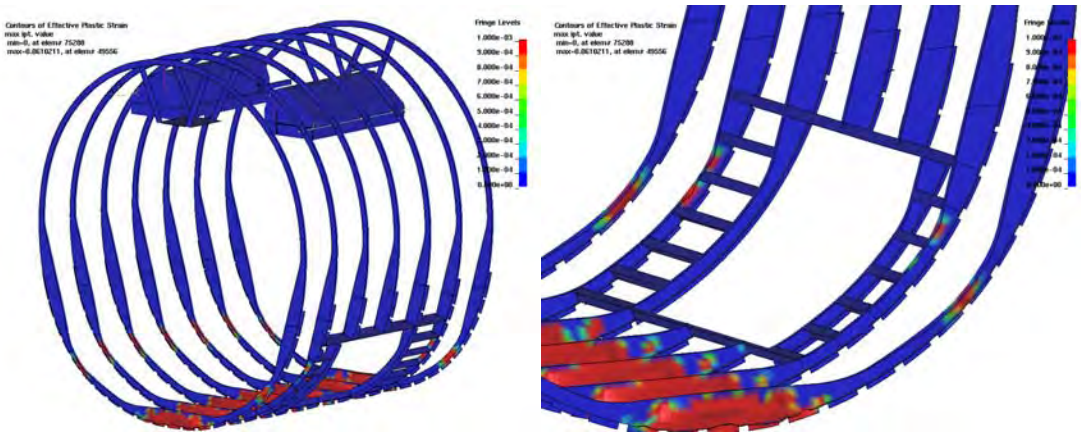

(b) Effective Plastic Strain at t = 7 ms

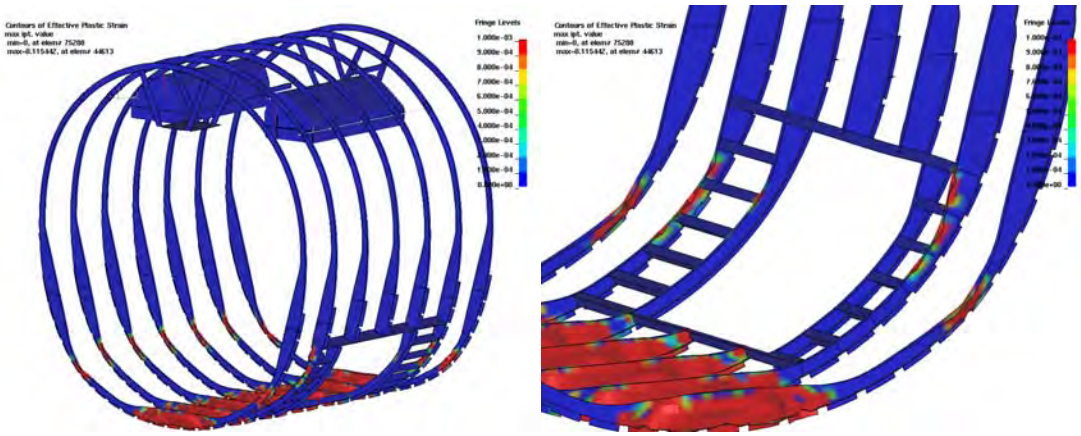

(c) Effective Plastic Strain at t = 13 ms

Figure 20. Effective Plastic Strain

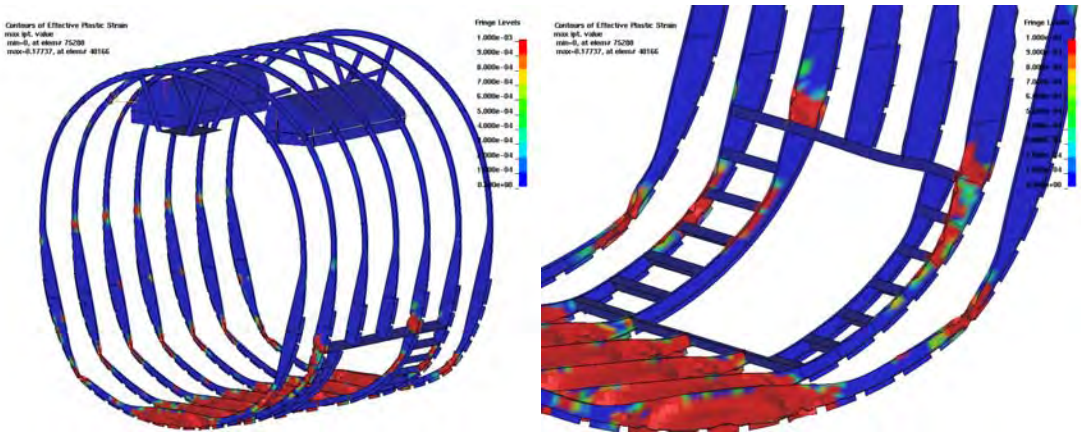

(d) Effective Plastic Strain at t = 20 ms

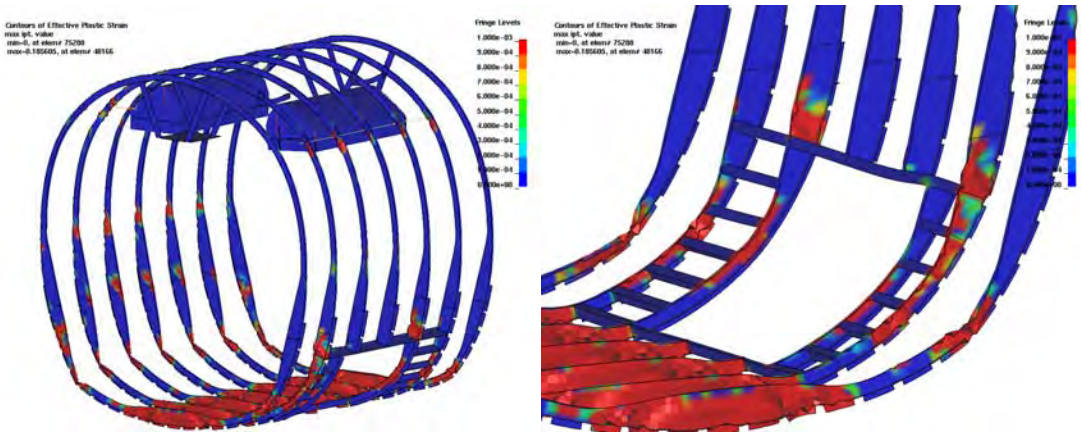

(e) Effective Plastic Strain at t = 30 ms

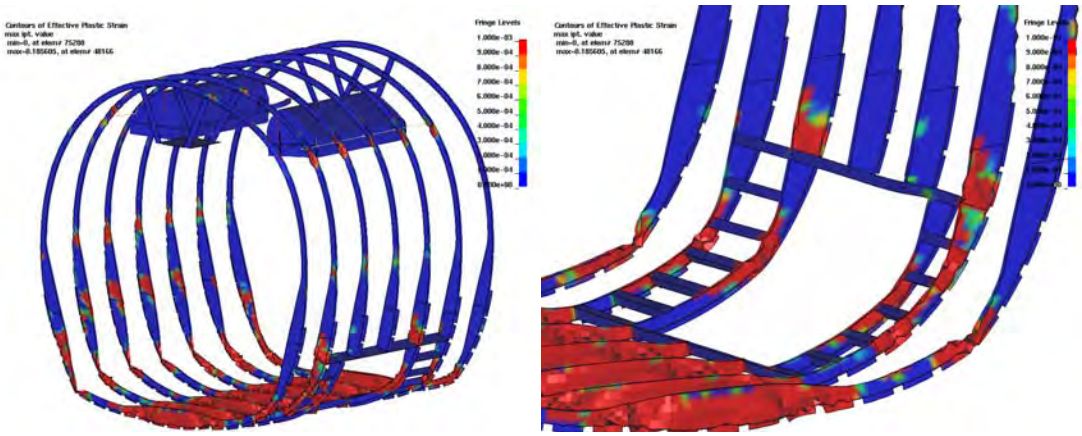

(f) Effective Plastic Strain at t = 40 ms

Figure 20. Effective Plastic Strain (Continued)

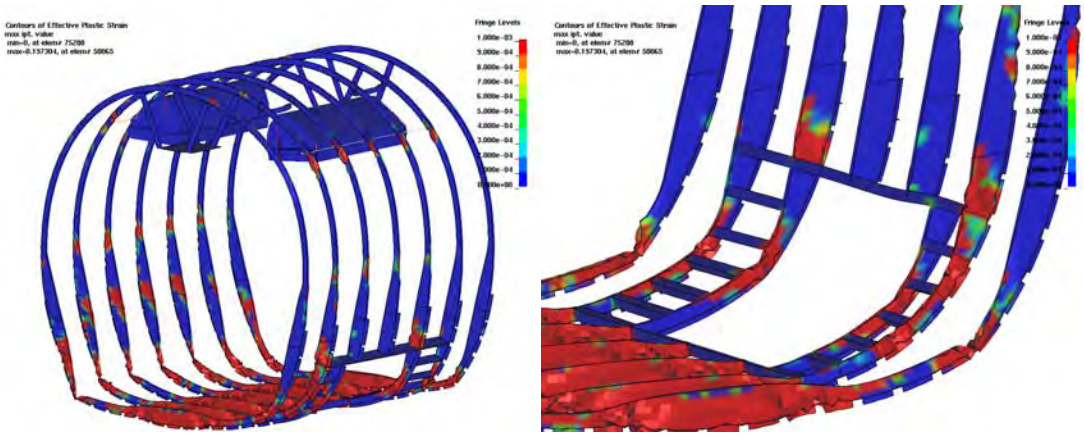

(g) Effective Plastic Strain at t = 50 ms

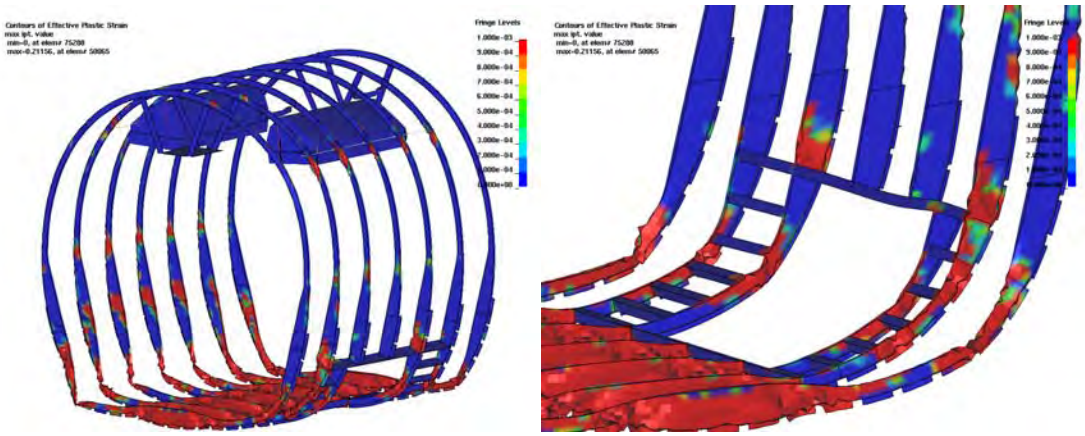

(h) Effective Plastic Strain at t = 60 ms

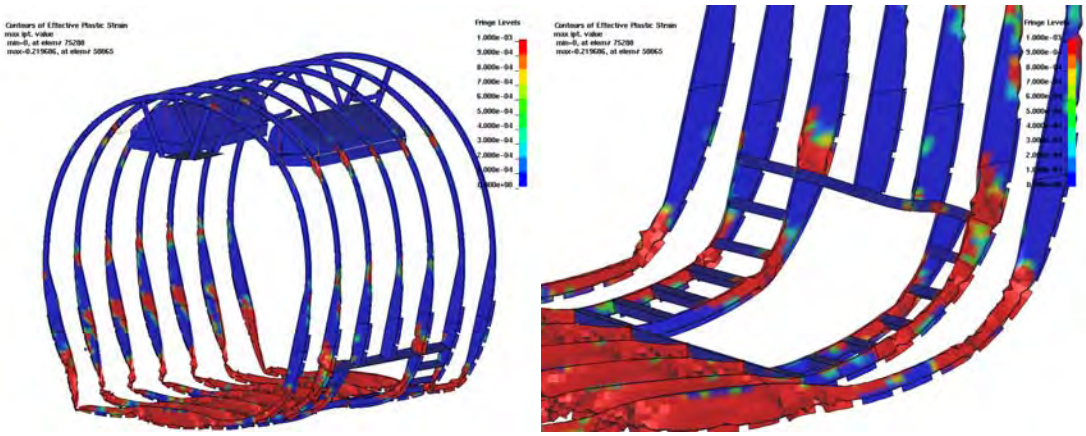

(i) Effective Plastic Strain at t = 70 ms

Figure 20. Effective Plastic Strain (Continued)

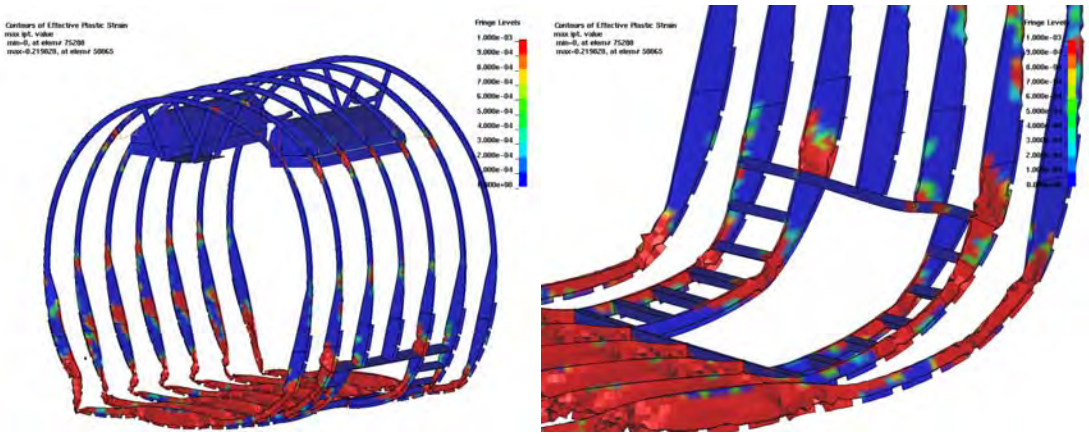

(j) Effective Plastic Strain at t = 80 ms

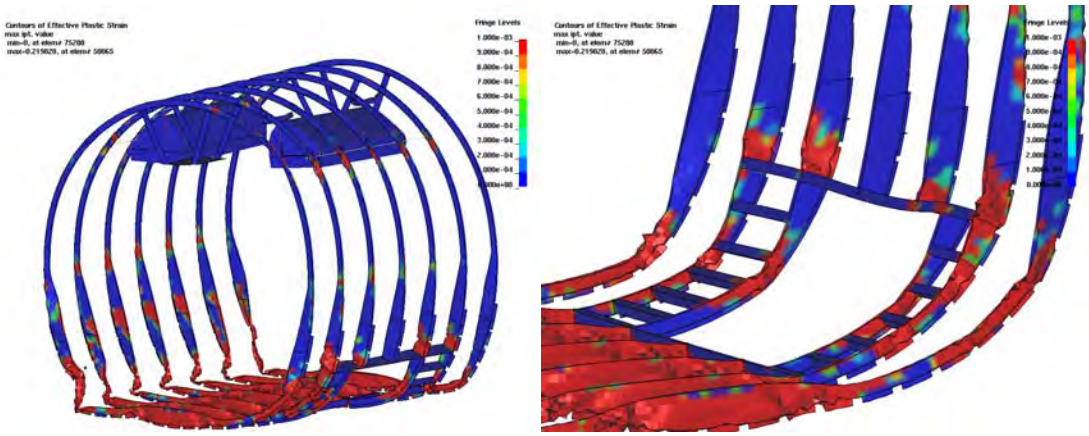

(k) Effective Plastic Strain at t = 90 ms

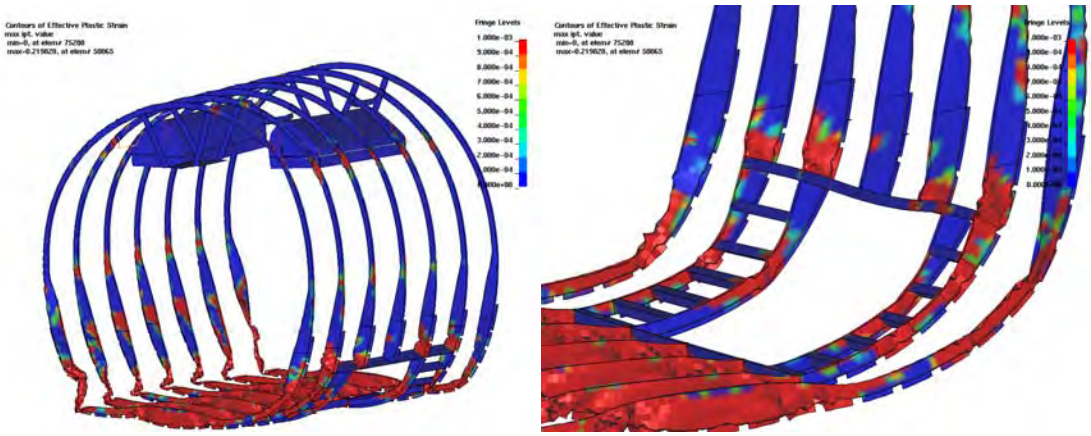

(l) Effective Plastic Strain at t = 100 ms

Figure 20. Effective Plastic Strain (Continued)

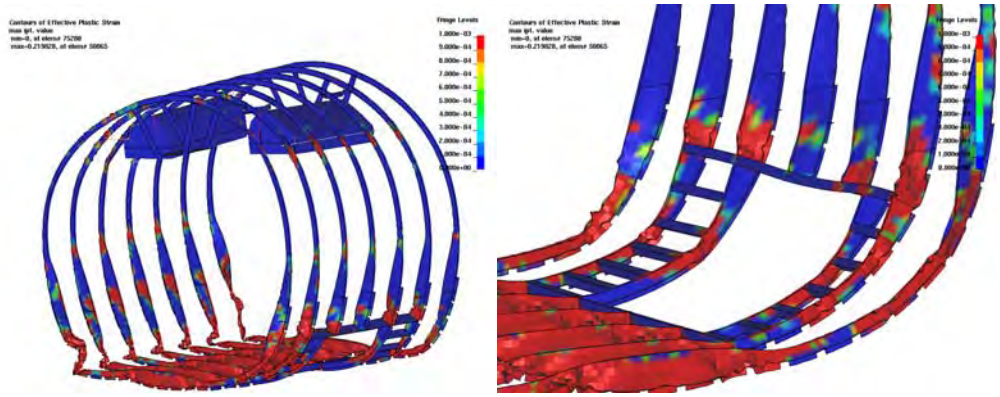

(m) Effective Plastic Strain at t = 120 ms

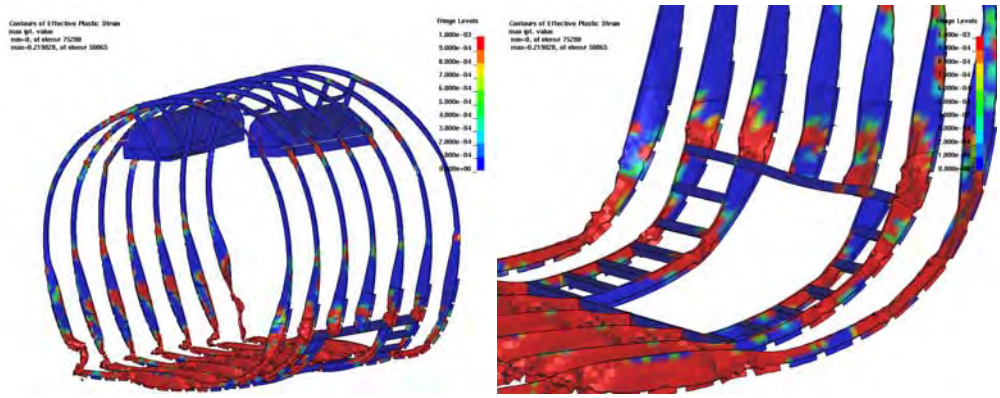

(n) Effective Plastic Strain at t = 140 ms

Figure 20. Effective Plastic Strain (Continued)

At 13 ms, the lower left and right corners (at approximately the 7 and 5 o'clock locations, respectively) of all frames, except the cargo doorframe, begin to yield. This is shown in figure 20(c). As the fuselage continues crushing, the bottom of the frame gradually flattens. At 20 ms, figure 20(d) shows that the flanges in areas with high plastic deformation begin to show signs of local buckling. For example, buckling begins in the forward and aft frames on the right side, while the cargo doorframe still shows very little deformation.

At 30 ms, figure 20(e) shows the lower left corners of all the frames are beginning to form plastic hinges. Plastic deformation is also seen developing on the left side just below the location of the window openings, and on frames at FS 380 and FS 500, where the extra under-floor beams are attached. On the right side, because of the stiff cargo doorframe, only the frames at FS 380 and FS 500 are forming plastic hinges. At this moment, even though the entire fuselage continues to move downward, impact energy is absorbed primarily by the plastic hinges that formed at the lower left corner of each frame. Significantly less energy is dissipated by the plastic deformation and local buckling that occurs at the lower right corners. As a result, the entire fuselage section begins tilting very slightly to the left. The upper portion of the structure experiences little deformation at this point in time compared to the lower portion.

At 40 ms, kinks have begun to form in the lower left corner of each frame, as shown in figure 20(f). These kinks appear where plastic hinges have previously formed. The plastic hinge on the right side of the frame at FS 380 deforms significantly less compared to the left side. This is because the cargo door frames limits buckling on the right side. Meanwhile, plastic deformation has developed quite extensively in the lower right frame at FS 500, yet the stiff aft doorframe continues to show very little deformation. The short reinforcement beams connecting the aft doorframe to the frame at FS 480 provide a very strong lateral support for the aft doorframe, making it the stiffest section of the entire lower fuselage structure. In fact, the aft doorframe deforms relatively little throughout the entire impact event. Consequently, significant shear force is exerted on the upper doorframe between FS 460 and FS 480, causing plastic deformations to develop, as will be seen at later times. Plastic deformation is also observed at the upper right corners of the frames where outboard supports of the Heath Tecna bin are attached. The upper-left-side frames show plastic deformation much later in the impact event.

At 50 to 70 ms, figure 20(g) through 20(i), the lower frames on the left side continue crushing as the plastic hinges collapse. By 60 ms, however, the lower right frames have reached the point of maximum buckling. Further buckling is limited by the relatively stiff cargo door frame, particularly on the frame surrounding the aft cargo door edge.

Around 80 ms, figure 20(j), the plastic hinges on the left side begin to hit the ground, crushing the frames and setting off a second left-side impact. Plastic deformation is also observed on the left side of each frame where the under-floor beams are joined. This deformation is not nearly as significant on the right side, due to the reinforcement described previously. For the two frames at FS 380 and FS 500, plastic deformation is largely concentrated in the areas where the extra under-floor beams meet the frames. In addition, plastic deformation is observed on frames at FS 480 and FS 500, where the aft camera mount supports are attached.

Between 90 and 120 ms, figure 20(k) through 20(m), the lower left frames continue to crush and are responsible for absorbing most of the impact energy. The lower right frames are no longer deforming to any significant degree, so that the test section continues to tilt downward on the left side. The upper portions of the frames show less deformation, though the areas where plastic deformation has already developed continue to grow.

Figure 20(n) shows the deformation at 140 ms. By this time, the maximum dynamic deformation has been reached, and the left side of the test section begins to rebound from the impact surface. This rebound is more noticeable on the left side and causes the structure to rotate slightly from left to right. The rebound is also more significant at the front of the test section than at the aft end. This agrees with the high-speed film of the drop test taken by the FAA, which shows more significant rebound at the front.

Energy conversion, as shown previously in figure 19, is largely completed by approximately 120 to 130 ms, but the upper frames continue to deform elastically. They reverberate before coming to rest in the final deformed shape. The time of completion of crushing (plastic deformation) is approximately 130 ms, as shown in table 2, and agrees with the experimental data, which shows that the floor reaches zero velocity around 130 ms. This coincides with the end of the plastic impact phase of the simulation.

The effect of the stiff cargo doorframe is shown again in figure 20(n), as the lower right side of the frame shows less deformation compared to the lower left side where the plastic hinges formed. It is noted that the upper cargo doorframe between FS 460 and FS 480 buckled due to the high shear force exerted from below by the very stiff aft doorframe. The buckling of this aft upper doorframe acts as a buffer that slows as well as dampens out the force transmission to the upper frames. In comparison to this, the forward doorframe aligns directly with the frame at FS 420, allowing a direct transmission of impact load to the upper frames. The difference in load transmission is significant, as it accounts for the difference in loads and acceleration time histories of the forward and aft end of the Heath Tecna bin.

Table 2 provides a summary of the significant events during the simulation. Most noteworthy is that the crushing phase, or period of plastic response, coincides with that observed for the test article.

Table 2. Summary of Significant Events During Simulated Impact

Time (ms)	Event in Simulation
3	Plastic deformation initiates.
7	Flanges of lower frames begin to yield.
13	Corners of lower frames begin to yield.
20	Plastic hinge develops on left side. This results from initial impact, which sets off the first acceleration pulse.
30	Lower corners of all left-side frames form plastic hinges. Only corners of forward and aft frames on right side form plastic hinges.
60	Point of maximum buckling reached on right side, setting off second right-side acceleration pulse. Further right-side buckling is limited by cargo door frame. Fuselage now begins to tilt to left.
80	Plastic hinge on left side impacts ground, setting off second left-side acceleration pulse.
90 to 130	Fuselage continues crushing, primarily on left side.
130 to 140	Point of maximum dynamic deformation reached. Point of maximum buckling of left-side frames is reached, setting off third, smaller, left-side acceleration pulse. Slight rebound begins.
280	Point of maximum rebound.
400	Section settles down again on simulated platform. Some reverberation still continues in upper fuselage.

Figure 21 shows a front view of the drop sequence up to 250 ms with two different values of initial luggage stiffness. The diagram on the left shows the results with an initial stiffness of E = 1.2 lb/in^2, while the diagram on the right shows the results with an initial stiffness of E = 0.6 lb/in^2. In comparing the right and left sides, for example at approximately 130 ms, (figure 21(n)), it is evident that luggage stiffness alone can increase or decrease the total deformation experienced by the test section. While figure 21 shows only the qualitative effects of luggage stiffness, it is clear that luggage modeling is a significant variable in determining overall crushing behavior. Maximum dynamic deformation occurs around 100 ms for the stiffer luggage and around 140 ms for the softer luggage. Thus, the softer luggage not only permits additional deformation, but also serves to lengthen the duration of impact. By 250 ms into the event, in both cases, the upper fuselage rebounds after flexing downward, there is also a slight rebound up from the platform, particularly on the left side. The right side shows less rebound. The simulation shows that the model will then settle back down onto the platform.

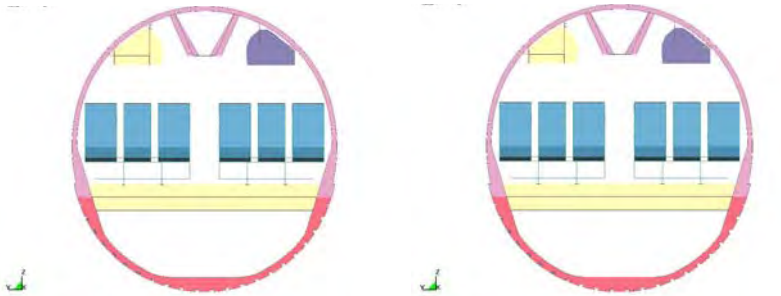

(a) Effect of Luggage Stiffness, E_0 = 1.2 (left) and E_0 = 0.6 (right) at t = 0 ms

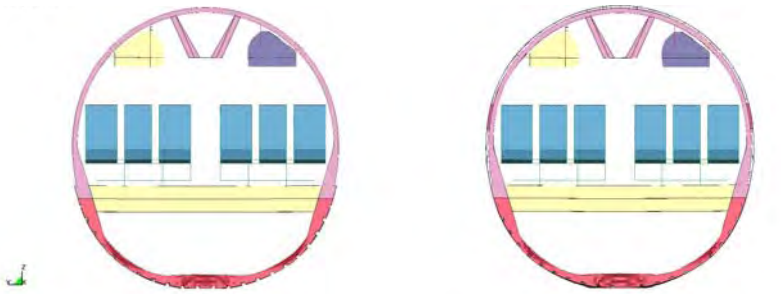

(b) Effect of Luggage Stiffness, E_0 = 1.2 (left) and E_0 = 0.6 (right) at t = 10 ms

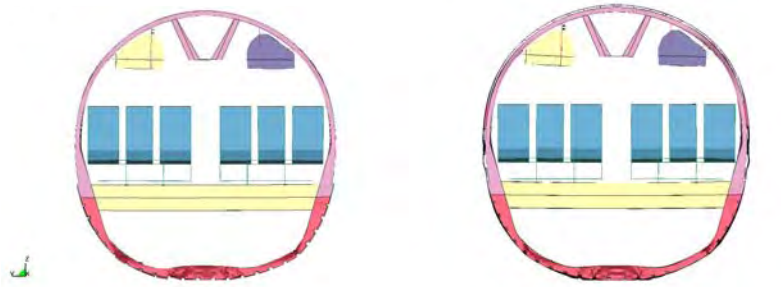

(c) Effect of Luggage Stiffness, E_0 = 1.2 (left) and E_0 = 0.6 (right) at t = 20 ms

Figure 21. Effect of Luggage Stiffness

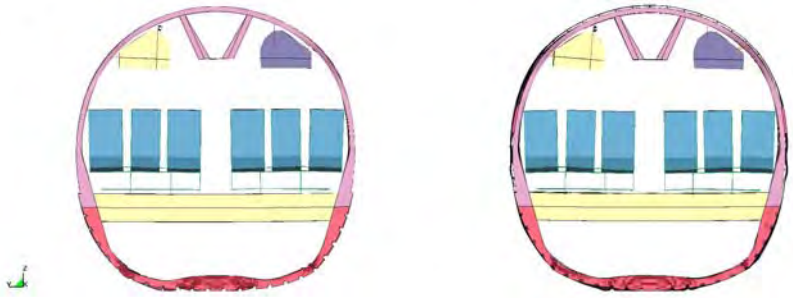

(d) Effect of Luggage Stiffness, E_0 = 1.2 (left) and E_0 = 0.6 (right) at t = 30 ms

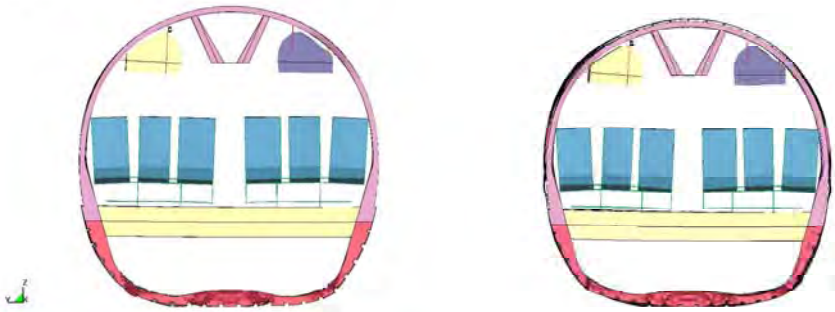

(e) Effect of Luggage Stiffness, E_0 = 1.2 (left) and E_0 = 0.6 (right) at t = 40 ms

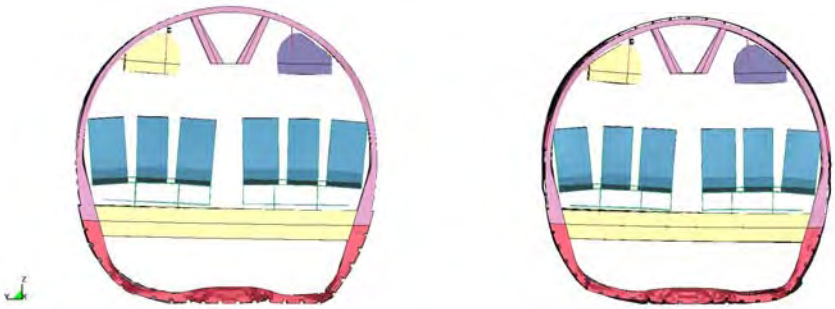

(f) Effect of Luggage Stiffness, E_0 = 1.2 (left) and E_0 = 0.6 (right) at t = 50 ms

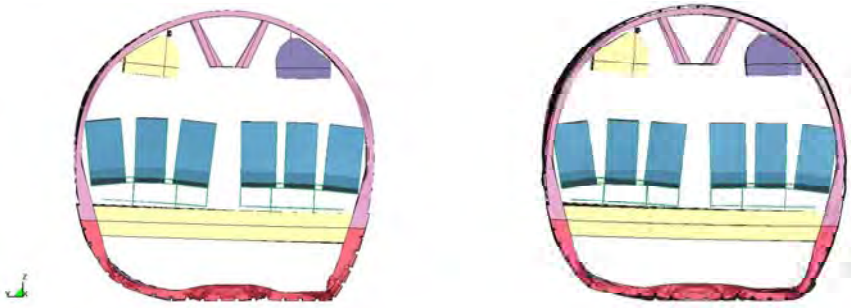

(g) Effect of Luggage Stiffness, E_0 = 1.2 (left) and E_0 = 0.6 (right) at t = 60 ms

Figure 21. Effect of Luggage Stiffness (Continued)

(h) Effect of Luggage Stiffness, E_0 = 1.2 (left) and E_0 = 0.6 (right) at t = 70 ms

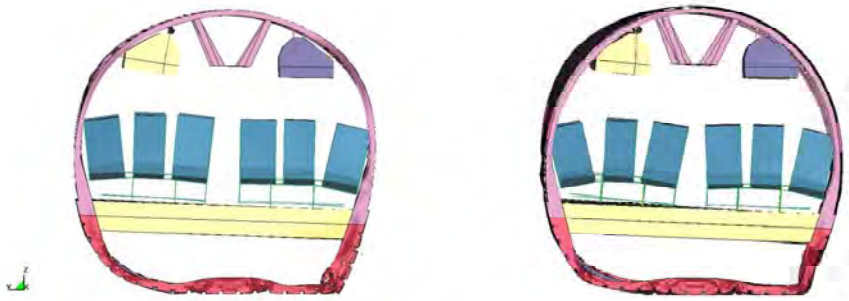

(i) Effect of Luggage Stiffness, E_0 = 1.2 (left) and E_0 = 0.6 (right) at t = 80 ms

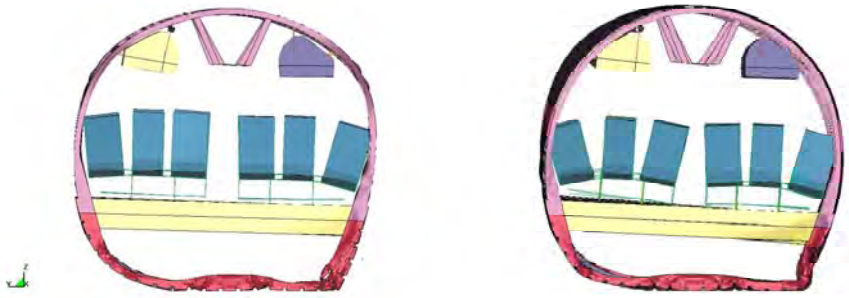

(j) Effect of Luggage Stiffness, E_0 = 1.2 (left) and E_0 = 0.6 (right) at t = 90 ms

(k) Effect of Luggage Stiffness, E_0 = 1.2 (left) and E_0 = 0.6 (right) at t = 100 ms

Figure 21. Effect of Luggage Stiffness (Continued)

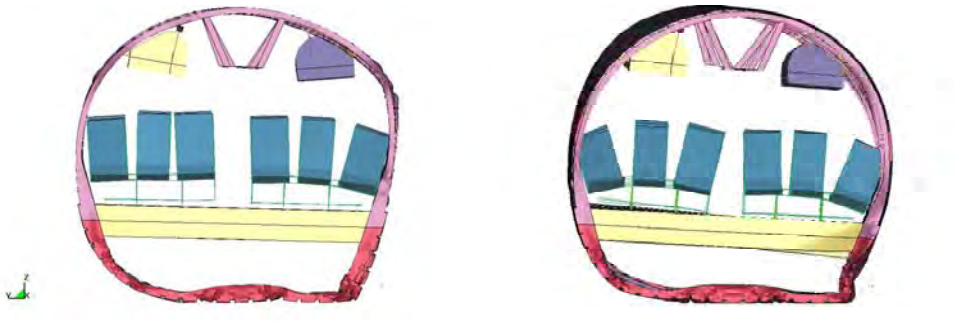

(l) Effect of Luggage Stiffness, E_0 = 1.2 (left) and E_0 = 0.6 (right) at t = 110 ms

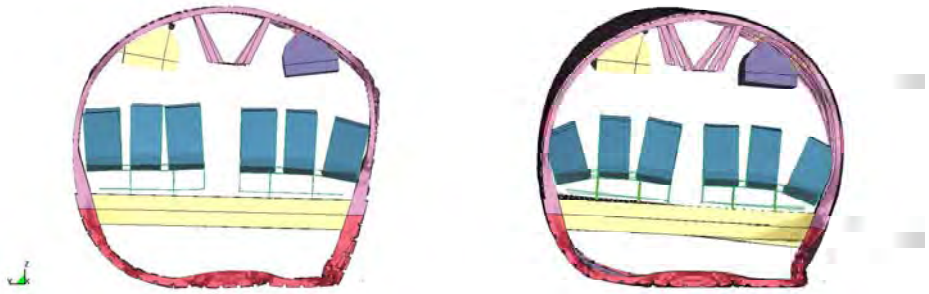

(m) Effect of Luggage Stiffness, E_0 = 1.2 (left) and E_0 = 0.6 (right) at t = 120 ms

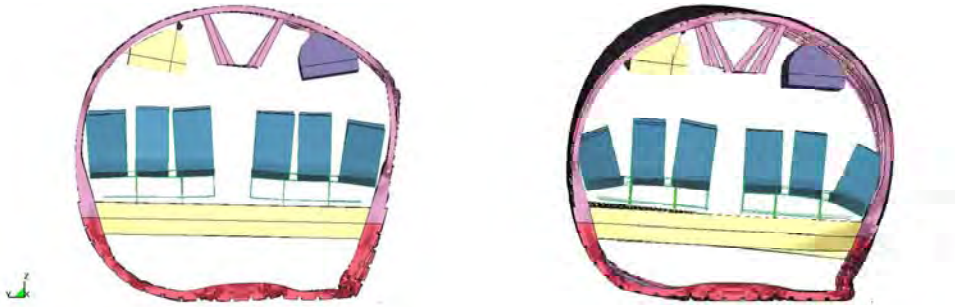

(n) Effect of Luggage Stiffness, E_0 = 1.2 (left) and E_0 = 0.6 (right) at t = 130 ms

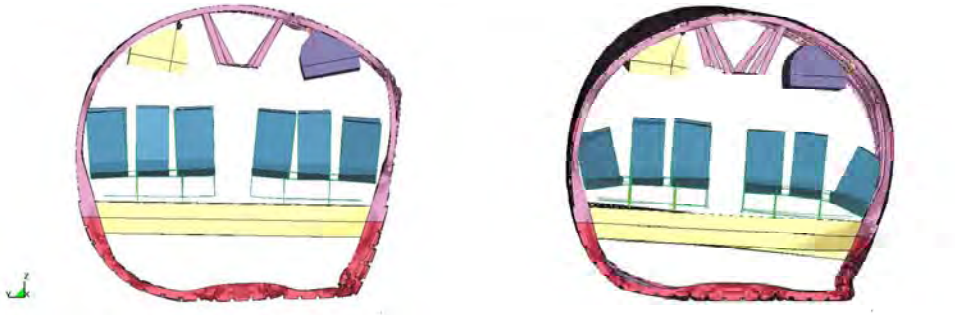

(o) Effect of Luggage Stiffness, E_0 = 1.2 (left) and E_0 = 0.6 (right) at t = 140 ms

Figure 21. Effect of Luggage Stiffness (Continued)

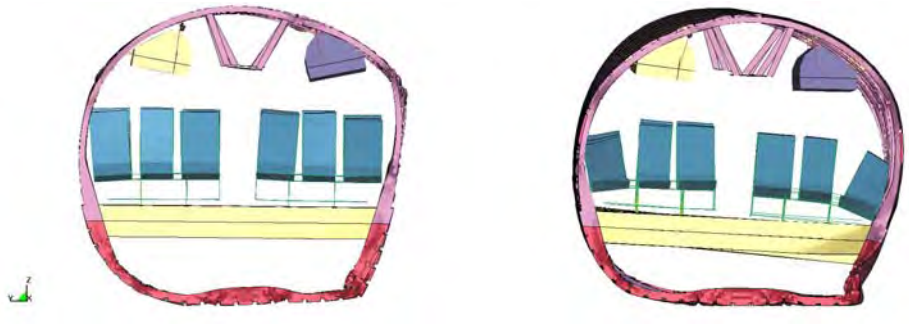

(p) Effect of Luggage Stiffness, E_0 = 1.2 (left) and E_0 = 0.6 (right) at t = 150 ms

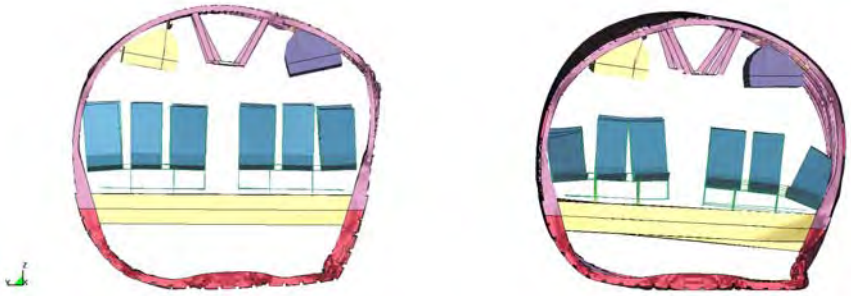

(q) Effect of Luggage Stiffness, E_0 = 1.2 (left) and E_0 = 0.6 (right) at t = 160 ms

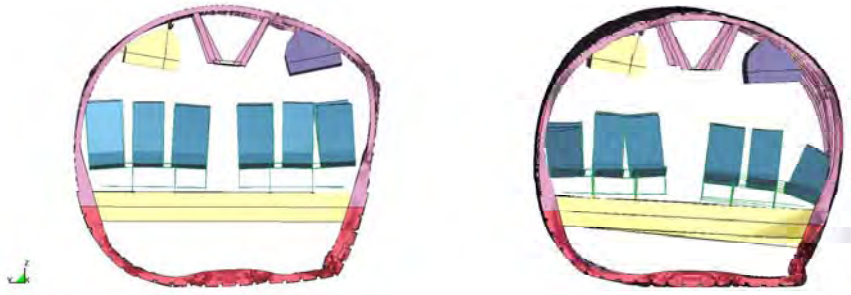

(r) Effect of Luggage Stiffness, E_0 = 1.2 (left) and E_0 = 0.6 (right) at t = 170 ms

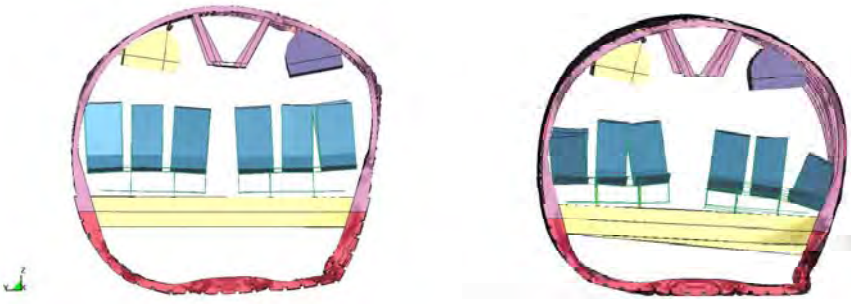

(s) Effect of Luggage Stiffness, E_0 = 1.2 (left) and E_0 = 0.6 (right) at t = 180 ms

Figure 21. Effect of Luggage Stiffness (Continued)

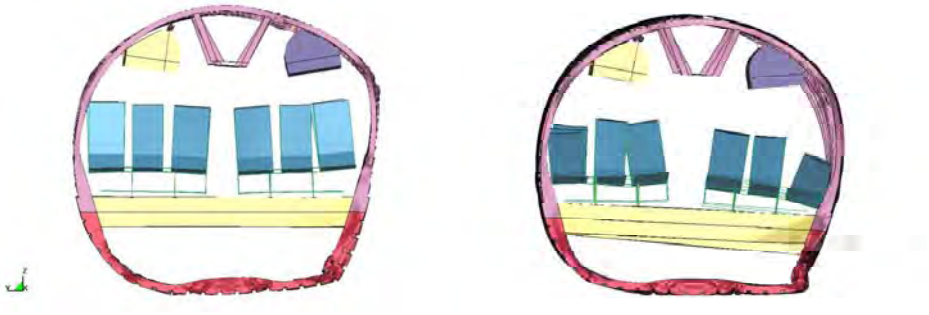

(t) Effect of Luggage Stiffness, E_0 = 1.2 (left) and E_0 = 0.6 (right) at t = 190 ms

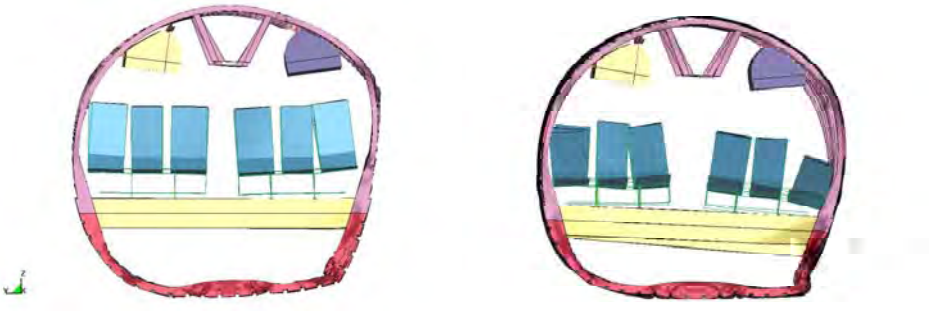

(u) Effect of Luggage Stiffness, E_0 = 1.2 (left) and E_0 = 0.6 (right) at t = 200 ms

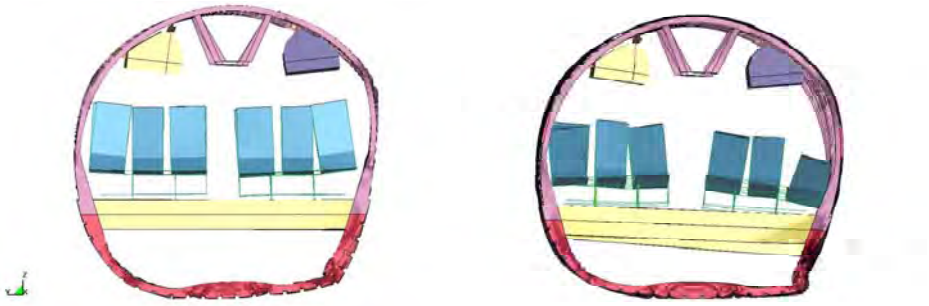

(v) Effect of Luggage Stiffness, E_0 = 1.2 (left) and E_0 = 0.6 (right) at t = 210 ms

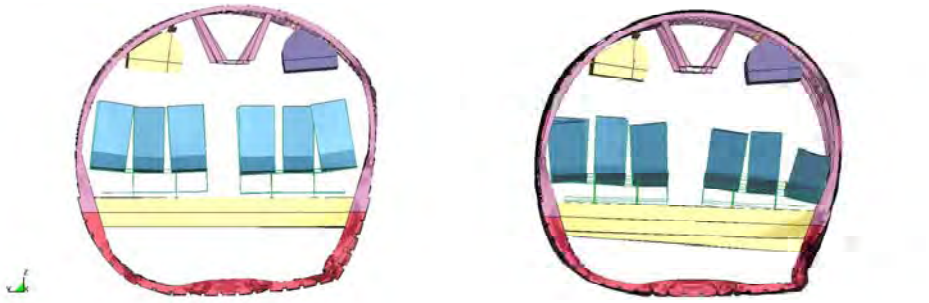

(w) Effect of Luggage Stiffness, E_0 = 1.2 (left) and E_0 = 0.6 (right) at t = 220 ms

Figure 21. Effect of Luggage Stiffness (Continued)

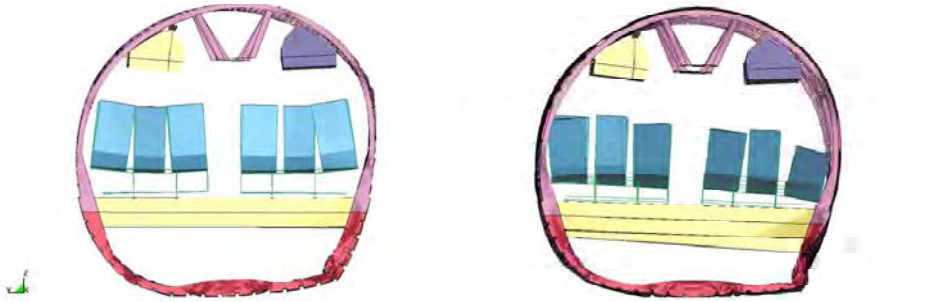

(x) Effect of Luggage Stiffness, E_0 = 1.2 (left) and E_0 = 0.6 (right) at t = 230 ms

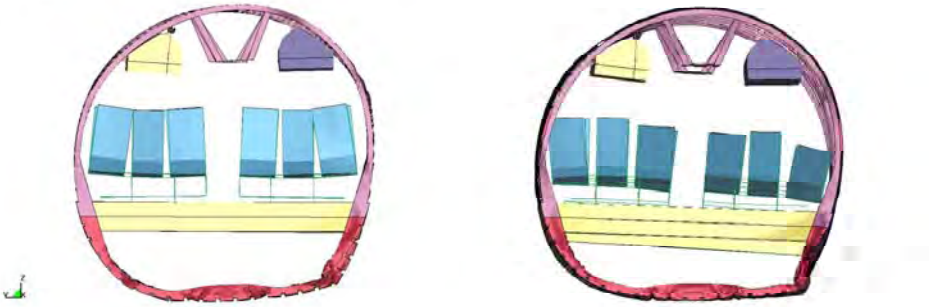

(y) Effect of Luggage Stiffness, E_0 = 1.2 (left) and E_0 = 0.6 (right) at t = 240 ms

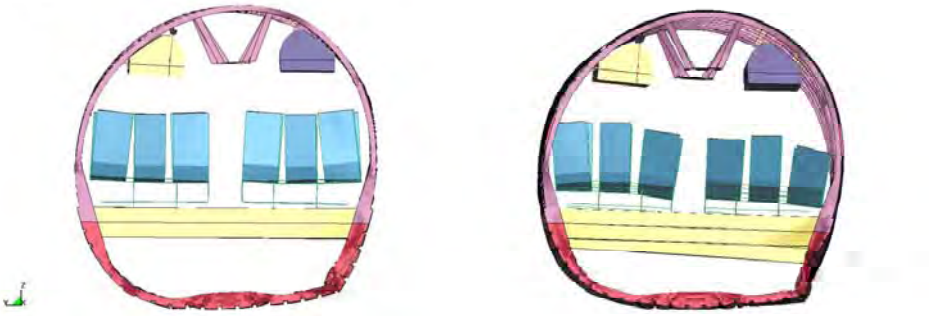

(z) Effect of Luggage Stiffness, E0 = 1.2 (left) and E0 = 0.6 (right) at t = 250 ms

Figure 21. Effect of Luggage Stiffness (Continued)

Figures 22 through 27 compare the deformed configurations of the fuselage section recorded after the drop test with those obtained from the FE simulation at 150 ms. Six different views are shown. It is noted from the drop test results that all seats on the right side failed, while all those on the left side survived. Both of the overhead stowage bins survived the impact as well. The luggage compartment was crushed extensively, indicating that the luggage must have absorbed a considerable amount of impact energy. The asymmetrical deformation resulting from the existence of the very stiff cargo doorframe on the right side is clearly shown in both the front and back views. This difference in right- and left-side deformation is illustrated in figure 28, showing typical deformation in inches for a point on each side of the airframe. In general, the simulation results compare reasonably well with those of the actual drop test.

(a) Experimental Drop Test

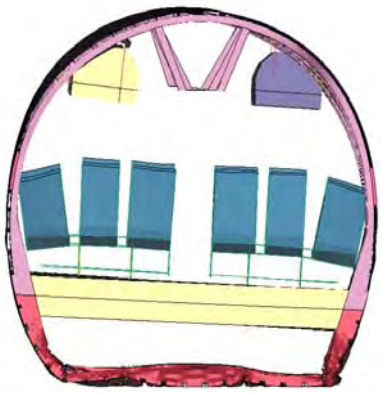

(b) Simulation at 150 ms

Figure 22. Front View of Comparison of the Deformed Configuration

(a) Experimental Drop Test

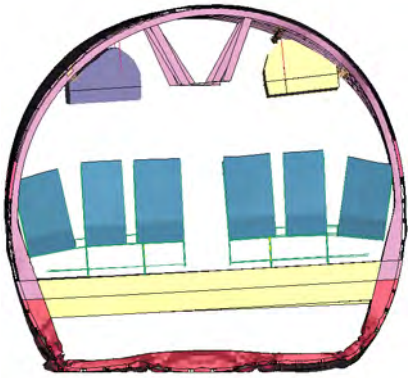

(b) Simulation at 150 ms

Figure 23. Aft View of Comparison of the Deformed Configuration

(a) Experimental Drop Test

(b) Simulation at 150 ms

Figure 24. Left View of Comparison of Deformed Configuration

(a) Experimental Drop Test (b) Simulation at 150 ms

Figure 25. Right View of Comparison of Deformed Configuration

Figure 26. Front Right-Side Angled View, Test and Simulation

Figure 27. Front Left-Side Angled View, Test and Simulation

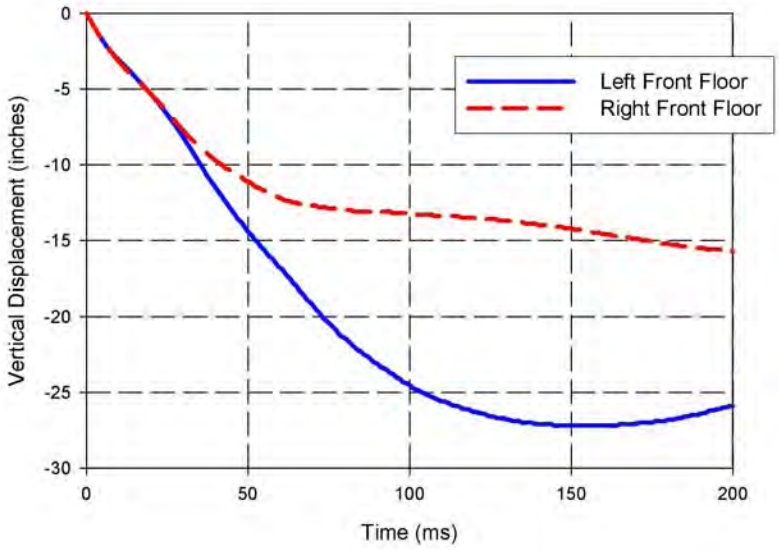

Figure 28. Typical Vertical Displacement—Crushing

Figures 24 and 25 show typical vertical crushing on the left and right sides of the test article. Figure 28 indicates that maximum deformation on the left side is reached at about 140 ms, with a slight rebound beginning near 160 ms. As previously noted, crushing on the right side is limited by the reinforced cargo door frame, though the right side continues to deform slightly up to 200 ms.

Table 3 compares experimental and simulated values for deformation. The dynamic value is at the point of maximum deformation during impact, while the static value represents a posttest measurement.

Table 3. Comparison of Crushing

Measurement Type	Front Left	Front Right	Aft Left	Aft Right
Experimental—Static	23	15.8	27.5	18.4
Experimental—Dynamic	28	21	30.3	24
Simulation—Dynamic	27.5	16.1	29.2	18

7.3 ACCELERATION AND LOAD TIME HISTORIES.

The impact response of the test article is determined primarily by the acceleration time histories measured with accelerometers and by load time histories recorded with calibrated strain gages. Validation of the simulation requires a close comparison of experimental and simulation time histories for all available data. Accordingly, acceleration time histories are presented below for selected points on the overhead stowage bins, floor tracks, and frames, where all selected points correspond to experimental sensor locations. For the overhead stowage bins, load time histories of the primary supporting structures are also presented. Before presenting these results, however, the assumptions employed in analyzing the data and the procedures used to obtain the results are discussed.

7.3.1 Data Analysis Procedure for Acceleration Time Histories.

When processing the time history data, it is important to understand the effect of using different filter frequencies on the results. While the automotive industry typically employs a 100-Hz filter in studying crash tests, the appropriate filter depends on the structural stiffness and impact velocity, both of which are higher in automotive crashes compared to those of aircraft. The FAA evaluated a range of filter frequencies between 20 and 100 Hz for presenting the experimental data. It was determined that the 20-Hz filter seemed to be most appropriate for the current test conditions.

A similar investigation was conducted on the results of FE simulations. Figure 29 shows the effect of using different filtering frequencies on the FE results. The comparison clearly indicates that the 20-Hz filter dampens the peak acceleration and spreads the acceleration impulse over a longer time interval. Furthermore, the pulse duration using a 20-Hz filter is a better match with the apparent pulse duration of the actual, unfiltered, acceleration pulse. The 100-Hz filter, in contrast, appears to calculate a shorter pulse duration than would be experienced by the occupants. Thus, the acceleration and load time histories presented herein are all filtered with a 20-Hz filter.

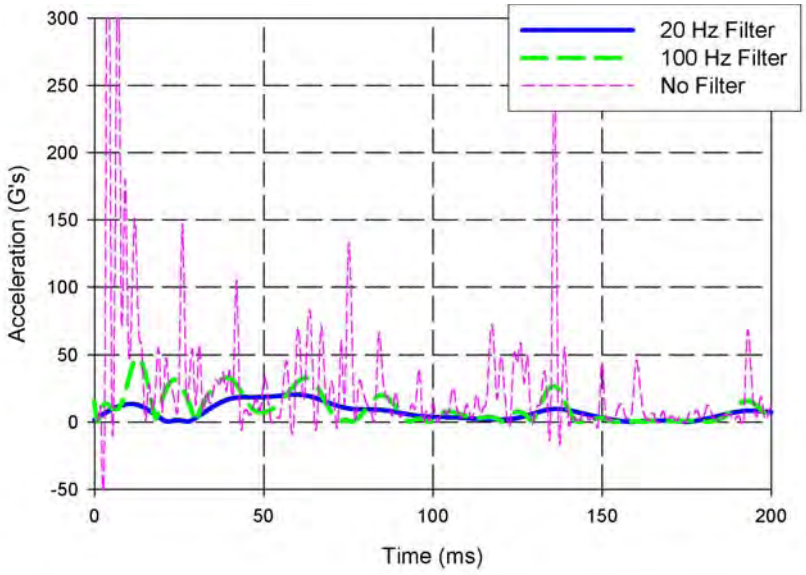

Figure 29. Effect of Different Filtering Frequencies on a Typical Simulation Result

In addition to evaluating pulse duration, it is important to determine if the use of a lower frequency filter would result in any significant loss of energy. For this purpose, the acceleration time histories obtained by using unfiltered, 100-Hz-filtered, and 20-Hz-filtered methods, respectively, were integrated to yield corresponding velocity time histories, as the energy is proportional to the square of velocity. The results from this comparison show that the 20-Hz filtering leads to only a slight loss in energy transferred to the structure.

When performing transient dynamic analysis, it is important to use an appropriate sampling interval to avoid aliasing. This occurs when the sampling interval is larger than the frequency

response, resulting in energy that is transferred incorrectly to other frequencies. A sampling interval of 0.5 ms, corresponding to a sampling frequency of 1000 Hz, was used. Sampling intervals ranging from 0.25 to 1.0 ms, corresponding to a frequency range of 4000 to 1000 Hz, were checked in calculating accelerations. The results show very little difference in either the peak accelerations or in the shape of the acceleration time history curves.

7.3.2 Heath Tecna Overhead Stowage Bin Results.

The primary goal of this simulation was to calculate the impact response of the two overhead stowage bins and compare these results with the experimental acceleration time histories.

Simulation results indicated that energy conversion is largely completed by 150 ms, indicating there is no additional plastic deformation past this point. However, simulation results also show that the upper frames continue to deform elastically and reverberate. Since the overhead bins are attached to the upper portion of the frames, their responses are influenced not only by the plastic deformation that occurs, but also by the elastic responses of the upper frames. For this reason, the acceleration and load time histories discussed in this section are all presented up to 250 ms.

Figures 30 through 33 present acceleration time histories for the Heath Tecna bin installed on the right side of the fuselage. The peak acceleration value ranges from 12.5 to 13.5 g's for the simulation, and approximately 10 to 12 g's for the experimental data. For the simulation, the timing of the peak acceleration comes near 50 to 55 ms, while the experimental data shows the peak occurring between 75 and 110 ms.

The mismatch in timing of the peak values indicates that the simulation may be too stiff on the right side. The experimental data indicates that buckling occurs on the right side after approximately 20 ms. After this point, the structure continues buckling, or crushing, for another 20 to 30 ms, after which it reaches its point of maximum deformation, effectively increasing its stiffness. This leads to a second acceleration pulse on the right side, which is reflected in the experimental data. The simulation apparently did not capture the right-side buckling with such accuracy, as there was only a very brief pause between pulses, as shown in the very slight change of slope near 20 ms in figures 30 through 33.

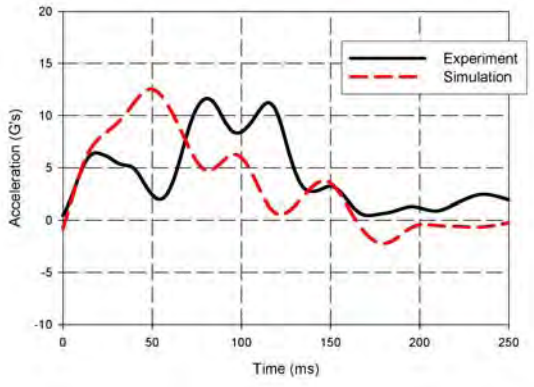

Figure 30. Heath Tecna Bin Acceleration Forward Location

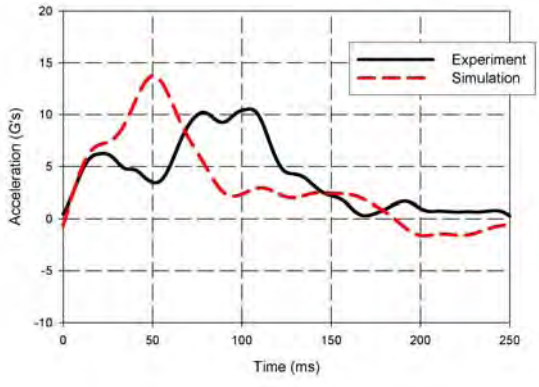

Figure 31. Heath Tecna Bin Acceleration Aft Location

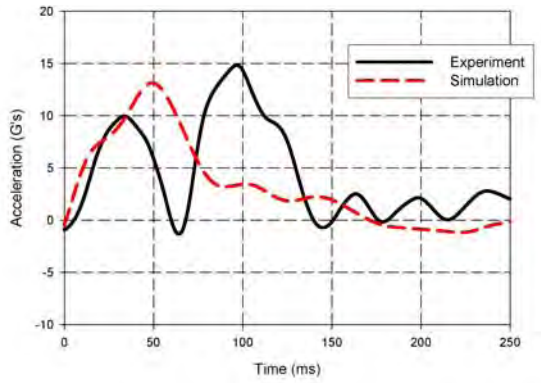

Figure 32. Heath Tecna Bin Acceleration Center Location

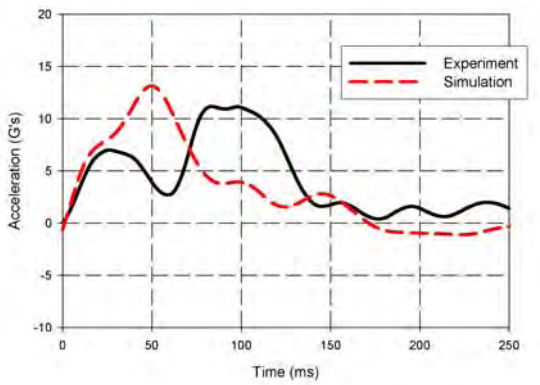

Figure 33. Heath Tecna Bin Acceleration Average

Load time histories for the supporting structural members of each bin were analyzed as well. As previously noted, each bin was supported by a pair of primary vertical members attached to the forward and aft ends of the bin. There was also an outboard supporting structure that reacts inboard-outboard loads and provides secondary vertical support for the bin. These load time history plots are significant because they can be used to predict the conditions under which the supporting structure may fail, assuming that a failure load is known experimentally.

Figures 34 and 35 present the load time histories of the vertical struts, which were the primary vertical supporting members of the Heath Tecna bin. The simulation peak loads match reasonably well with the experimental values, although the exact timing of the peak values show some discrepancy with the experiment. Figures 36 through 45 present the load time histories of the L brackets.

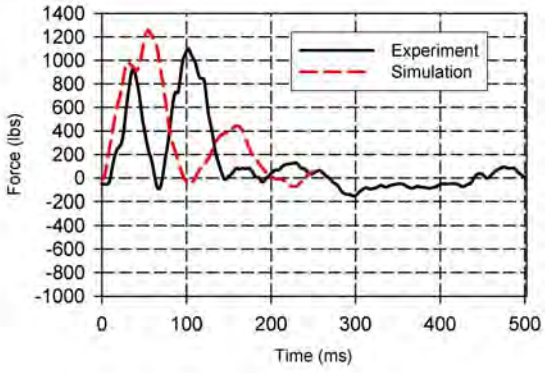

Figure 34. Heath Tecna Bin Load Forward Strut

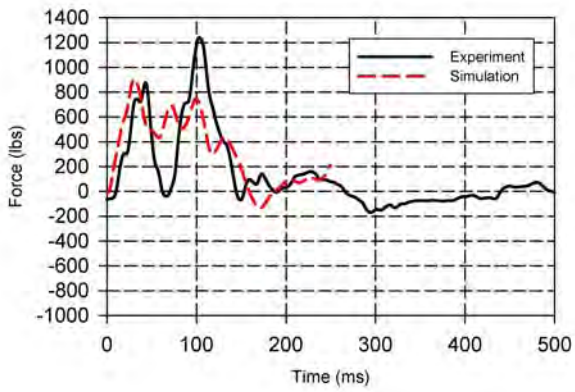

Figure 35. Heath Tecna Bin Load Aft Strut

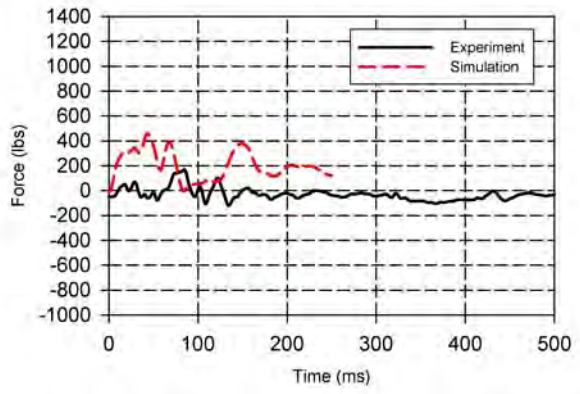

Figure 36. Heath Tecna Bin Load
FS 400—A Leg of Bracket

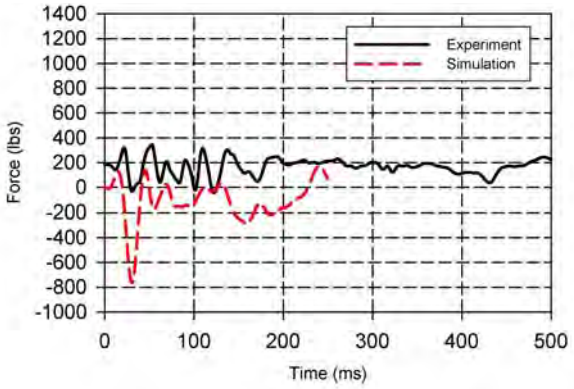

Figure 37. Heath Tecna Bin Load
FS 400—B Leg of Bracket

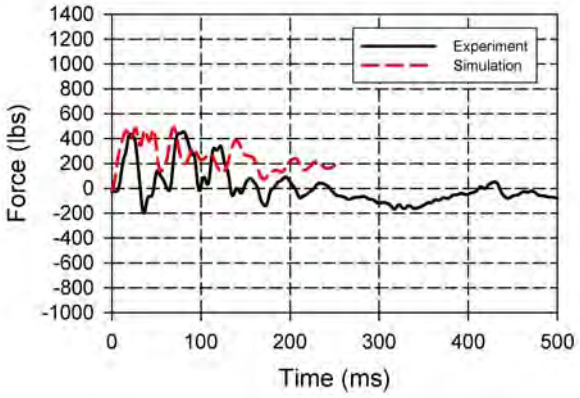

Figure 38. Heath Tecna Bin Load
FS 420—A Leg of Bracket

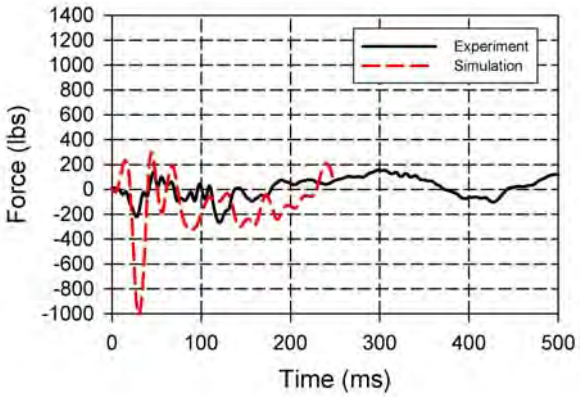

Figure 39. Heath Tecna Bin Load
FS 420—B Leg of Bracket

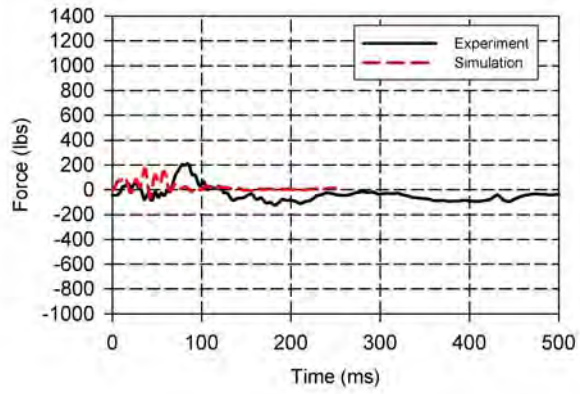

Figure 40. Heath Tecna Bin Load
FS 440—A Leg of Bracket

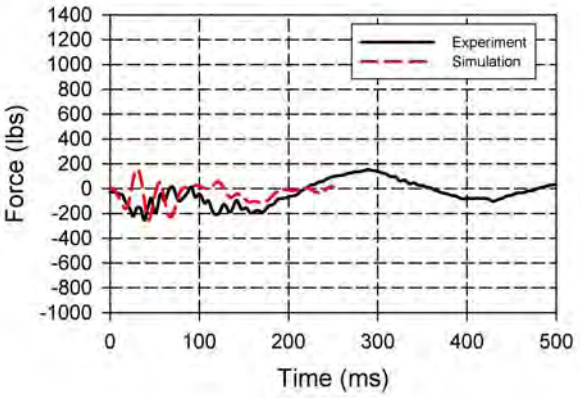

Figure 41. Heath Tecna Bin Load
FS 440—B Leg of Bracket

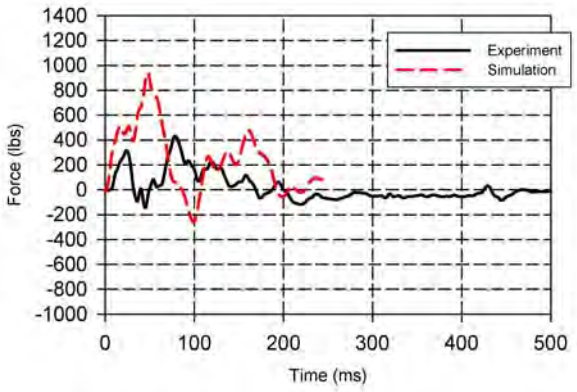

Figure 42. Heath Tecna Bin Load
FS 460—A Leg of Bracket

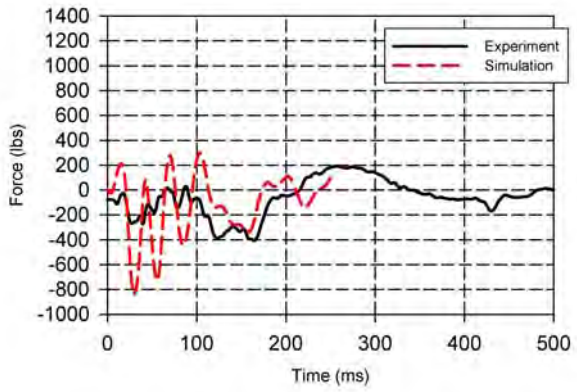

Figure 43. Heath Tecna Bin Load
FS 460—B Leg of Bracket

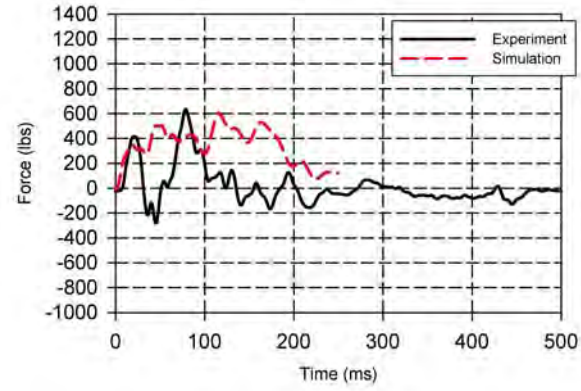

Figure 44. Heath Tecna Bin Load
FS 480—A Leg of Bracket

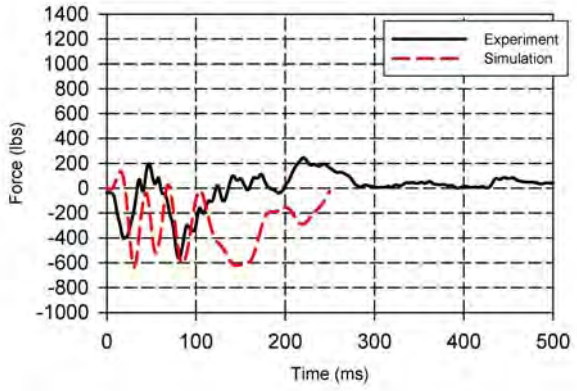

Figure 45. Heath Tecna Bin Load
FS 480—B Leg of Bracket

It is noteworthy to compare the loads carried by the inboard and outboard vertical supports. The load distribution between supporting structures changes during the dynamic impact event. This is significant because static tests of the structural adequacy of each bin assume that the load distribution is constant between the supporting structures. The dynamic load distribution can be plotted as an influence coefficient for any chosen member. The influence coefficient represents the percentage of total vertical load carried by the selected member. The influence coefficient is of most concern during the periods of peak loading. During such times, an extreme load distribution may result in much higher loading in some structures than would be assumed under static loading conditions.

Figure 46 shows a dynamic influence coefficient for the load carried by the combined inboard vertical struts of the Heath Tecna bin. The vertical struts carry the majority of the load, as observed from the 66% static load distribution on the two struts. Outboard vertical support is provided by the A legs of the L brackets. Only the vertical component of load is used in figure 46.

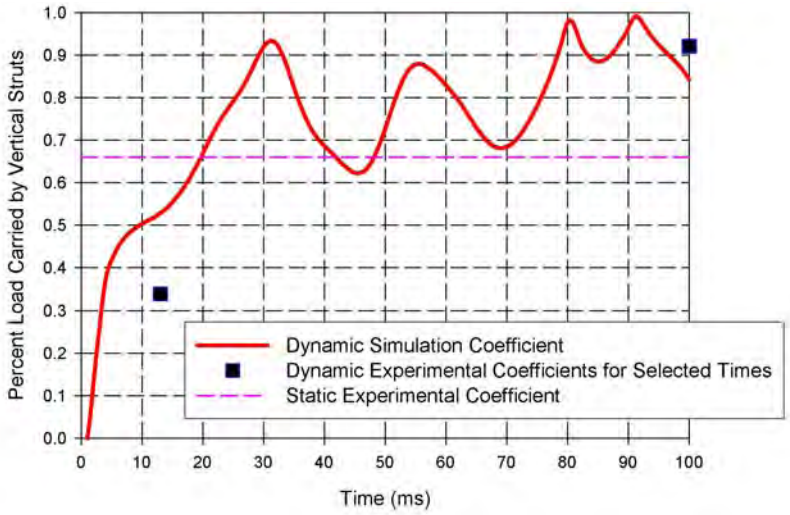

Figure 46. Influence Coefficient for Combined Vertical Struts of Heath Tecna Bin

Load peaks occur, experimentally, around 13 and 102 ms. The experimental dynamic influence coefficients were therefore calculated at these times. Peak loading in the simulation occurs near 55 ms, with an influence coefficient of 0.88. The experimental influence coefficient at 102 ms is 0.93, while at this point in time, the simulation shows a coefficient of 0.85. Thus, figure 46 shows that the simulation can be used to track the influence coefficient with reasonable accuracy.

7.3.3 Hitco Overhead Stowage Bin Results.

Figures 47 through 50 present the acceleration time histories calculated for the Hitco bin, which is on the left side of the fuselage. These locations correspond to points where accelerometers were attached in the test article.

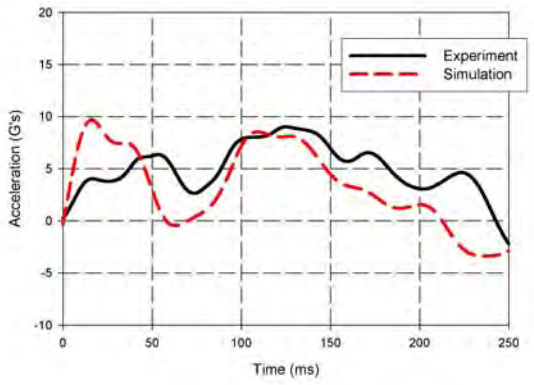

Figure 47. Hitco Bin Acceleration Forward Location

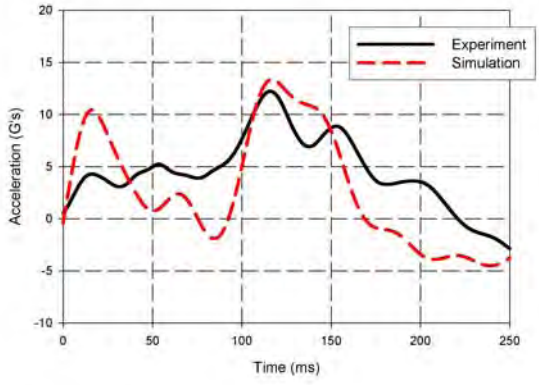

Figure 48. Hitco Bin Acceleration Aft Location

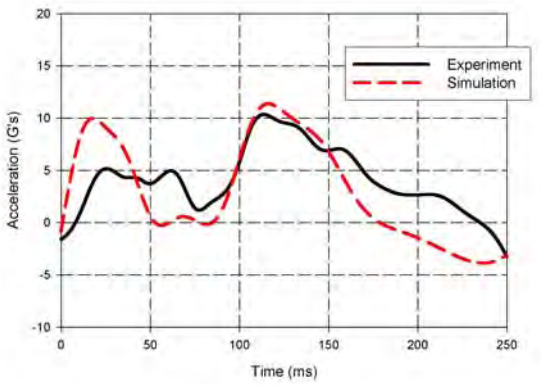

Figure 49. Hitco Bin Acceleration Center

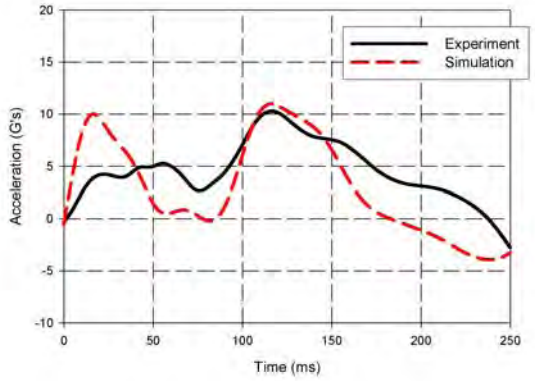

Figure 50. Hitco Bin Acceleration Average

The figures show that the peak acceleration values match well between the simulated and experimental data. Timing of the acceleration peaks also match well, indicating an acceleration pulse at approximately 100 to 150 ms for both simulated and experimental results. Only the initial acceleration pulse in the simulation results is discrepant, with the simulation showing a stronger pulse near 15 ms, prior to the initiation of buckling on the left side. As the following time histories match reasonably well, it is unlikely that the structural modeling is excessively stiff. Other possible reasons for this initial discrepancy will be noted in the following section.

These time histories also show that the aft end of the stowage bin experiences a higher peak acceleration pulse than the forward end. This response is captured in both the experimental and simulated results. The difference in peak acceleration between the two ends of the overhead stowage bin is due to asymmetry in the test article, introduced by the location and design of the cargo door. Thus, even acceleration responses on the left side of the airframe are affected by the cargo door reinforcement.

Figures 51 and 52 present the load time histories of the primary vertical supporting members of the Hitco bin. Figures 53 through 60 present the load time histories of the other support links. Peak load values match very closely with the experimental data, again with the exception of a higher than expected initial peak near 20 ms. Timing of the loads shows that the simulation has captured the basic structural response of the Hitco bin.

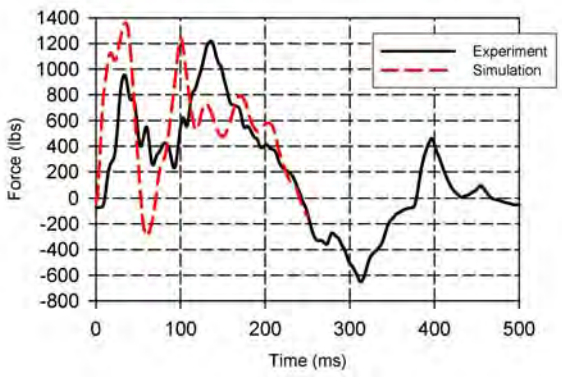

Figure 51. Hitco Bin Load Forward Tie Rod

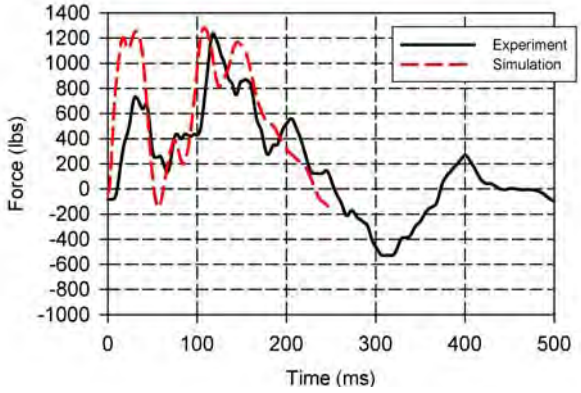

Figure 52. Hitco Bin Load Aft Tie Rod

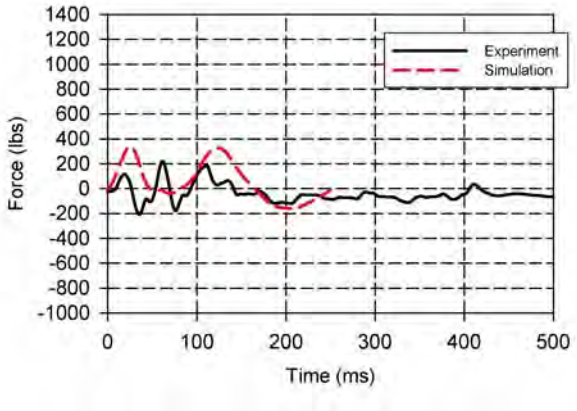

Figure 53. Hitco Bin Load
FS 400 Vertical Link

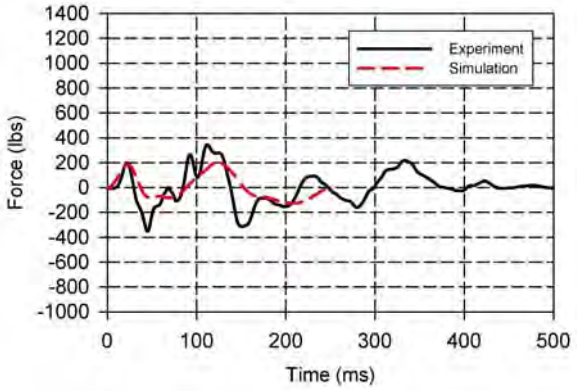

Figure 54. Hitco Bin Load
FS 400 Horizontal Link

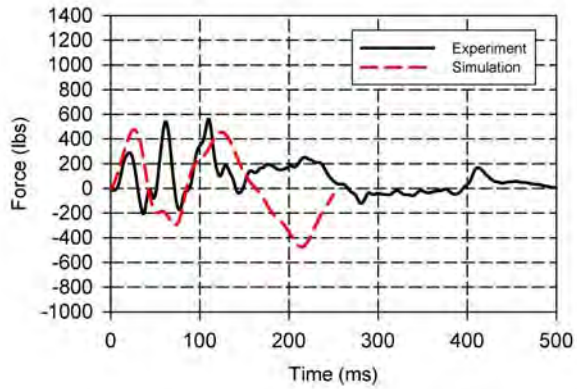

Figure 55. Hitco Bin Load
FS 420 Vertical Link

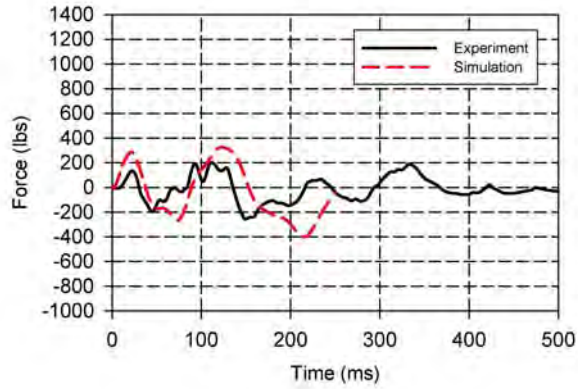

Figure 56. Hitco Bin Load
FS 420 Horizontal Link

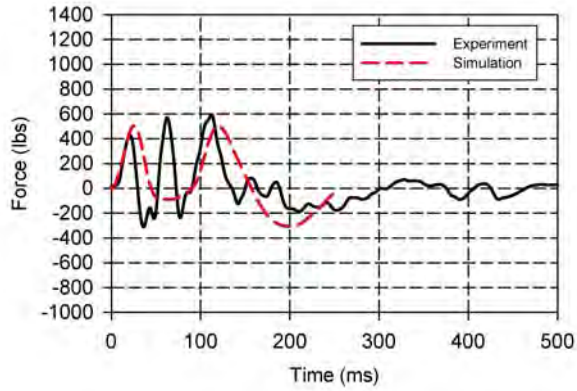

Figure 57. Hitco Bin Load
FS 460 Vertical Link

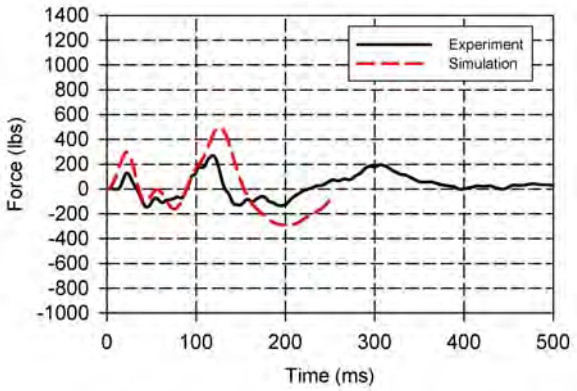

Figure 58. Hitco Bin Load
FS 460 Horizontal Link

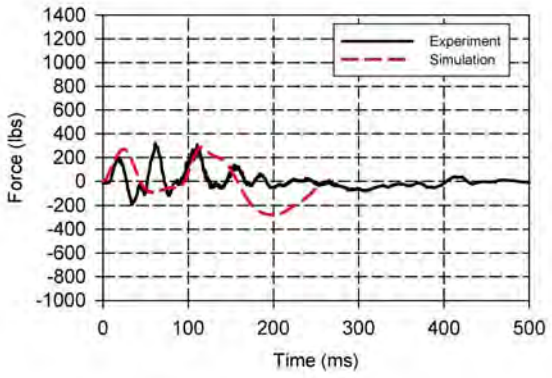

Figure 59. Hitco Bin Load
FS 480 Vertical Link

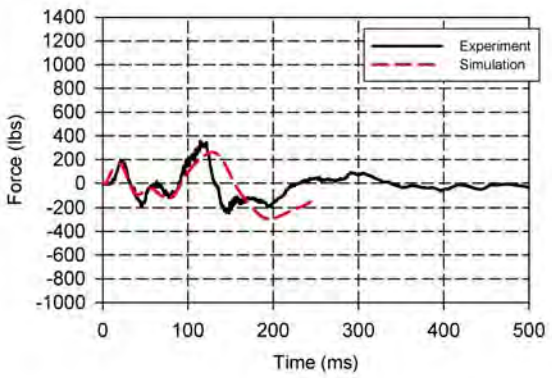

Figure 60. Hitco Bin Load
FS 480 Horizontal Link

Like the Heath Tecna bin, it was possible to plot the percentage of load carried by the two primary vertical supports of the Hitco bin. These supports are the tie rods that attached toward the inboard side of the Hitco bin. Figure 61 shows a plot of a dynamic influence coefficient for the load carried by the combined inboard tie rods of the Hitco bin. The vertical tie rods carried the majority of the load, with 66.5% of the load carried under static test conditions. Outboard vertical support was provided primarily by vertical links. Again, only the vertical component of load is used in figure 61.

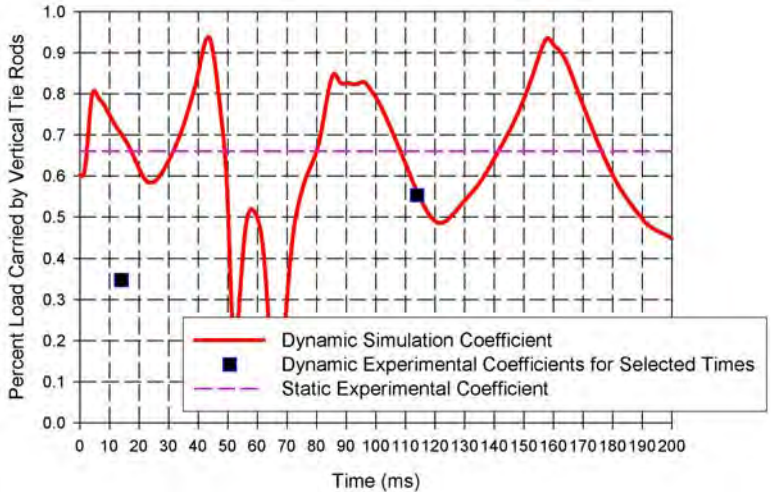

Figure 61. Influence Coefficient for Combined Vertical Tie Rods of Hitco Bin

Load peaks occurred experimentally around 14 and 114 ms. Therefore, the experimental dynamic influence coefficients were calculated at these times. Peak loading in the simulation occurred between 100 and 120 ms, similar to the experimental results. At 114 ms, the simulation and experimental coefficients matched exactly. In general, the simulation coefficient fluctuated around the static value. The time from 50 to 70 ms occurred when the overhead stowage bin was lightly loaded, and the values during this period were, therefore, not significant. Figure 61 shows that the simulation can also be used to track the influence coefficient of the Hitco bin with reasonable accuracy.

7.3.4 Acceleration Time Histories of Floor Tracks.

During an impact event, energy is transmitted from the fuselage structure to the passengers through seats that are anchored to the floor along the floor tracks. This report neither addresses energy absorption in the seat structures nor looks at the acceleration response of the instrumented test dummies. Therefore, the seats were not modeled in detail. However, the basic seat structures were included in the simulation since they affect the timing and magnitude of the response, which is measured at the floor track.

In the test article, the seat cushions absorb energy and serve to delay the time at which inertial forces are transferred from the occupants to the seat frames. Further, the seat frames may deform considerably, also affecting the load transfer to the floor tracks. In fact, the seats on the right side of the test article failed during impact, significantly altering both the magnitude and timing of the load transferred to the floor track.

In the simulation, structural failure of the seats was not permitted, due to a lack of appropriate data on the failure loads. Thus, the seats responded elastically, even though permanent plastic deformation was expected in several locations. This was observed in the simulation, as outboard (window) seats deflected significantly. The test results also showed that these seats experienced permanent deformation, even where the basic seat structure remained intact. The seat frame structure was modeled based on measurements from the test article, while estimates were made concerning the material properties of the seat cushions and seating surfaces.

Fourteen locations were selected for calculating acceleration time histories, as shown in figure 62. These locations correspond to experimental sensor locations. Typical results are shown in figures 63 through 76.

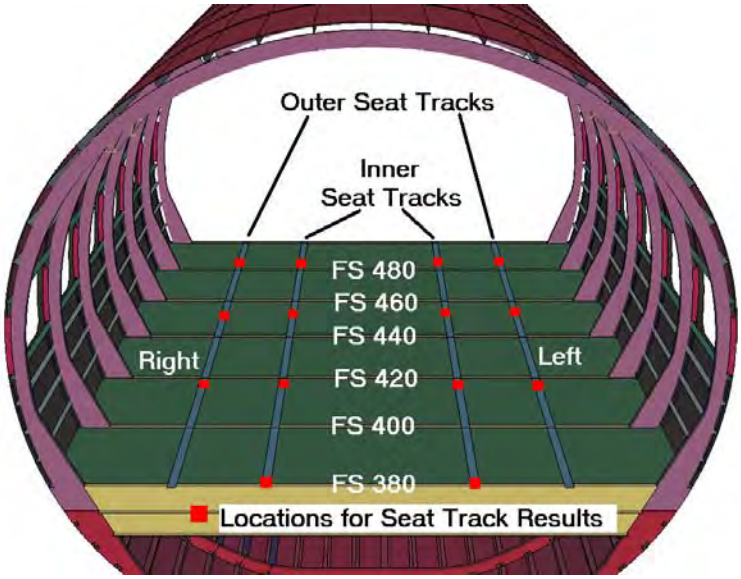

Figure 62. Locations of Acceleration Results on Floor Tracks

The experimental and simulation results match well for the floor track locations on FS 380. For this case, the right-side acceleration pulse is higher in magnitude than the left-side acceleration pulse. This is expected, as the right-side response is influenced by the relatively stiff cargo door reinforcing structure.

At FS 418, however, the simulation shows higher peak accelerations on the left side, though these peaks are more transient. While the right-side results appear to match the experimental values in a reasonable manner, the left side appears to be undergoing oscillations, perhaps induced by the interplay between the seats and floor. Because the seats do not deform plastically, it is possible that a vibrational mode was induced in the left-side seat-floor structure, resulting in the observed peaks. This effect is more noticeable at the outboard left-side floor track. The inboard left floor track shows similar but less severe oscillations.

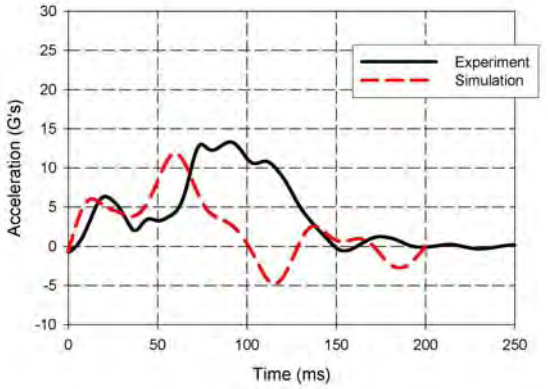

Figure 63. Floor Track Acceleration
FS 380—Left Inside Floor Track

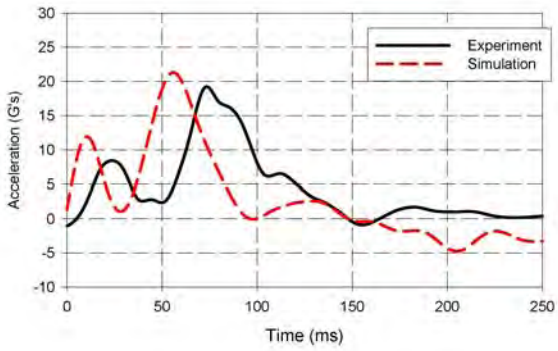

Figure 64. Floor Track Acceleration
FS 380—Right Inside Floor Track

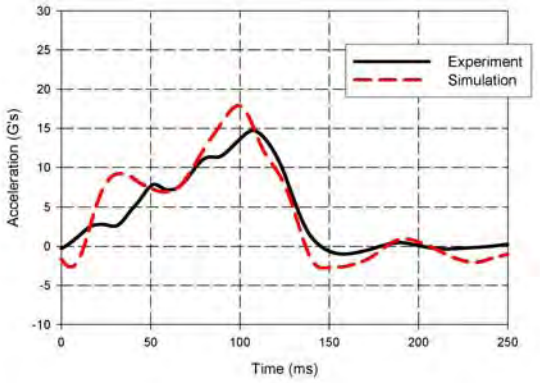

Figure 65. Floor Track Acceleration
FS 418—Left Outside Floor Track

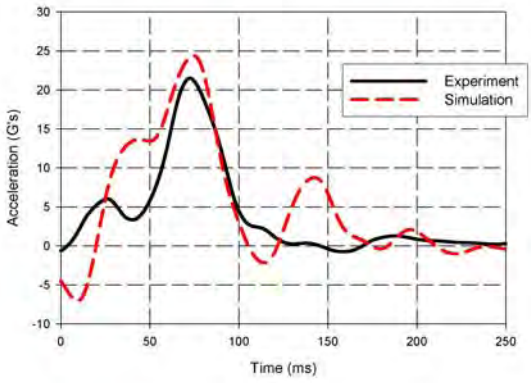

Figure 66. Floor Track Acceleration
FS 418—Right Outside Floor Track

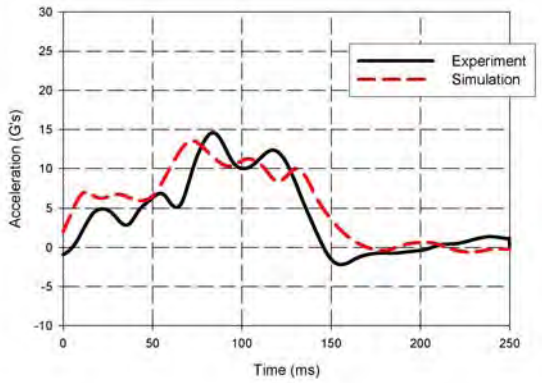

Figure 67. Floor Track Acceleration
FS 418—Left Inside Floor Track

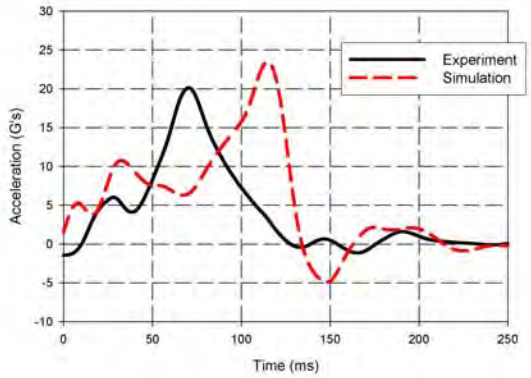

Figure 68. Floor Track Acceleration
FS 418—Right Inside Floor Track

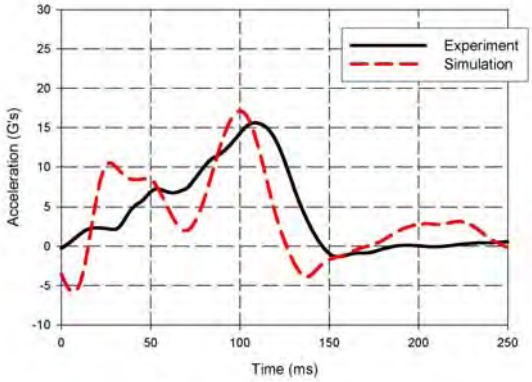

Figure 69. Floor Track Acceleration
FS 452—Left Outside Floor Track

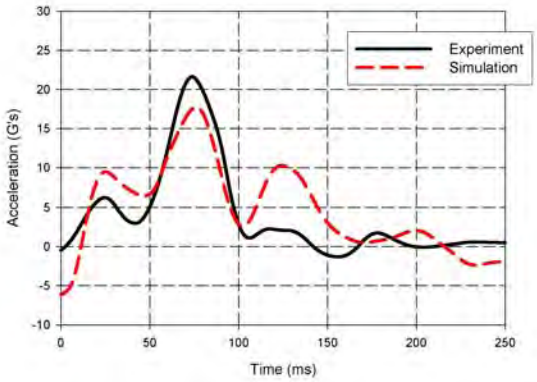

Figure 70. Floor Track Acceleration
FS 452—Right Outside Floor Track

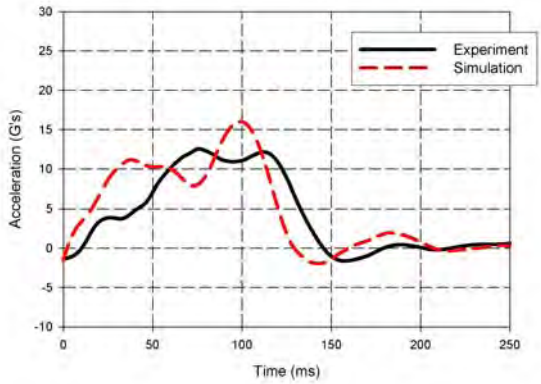

Figure 71. Floor Track Acceleration
FS 452—Left Inside Floor Track

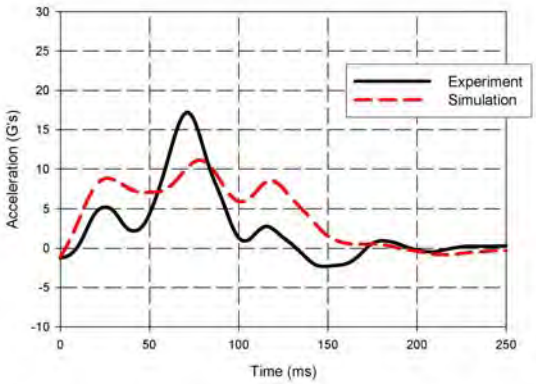

Figure 72. Floor Track Acceleration
FS 452—Right Inside Floor Track

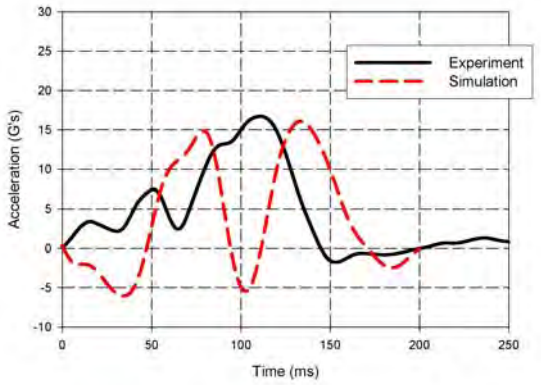

Figure 73. Floor Track Acceleration
FS 484—Left Outside Floor Track

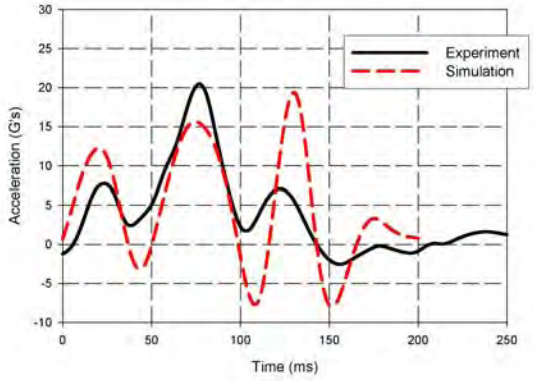

Figure 74. Floor Track Acceleration
FS 484—Right Outside Floor Track

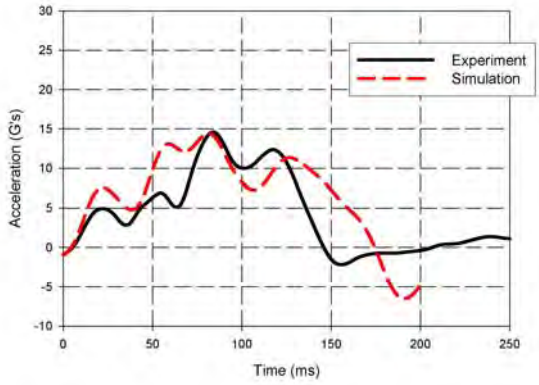

Figure 75. Floor Track Acceleration
FS 484—Left Inside Floor Track

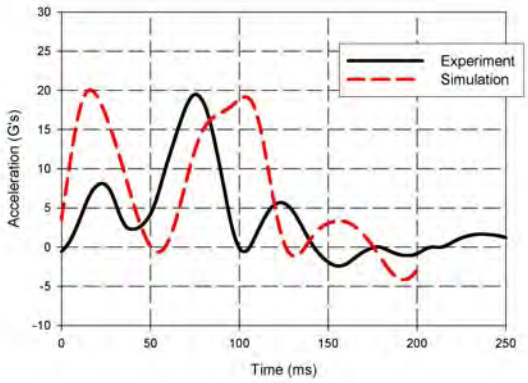

Figure 76. Floor Track Acceleration
FS 484—Right Inside Floor Track

7.3.5 Acceleration Time Histories of Frames.

Acceleration time histories were computed at six locations on the upper frames, three on each side, as shown in figure 77. Similarly, results were obtained from six locations on the lower sidewalls, as shown in figure 78. The lower sidewall nodes are located 12 inches above the floor, in the center of the frame.

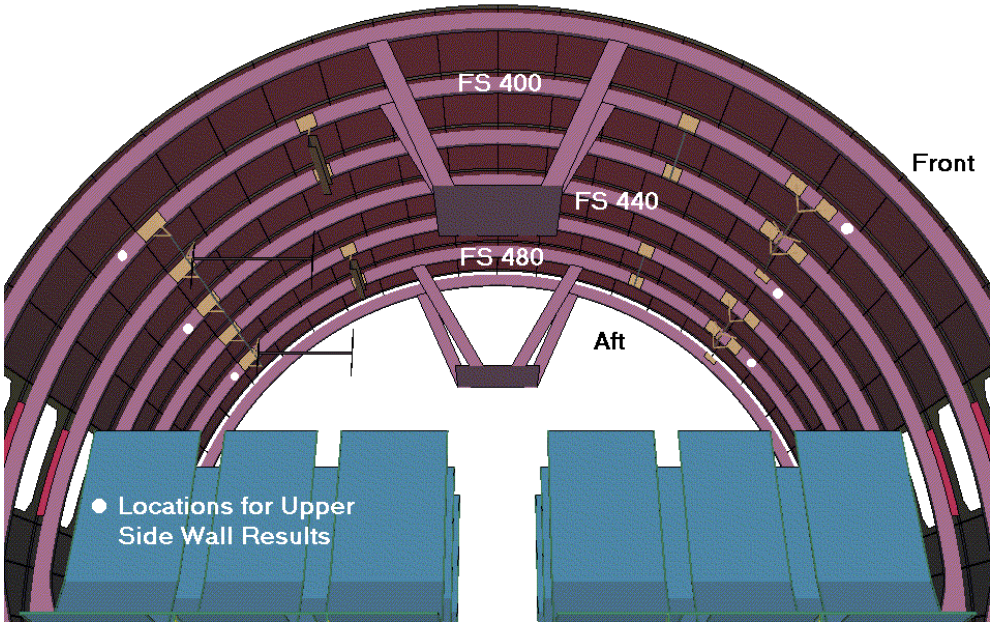

Figure 77. Locations for Upper Sidewall Acceleration Results

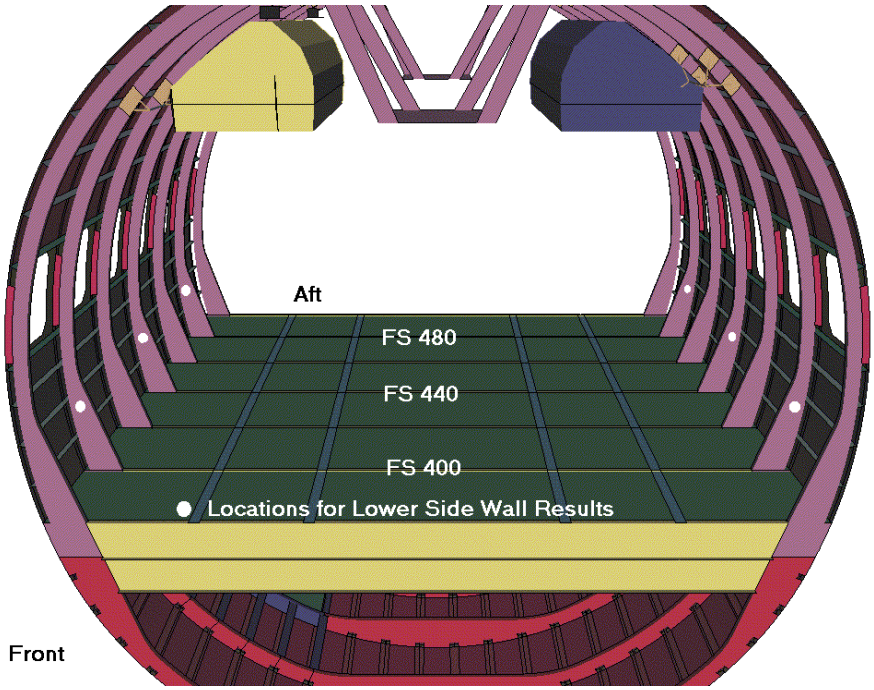

Figure 78. Locations for Lower Sidewall Acceleration Results

Figures 79 through 90 show typical acceleration time histories on the upper and lower sidewalls. Peak acceleration values on the right sidewall showed a close correlation between experimental and simulation results, though the timing again indicates that the right side experiences additional buckling not captured in the simulation. This would account for the early acceleration

pulse in the simulation compared to the experiment. The results for the left side showed a moderate correlation between experimental and simulation acceleration time histories.

It is interesting to note that the right-side peak acceleration values are nearly identical for both the lower and upper sidewalls. This indicates very little plastic deformation or buckling occurs in the right-side frames, as the acceleration pulse is transmitted directly through the frames. This observation is supported by a posttest examination of the test article, which indicated only slight buckling of the inside portion of the frames on the right side.

In contrast, the left-side results for both test and simulation showed that peak acceleration value in the upper frame is approximately 25% to 30% lower than in the lower frame. This would indicate that substantial plastic deformation, or failure, occurred in the left-side frames. Again, this is supported by a posttest examination, which indicated substantial failures in each of the frames on the left side. Although the magnitude of this effect is overestimated in the simulation, it nevertheless agrees with the basic trend, showing significant plastic deformation on the left side.

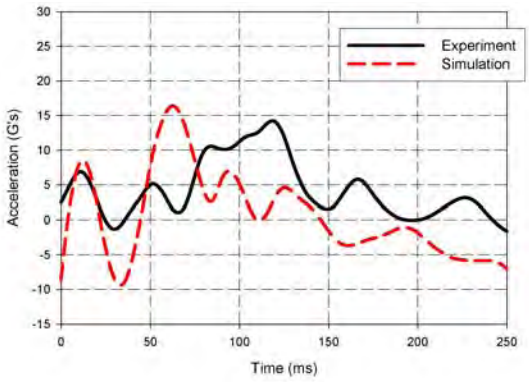

Figure 79. Upper Sidewall Acceleration FS 400—Left Sidewall

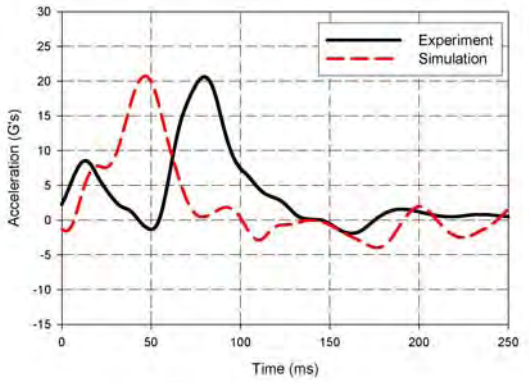

Figure 80. Upper Sidewall Acceleration FS 400—Right Sidewall

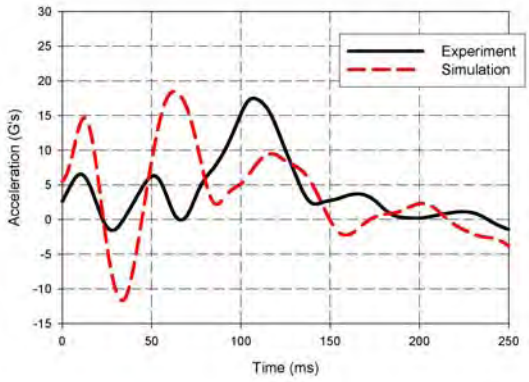

Figure 81. Upper Sidewall Acceleration FS 440—Left Sidewall

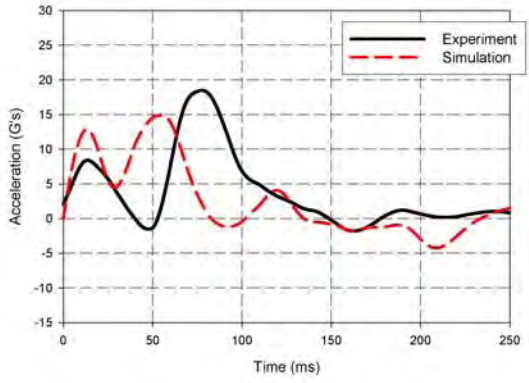

Figure 82. Upper Sidewall Acceleration FS 440—Right Sidewall

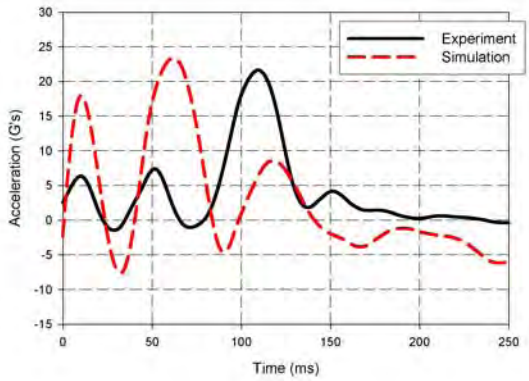

Figure 83. Upper Sidewall Acceleration FS 480—Left Sidewall

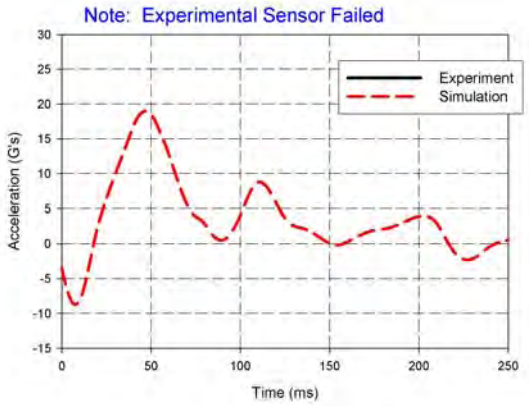

Figure 84. Upper Sidewall Acceleration FS 480—Right Sidewall

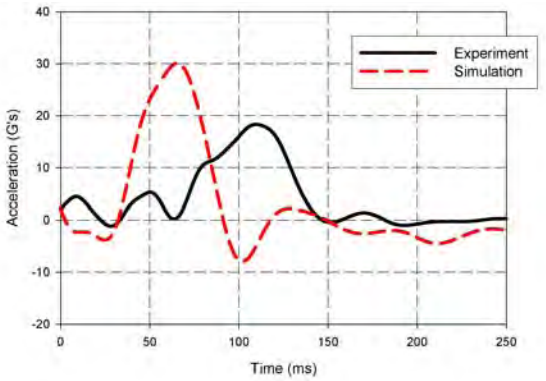

Figure 85. Lower Sidewall Acceleration FS 400—Left Sidewall

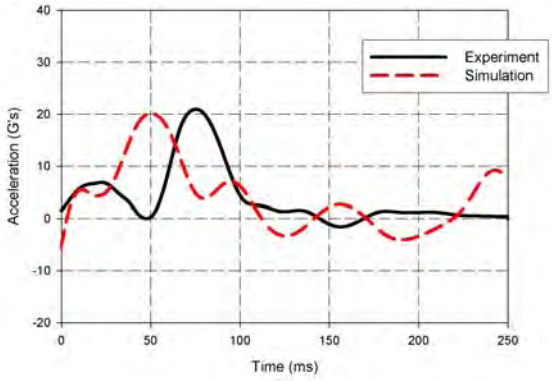

Figure 86. Lower Sidewall Acceleration FS 400—Right Sidewall

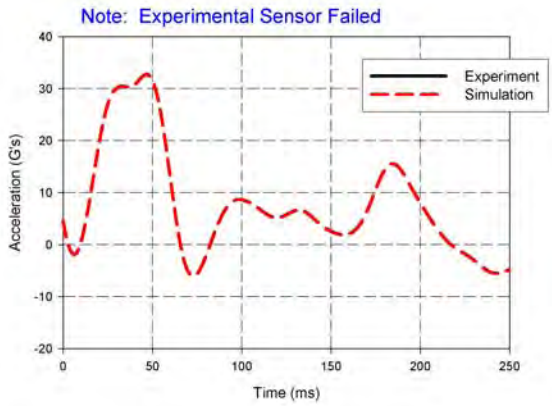

Figure 87. Lower Sidewall Acceleration FS 440—Left Sidewall

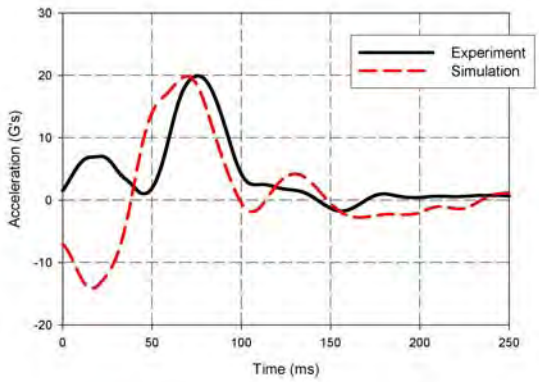

Figure 88. Lower Sidewall Acceleration FS 440—Right Sidewall

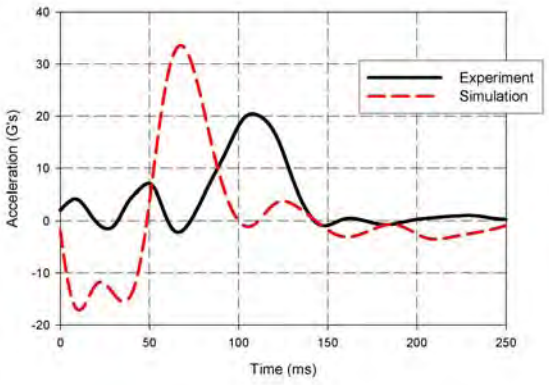

Figure 89. Lower Sidewall Acceleration FS 480—Left Sidewall

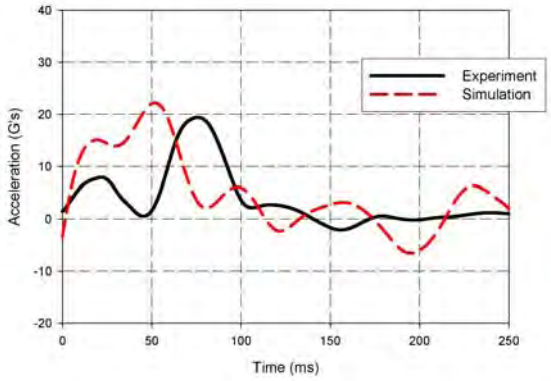

Figure 90. Lower Sidewall Acceleration FS 480—Right Sidewall

7.3.6 Acceleration Time Histories of Seat Cushions.

Figure 91 shows the location of the accelerations of the simulated seat cushions that were used to compare with the experimental results from the ATDs. Each ATD had an accelerometer mounted near the pelvis. These experimental results were compared to the simulation results, which used the seat cushion location. However, the proximity of the seat cushion to the ATD's accelerometer provides a reasonable point of comparison.

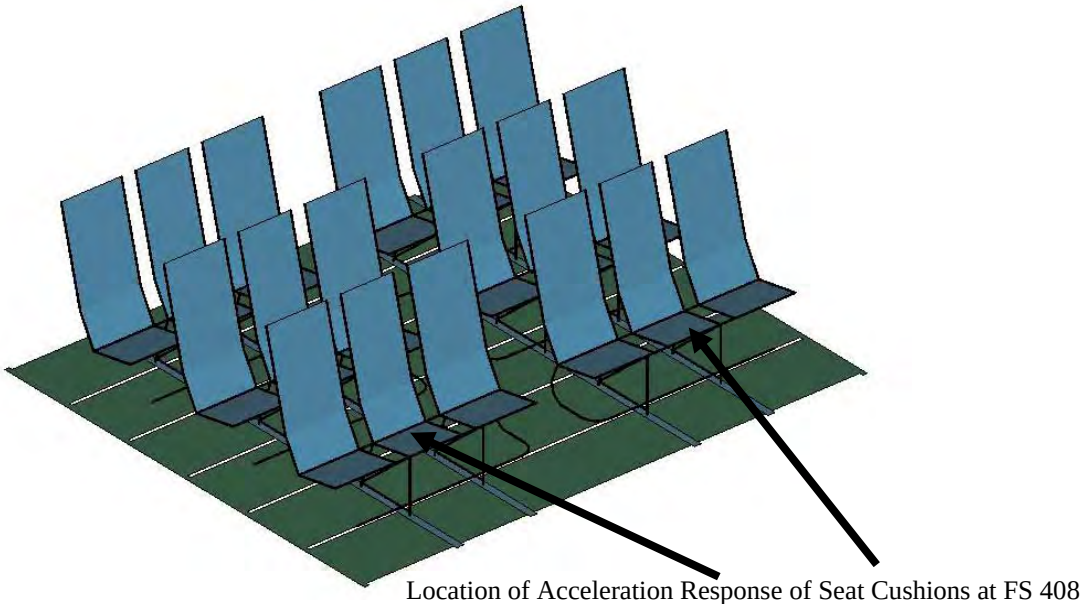

Figure 91. Location of Acceleration Response for Seat Cushions

Figure 92 shows the left-side response for the center seat and ATD. The simulation correctly identified the peak acceleration value, although the simulated cushion showed a slightly higher frequency rebound than the ATD. Figure 93 shows the right-side response, again comparing the simulated seat response to the ATD. It must be noted that the right-side seats collapsed in the experimental event, which explains the lower peak acceleration value for the experimental

sensor. In the simulation, where no collapse occurred, the peak acceleration response was higher than on the left side, as expected. This agrees with the trends observed in the experimental results, as well as the results for the floor track response in both experimental and simulation. The right-side seats consistently experienced an acceleration pulse, which was approximately 5 g's higher for the left-side seats. The acceleration pulse shape and duration for the simulated seat agrees very well with the experimental ATD.

This comparison shows that the simulation may be used in conjunction with occupant injury calculations. One option would be to use the acceleration time history data as input into an occupant model to determine the occupant response. A second approach would be to include an occupant model in the existing simulation. Several choices currently exist for fully FE occupant models, one of which could be included using the existing seat structure. More accurate modeling of the seat pan and seat cushion, however, would be required to have confidence in the resulting data.

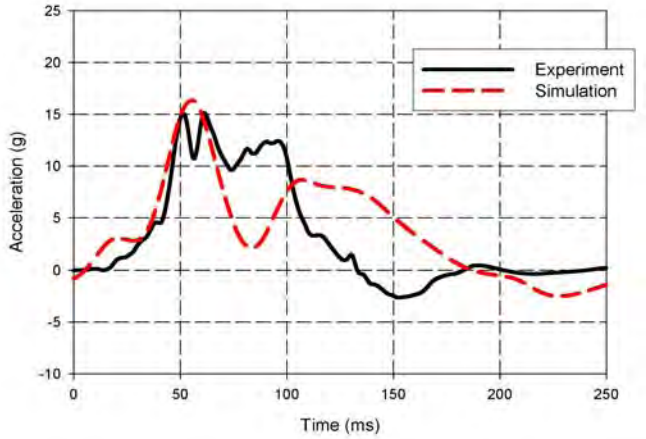

Figure 92. Left-Side Response—ATD and Simulation at FS 408 (Front Row Center)

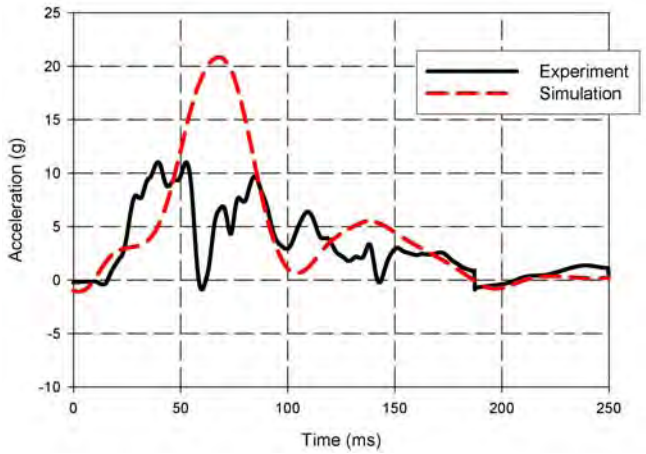

Note: Right-side seats collapse, leading to lower acceleration response for ATD

Figure 93. Right-Side Response—ATD and Simulation at FS 408 (Front Row Center)

8. STUDY OF SIMULATION PARAMETERS.

Six parametric studies were conducted to evaluate their effect on the response of the fuselage, overhead stowage bins, floor tracks, and sidewalls. The six parameters were friction, material yield strength, element failure criteria, roll, luggage, and horizontal-vertical combined loading.

8.1 EFFECT OF FRICTION BETWEEN AIRFRAME AND PLATFORM.

Friction may influence the surface type (such as concrete, soft soil, or sand, which will affect the impact response of the airframes [30]), and under each condition, the value of friction is different. To evaluate the effects of friction on the fuselage, two conditions were used. The first was a fixed airframe-to-platform contact and the second was a sliding (zero coefficient of friction) contact.

8.1.1 Fuselage.

Up to this point, the study assumed that the skin of the airframe does not slide on the platform surface. This assumption is based in part on detailed observations of the experimental impact sequence. Close study of the high-speed film, as recorded by the FAA, shows no discernable slipping between the skin and platform. The airframe does not rotate or slide, though a vertical rebound does occur after the initial impact. Even during rebound, however, no sliding appears to occur. A second reason for this assumption is that the surface of the airframe contains numerous rivets, resulting in a bumpy surface along rivet lines where frames and skin, or stringers and skin, are attached. Furthermore, the surface was a rough, hardwood platform with distinct grain patterns. The bumpy surface of the airframe combines with the rough wood platform to form a contact patch that strongly resists slipping, particularly for the vertical impact case under consideration.

The effect of friction on the structural impact response can be readily addressed with the simulation, by permitting slipping between the airframe and the impact surface. The simulation was modified to allow sliding by setting the coefficient of friction to zero.

Results from this simulation show that the absence of friction significantly alters the pattern of deformation, and that sliding does indeed occur. Figure 94(a) through 94(f) show that the center section of the airframe crushes upward, as each side of the frame tends to slide inward. This upward deflection at the center is clearly evident compared to the fixed case and to the previously shown experimental results. Figure 94(g), for example, which shows deformation at 140 ms, clearly shows the degree to which the frame sections slide inward. The lower left corner (with respect to occupants) curves in for the sliding case, while the same corner buckles outward in the case with friction. The inward motion of the frames near the point of initial contact forms a cusp in the sliding case. The height of this cusp is limited only by the luggage, which pushes downward on the lower frames. No such cusp develops in the experimental case or the simulated case with friction.

When viewed from the front, the fuselage section begins to rotate clockwise, especially when initiating the rebound, at about 140 ms. This rotation is clearly not consistent with the behavior of the experimental test article.

(a) No Friction (Left) and Fixed Contact (Right) at t = 20 ms

(b) No Friction (Left) and Fixed Contact (Right) at t = 40 ms

(c) No Friction (Left) and Fixed Contact (Right) at t = 60 ms

(d) No Friction (Left) and Fixed Contact (Right) at t = 80 ms

Figure 94. Effect of Friction Between Airframe and Platform

(e) No Friction (Left) and Fixed Contact (Right) at t = 100 ms

(f) No Friction (Left) and Fixed Contact (Right) at t = 120 ms

(g) No Friction (Left) and Fixed Contact (Right) at t = 140 ms

(h) No Friction (Left) and Fixed Contact (Right) at t = 160 ms

Figure 94. Effect of Friction Between Airframe and Platform (Continued)

(i) No Friction (Left) and Fixed Contact (Right) at t = 180 ms

(j) No Friction (Left) and Fixed Contact (Right) at t = 180 ms

Figure 94. Effect of Friction Between Airframe and Platform (Continued)

8.1.2 Overhead Stowage Bins.

8.1.2.1 Heath Tecna Bin.

The effects of sliding on the bin acceleration results are less pronounced than the fuselage response. The most typical effect is illustrated in the acceleration response of the overhead stowage bins, beginning with the Heath Tecna bin. Figures 95 through 98 compare the acceleration response of the Heath Tecna bin, showing that the initial acceleration pulse is steeper for the case with friction = 1 (sticking) and less pronounced for the case with friction = 0 (sliding). Sliding reduces the severity of the initial pulse from 20 to 50 ms by allowing lateral motion at the point of contact, effectively reducing the stiffness of the frames. It also effectively provides a longer time span for crushing, as the frames slide during loading to the point where they buckle. This is analogous to a column with one fixed end, as opposed to a column with one end permitted to slide, at least to some degree. For similar impact velocities, the sliding column will be loaded more gradually.

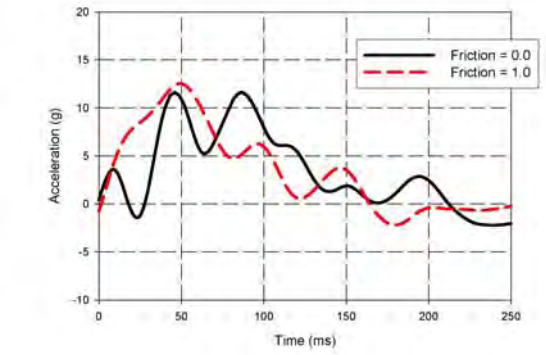

Figure 95. Heath Tecna Bin Acceleration Friction Study—Forward Location

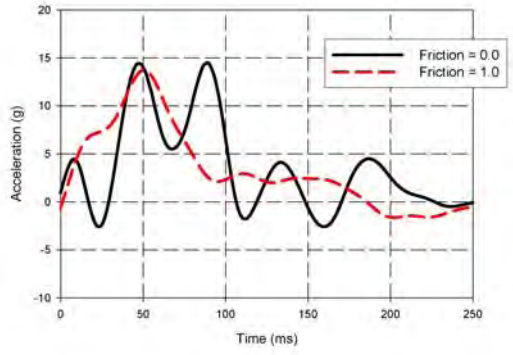

Figure 96. Heath Tecna Bin Acceleration Friction Study—Aft Location

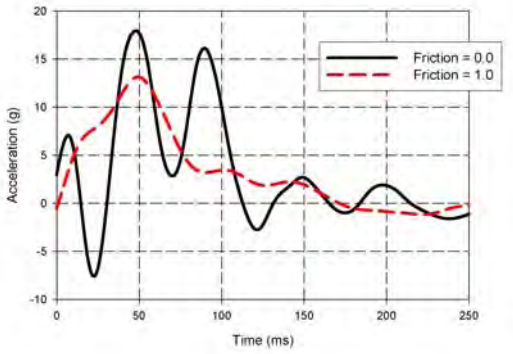

Figure 97. Heath Tecna Bin Acceleration Friction Study—Center Location

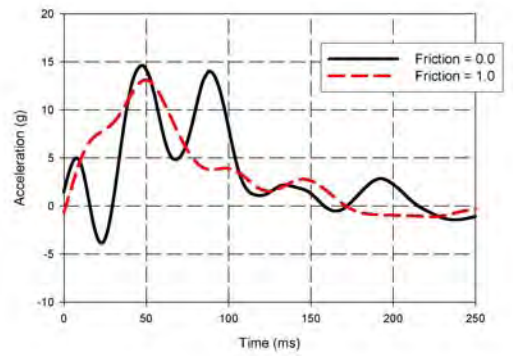

Figure 98. Heath Tecna Bin Acceleration Friction Study—Average All Locations

Figures 99 through 108 present the load time histories of the Heath Tecna bin supports. Again, the initial peak load is generally reduced compared to the case with friction. This closely follows the observed changes in acceleration time histories.

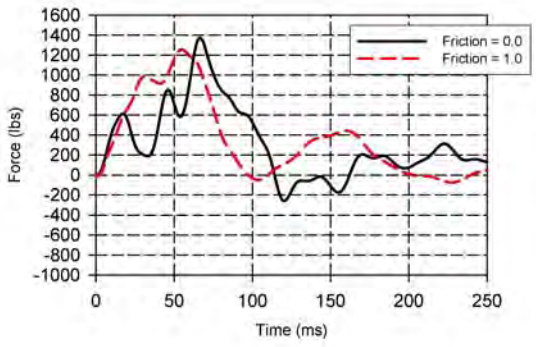

Figure 99. Heath Tecna Bin Load Friction Study—Forward Strut

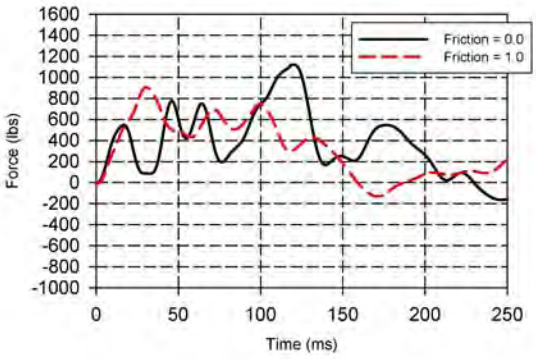

Figure 100. Heath Tecna Bin Load Friction Study—Aft Strut

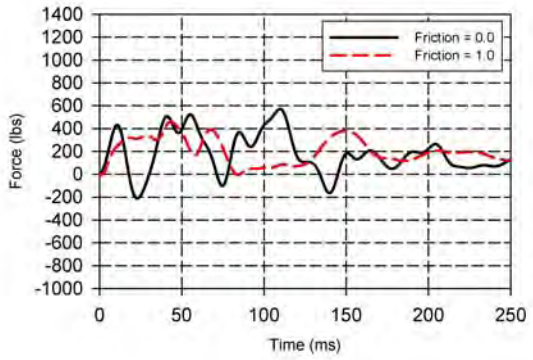

Figure 101. Heath Tecna Bin Load Friction Study, FS 400—A Leg of Bracket

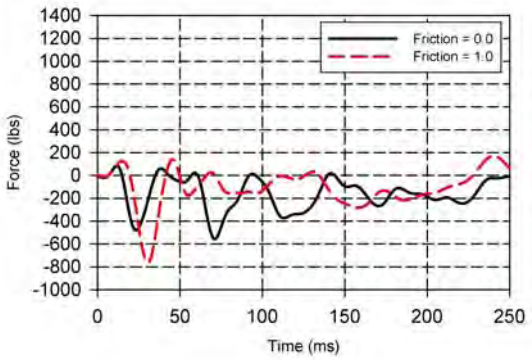

Figure 102. Heath Tecna Bin Load Friction Study, FS 400—B Leg of Bracket

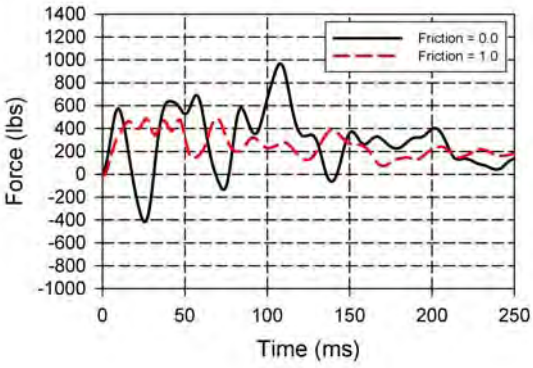

Figure 103. Heath Tecna Bin Load Friction Study, FS 420—A Leg of Bracket

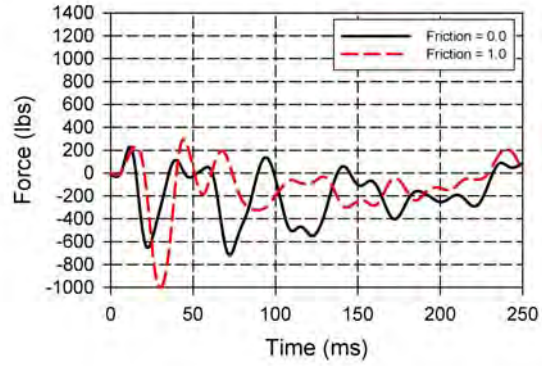

Figure 104. Heath Tecna Bin Load Friction Study, FS 420—B Leg of Bracket

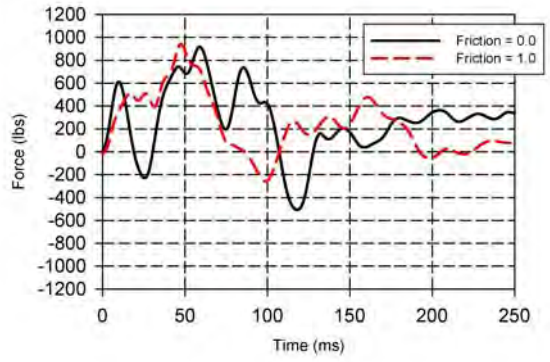

Figure 105. Heath Tecna Bin Load Friction Study, FS 460—A Leg of Bracket

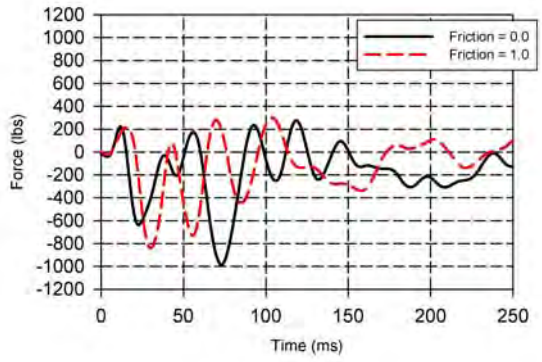

Figure 106. Heath Tecna Bin Load Friction Study, FS 460—B Leg of Bracket

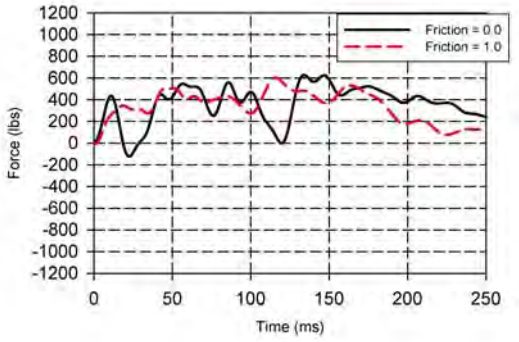

Figure 107. Heath Tecna Bin Load Friction Study, FS 480—A Leg of Bracket

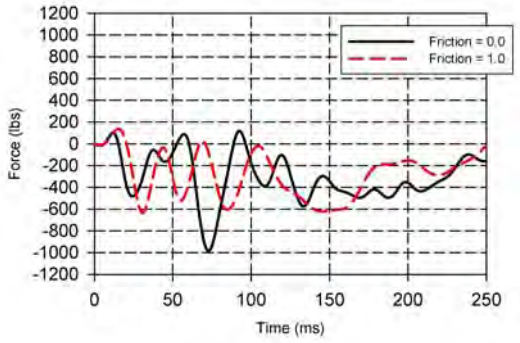

Figure 108. Heath Tecna Bin Load Friction Study, FS 480—B Leg of Bracket

8.1.2.2 Hitco Bin.

Figures 109 to 112 show the acceleration response results for the Hitco bin, comparing friction to sliding. The initial peak, illustrated in figure 110, is lower for the sliding case and is also delayed due to the sliding that occurs prior to the load being transferred up through the frames. The initial peak with friction occurs at about 20 ms, while this occurs at approximately 45 ms when sliding is permitted. The primary acceleration pulse, which is about 120 ms, is identical in magnitude and timing for the friction and sliding conditions.

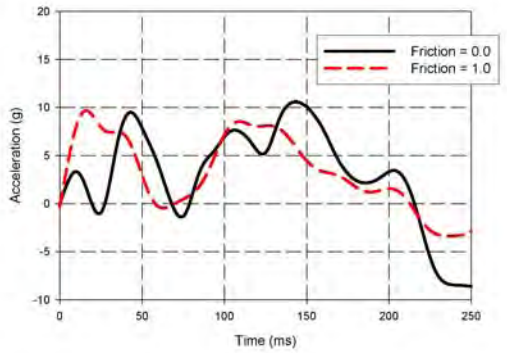

Figure 109. Hitco Bin Acceleration Friction Study, Forward Location

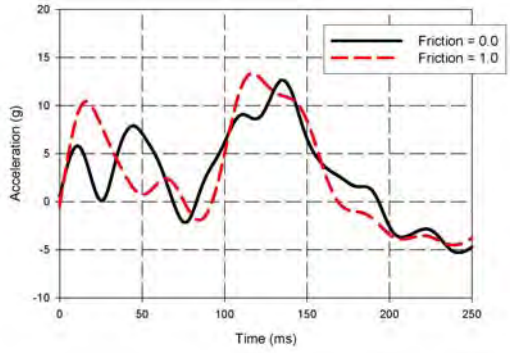

Figure 110. Hitco Bin Acceleration Friction Study, Aft Location

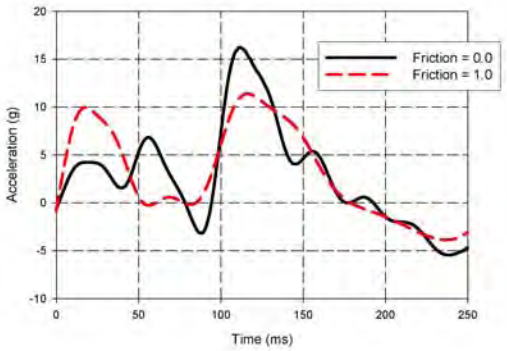

Figure 111. Hitco Bin Acceleration Friction Study, Center Location

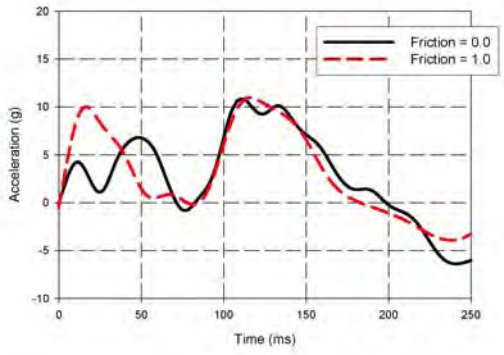

Figure 112. Hitco Bin Acceleration Friction Study, Average All Locations

Figures 113 through 122 present the load time histories of the Hitco bin supports. Similar to the acceleration responses, the initial peak loads for the sliding condition are generally reduced and delayed in comparison to the case with the friction condition.

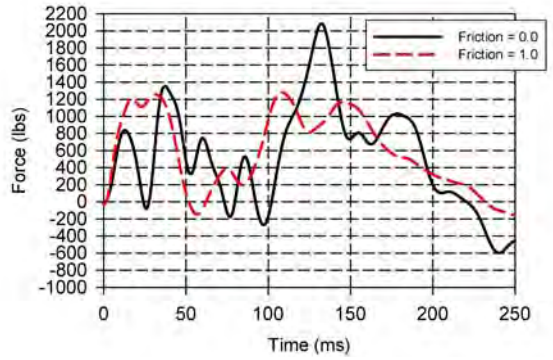

Figure 113. Hitco Bin Load Friction Study, Forward Strut

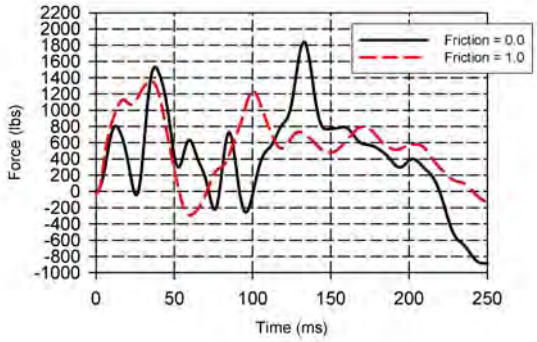

Figure 114. Hitco Bin Load Friction Study, Aft Strut

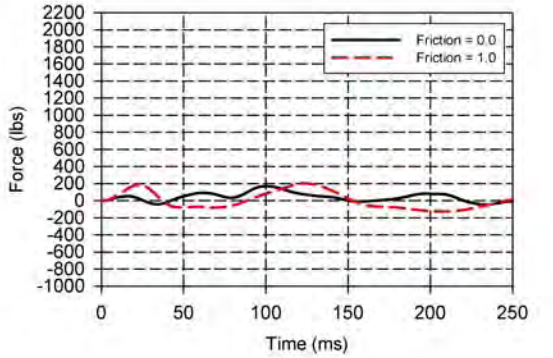

Figure 115. Hitco Bin Load Friction Study, FS 400 Vertical Link

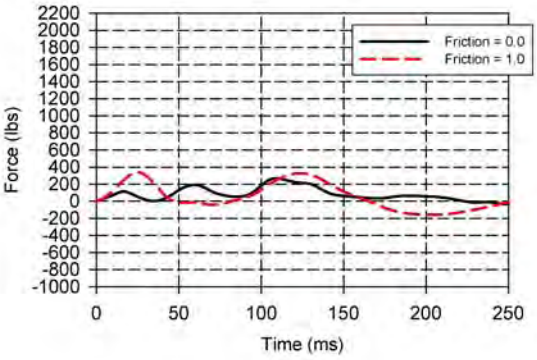

Figure 116. Hitco Bin Load Friction Study, FS 400 Horizontal Link

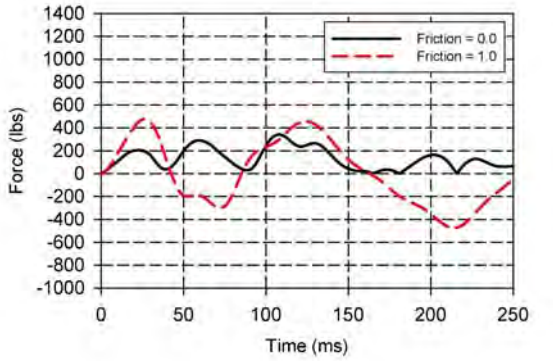

Figure 117. Hitco Bin Load Friction Study, FS 420 Vertical Link

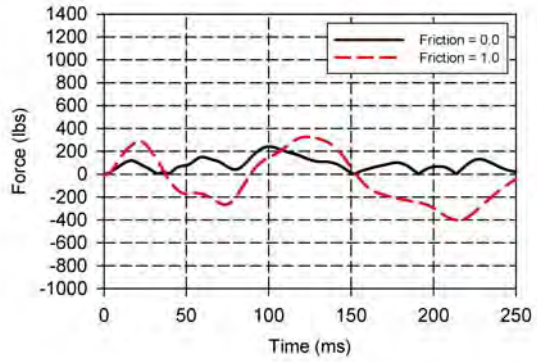

Figure 118. Hitco Bin Load Friction Study, FS 420 Horizontal Link

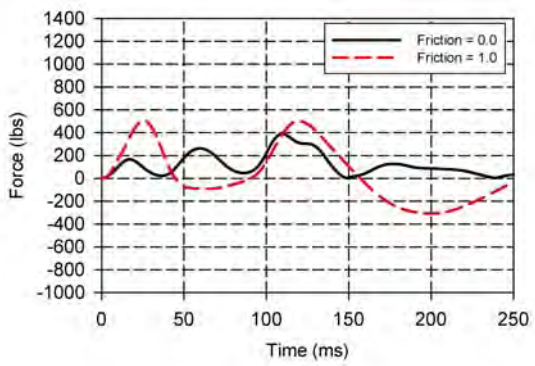

Figure 119. Hitco Bin Load Friction Study, FS 460 Vertical Link

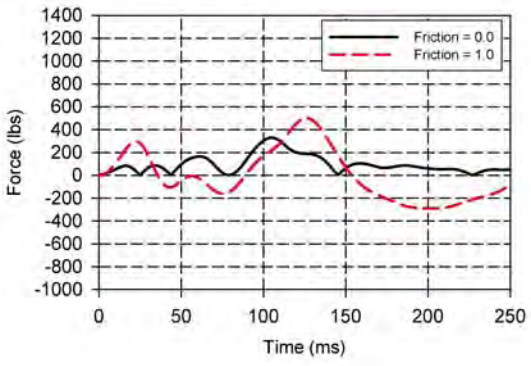

Figure 120. Hitco Bin Load Friction Study, FS 460 Horizontal Link

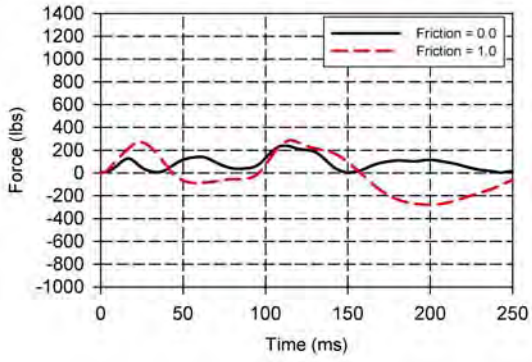

Figure 121. Hitco Bin Load Friction Study, FS 480 Vertical Link

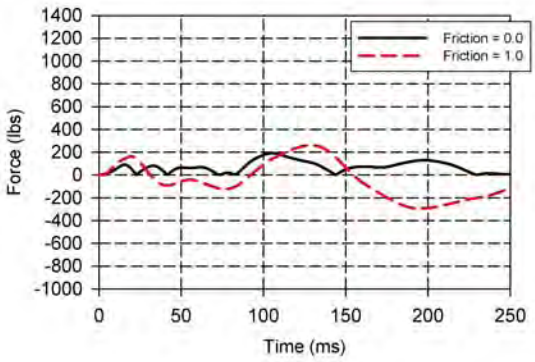

Figure 122. Hitco Bin Load Friction Study, FS 480 Horizontal Link

8.1.2.3 Floor Tracks.

The results for the floor track accelerations, comparing friction and sliding contacts, are shown in figures 123 to 136. The magnitude of the responses is similar; however, the timing of the peaks is shifted.

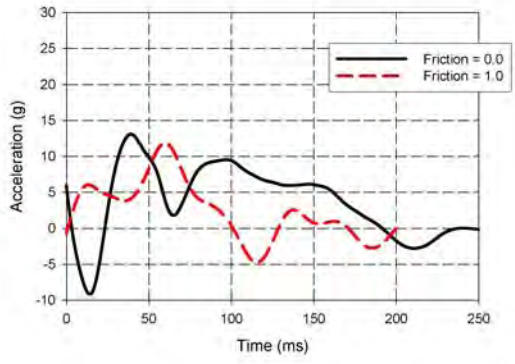

Figure 123. Floor Track Acceleration Friction Study, FS 380—Left Inside Floor Track

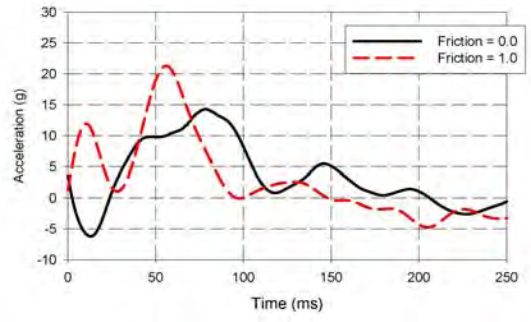

Figure 124. Floor Track Acceleration Friction Study, FS 380—Right Inside Floor Track

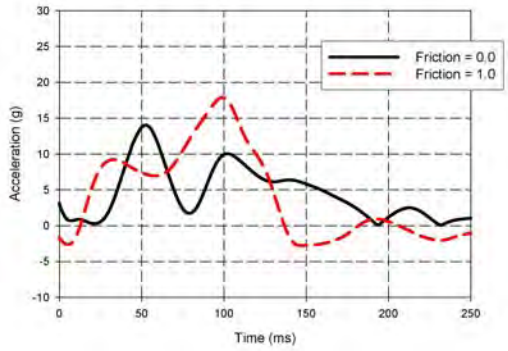

Figure 125. Floor Track Acceleration Friction Study, FS 418—Left Outside Floor Track

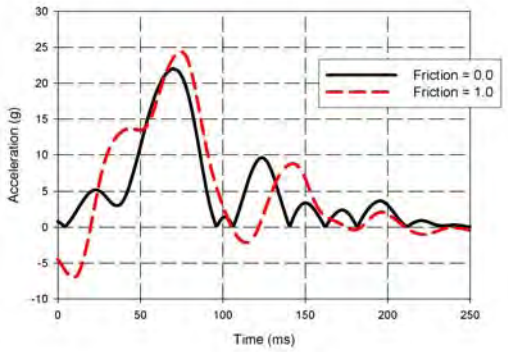

Figure 126. Floor Track Acceleration Friction Study, FS 418—Right Outside Floor Track

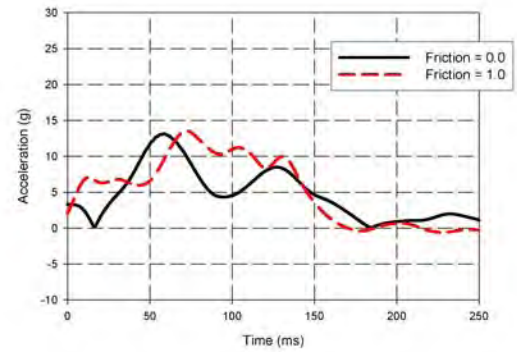

Figure 127. Floor Track Acceleration Friction Study, FS 418—Left Inside Floor Track

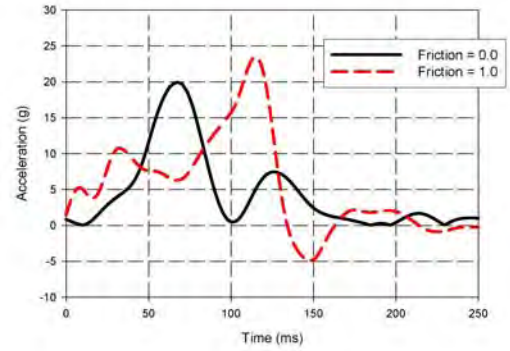

Figure 128. Floor Track Acceleration Friction Study, FS 418—Right Inside Floor Track

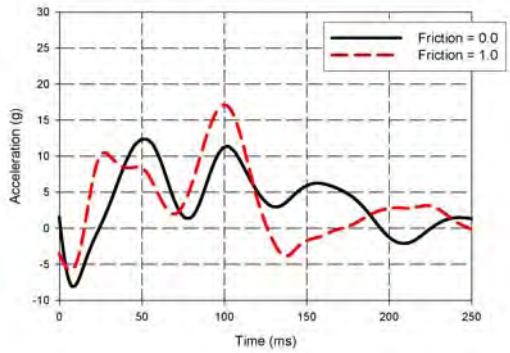

Figure 129. Floor Track Acceleration Friction Study, FS 452—Left Outside Floor Track

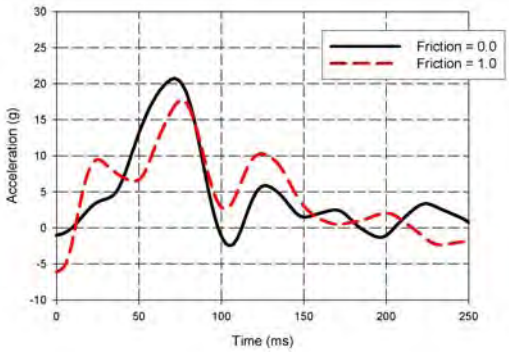

Figure 130. Floor Track Acceleration Friction Study, FS 452—Right Outside Floor Track

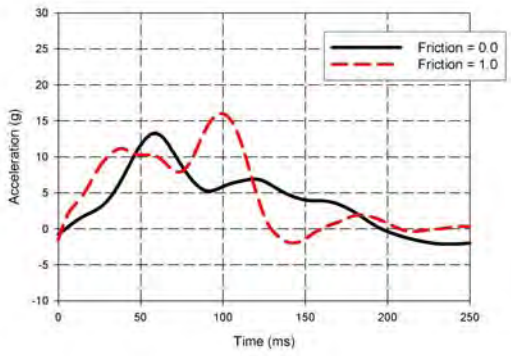

Figure 131. Floor Track Acceleration Friction Study, FS 452—Left Inside Floor Track

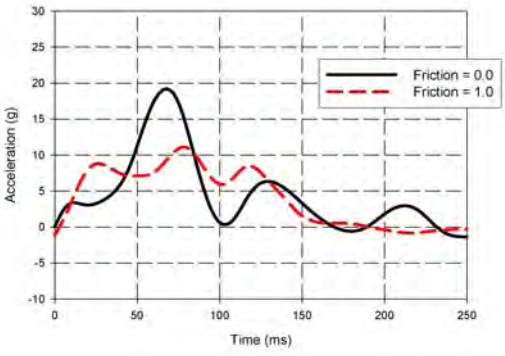

Figure 132. Floor Track Acceleration Friction Study, FS 452—Right Inside Floor Track

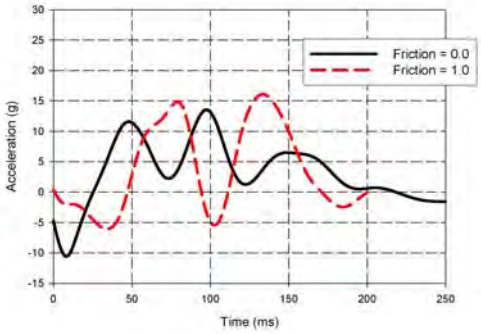

Figure 133. Floor Track Acceleration Friction Study, FS 484—Left Outside Floor Track

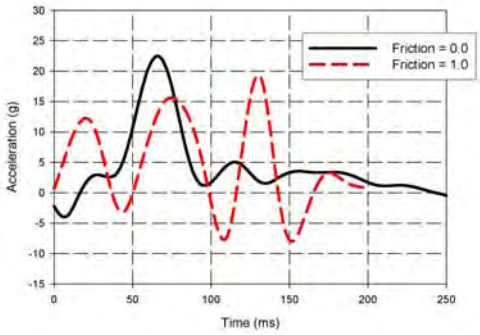

Figure 134. Floor Track Acceleration Friction Study, FS 484—Right Outside Floor Track

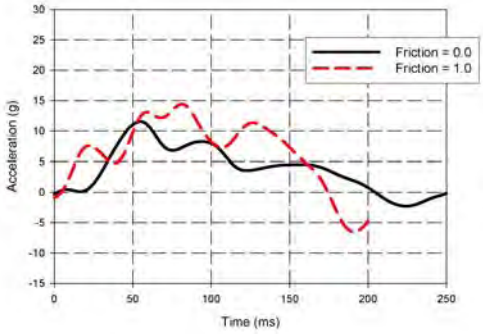

Figure 135. Floor Track Acceleration Friction Study, FS 484—Left Inside Floor Track

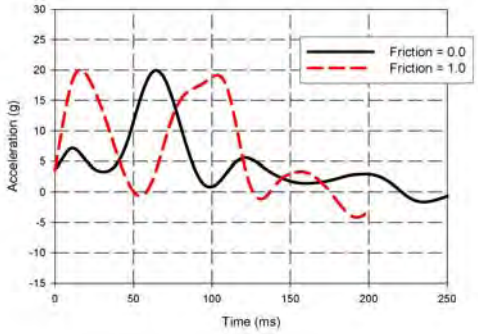

Figure 136. Floor Track Acceleration Friction Study, FS 484—Right Inside Floor Track

8.1.2.4 Sidewall.

The results for the sidewall accelerations, comparing friction and sliding contacts, are shown in figures 137 to 148. The magnitude of the responses is similar; however, the timing of the peaks is shifted.

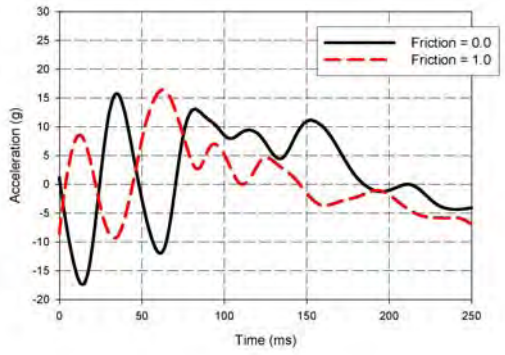

Figure 137. Upper Sidewall Acceleration Friction Study, FS 400—Left Sidewall

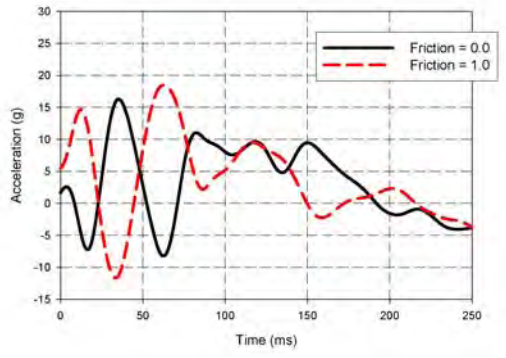

Figure 138. Upper Sidewall Acceleration Friction Study, FS 400—Right Sidewall

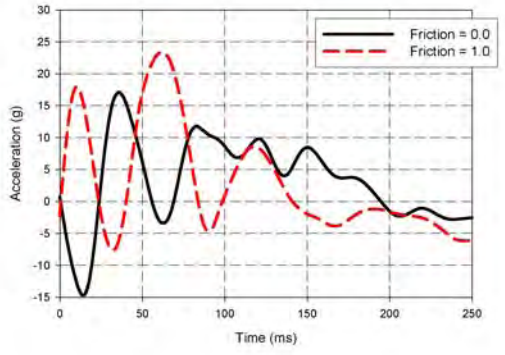

Figure 139. Upper Sidewall Acceleration Friction Study, FS 440—Left Sidewall

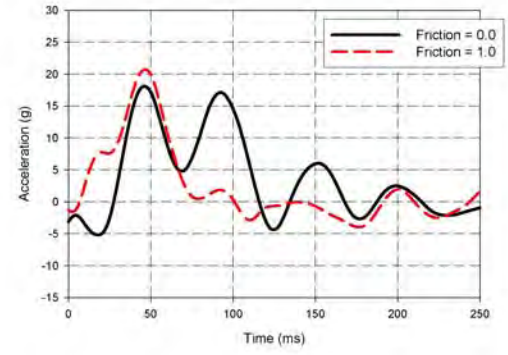

Figure 140. Upper Sidewall Acceleration Friction Study, FS 440—Right Sidewall

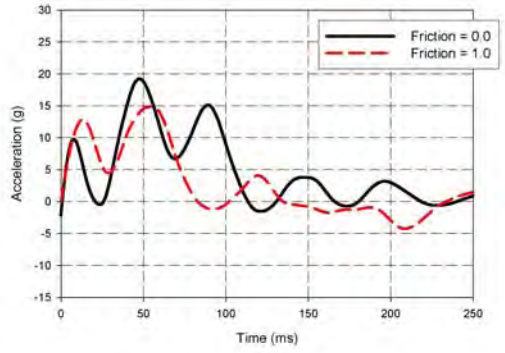

Figure 141. Upper Sidewall Acceleration Friction Study, FS 480—Left Sidewall

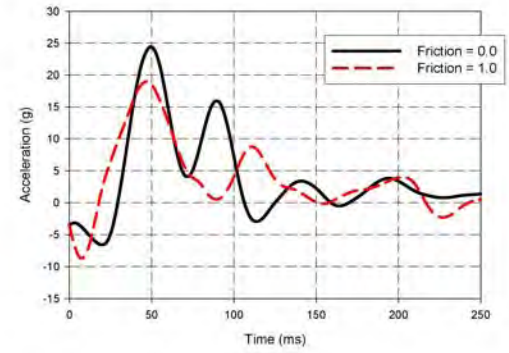

Figure 142. Upper Sidewall Acceleration Friction Study, FS 480—Right Sidewall

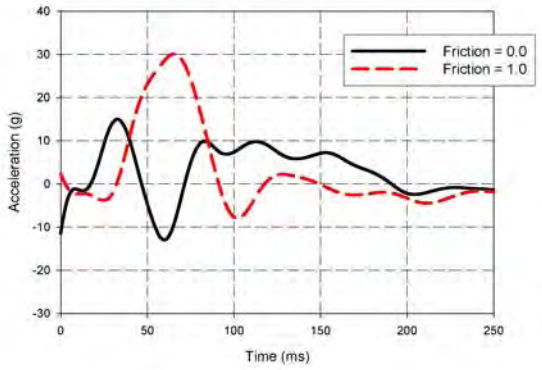

Figure 143. Lower Sidewall Acceleration Friction Study, FS 400—Left Sidewall

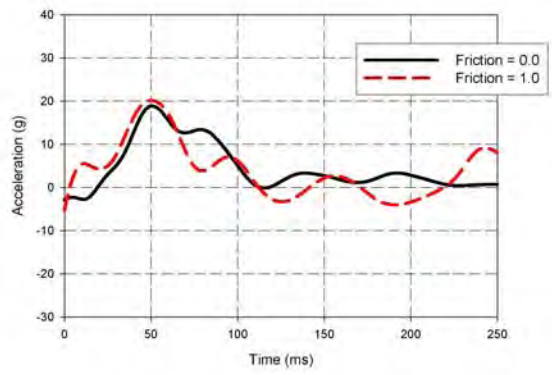

Figure 144. Lower Sidewall Acceleration Friction Study, FS 400—Right Sidewall

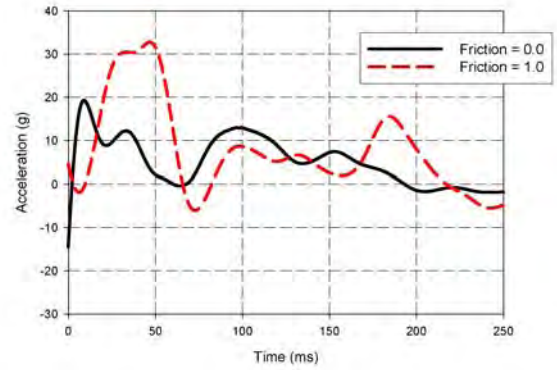

Figure 145. Lower Sidewall Acceleration Friction Study, FS 440—Left Sidewall

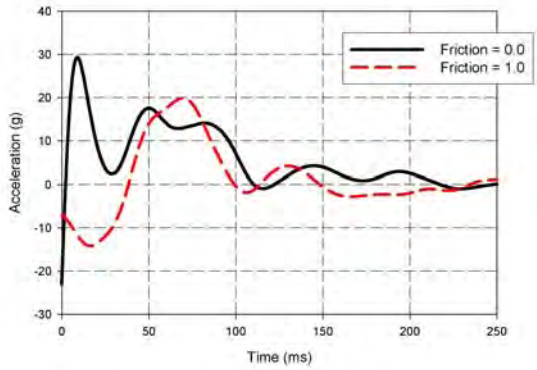

Figure 146. Lower Sidewall Acceleration Friction Study, FS 440—Right Sidewall

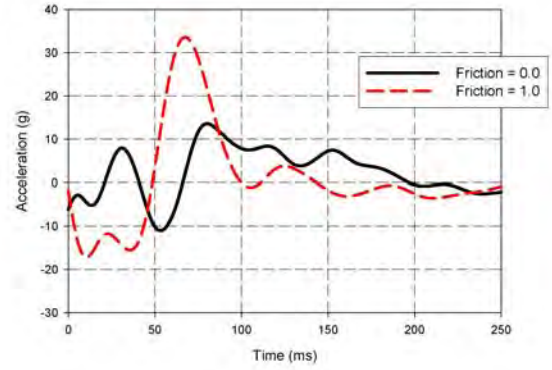

Figure 147. Lower Sidewall Acceleration Friction Study, FS 480—Left Sidewall

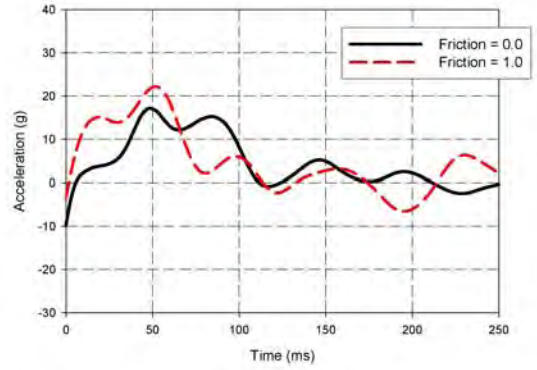

Figure 148. Lower Sidewall Acceleration Friction Study, FS 480—Right Sidewall

8.2 MATERIAL YIELD STRENGTH.

8.2.1 Fuselage.

The frame material, 7075-T6 aluminum, is an alloy known to be sensitive to corrosion. Given the 20- to 25-year service life of the test article, it is possible that both exposure to moisture and fatigue may have degraded the original material properties, resulting a lower yield stress than would otherwise be expected.

A 20% decrease in yield strength was selected to study the effects a lower yield stress might have on simulation results. Although the simulation shows a slight increase in total vertical crushing, the acceleration response results show that the change in yield strength plays a minor role in determining the basic simulation results.

Figure 149 shows the time history of deformation. Little difference is observed between the baseline case and the case with reduced yield strength. Figures 149(g) and (h) show that the change in yield strength results in additional crushing, but that the overall pattern of deformation remains the same.

(a) Reduced Yield Strength (Left) and Baseline (Right) at t = 20 ms

(b) Reduced Yield Strength (Left) and Baseline (Right) at t = 40 ms

Figure 149. Material Yield Strength

(c) Reduced Yield Strength (Left) and Baseline (Right) at t = 60 ms

(d) Reduced Yield Strength (Left) and Baseline (Right) at t = 80 ms

(e) Reduced Yield Strength (Left) and Baseline (Right) at t = 100 ms

(f) Reduced Yield Strength (Left) and Baseline (Right) at t = 120 ms

Figure 149. Material Yield Strength (Continued)

(g) Reduced Yield Strength (Left) and Baseline (Right) at t = 140 ms

(h) Reduced Yield Strength (Left) and Baseline (Right) at t = 160 ms

(i) Reduced Yield Strength (Left) and Baseline (Right) at t = 180 ms

(j) Reduced Yield Strength (Left) and Baseline (Right) at t = 200 ms

Figure 149. Material Yield Strength (Continued)

8.2.2 Overhead Stowage Bins.

8.2.2.1 Heath Tecna Bin.

Figures 150 through 153 show that the peak acceleration value is nearly identical for each case. Some additional reverberations are experienced in the case with lowered yield strength. The overall pulse shape and duration show only minor changes.

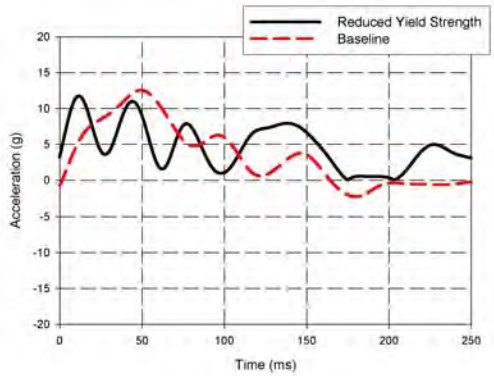

Figure 150. Heath Tecna Bin Acceleration Reduced Yield—Forward Location

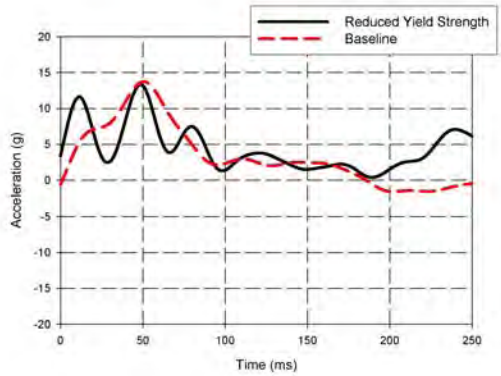

Figure 151. Heath Tecna Bin Acceleration Reduced Yield—Aft Location

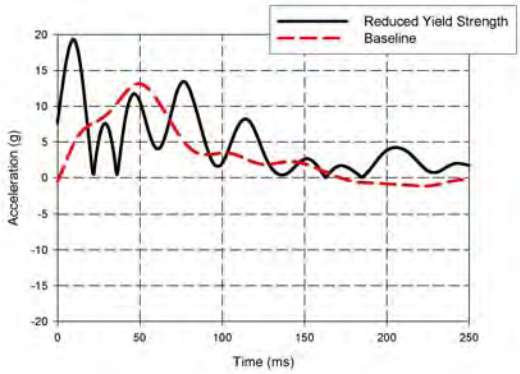

Figure 152. Heath Tecna Bin Acceleration Reduced Yield—Center Location

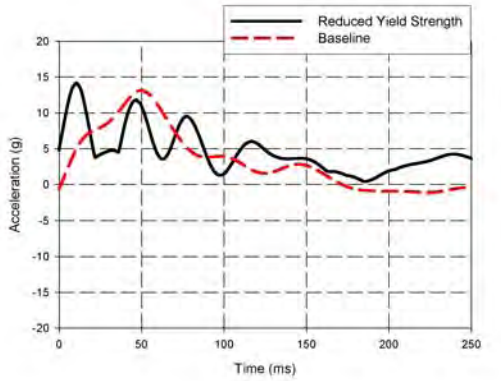

Figure 153. Heath Tecna Bin Acceleration Reduced Yield—Average All Locations

The time history of loading in the supporting structures shows a similarly predictable pattern, with only relatively minor changes in peak loading. These are shown in figures 154 through 163.

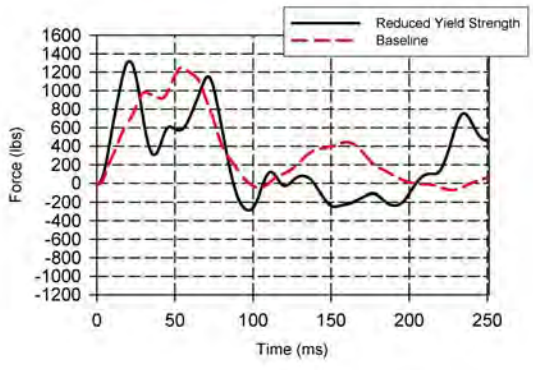

Figure 154. Heath Tecna Bin Load Reduced Yield, Forward Strut

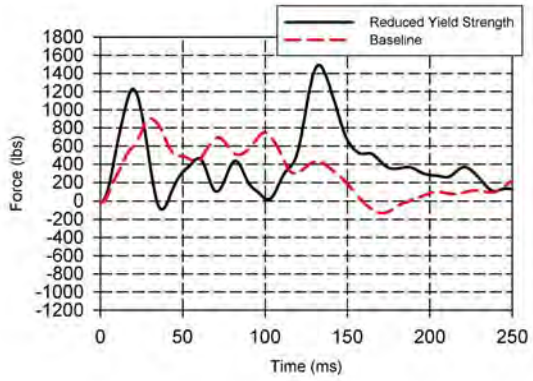

Figure 155. Heath Tecna Bin Load Reduced Yield, Aft Strut

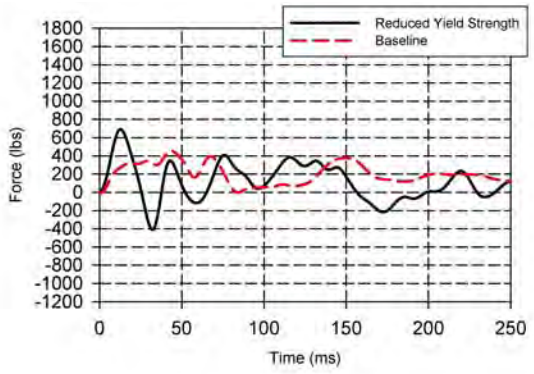

Figure 156. Heath Tecna Bin Load Reduced Yield, FS 400—A Leg of Bracket

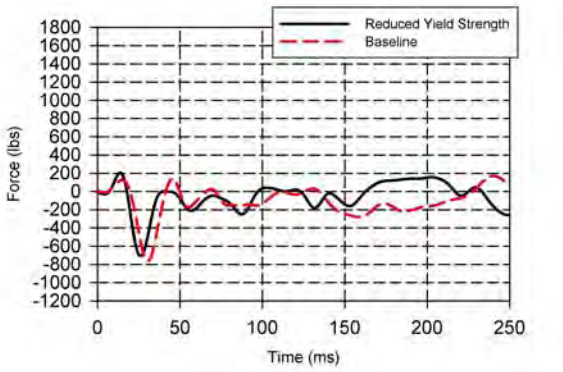

Figure 157. Heath Tecna Bin Load Reduced Yield, FS 400—B Leg of Bracket

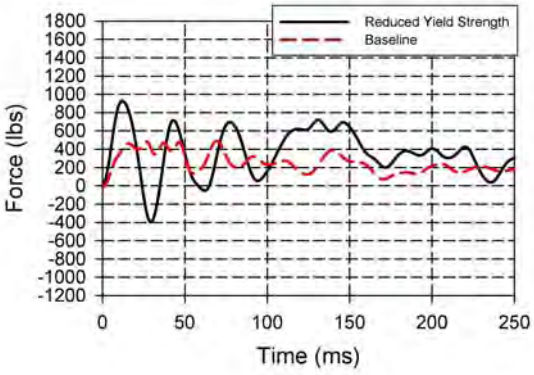

Figure 158. Heath Tecna Bin Load Reduced Yield, FS 420—A Leg of Bracket

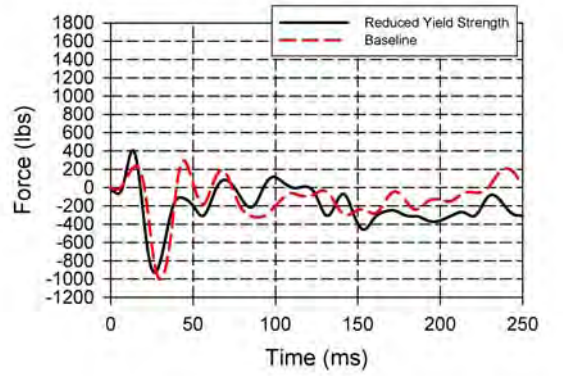

Figure 159. Heath Tecna Bin Load Reduced Yield, FS 420—B Leg of Bracket

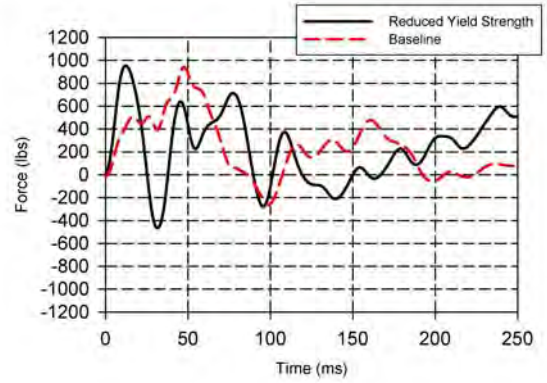

Figure 160. Heath Tecna Bin Load Reduced Yield, FS 460—A Leg of Bracket

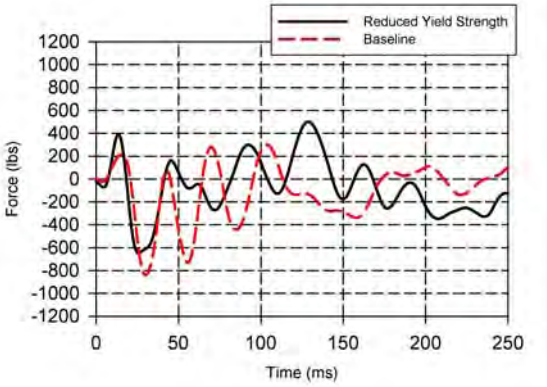

Figure 161. Heath Tecna Bin Load Reduced Yield, FS 460—B Leg of Bracket

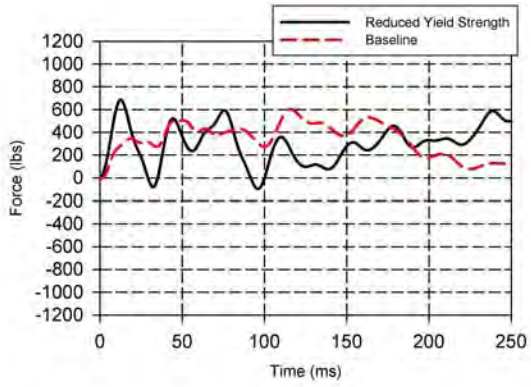

Figure 162. Heath Tecna Bin Load Reduced Yield, FS 480—A Leg of Bracket

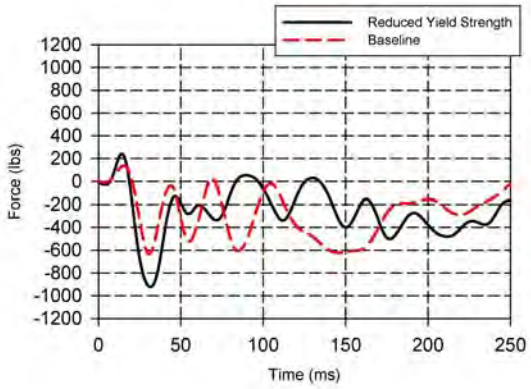

Figure 163. Heath Tecna Bin Load Reduced Yield, FS 480—B Leg of Bracket

8.2.2.2 Hitco Bin.

Figures 164 to 167 show the acceleration response results for the Hitco bin. Similar to the Heath Tecna bins, these show only minor variations with the reduction in allowable yield stress. Figures 168 to 177 show the corresponding load time histories in the supporting tie rods and links.

In general, the results from the left side of the fuselage (Hitco bin) show less change resulting from the lowered yield stress compared to the right (Heath Tecna) side.

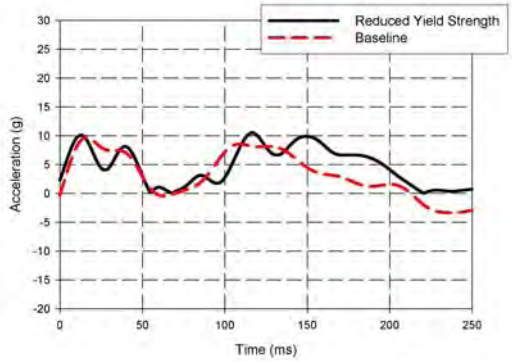

Figure 164. Hitco Bin Acceleration Reduced Yield, Forward Location

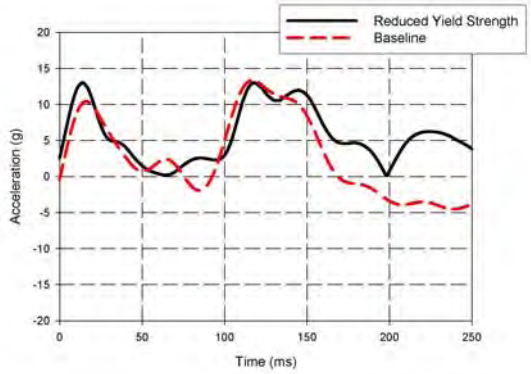

Figure 165. Hitco Bin Acceleration Reduced Yield, Aft Location

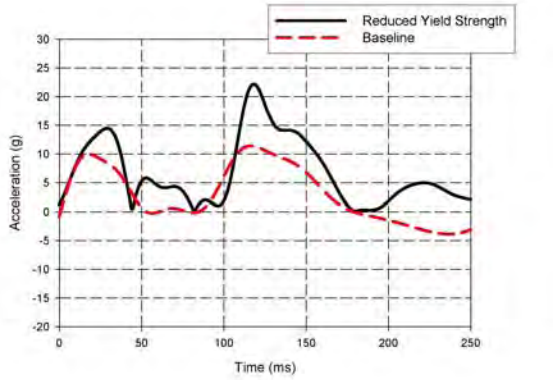

Figure 166. Hitco Bin Acceleration
Reduced Yield, Center Location

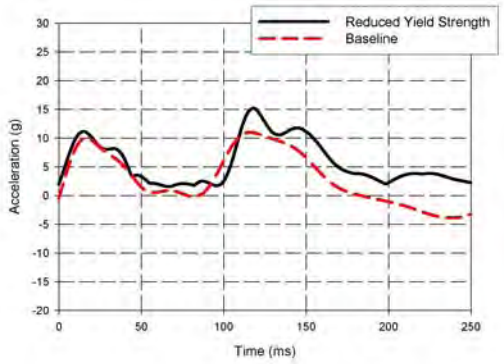

Figure 167. Hitco Bin Acceleration
Reduced Yield, Average All Locations

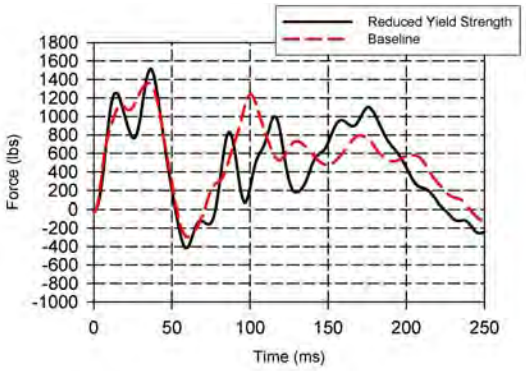

Figure 168. Hitco Bin Load
Reduced Yield, Forward Strut

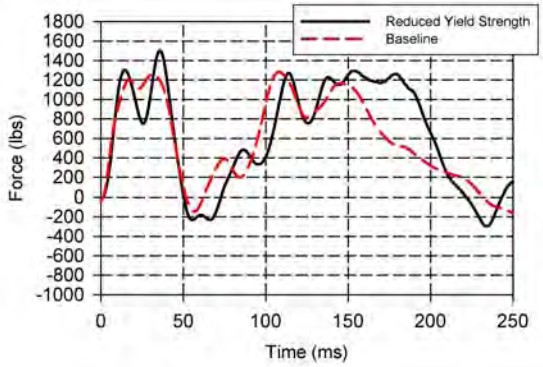

Figure 169. Hitco Bin Load
Reduced Yield, Aft Strut

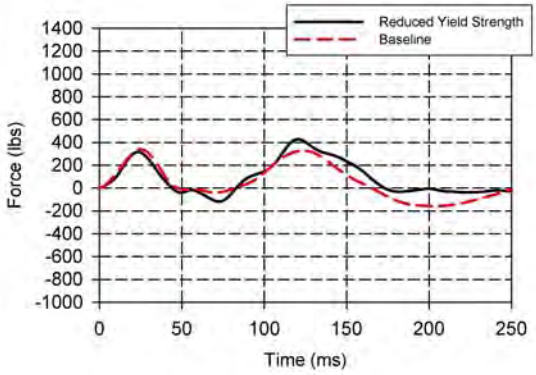

Figure 170. Hitco Bin Load
Reduced Yield, FS 400 Vertical Link

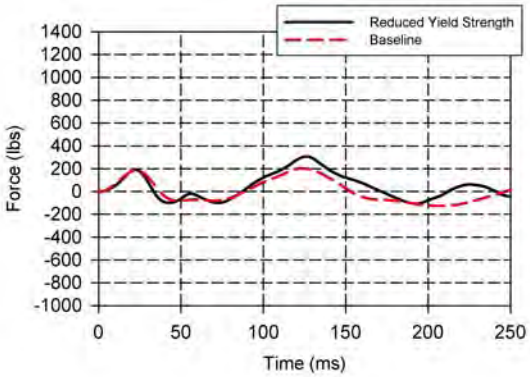

Figure 171. Hitco Bin Load
Reduced Yield, FS 400 Horizontal Link

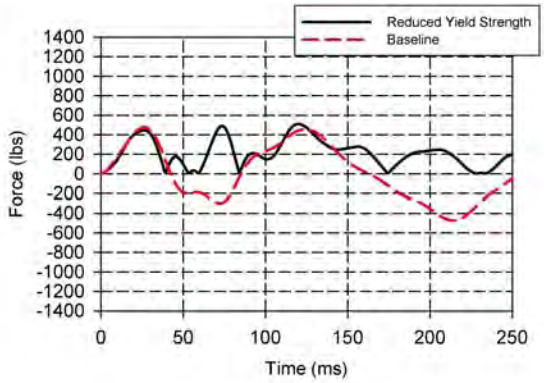

Figure 172. Hitco Bin Load
Reduced Yield, FS 420 Vertical Link

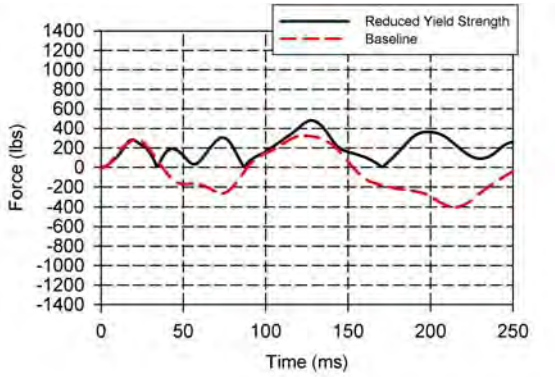

Figure 173. Hitco Bin Load
Reduced Yield, FS 420 Horizontal Link

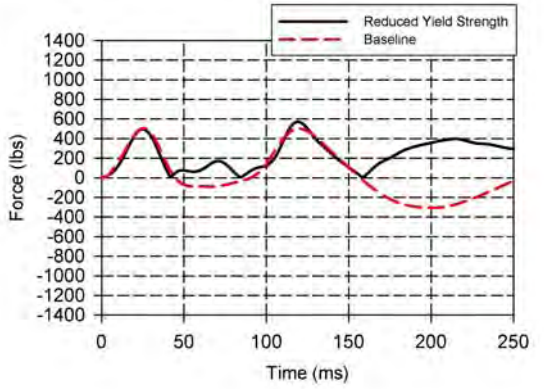

Figure 174. Hitco Bin Load
Reduced Yield, FS 460 Vertical Link

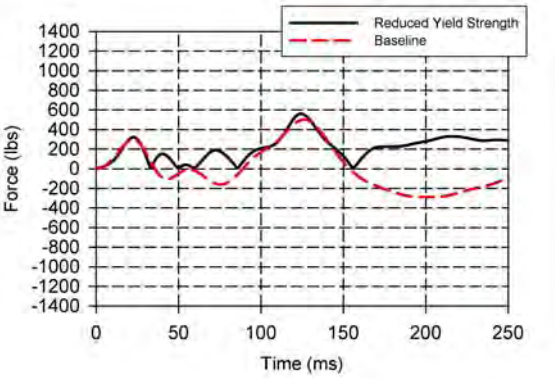

Figure 175. Hitco Bin Load
Reduced Yield, FS 460 Horizontal Link

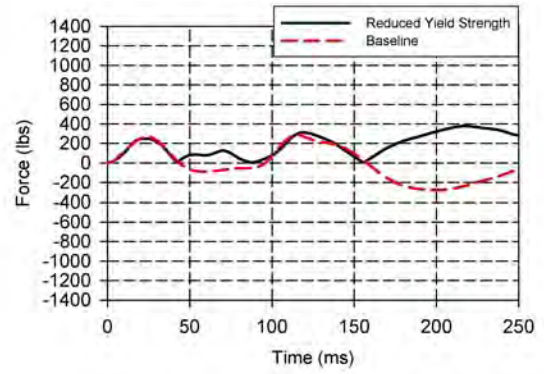

Figure 176. Hitco Bin Load
Reduced Yield, FS 480 Vertical Link

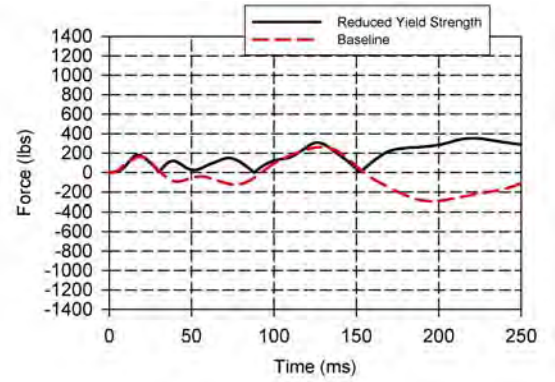

Figure 177. Hitco Bin Load
Reduced Yield, FS 480 Horizontal Link

8.2.3 Floor Tracks.

Figures 178 to 191 show the effect of reduced material yield strength on floor track acceleration. Generally, the peak responses are lower for the reduced yield strength.

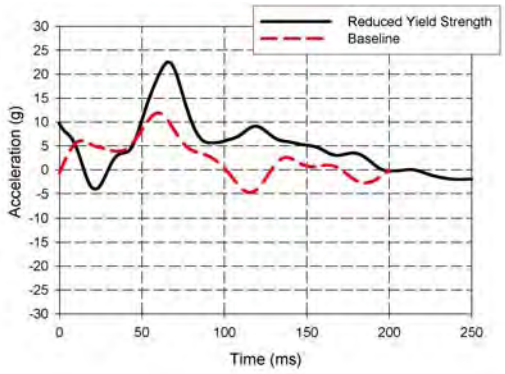

Figure 178. Floor Track Acceleration Reduced Yield, FS 380—Left Inside Floor Track

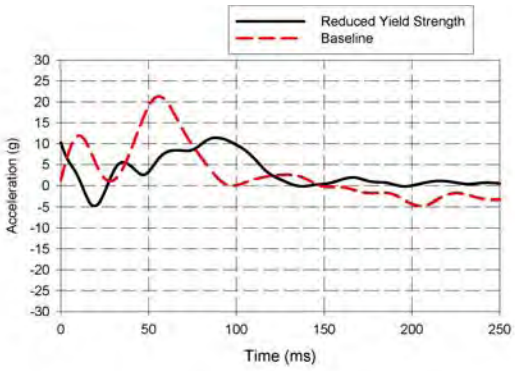

Figure 179. Floor Track Acceleration Reduced Yield, FS 380—Right Inside Floor Track

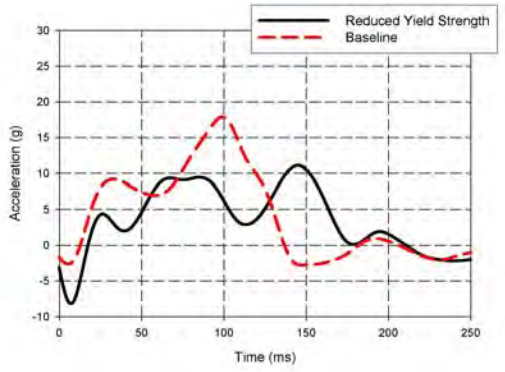

Figure 180. Floor Track Acceleration Reduced Yield, FS 418—Left Outside Floor Track

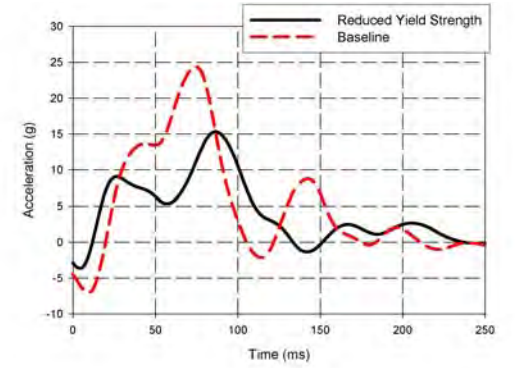

Figure 181. Floor Track Acceleration Reduced Yield, FS 418—Right Outside Floor Track

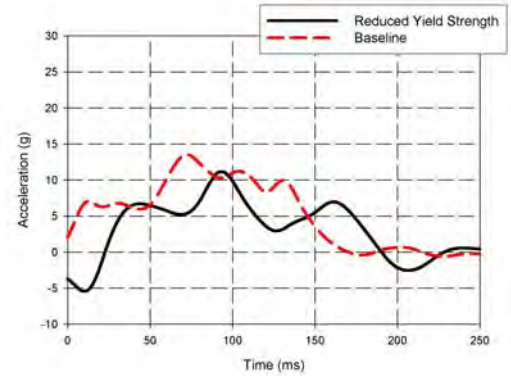

Figure 182. Floor Track Acceleration Reduced Yield, FS 418—Left Inside Floor Track

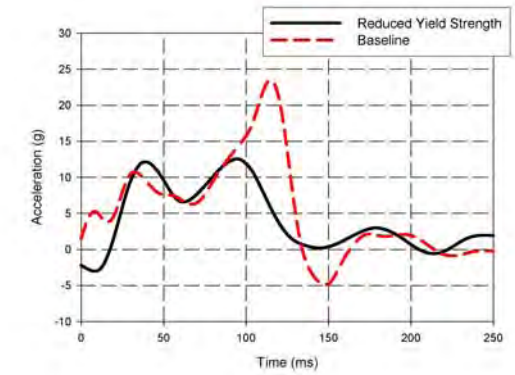

Figure 183. Floor Track Acceleration Reduced Yield, FS 418—Right Inside Floor Track

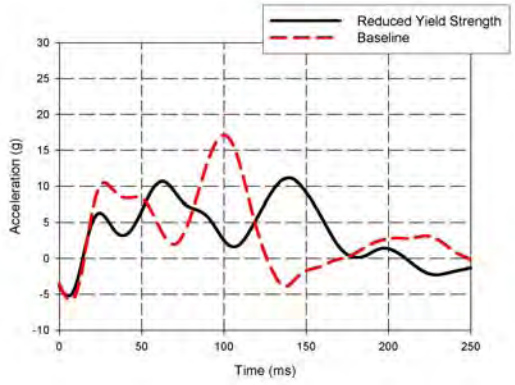

Figure 184. Floor Track Acceleration Reduced Yield, FS 452—Left Outside Floor Track

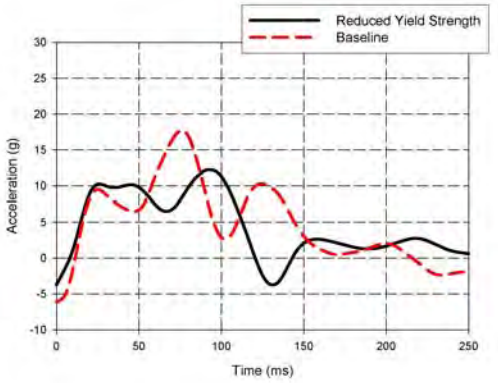

Figure 185. Floor Track Acceleration Reduced Yield, FS 452—Right Outside Floor Track

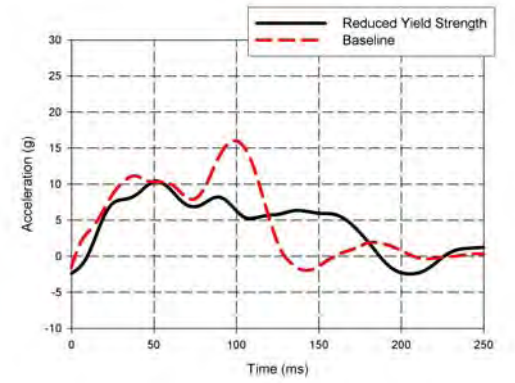

Figure 186. Floor Track Acceleration Reduced Yield, FS 452—Left Inside Floor Track

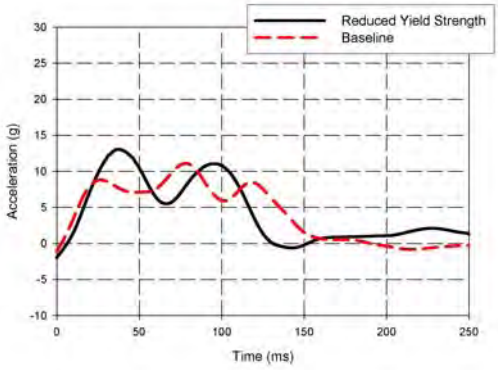

Figure 187. Floor Track Acceleration Reduced Yield, FS 452—Right Inside Floor Track

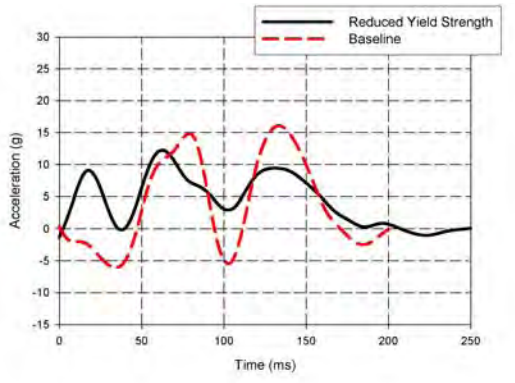

Figure 188. Floor Track Acceleration Reduced Yield, FS 484—Left Outside Floor Track

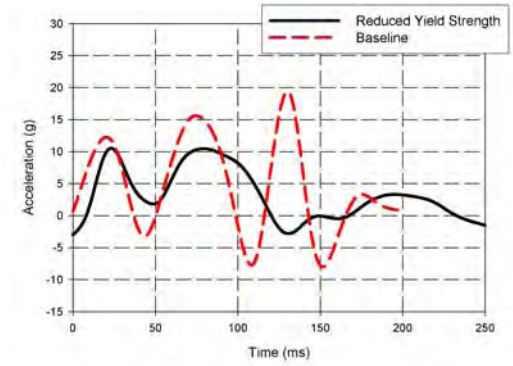

Figure 189. Floor Track Acceleration Reduced Yield, FS 484—Right Outside Floor Track

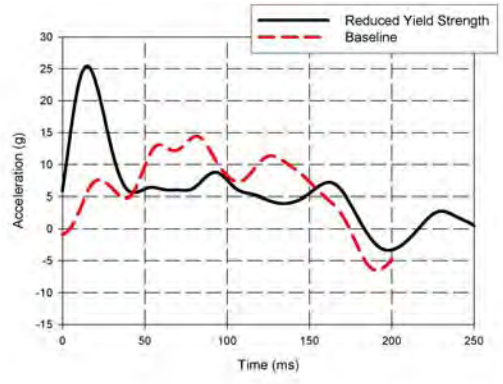

Figure 190. Floor Track Acceleration Reduced Yield, FS 484—Left Inside Floor Track

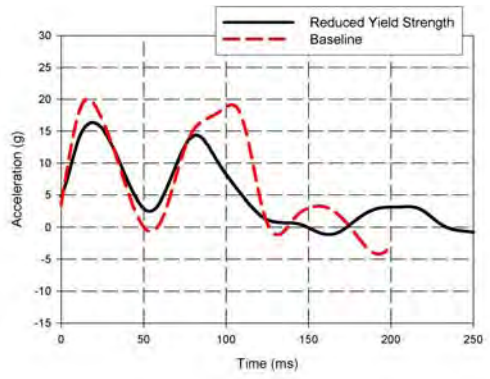

Figure 191. Floor Track Acceleration Reduced Yield, FS 484—Right Inside Floor Track

8.2.4 Sidewalls.

The upper sidewall results show either little change in peak acceleration pulse or a slight decrease in peak acceleration pulse, resulting from the lowered yield stress. This is expected, as the lowered yield stress permits greater deformation in the upper frames, resulting in lower acceleration values. The sidewall results are shown in figures 192 through 203.

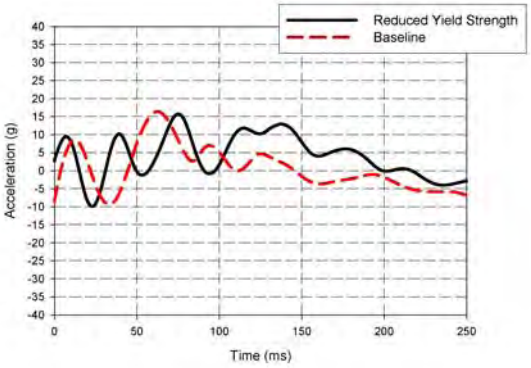

Figure 192. Upper Sidewall Acceleration Reduced Yield, FS 400—Left Sidewall

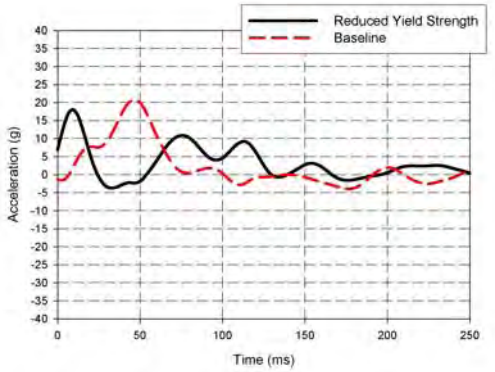

Figure 193. Upper Sidewall Acceleration Reduced Yield, FS 400—Right Sidewall

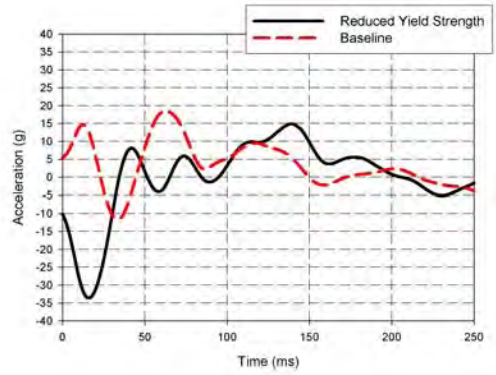

Figure 194. Upper Sidewall Acceleration Reduced Yield, FS 440—Left Sidewall

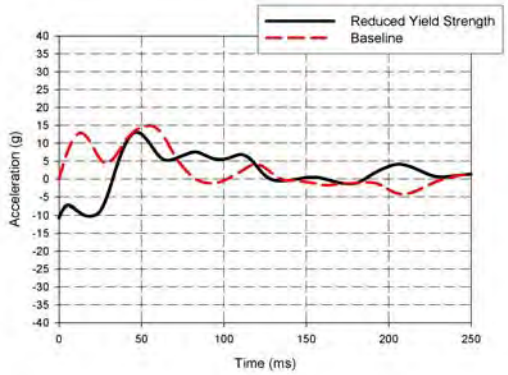

Figure 195. Upper Sidewall Acceleration Reduced Yield, FS 440—Right Sidewall

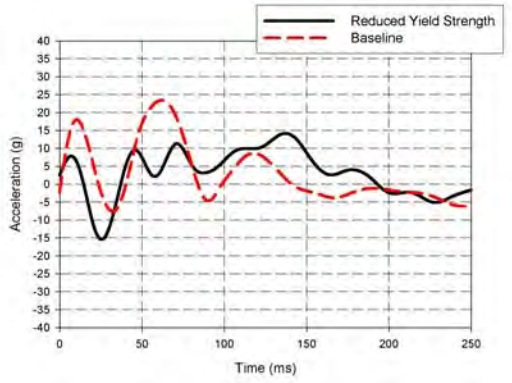

Figure 196. Upper Sidewall Acceleration Reduced Yield, FS 480—Left Sidewall

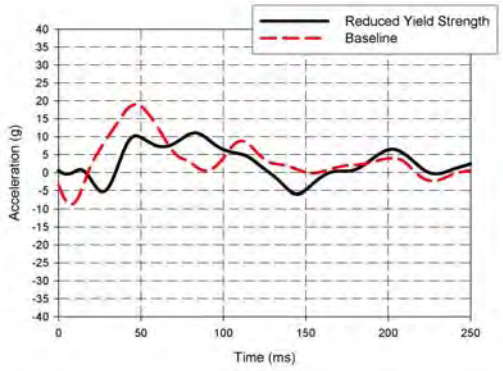

Figure 197. Upper Sidewall Acceleration Reduced Yield, FS 480—Right Sidewall

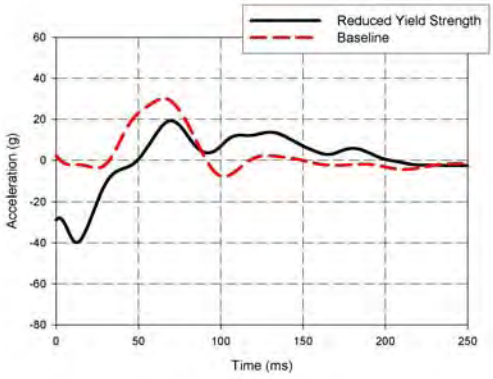

Figure 198. Lower Sidewall Acceleration Reduced Yield, FS 400—Left Sidewall

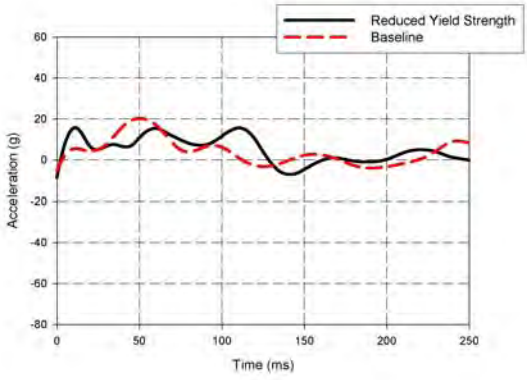

Figure 199. Lower Sidewall Acceleration Reduced Yield, FS 400—Right Sidewall

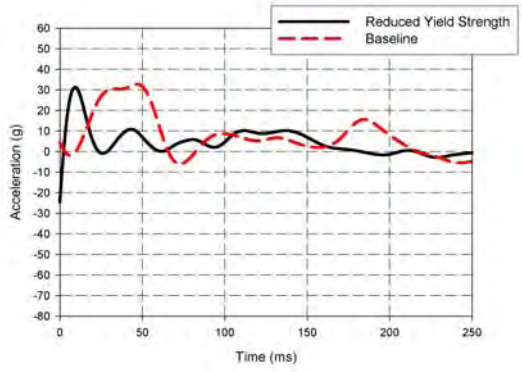

Figure 200. Lower Sidewall Acceleration Reduced Yield, FS 440—Left Sidewall

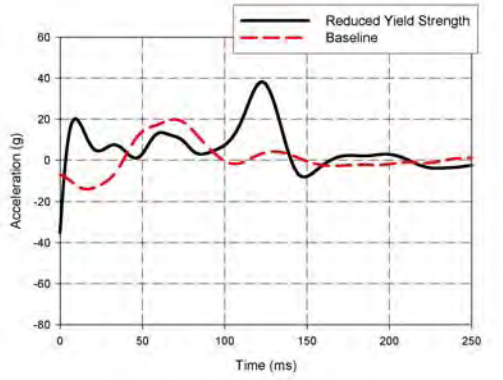

Figure 201. Lower Sidewall Acceleration Reduced Yield, FS 440—Right Sidewall

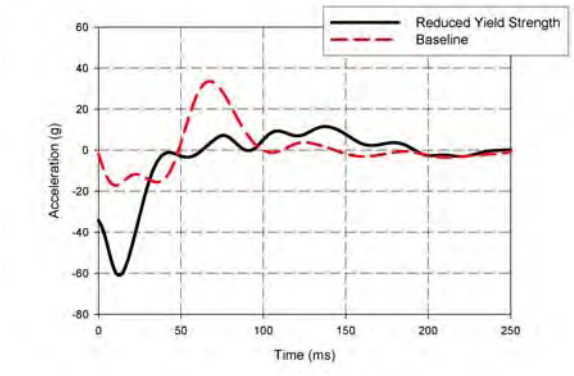

Figure 202. Lower Sidewall Acceleration Reduced Yield, FS 480—Left Sidewall

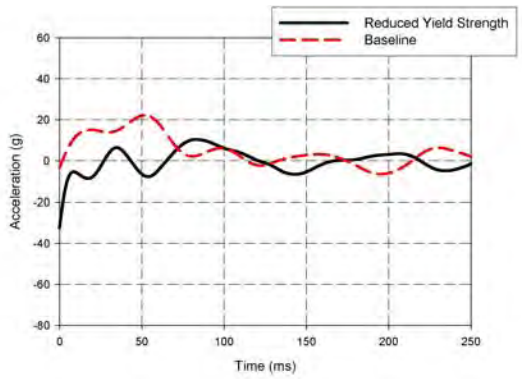

Figure 203. Lower Sidewall Acceleration Reduced Yield, FS 480—Right Sidewall

8.3 ELEMENT FAILURE CRITERIA.

The use of an element failure criterion was studied to determine if such failures have a significant effect on the simulated impact response of the test article. The current simulation employed elastic-plastic material properties, based on published stress-strain curves for aluminum alloys. The baseline simulation did not include failure and assumed that the material would yield indefinitely, based on the extrapolation from the given curve.

Numerous options are available for use in simulating element failure. The option chosen for this case was based on effective plastic strain with a failure limit of 12%.

A review of the literature on dynamic inelastic failure by Jones [8], including some of his own work, notes that there is still great debate on the appropriate failure criterion for beams under impact conditions. Plastic work per unit volume, according to Jones, appears to be a good candidate for widespread use as a failure criterion, though there are numerous other candidates, depending on whether failure is tensile or shear.

Even with a selected failure criterion, the choice of failure limit is also uncertain. Vignjevic and Cavalcanti [30] studied the effect of failure limits with effective plastic strain of 12% and 18% in aluminum alloys, as well as the use of Tresca stress for predicting failure. Their study was performed with the main frame of the Lynx helicopter, which was modeled with a very fine mesh. They determined that all three simulations, with three different failure criteria, produced very similar results, though the Tresca criterion led to a slightly different buckling pattern in the outside flange. They concluded that the choice of a failure criterion did not significantly affect either the collapse mechanism or the force-displacement results. All three simulations corresponded well with the observed experimental buckling. Based on this study, no clear recommendation could be made for an optimal failure criterion.

8.3.1 Fuselage.

Simulation of element failure is potentially important, however, as fractures will result in changing load paths during impact. Fractures will also affect the pattern of buckling that result

and could alter the shape of the collapsing frames, leading to changes in the acceleration pulses experienced by the occupants or by cabin items.

The test article shows postimpact fractures in several places, including the upper frames on both sides, multiple fractures and crushing in the lower frame sections, and fractures near the door. Figure 204 shows a failure in the reinforced frame around the forward edge of the door. The failure, however, does not include a complete fracture of the section, despite the substantial buckling and permanent deformation that was observed. A similar pattern of failure in the supporting frame around the cargo door was observed around the aft edge.

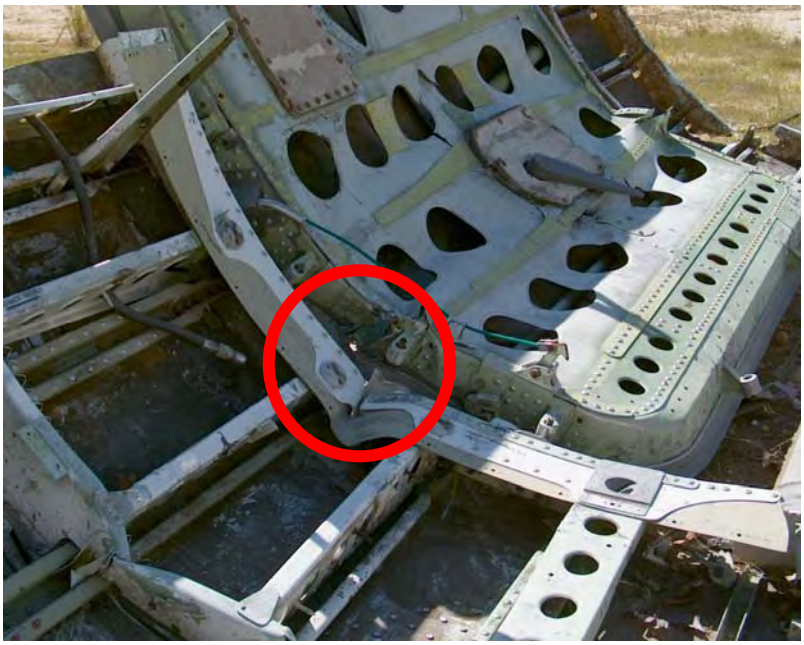

Figure 204. Posttest Failure of Cargo Door Frame

It is significant to note that the failure in the FE simulation leads to removal of the element, effectively resulting in a fracture with the width of the failed element. In the test article, fractures in the frame sections were frequently partial, so that the frame was still able to transmit load and resist crushing. With the complete removal of elements in a section of the frame, as shown in figure 205, the section was no longer able to resist bending. The frame with the failed elements could no longer carry any loads or transmit forces to the upper frames. Also, the failed elements led immediately to the formation of a plastic hinge on the right side, permitting the frames to buckle to a greater degree than expected.

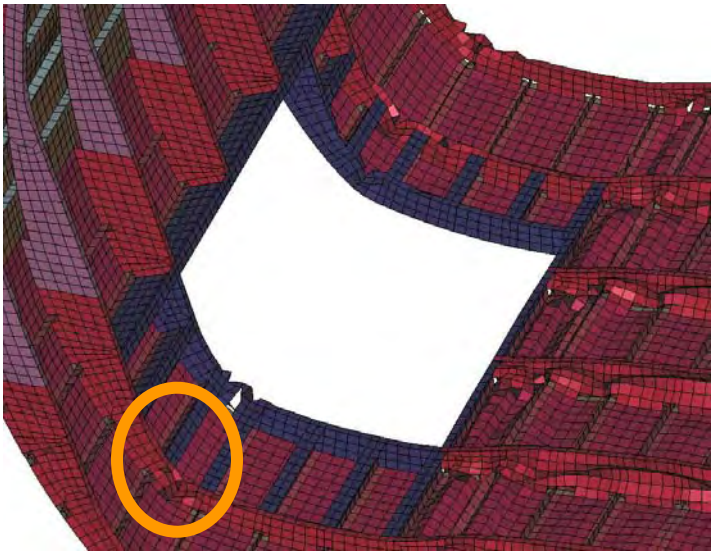

Figure 205. Failure of Elements in Door Frame on the Right-Hand Side, t = 60 ms

Figure 206 shows the location of partial failures in the frames on the left-hand side. Figure 207 is a close-up view of the frame at FS 380.

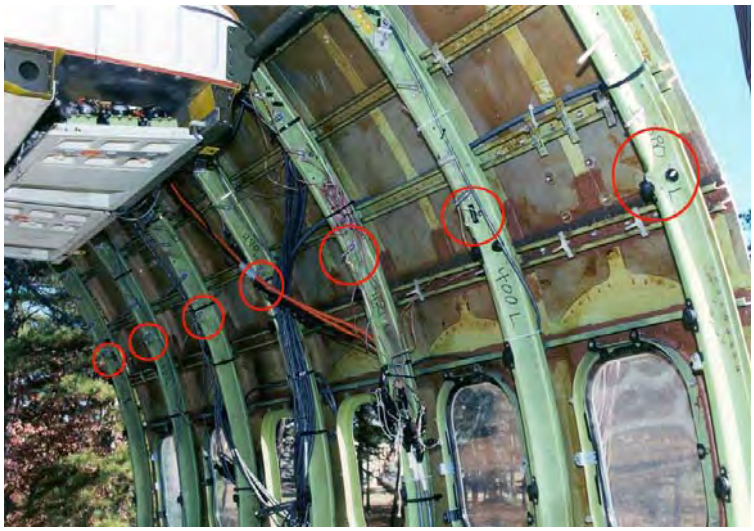

Figure 206. Fractures in Upper Frames on the Left-Hand Side

Figure 207. Close-Up View of Partial Failure in Frame at FS 380

The simulation results for the upper frames did not show any deleted or failed elements. This corresponded reasonably well with the observation that very small fractures are typically found in the upper frames, rather than in complete failure of the frame section.

Figure 208 shows the pattern of deformation for the impact sequence both with and without element failure. In figure 208(c) and 208(d), at 60 and 80 ms, the right-hand side shows evidence of crippling, resulting from the failure of elements around the reinforced cargo door frame. The failed elements, as shown previously in figure 205, led to a greater degree of deformation on the right side than was observed in either the baseline simulation or the actual drop test. In this case, the use of element failure resulted in a less accurate simulation of the impact event.

By 100-120 ms, it is clear that the use of the failure criterion resulted in no noticeable downward slant toward the left-hand side, and that crushing on both the right and left sides was equal. Again, this is due to the failure of elements on the right-hand side. This behavior, with equal crushing on both the right and left sides, does not correspond with either the experimental or baseline simulation results.

Both the observed pattern of deformation and the acceleration time histories show that the use of this failure criterion had either a limited or deleterious effect on the simulation results.

It is possible that a much finer mesh or use of a different failure criterion could improve the overall simulation results. However, given the current uncertainty concerning failure modeling under dynamic conditions, it appears likely that improvements in the simulation would be marginal.

(a) 12% Failure Criterion (Left) and No Failure (Right) at t = 20 ms

(b) 12% Failure Criterion (Left) and No Failure (Right) at t = 40 ms

(c) 12% Failure Criterion (Left) and No Failure (Right) at t = 60 ms

(d) 12% Failure Criterion (Left) and No Failure (Right) at t = 80 ms

Figure 208. Element Failure Criterion

(e) 12% Failure Criterion (Left) and No Failure (Right) at t = 100 ms

(f) 12% Failure Criterion (Left) and No Failure (Right) at t = 120 ms

(g) 12% Failure Criterion (Left) and No Failure (Right) at t = 140 ms

(h) 12% Failure Criterion (Left) and No Failure (Right) at t = 160 ms

Figure 208. Element Failure Criterion (Continued)

(i) 12% Failure Criterion (Left) and No Failure (Right) at t = 180 ms

(j) 12% Failure Criterion (Left) and No Failure (Right) at t = 200 ms

Figure 208. Element Failure Criterion (Continued)

8.3.2 Overhead Stowage Bins.

8.3.2.1 Heath Tecna Bin.

Figures 209 through 212 show the effect of element failure on the acceleration time histories of the Heath Tecna overhead stowage bin. In general, the peak acceleration response was similar for both cases, although the timing and number of pulses varied. A significant pulse occurred at about 120 ms in the simulation with failure, due to the buckling and collapse of the right-hand-side frame around the cargo door.

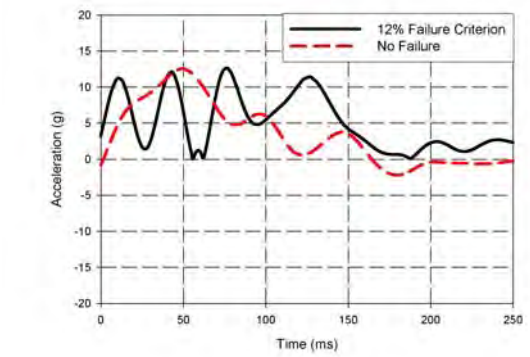

Figure 209. Heath Tecna Bin Acceleration Failure Criterion, Forward Location

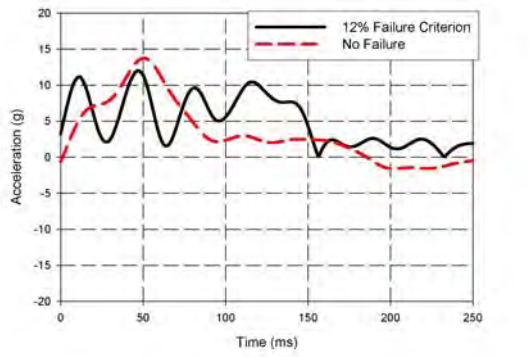

Figure 210. Heath Tecna Bin Acceleration Failure Criterion, Aft Location

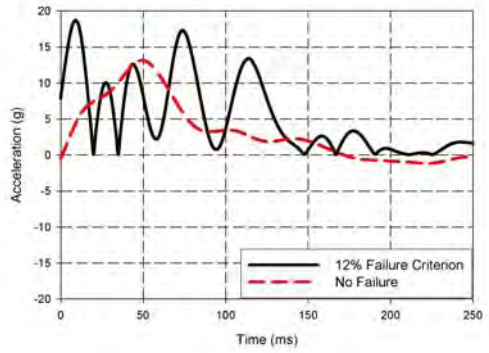

Figure 211. Heath Tecna Bin Acceleration Failure Criterion, Center Location

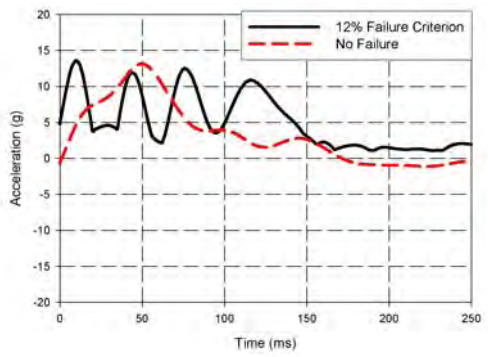

Figure 212. Heath Tecna Bin Acceleration Failure Criterion, Average All Locations

Figures 213 and 214 show the expected pattern of loading in the primary struts of the Heath Tecna overhead stowage bin. The aft strut showed a noticeable, but not extreme, increase in the peak load, to almost 1400 lb. Loads in the A leg of the bracket, which angles upward at 45°, increased significantly, while loads in the B leg were similar for both cases. These results are shown in figures 215 through 222.

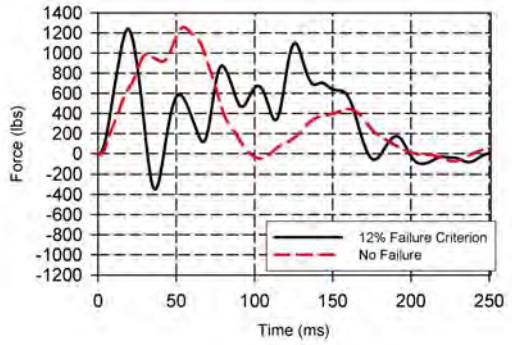

Figure 213. Heath Tecna Bin Acceleration Failure Criterion, Forward Strut

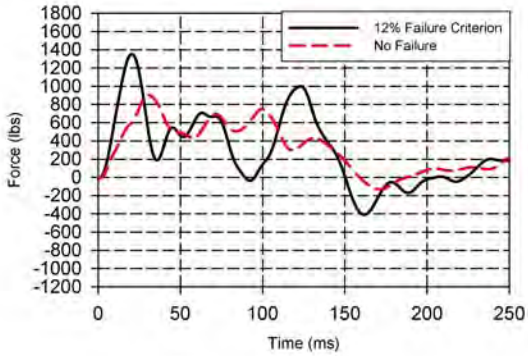

Figure 214. Heath Tecna Bin Acceleration Failure Criterion, Aft Strut

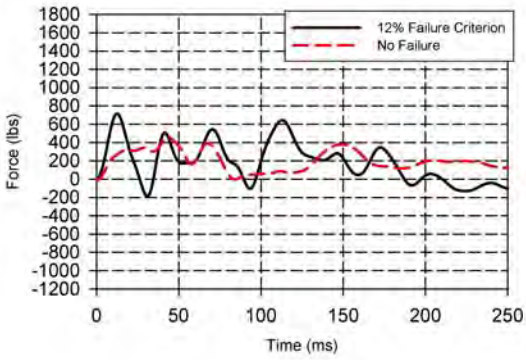

Figure 215. Heath Tecna Bin Load Failure Criterion, FS 400—A Leg of Bracket

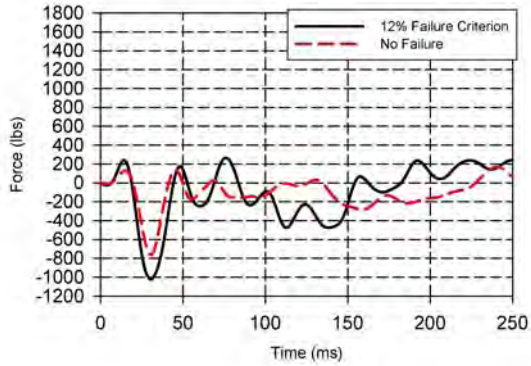

Figure 216. Heath Tecna Bin Load Failure Criterion, FS 400—B Leg of Bracket

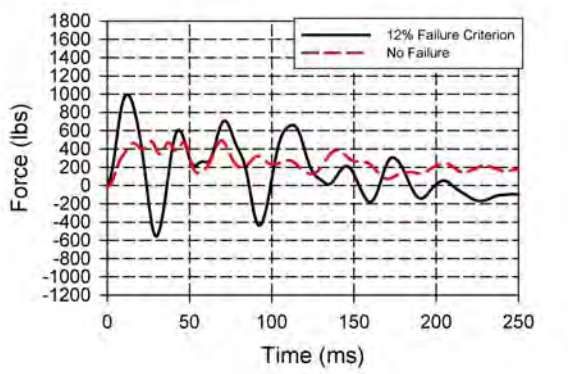

Figure 217. Heath Tecna Bin Load Failure Criterion, FS 420—A Leg of Bracket

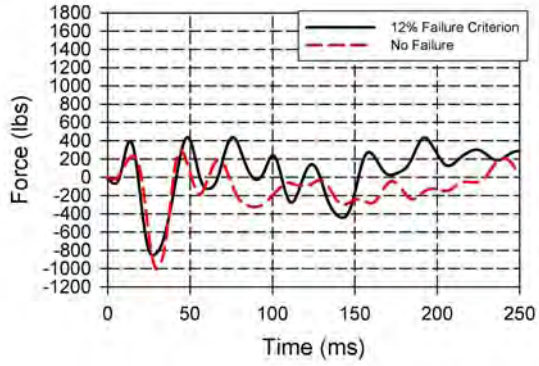

Figure 218. Heath Tecna Bin Load Failure Criterion, FS 420—B Leg of Bracket

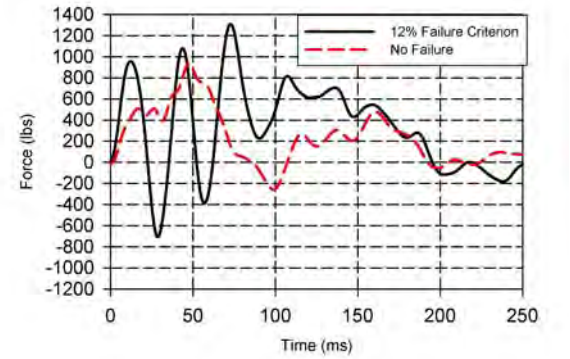

Figure 219. Heath Tecna Bin Load Failure Criterion, FS 460—A Leg of Bracket

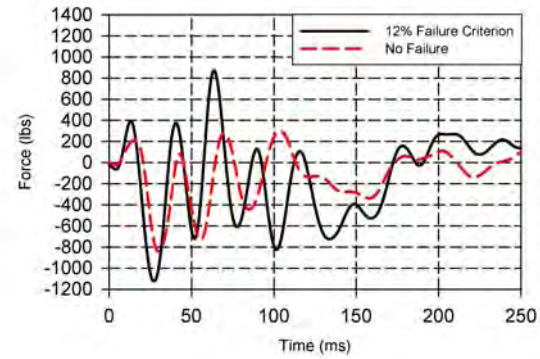

Figure 220. Heath Tecna Bin Load Failure Criterion, FS 460—B Leg of Bracket

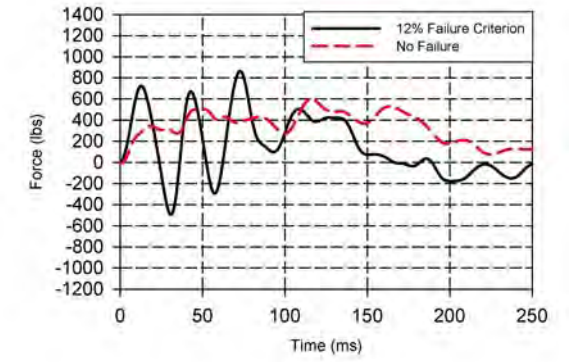

Figure 221. Heath Tecna Bin Load Failure Criterion, FS 480—A Leg of Bracket

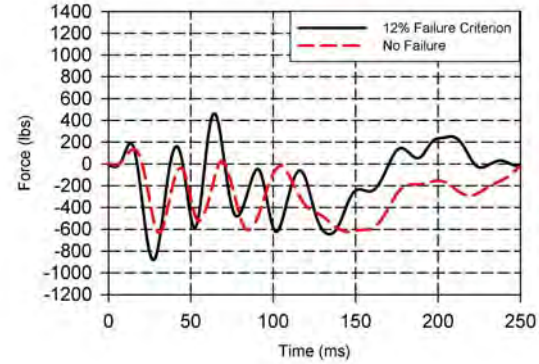

Figure 222. Heath Tecna Bin Load Failure Criterion, FS 480—B Leg of Bracket

8.3.2.2 Sidewalls.

Figures 223 through 226 show the effect of element failure on the acceleration time histories of the Hitco overhead stowage bin. In general, the peak acceleration response was similar for both cases, although the timing and number of pulses varied.

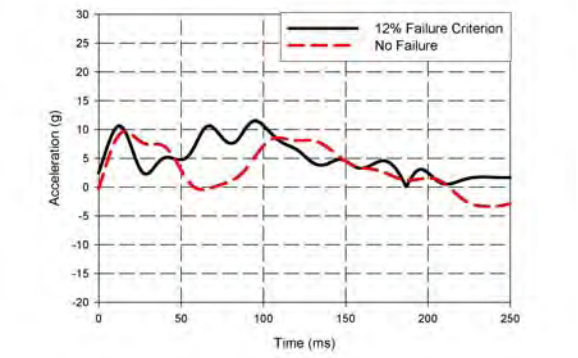

Figure 223. Heath Tecna Bin Load Failure Criterion, Forward Location

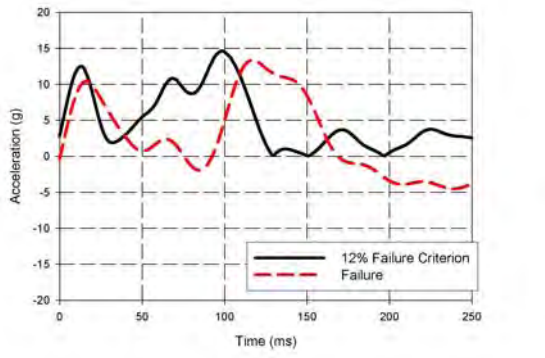

Figure 224. Heath Tecna Bin Load Failure Criterion, Aft Location

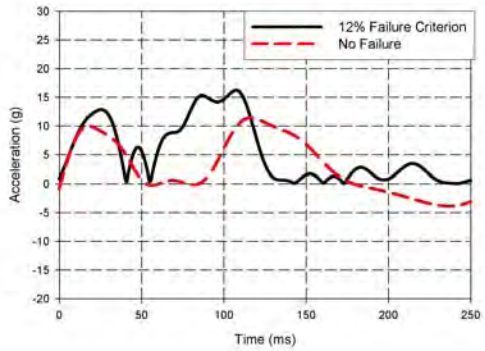

Figure 225. Hitco Bin Acceleration Failure Criterion, Center Location

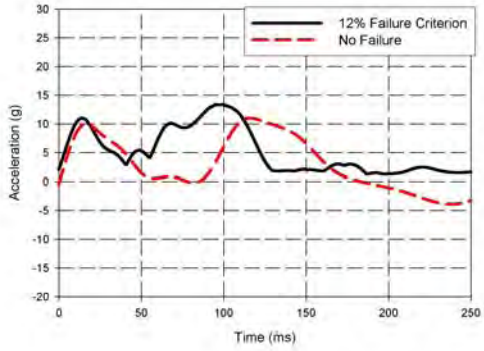

Figure 226. Hitco Bin Acceleration Failure Criterion, Average All Locations

Figures 227 and 228 show the expected pattern of loading in the primary struts of the Hitco overhead stowage bin. The aft and forward struts show a noticeable increase in the peak load to approximately 2100 lb at 85 ms. Peak loads in the other supports did not have a similar response at that time; the results are shown in figures 229 through 236.

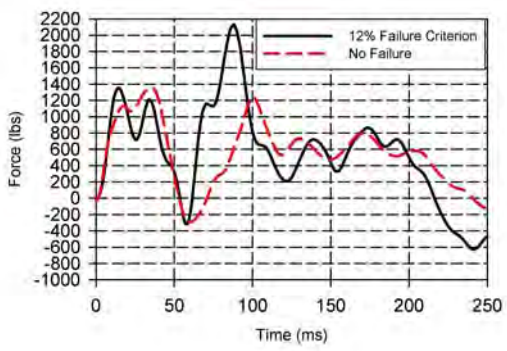

Figure 227. Hitco Bin Load Failure Criterion, Forward Strut

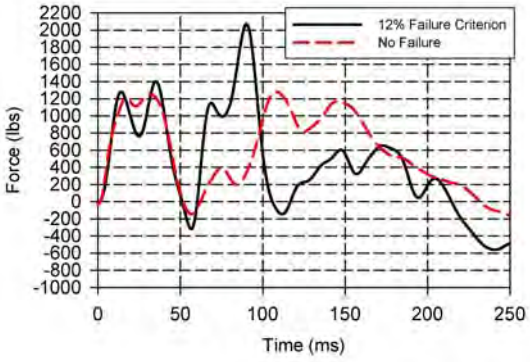

Figure 228. Hitco Bin Load Failure Criterion, Aft Strut

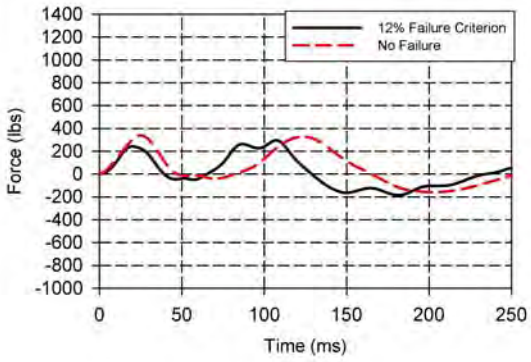

Figure 229. Hitco Bin Load Failure Criterion, FS 400 Vertical Link

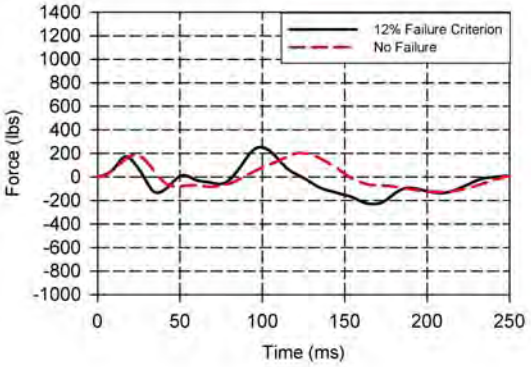

Figure 230. Hitco Bin Load Failure Criterion, FS 400 Horizontal Link

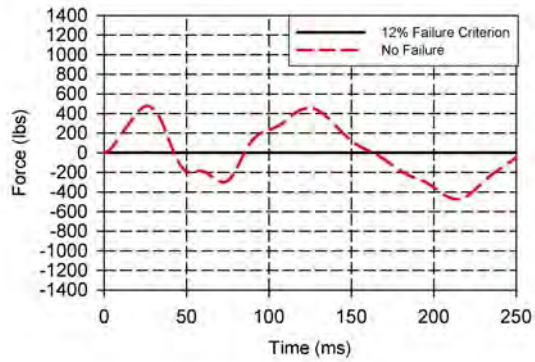

Figure 231. Hitco Bin Load Failure Criterion, FS 420 Vertical Link

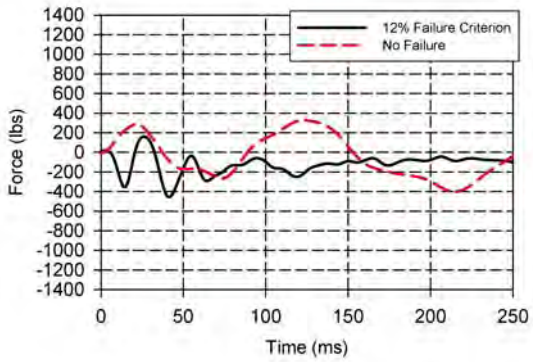

Figure 232. Hitco Bin Load Failure Criterion, FS 420 Horizontal Link

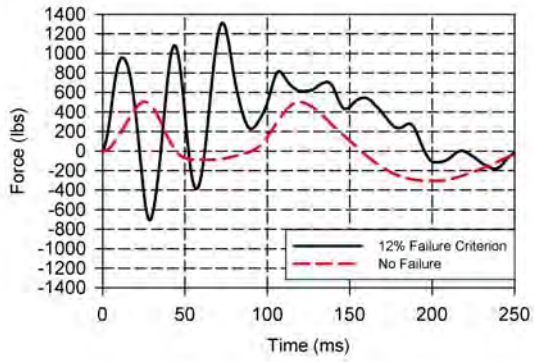

Figure 233. Hitco Bin Load Failure Criterion, FS 460 Vertical Link

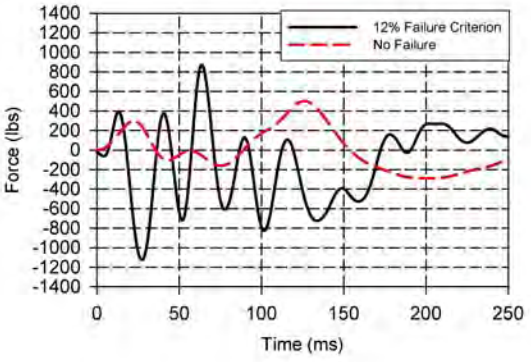

Figure 234. Hitco Bin Load Failure Criterion, FS 460 Horizontal Link

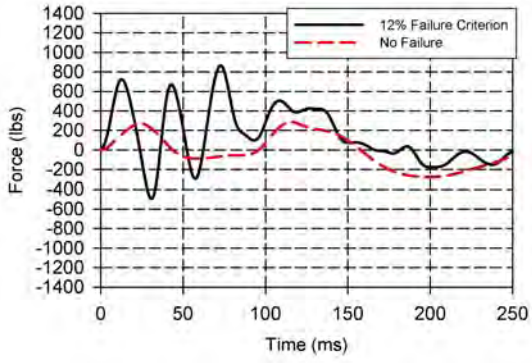

Figure 235. Hitco Bin Load Failure Criterion, FS 480 Vertical Link

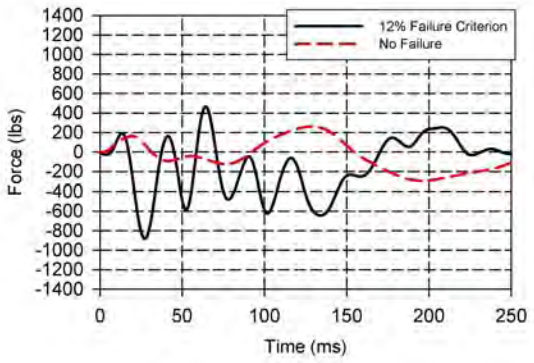

Figure 236. Hitco Bin Load Failure Criterion, FS 480 Horizontal Link

8.3.3 Floor Tracks.

Figures 237 through 250 show the floor track acceleration results. The results show no conclusive trends.

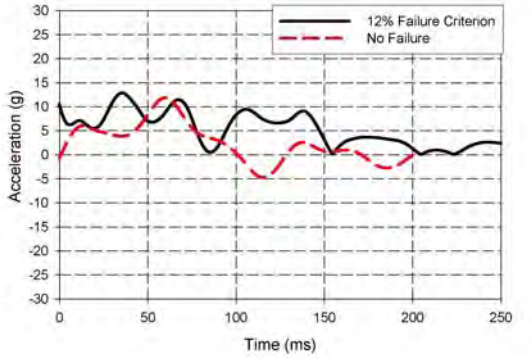

Figure 237. Floor Track Acceleration Failure Criterion, FS 380—Left Inside Floor Track

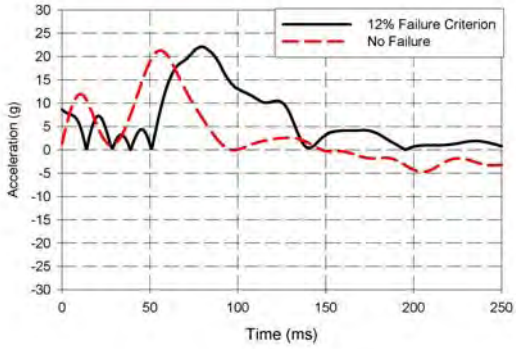

Figure 238. Floor Track Acceleration Failure Criterion, FS 380—Right Inside Floor Track

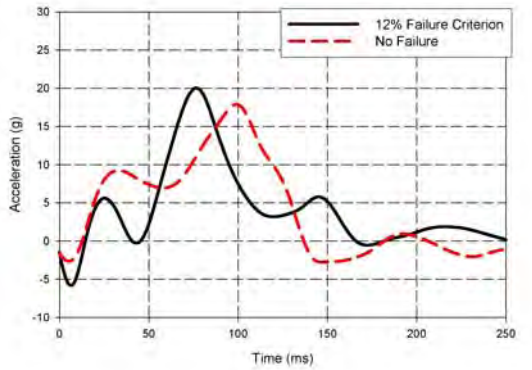

Figure 239. Floor Track Acceleration Failure Criterion, FS 418—Left Outside Floor Track

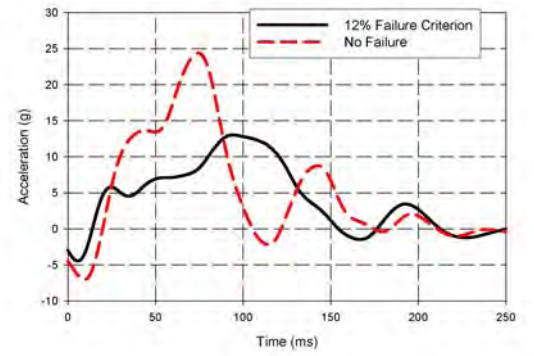

Figure 240. Floor Track Acceleration Failure Criterion, FS 418—Right Outside Floor Track

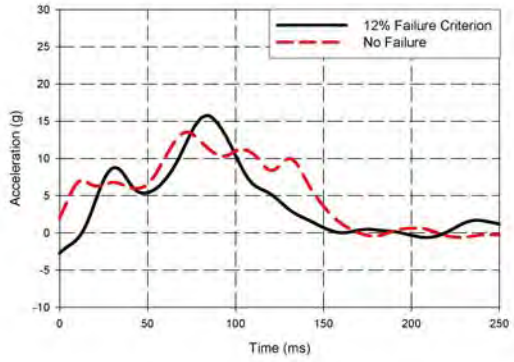

Figure 241. Floor Track Acceleration Failure Criterion, FS 418—Left Inside Floor Track

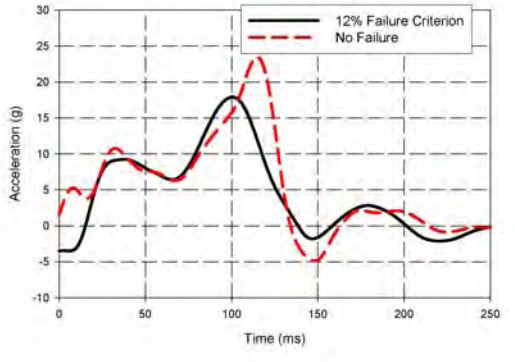

Figure 242. Floor Track Acceleration Failure Criterion, FS 418—Right Inside Floor Track

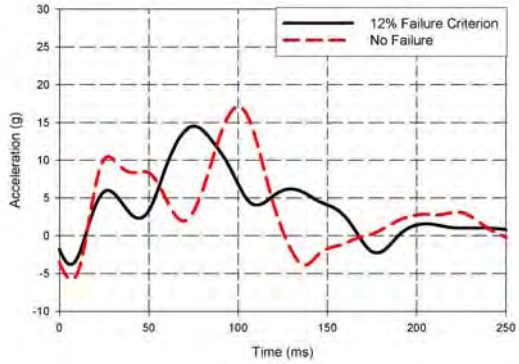

Figure 243. Floor Track Acceleration Failure Criterion, FS 452—Left Outside Floor Track

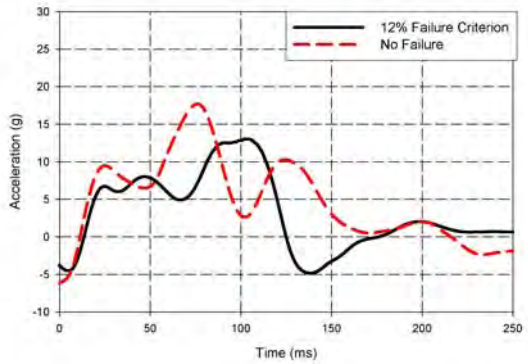

Figure 244. Floor Track Acceleration Failure Criterion, FS 452—Right Outside Floor Track

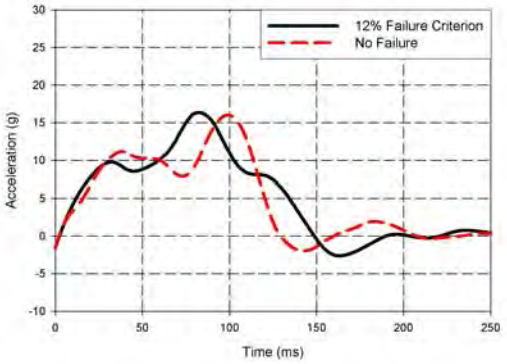

Figure 245. Floor Track Acceleration Failure Criterion, FS 452—Left Inside Floor Track

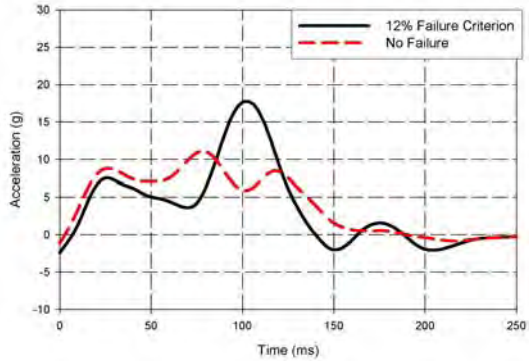

Figure 246. Floor Track Acceleration Failure Criterion, FS 452—Right Inside Floor Track

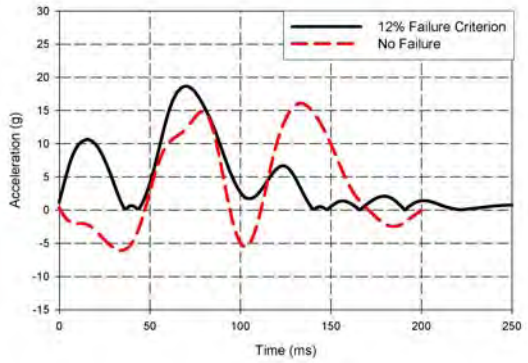

Figure 247. Floor Track Acceleration Failure Criterion, FS 484—Left Outside Floor Track

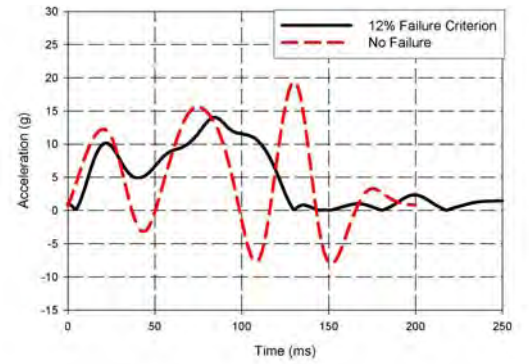

Figure 248. Floor Track Acceleration Failure Criterion, FS 484—Right Outside Floor Track

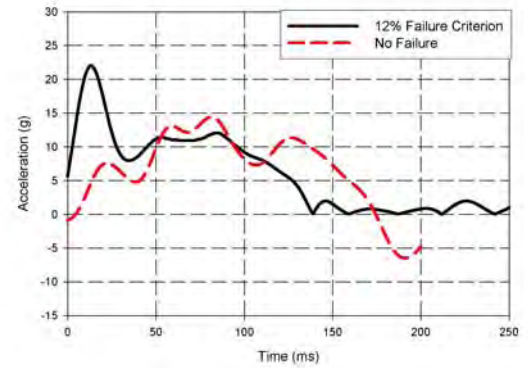

Figure 249. Floor Track Acceleration Failure Criterion, FS 484—Left Inside Floor Track

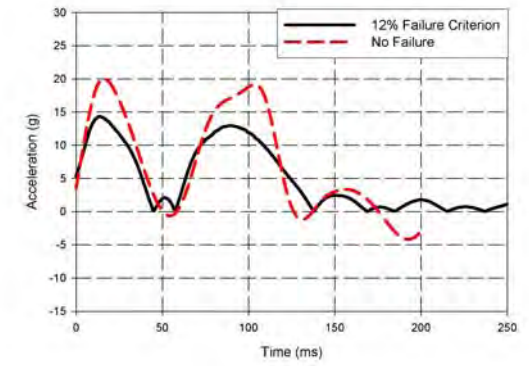

Figure 250. Floor Track Acceleration Failure Criterion, FS 484—Right Inside Floor Track

8.3.4 Sidewalls.

The upper and lower sidewall responses are shown in figures 251 through 262.

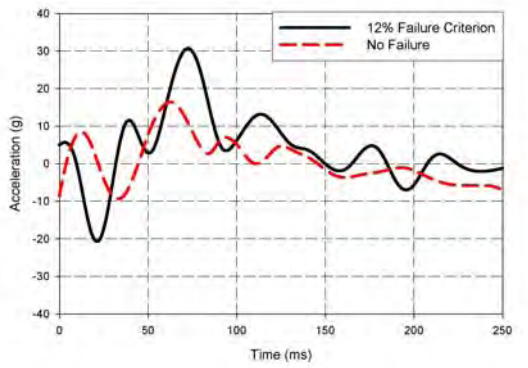

Figure 251. Upper Sidewall Acceleration Failure Criterion, FS 400—Left Sidewall

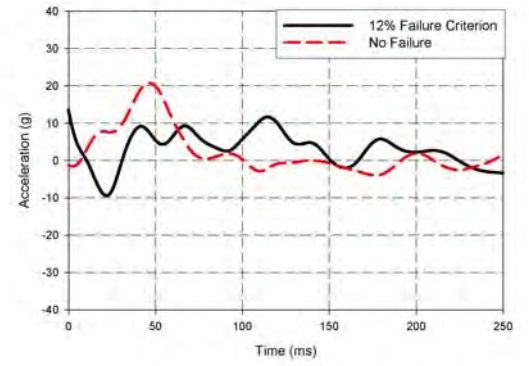

Figure 252. Upper Sidewall Acceleration Failure Criterion, FS 400—Right Sidewall

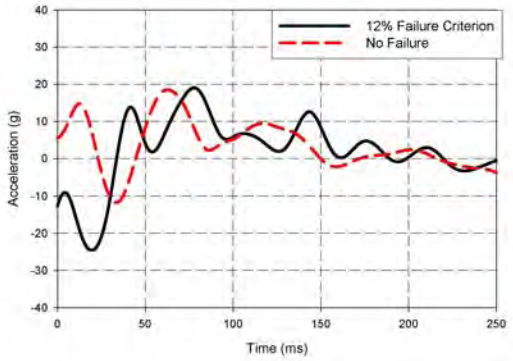

Figure 253. Upper Sidewall Acceleration Failure Criterion, FS 440—Left Sidewall

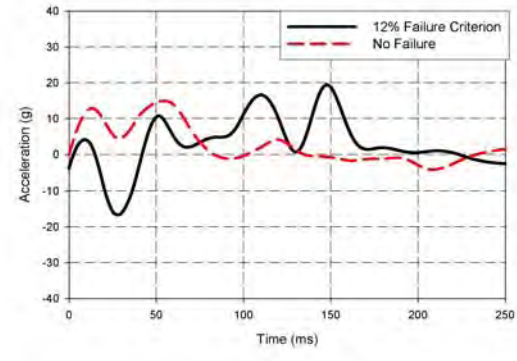

Figure 254. Upper Sidewall Acceleration Failure Criterion, FS 440—Right Sidewall

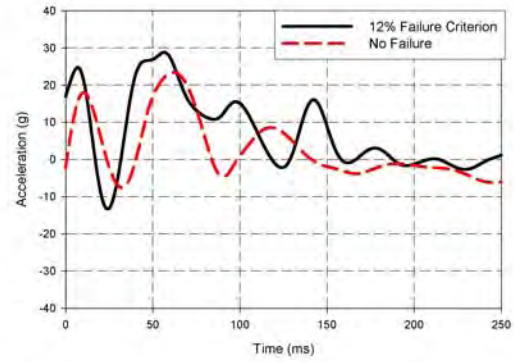

Figure 255. Upper Sidewall Acceleration Failure Criterion, FS 480—Left Sidewall

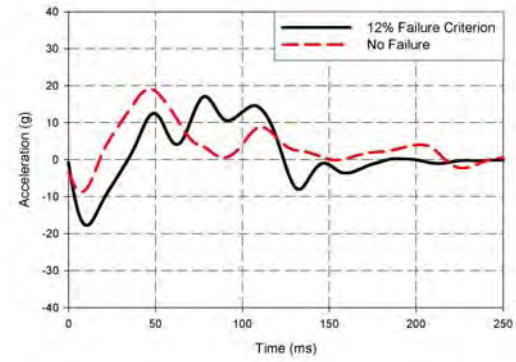

Figure 256. Upper Sidewall Acceleration Failure Criterion, FS 480—Right Sidewall

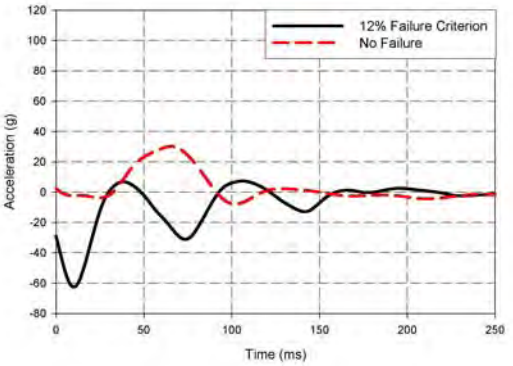

Figure 257. Lower Sidewall Acceleration Failure Criterion, FS 400—Left Sidewall

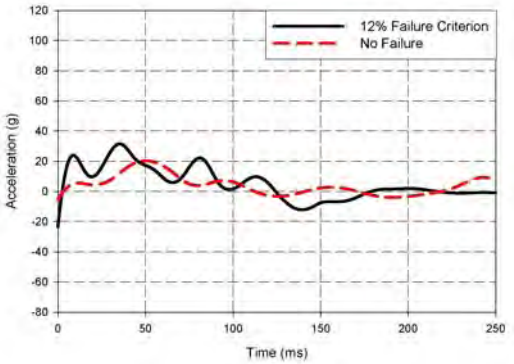

Figure 258. Lower Sidewall Acceleration Failure Criterion, FS 400—Right Sidewall

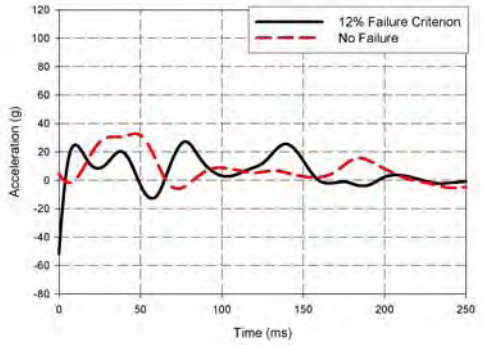

Figure 259. Lower Sidewall Acceleration Failure Criterion, FS 440—Left Sidewall

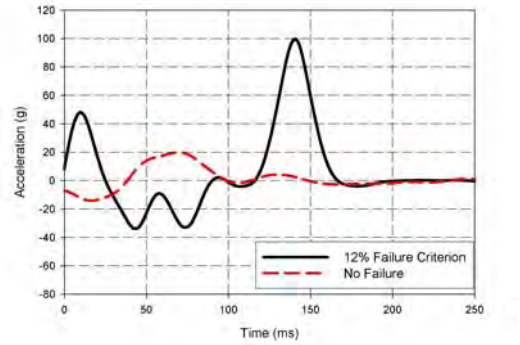

Figure 260. Lower Sidewall Acceleration Failure Criterion, FS 440—Right Sidewall

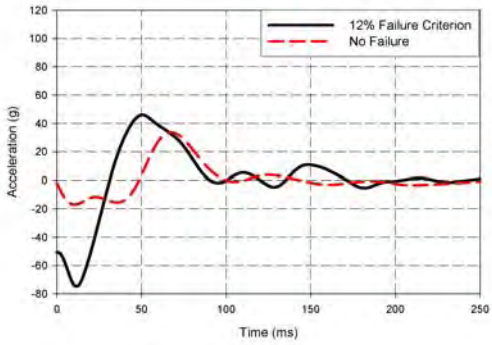

Figure 261. Lower Sidewall Acceleration Failure Criterion, FS 480—Left Sidewall

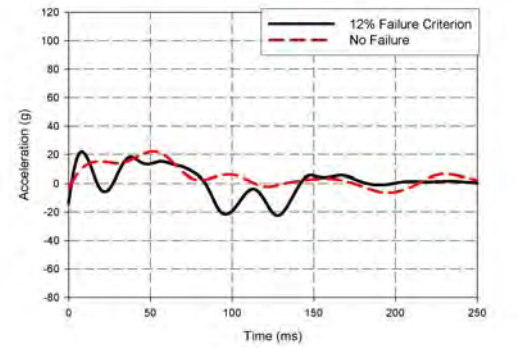

Figure 262. Lower Sidewall Acceleration Failure Criterion, FS 480—Right Sidewall

8.4 IMPACT CONDITIONS AND CONFIGURATIONS.

8.4.1 Roll Angle at Impact.

The experimental drop test was intended primarily to address the impact response of overhead stowage bins and to determine if static testing is a reasonable method of certifying bins for dynamic impact loading. A related issue that was examined was whether a roll angle at impact, as opposed to a straight vertical impact, has a significant effect on the distribution and magnitude of loads in the stowage bin supporting structures. A significant change in acceleration pulse or in the peak loads of individual supporting links could indicate that the experimental vertical drop test results are limited in applicability to a single impact condition.

8.4.1.1 Fuselage.

A left 10° roll angle at impact was introduced in the simulation, and the results are compared with the baseline simulation results having a 0° roll. The impact sequence is shown in figure 263, and shows the effect of impact angle on the resulting pattern of deformation. As expected, substantial crushing is observable on the left-hand side. Very little roll occurs after impact, although a rebound is observable beginning at about 160 ms. Total time duration of the impact was very similar to the baseline case, with vertical velocity reaching zero at about 150 ms.

(a) Left 10° Roll Angle and Baseline at t = 20 ms

(b) Left 10° Roll Angle and Baseline at t = 40 ms

(c) Left 10° Roll Angle and Baseline at t = 60 ms

(d) Left 10° Roll Angle and Baseline at t = 80 ms

Figure 263. Roll Angle at Impact

(e) Left 10° Roll Angle and Baseline at t = 100 ms

(f) Left 10° Roll Angle and Baseline at t = 120 ms

(g) Left 10° Roll Angle and Baseline at t = 140 ms

(h) Left 10° Roll Angle and Baseline at t = 160 ms

Figure 263. Roll Angle at Impact (Continued)

(i) Left 10° Roll Angle and Baseline at t = 180 ms

(j) Left 10° Roll Angle and Baseline at t = 200 ms

Figure 263. Roll Angle at Impact (Continued)

8.4.2 Overhead Stowage Bins.

8.4.2.1 Heath Tecna Bins.

The acceleration responses of the Heath Tecna bin are shown in figures 264 to 267, with figure 267 showing the average response of all acceleration locations. The peak acceleration response increased slightly for the roll angle condition, with the average peak acceleration increasing from 13 to 15 g's. These results are reasonable, as the Heath Tecna bin was on the high side of the fuselage, and therefore, somewhat cushioned from the impact. The timing of the pulses, however, changed noticeably, and an additional pulse was found between 100 and 150 ms. This variation in timing and duration of the acceleration pulses led to a noticeable increase in loading of the supporting structure.

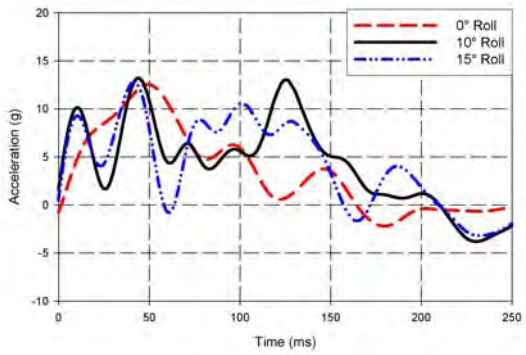

Figure 264. Heath Tecna Bin Acceleration Roll Angle Study, Forward Location

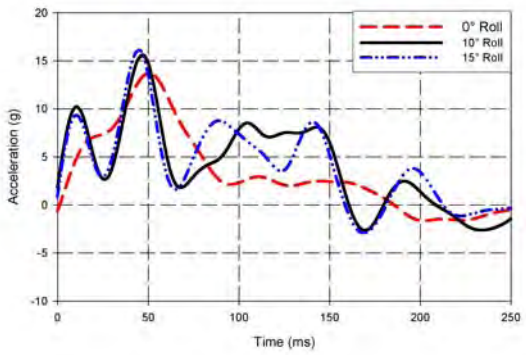

Figure 265. Heath Tecna Bin Acceleration Roll Angle Study, Aft Location

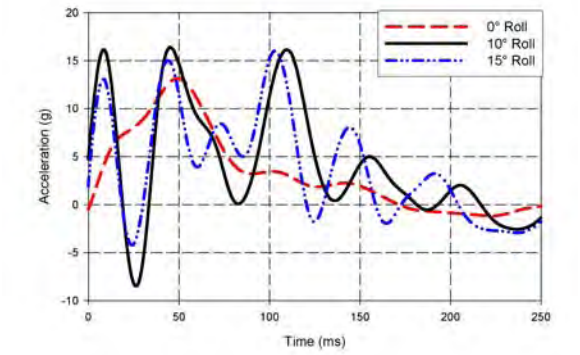

Figure 266. Heath Tecna Bin Acceleration Roll Angle Study, Center Location

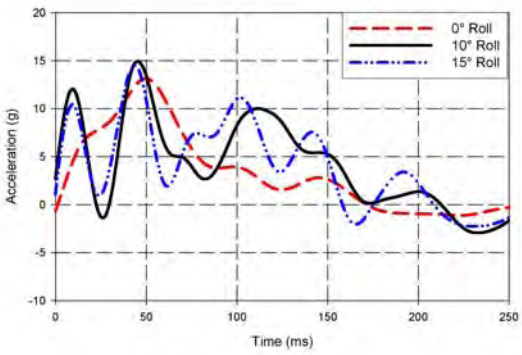

Figure 267. Heath Tecna Bin Acceleration Roll Angle Study, Average All Locations

Figures 268 through 277 present the load time histories of the Heath Tecna bin supports. Both forward and aft struts show an increase in peak load and a significant loading pulse at approximately 120 ms. For the aft strut, the peak load occurred in this later pulse, with a load of 1350 lb. The previous peak for the aft strut was 900 lb. Loading in the bracket was similar in magnitude for cases with and without a roll angle, although timing of the peak loads varied with roll angle.

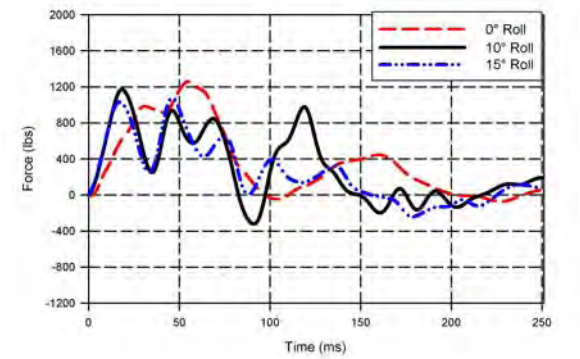

Figure 268. Heath Tecna Bin Load Roll Angle Study, Forward Strut

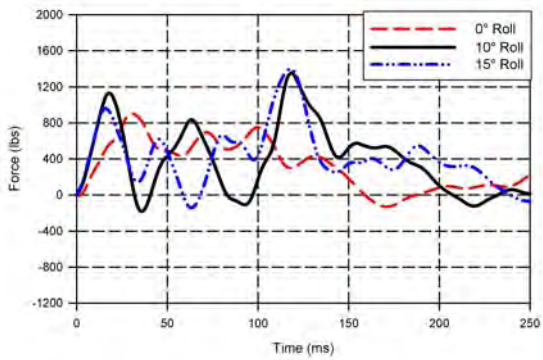

Figure 269. Heath Tecna Bin Load Roll Angle Study, Aft Strut

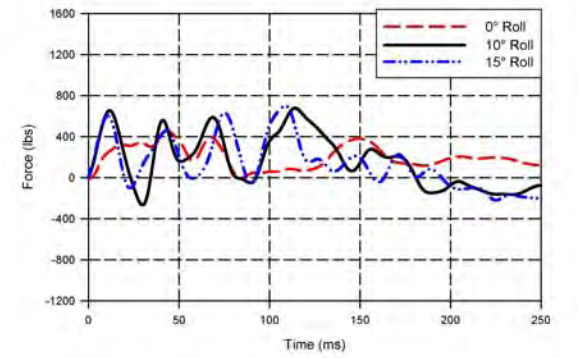

Figure 270. Heath Tecna Bin Load Roll Angle Study, FS 400—A Leg of Bracket

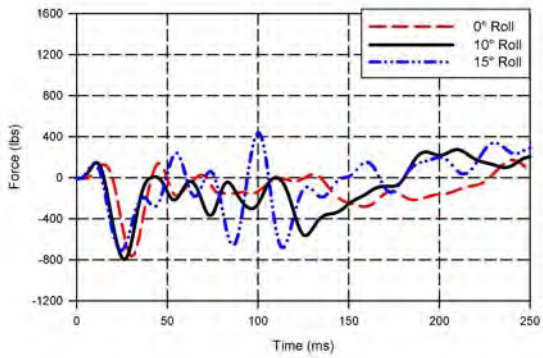

Figure 271. Heath Tecna Bin Load Roll Angle Study, FS 400—B Leg of Bracket

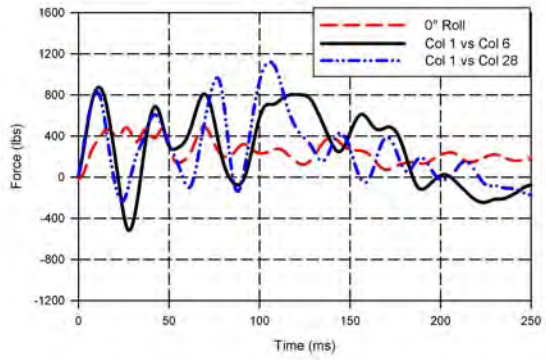

Figure 272. Heath Tecna Bin Load Roll Angle Study, FS 420—A Leg of Bracket

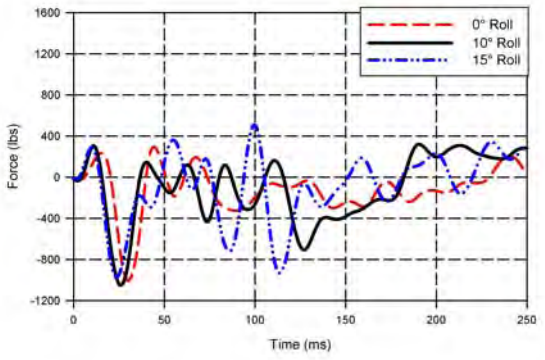

Figure 273. Heath Tecna Bin Load Roll Angle Study, FS 420—B Leg of Bracket

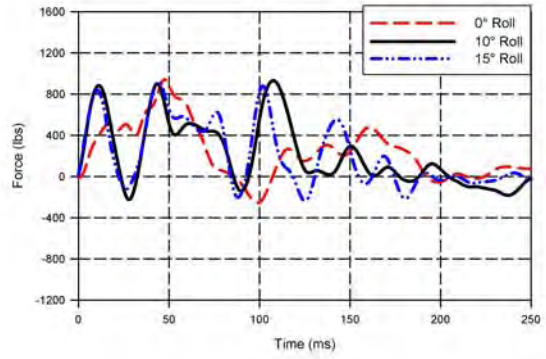

Figure 274. Heath Tecna Bin Load Roll Angle Study, FS 460—A Leg of Bracket

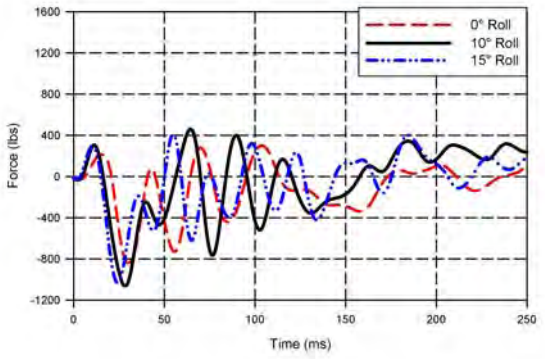

Figure 275. Heath Tecna Bin Load Roll Angle Study, FS 460—B Leg of Bracket

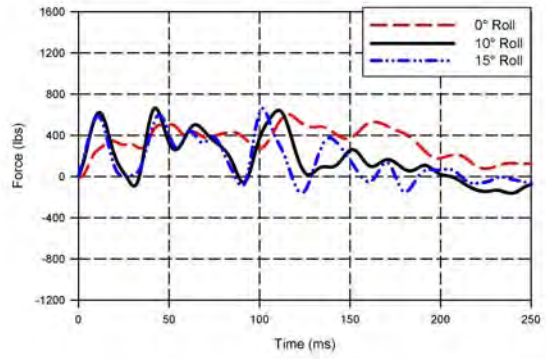

Figure 276. Heath Tecna Bin Load Roll Angle Study, FS 480—A Leg of Bracket

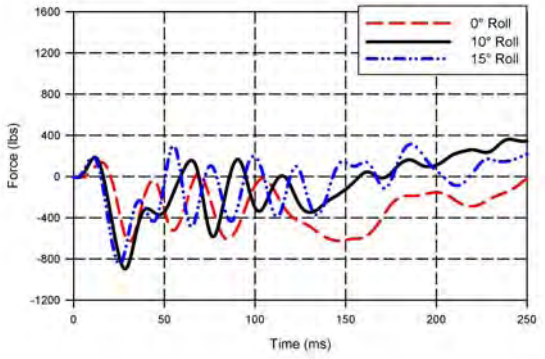

Figure 277. Heath Tecna Bin Load Roll Angle Study, FS 480—A Leg of Bracket

8.4.2.2 Hitco Bin.

Figures 278 through 281 show the acceleration response results for the Hitco bin, comparing the effect of a 10° and 15° roll angle. The effect, clearly shown in figure 281, is that the acceleration pulse with a roll angle arrives earlier, is slightly higher, and is significantly longer than the baseline case. Peak acceleration increased from 11 to 13 g's, and pulse duration was close to

100 ms, up from 70 ms for a no roll angle case. This leads to a significant increase in the peak loads for structural supports.

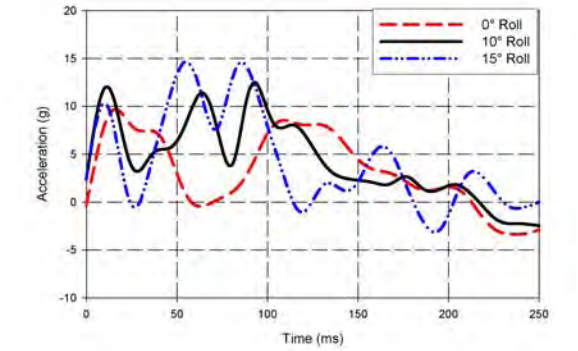

Figure 278. Hitco Bin Acceleration Roll Angle Study, Forward Location

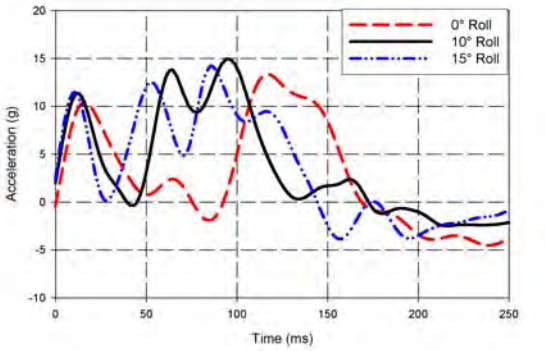

Figure 279. Hitco Bin Acceleration Roll Angle Study, Aft Location

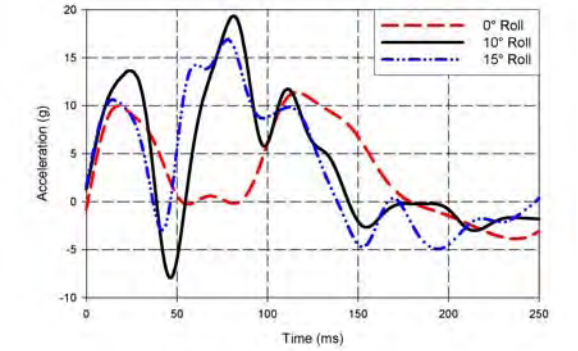

Figure 280. Hitco Bin Acceleration Roll Angle Study, Center Location

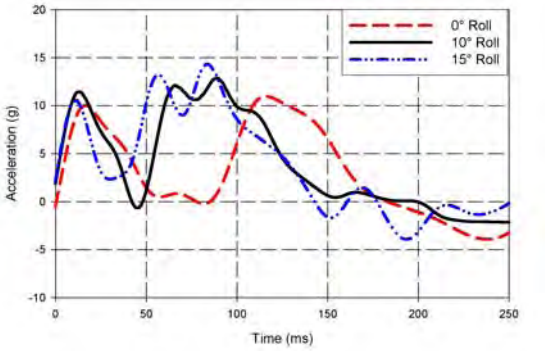

Figure 281. Hitco Bin Acceleration Roll Angle Study, Average All Locations

Figures 282 and 283 show the significant increase in peak load that follows the introduction of a roll angle. The baseline peak axial load was 1400 lb, while the 10° roll condition showed a peak load of over 2400 lb for the forward strut and 2200 lb for the aft strut.

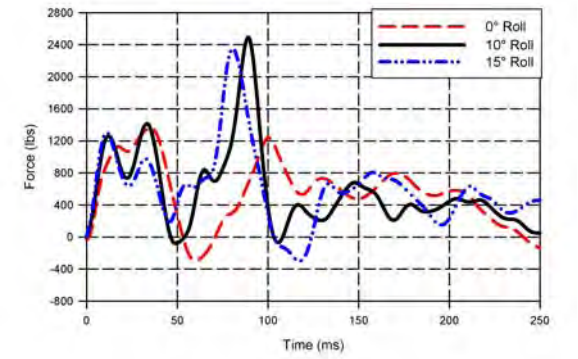

Figure 282. Hitco Bin Load Roll Angle Study, Forward Strut

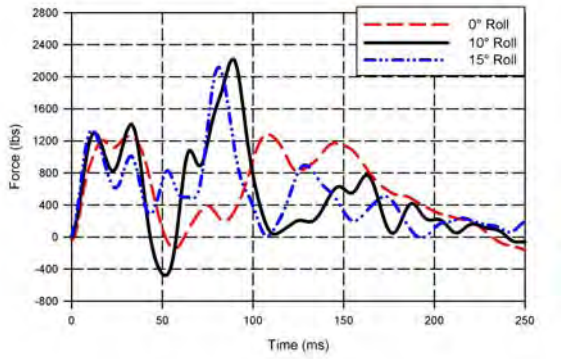

Figure 283. Hitco Bin Load Roll Angle Study, Aft Strut

Figures 284 through 291 show that the inboard links were not significantly affected by the roll angle. They exhibited a slight increase in peak loading and a phase shift in timing of the peak loads.

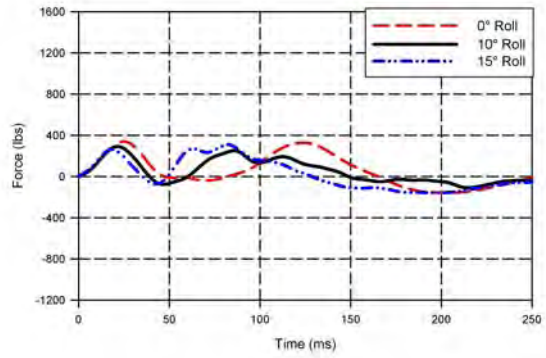

Figure 284. Hitco Bin Load Roll Angle Study, FS 400 Vertical Link

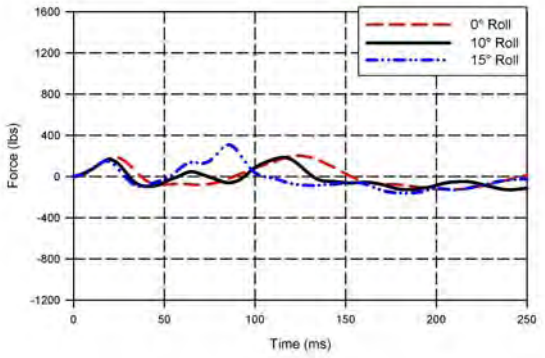

Figure 285. Hitco Bin Load Roll Angle Study, FS 400 Horizontal Link

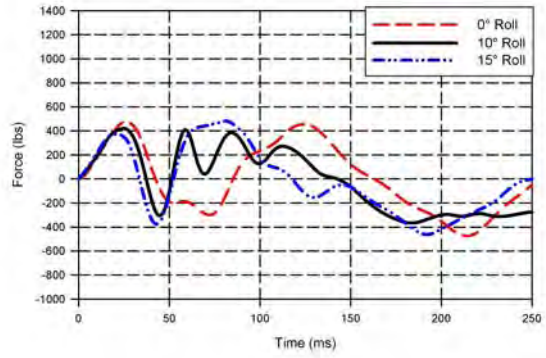

Figure 286. Hitco Bin Load Roll Angle Study, FS 420 Vertical Link

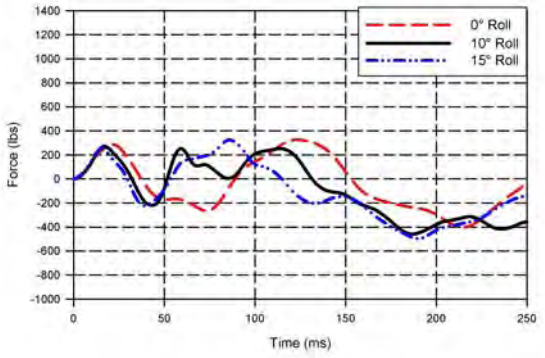

Figure 287. Hitco Bin Load Roll Angle Study, FS 420 Horizontal Link

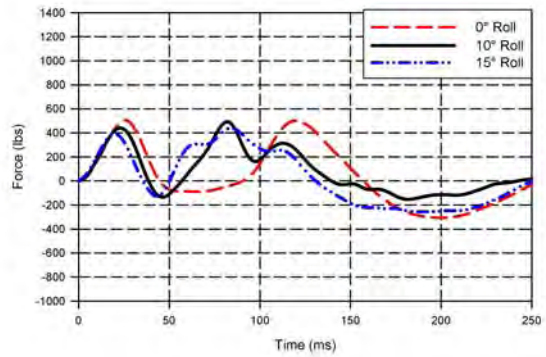

Figure 288. Hitco Bin Load Roll Angle Study, FS 460 Vertical Link

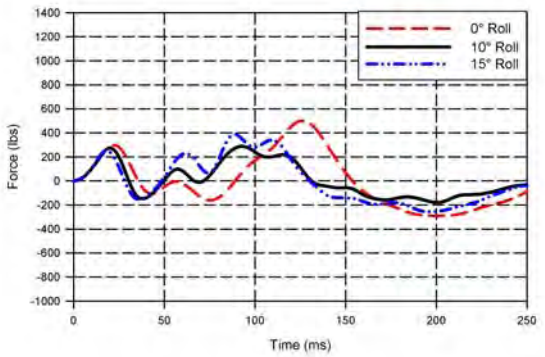

Figure 289. Hitco Bin Load Roll Angle Study, FS 460 Horizontal Link

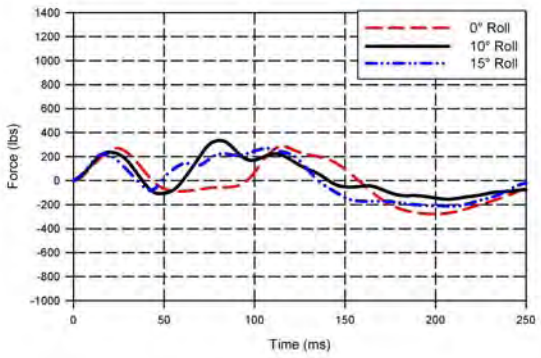

Figure 290. Hitco Bin Load Roll Angle Study, FS 480 Vertical Link

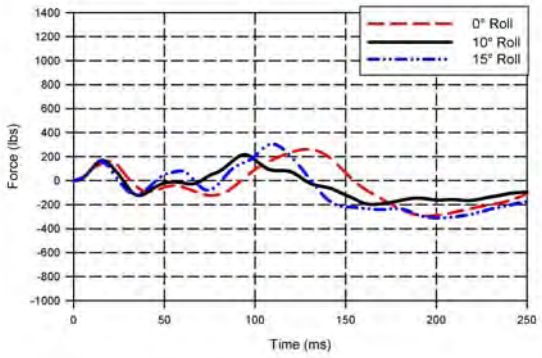

Figure 291. Hitco Bin Load Roll Angle Study, FS 480 Horizontal Link

8.4.3 Floor Tracks.

Figures 292 and 293 illustrate the expected effect of roll angle on acceleration pulses for the left and right floor tracks, with the left side showing an increase in peak acceleration and the right side showing a decrease in peak acceleration. This change would affect the behavior of the seats, and would likely lead to the collapse of seats on the left-hand side. Figures 294 through 305 present the remaining floor track acceleration data.

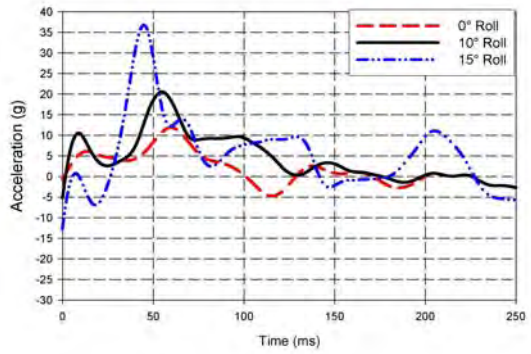

Figure 292. Floor Track Acceleration Roll Angle Study, FS 380—Left Inside Floor Track

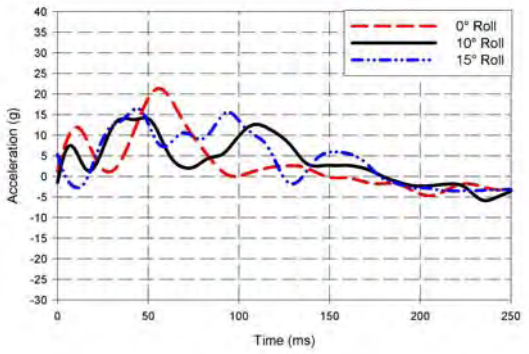

Figure 293. Floor Track Acceleration Roll Angle Study, FS 380—Right Inside Floor Track

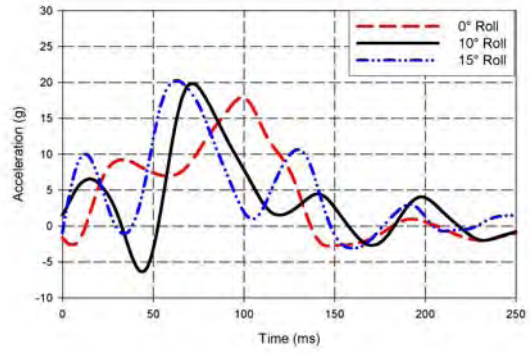

Figure 294. Floor Track Acceleration Roll Angle Study, FS 418—Left Outside Floor Track

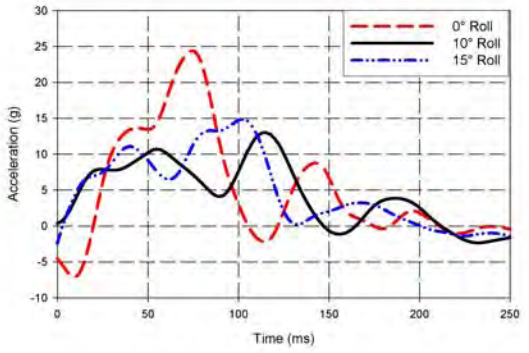

Figure 295. Floor Track Acceleration Roll Angle Study, FS 418—Right Outside Floor Track

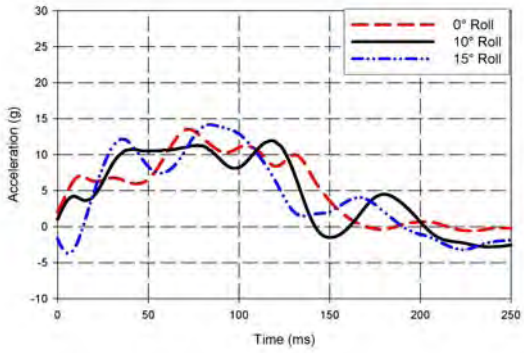

Figure 296. Floor Track Acceleration Roll Angle Study, FS 418—Left Inside Floor Track

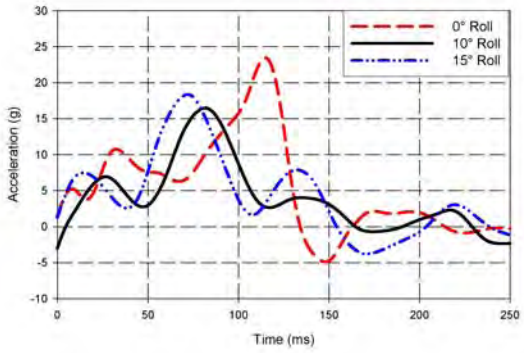

Figure 297. Floor Track Acceleration Roll Angle Study, FS 418—Right Inside Floor Track

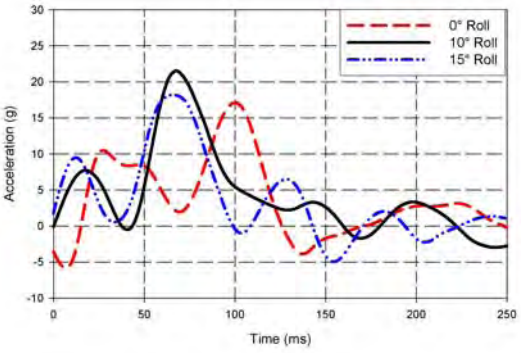

Figure 298. Floor Track Acceleration Roll Angle Study, FS 452—Left Outside Floor Track

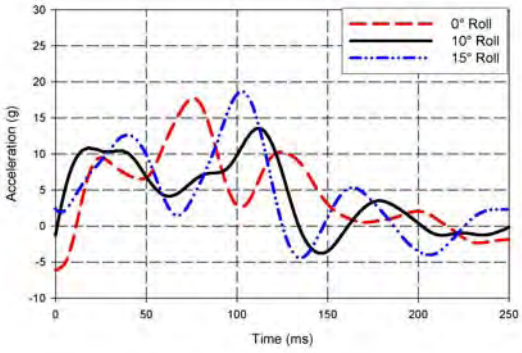

Figure 299. Floor Track Acceleration Roll Angle Study, FS 452—Right Outside Floor Track

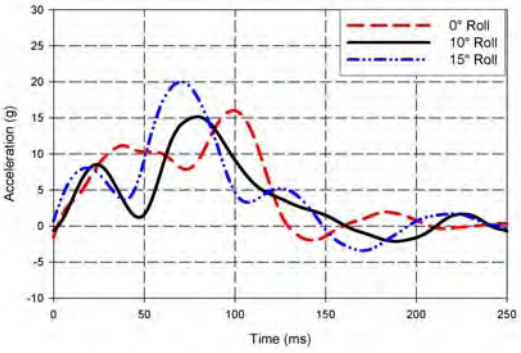

Figure 300. Floor Track Acceleration Roll Angle Study, FS 452—Left Inside Floor Track

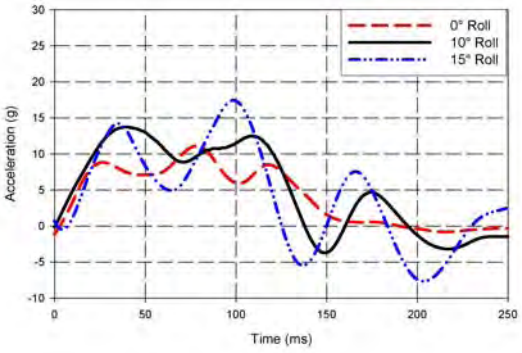

Figure 301. Floor Track Acceleration Roll Angle Study, FS 452—Right Inside Floor Track

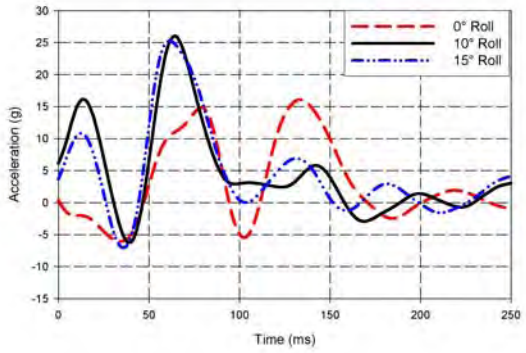

Figure 302. Floor Track Acceleration Roll Angle Study, FS 484—Left Outside Floor Track

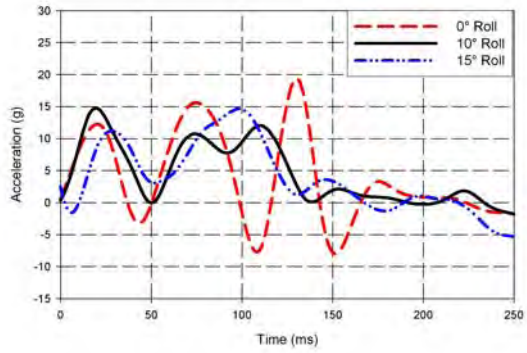

Figure 303. Floor Track Acceleration Roll Angle Study, FS 484—Right Outside Floor Track

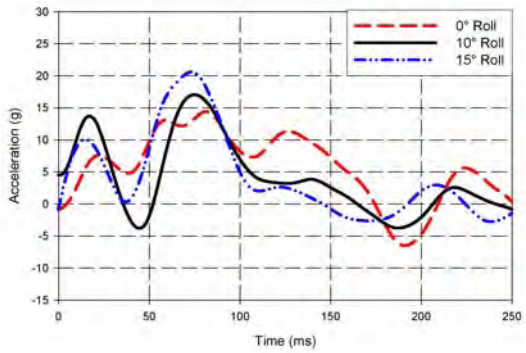

Figure 304. Floor Track Acceleration Roll Angle Study, FS 484—Left Inside Floor Track

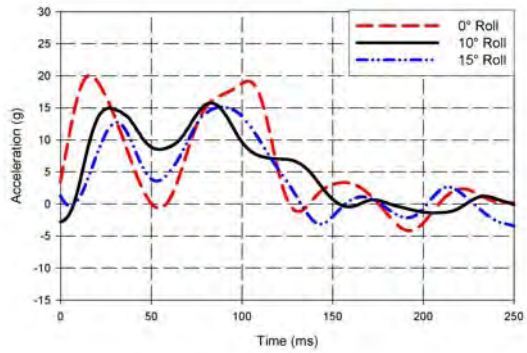

Figure 305. Floor Track Acceleration Roll Angle Study, FS 484—Right Inside Floor Track

8.4.4 Sidewalls.

The sidewall acceleration results are presented in figures 306 through 317.

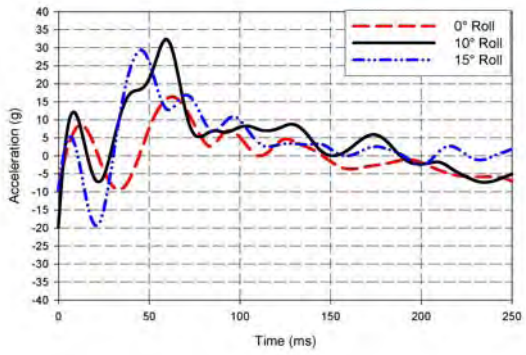

Figure 306. Upper Sidewall Acceleration Roll Angle Study, FS 400—Left Sidewall

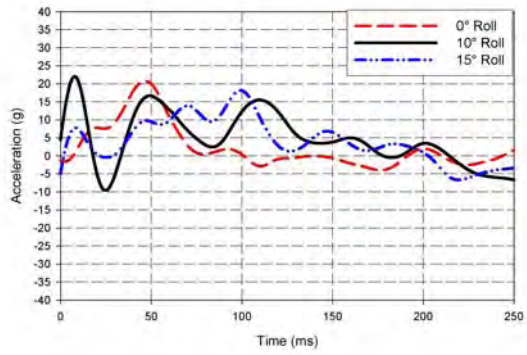

Figure 307. Upper Sidewall Acceleration Roll Angle Study, FS 400—Right Sidewall

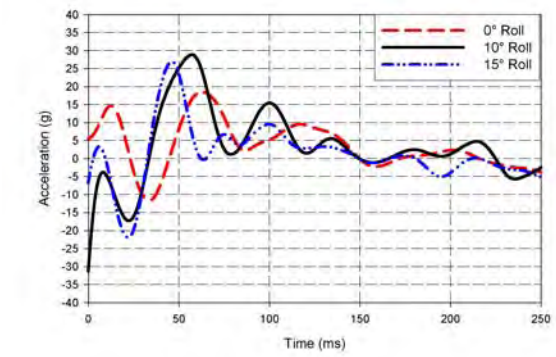

Figure 308. Upper Sidewall Acceleration Roll Angle Study, FS 440—Left Sidewall

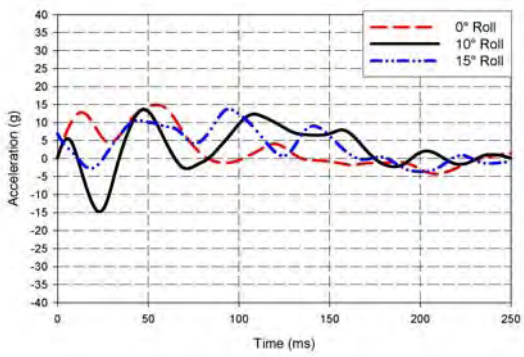

Figure 309. Upper Sidewall Acceleration Roll Angle Study, FS 440—Right Sidewall

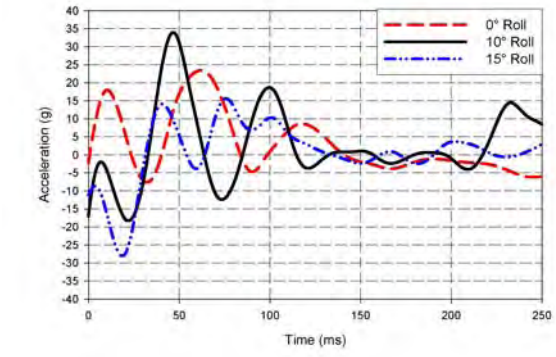

Figure 310. Upper Sidewall Acceleration Roll Angle Study, FS 480—Left Sidewall

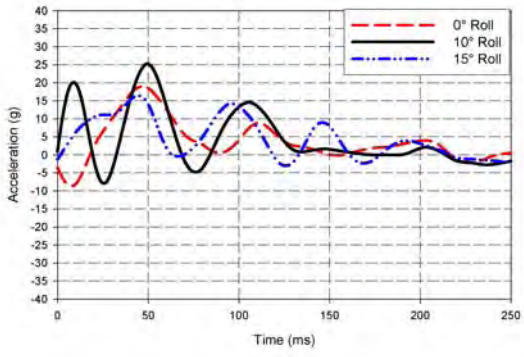

Figure 311. Upper Sidewall Acceleration Roll Angle Study, FS 480—Right Sidewall

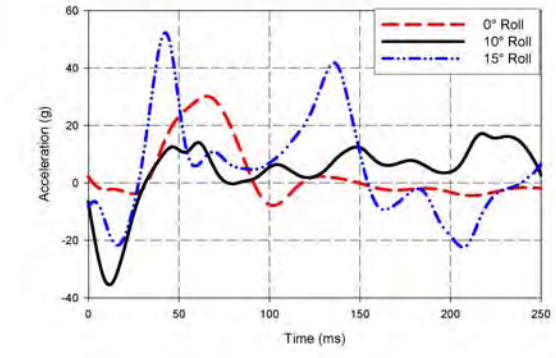

Figure 312. Lower Sidewall Acceleration Roll Angle Study, FS 400—Left Sidewall

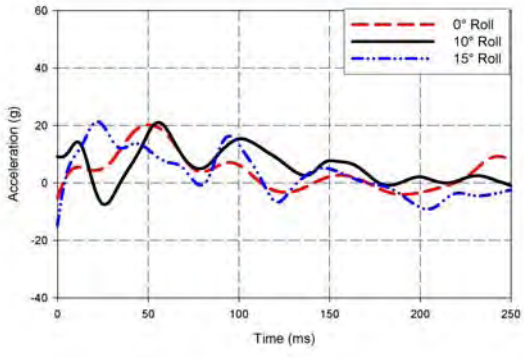

Figure 313. Lower Sidewall Acceleration Roll Angle Study, FS 400—Right Sidewall

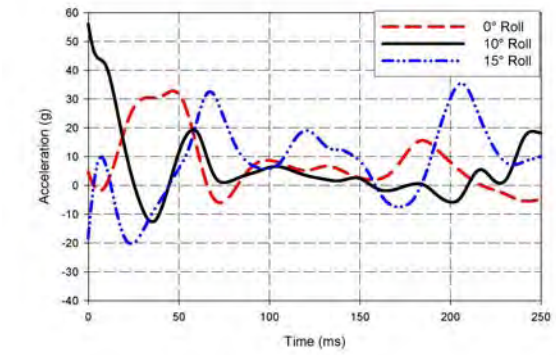

Figure 314. Upper Sidewall Acceleration Roll Angle Study, FS 440—Left Sidewall

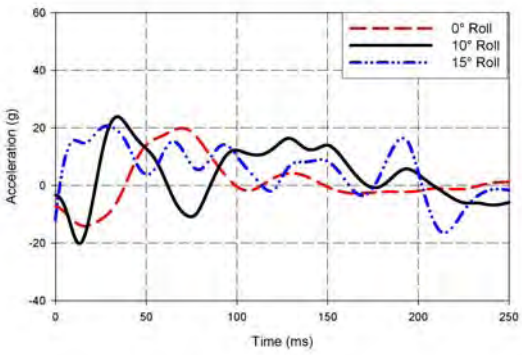

Figure 315. Upper Sidewall Acceleration Roll Angle Study, FS 440—Right Sidewall

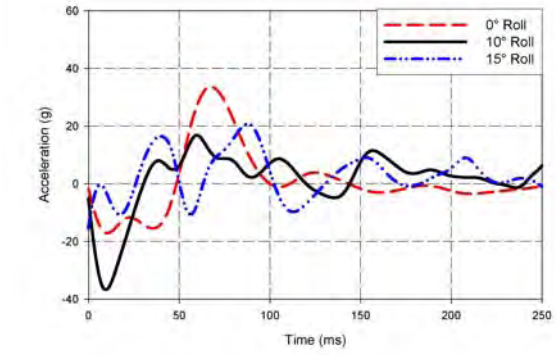

Figure 316. Upper Sidewall Acceleration Roll Angle Study, FS 480—Left Sidewall

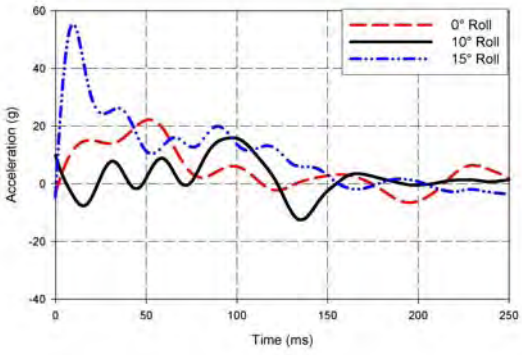

Figure 317. Upper Sidewall Acceleration Roll Angle Study, FS 480—Right Sidewall

8.5 EFFECT OF LUGGAGE.

The baseline simulation showed that the luggage plays a significant role in absorbing impact energy. To more clearly show the effect of luggage on the impact response of the fuselage section, a simulation was conducted with the luggage removed. The weight of the luggage was deleted, and the new weight was 3024 lb lighter than the fuselage model with luggage.

8.5.1 Fuselage.

As expected, the lack of luggage led to a very different pattern of deformation during impact, as shown in figure 318. It should be noted that no contact surface was defined between the lower frames and the floor. As a result, the lower frames moved through the floor, although this clearly could not occur in an experimental setting.

Deformation in the case without luggage continued until the frame sides just below the floor beams were able to resist the crushing load. The greater degree of vertical crushing also shows that the luggage adds a degree of stiffness to the fuselage section, in addition to dissipating impact energy. The lack of energy absorption without luggage is clearly illustrated in figure 318(j), which shows a greater degree of deflection in the upper frames. This occurred because of the secondary impact of the right and left frames after buckling, and resulted in a significant

acceleration pulse that transferred through the frames. This acceleration peak occurred on both the right and left sides of the airframe, but was more pronounced on the left-hand side. This will be shown later in the acceleration time histories.

(a) No Luggage (Left) and With Luggage (Right) at t = 20 ms

(b) No Luggage (Left) and With Luggage (Right) at t = 40 ms

(c) No Luggage (Left) and With Luggage (Right) at t = 60 ms

(d) No Luggage (Left) and With Luggage (Right) at t = 80 ms

Figure 318. Effect of Luggage

(e) No Luggage (Left) and With Luggage (Right) at t = 100 ms

(f) No Luggage (Left) and With Luggage (Right) at t = 120 ms

(g) No Luggage (Left) and With Luggage (Right) at t = 140 ms

(h) No Luggage (Left) and With Luggage (Right) at t = 160 ms

(i) No Luggage (Left) and With Luggage (Right) at t = 180 ms

Figure 318. Effect of Luggage (Continued)

(j) No Luggage (Left) and With Luggage (Right) at t = 200 ms

Figure 318. Effect of Luggage (Continued)

8.5.2 Overhead Stowage Bins.

8.5.2.1 Heath Tecna Bin.

The acceleration responses of the Heath Tecna bin are shown in figures 319 through 322, with figure 322 showing the average response of all acceleration locations. The initial peak occurred earlier for the case without luggage, although the value was similar to the baseline case. The no luggage case also showed a noticeable pulse approximately between 130 and 180 ms, and another pulse cresting near 250 ms, at a time when the baseline case is clearly moving toward zero. The duration of the impact event was longer for the no luggage case, and significant pulses were experienced after the frames reached their final crushing stroke.

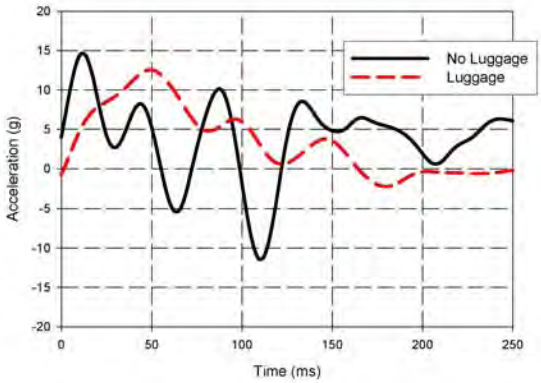

Figure 319. Heath Tecna Bin Acceleration Luggage Study, Forward Location

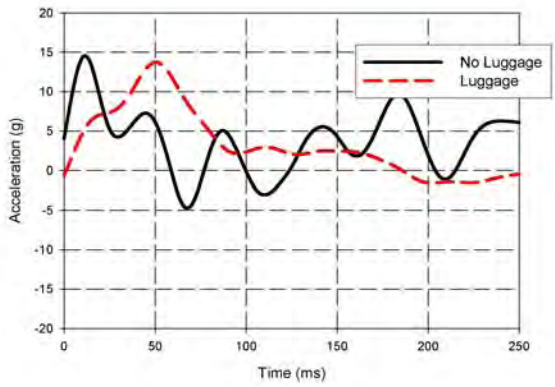

Figure 320. Heath Tecna Bin Acceleration Luggage Study, Aft Location

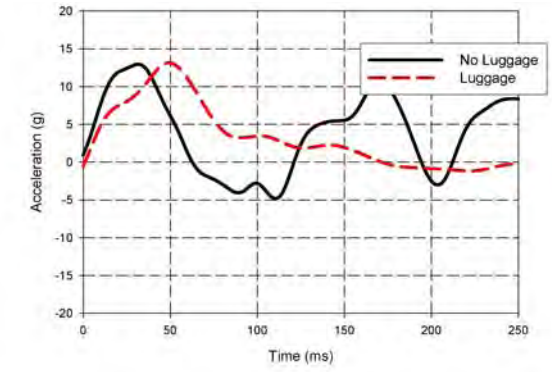

Figure 321. Heath Tecna Bin Acceleration Luggage Study, Center Location

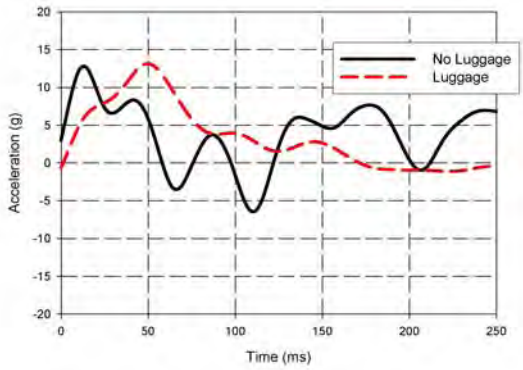

Figure 322. Heath Tecna Bin Acceleration Luggage Study, Average All Locations

Figures 323 through 332 present the load time histories of the Heath Tecna bin supports. Both forward and aft struts showed an increase in peak loading, ranging from 400 to 700 lb. The brackets, particularly at FS 420, also showed an increase in loading. Furthermore, as previously noted, all supports showed the lack of damping due to the absence of luggage. These continued oscillations contrast with the damped response of the baseline case and the experimental test, both of which showed that the bin response approached zero before 250 ms. This is significant, as it indicates that the viscous foam model, which includes damping, may be an appropriate means of simulating the luggage.

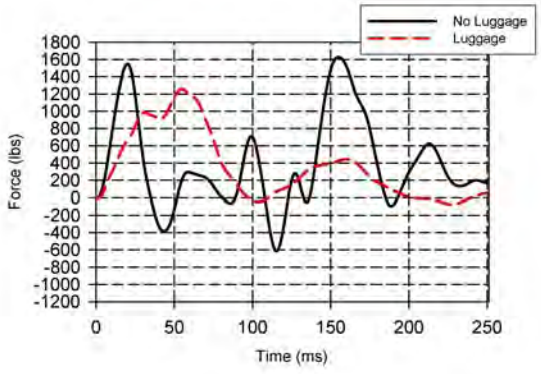

Figure 323. Heath Tecna Bin Load Luggage Study, Forward Strut

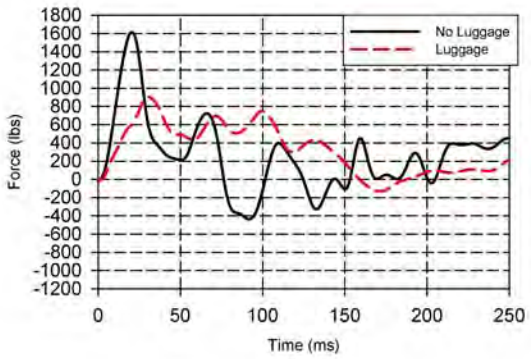

Figure 324. Heath Tecna Bin Load Luggage Study, Aft Strut

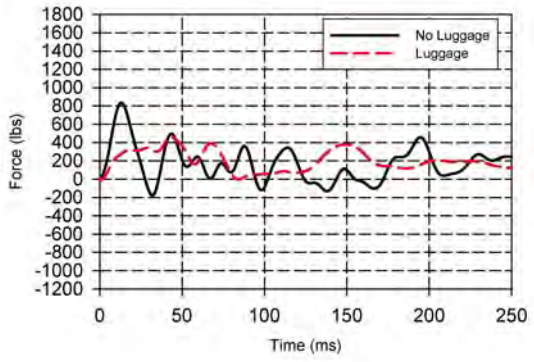

Figure 325. Heath Tecna Bin Load Luggage Study, FS 400—A Leg of Bracket

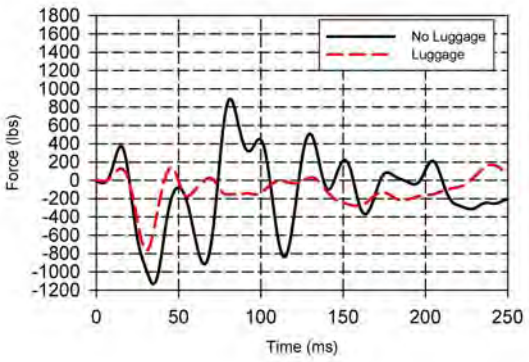

Figure 326. Heath Tecna Bin Load Luggage Study, FS 400—B Leg of Bracket

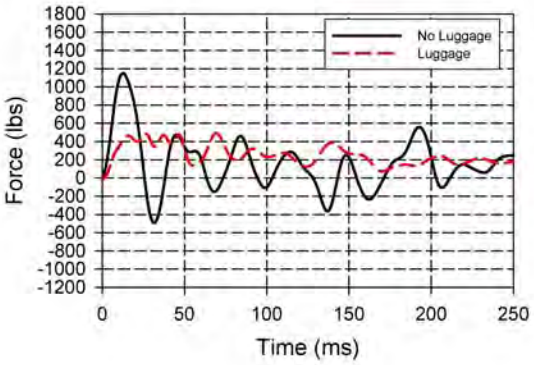

Figure 327. Heath Tecna Bin Load Luggage Study, FS 420—A Leg of Bracket

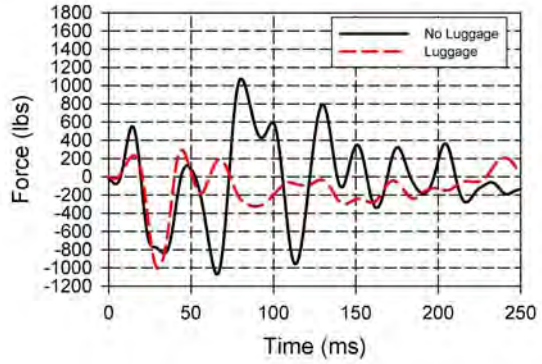

Figure 328. Heath Tecna Bin Load Luggage Study, FS 420—B Leg of Bracket

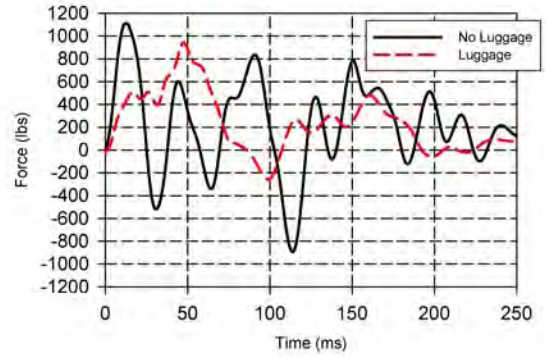

Figure 329. Heath Tecna Bin Load Luggage Study, FS 460—A Leg of Bracket

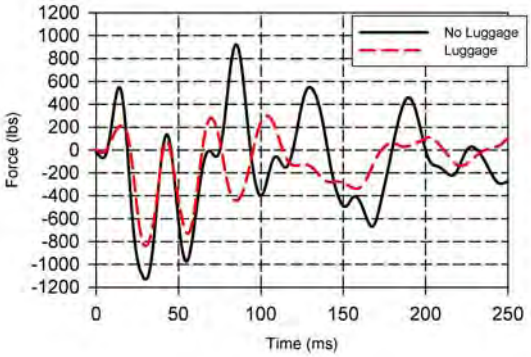

Figure 330. Heath Tecna Bin Load Luggage Study, FS 460—B Leg of Bracket

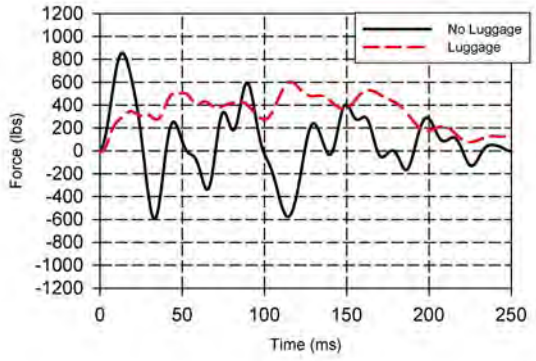

Figure 331. Heath Tecna Bin Load Luggage Study, FS 480—A Leg of Bracket

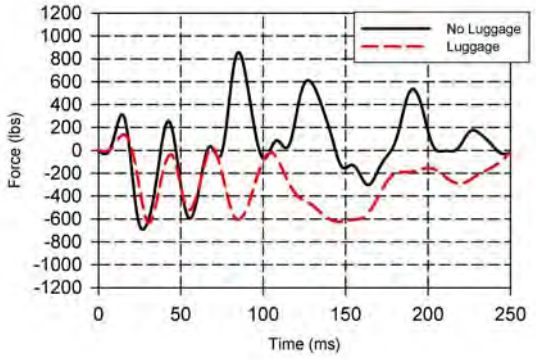

Figure 332. Heath Tecna Bin Load Luggage Study, FS 480—B Leg of Bracket

8.5.2.2 Hitco Bin.

Figures 333 through 336 show the acceleration response results for the Hitco bin, comparing the no luggage case with the baseline simulation. The average acceleration results, shown in figure 336, show an increase of approximately 50% in peak acceleration value for the no luggage condition.

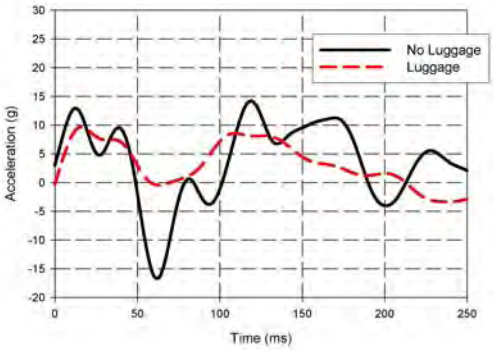

Figure 333. Hitco Bin Acceleration Luggage Study, Forward Location

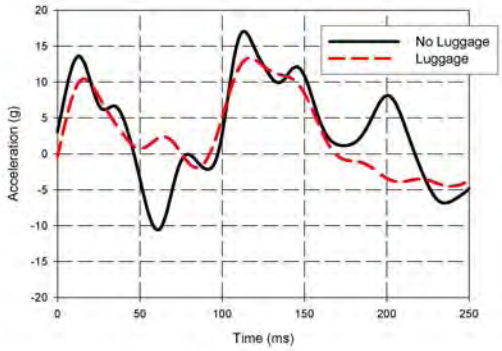

Figure 334. Hitco Bin Acceleration Luggage Study, Aft Location

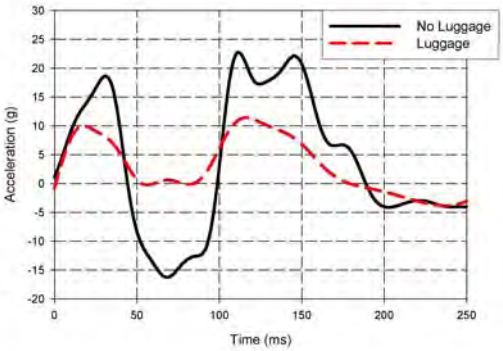

Figure 335. Hitco Bin Acceleration Luggage Study, Center Location

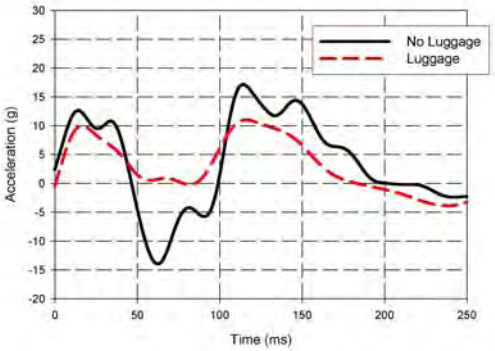

Figure 336. Hitco Bin Acceleration Luggage Study, Average All Locations

Figures 337 and 338 show even more dramatic results, with oscillations resulting in a compressive load near 2200 lb for the aft tie rod. Peak tension loads also increased to between 1600 and 1900 lb.

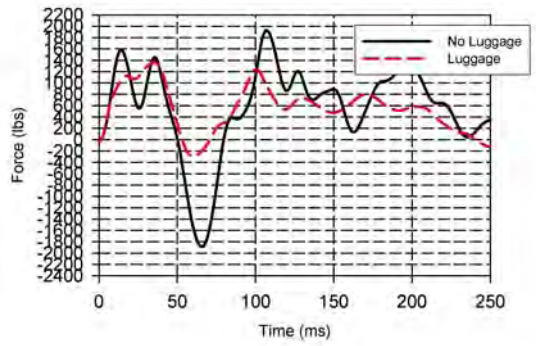

Figure 337. Hitco Bin Load Luggage Study, Forward Strut

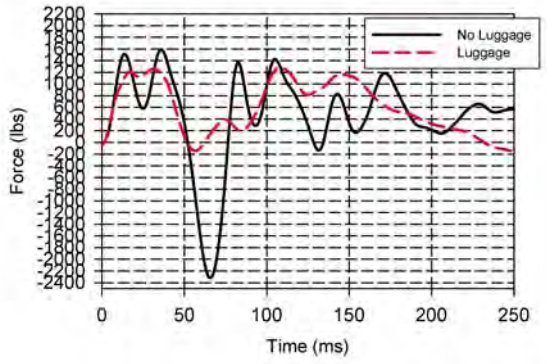

Figure 338. Hitco Bin Load Luggage Study, Aft Strut

Figures 339 through 346 show that the inboard links experienced similar changes, with significant compressive loads alternating with slightly increased tensile loads.

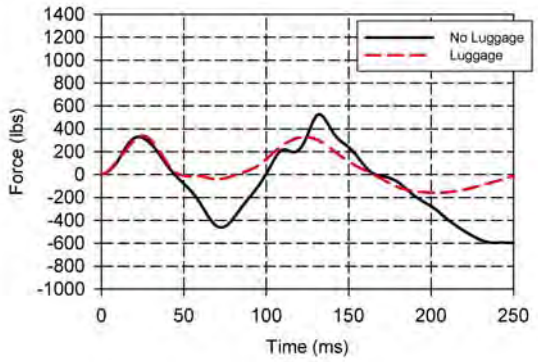

Figure 339. Hitco Bin Load Luggage Study, FS 400 Vertical Link

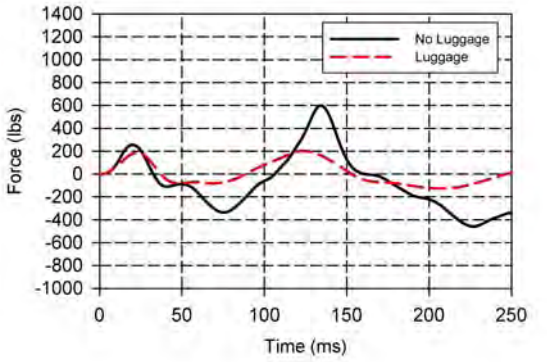

Figure 340. Hitco Bin Load Luggage Study, FS 400 Horizontal Link

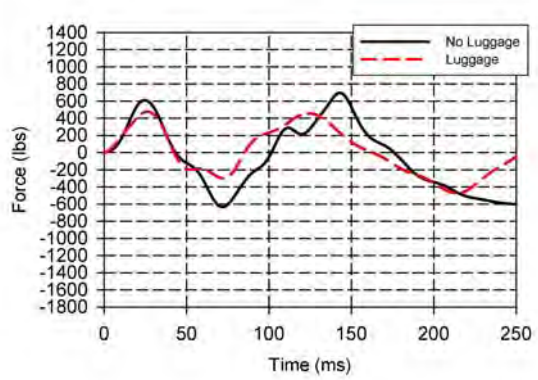

Figure 341. Hitco Bin Load Luggage Study, FS 420 Vertical Link

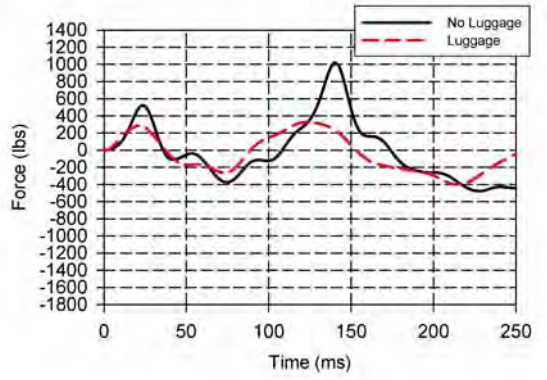

Figure 342. Hitco Bin Load Luggage Study, FS 420 Horizontal Link

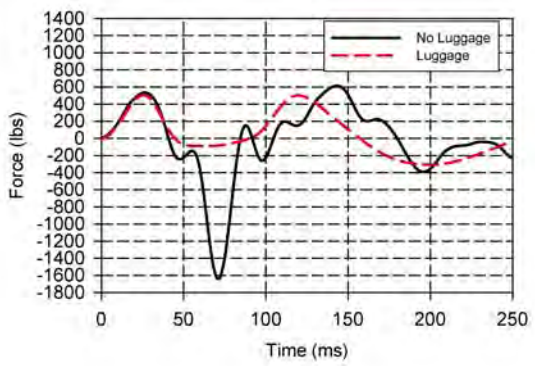

Figure 343. Hitco Bin Load Luggage Study, FS 460 Vertical Link

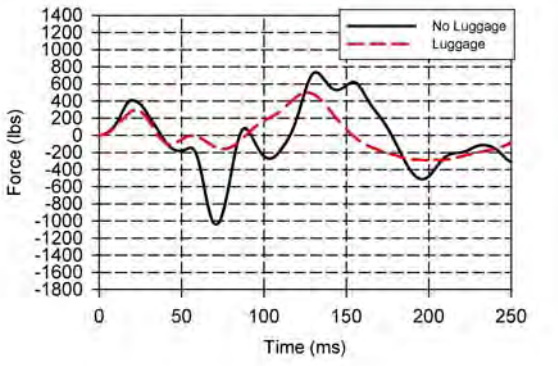

Figure 344. Hitco Bin Load Luggage Study, FS 460 Horizontal Link

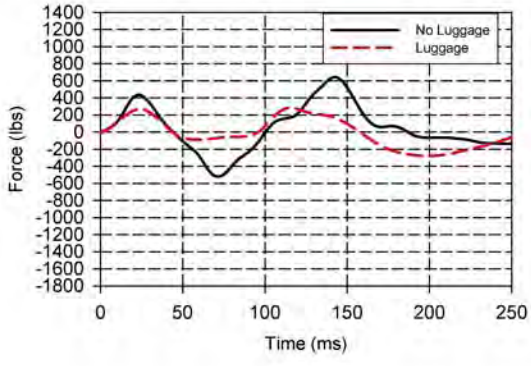

Figure 345. Hitco Bin Load Luggage Study, FS 480 Vertical Link

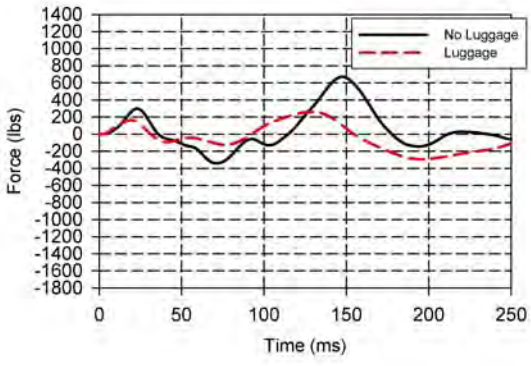

Figure 346. Hitco Bin Load Luggage Study, FS 480 Horizontal Link

8.5.3 Floor Tracks.

Figures 347 and 360 illustrate the expected effect on acceleration pulses for the left and right floor tracks, with the left side showing more significant increases in the calculated acceleration response. In some locations, the right-side floor tracks decreased in the calculated acceleration response with no luggage. However, the lower frames were permitted to penetrate the floor beams and floor section, although this could not occur in practice.

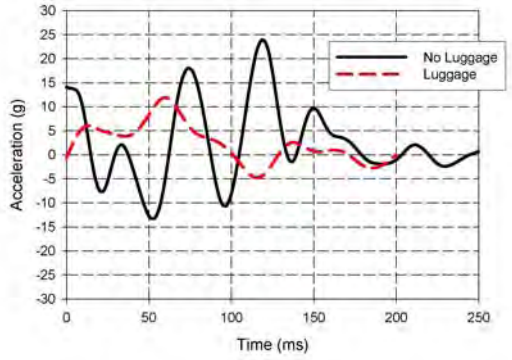

Figure 347. Floor Track Acceleration Luggage Study, FS 380—Left Inside Seat Track

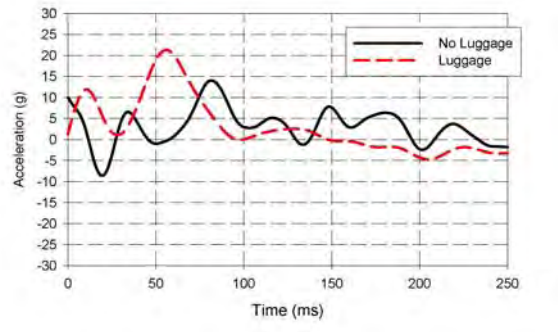

Figure 348. Floor Track Acceleration Luggage Study, FS 380—Right Inside Seat Track

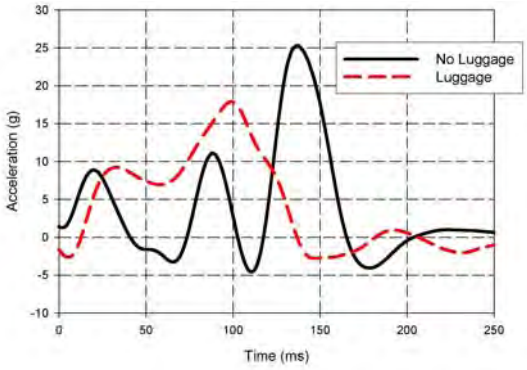

Figure 349. Floor Track Acceleration Luggage Study, FS 418—Left Outside Floor Track

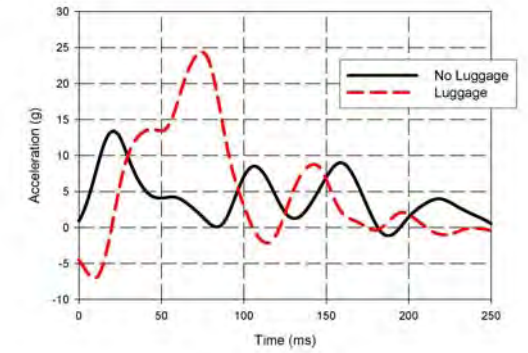

Figure 350. Floor Track Acceleration Luggage Study, FS 418—Right Outside Floor Track

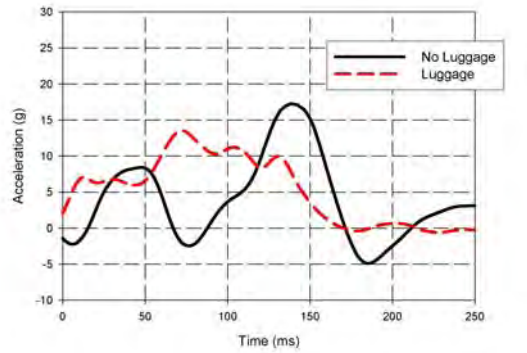

Figure 351. Floor Track Acceleration Luggage Study, FS 418—Left Inside Floor Track

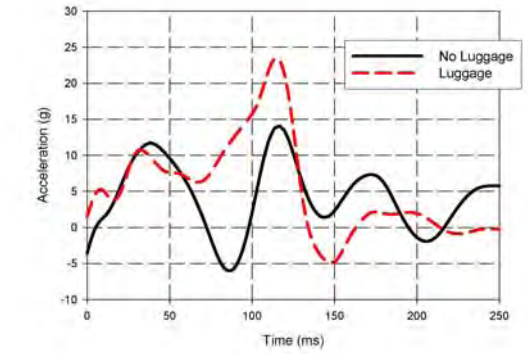

Figure 352. Floor Track Acceleration Luggage Study, FS 418—Right Inside Floor Track

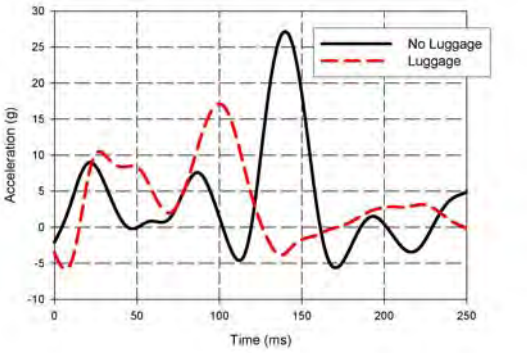

Figure 353. Floor Track Acceleration Luggage Study, FS 452—Left Outside Floor Track

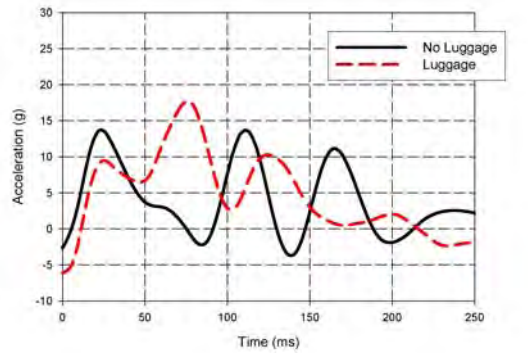

Figure 354. Floor Track Acceleration Luggage Study, FS 452—Right Outside Floor Track

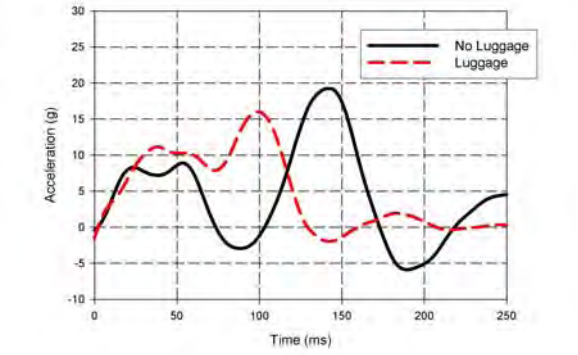

Figure 355. Floor Track Acceleration Luggage Study, FS 452—Left Inside Floor Track

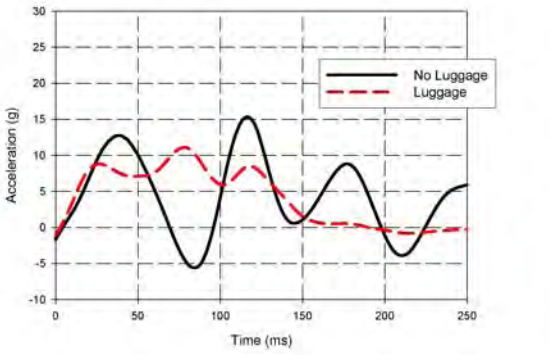

Figure 356. Floor Track Acceleration Luggage Study, FS 452—Right Inside Floor Track

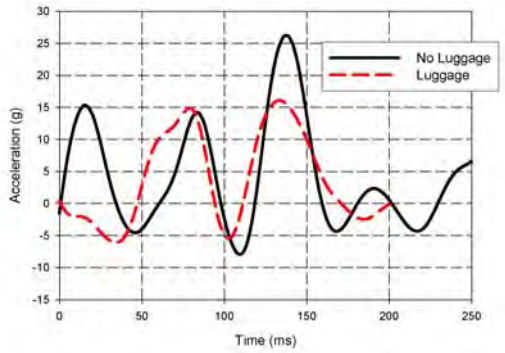

Figure 357. Floor Track Acceleration Luggage Study, FS 484—Left Outside Floor Track

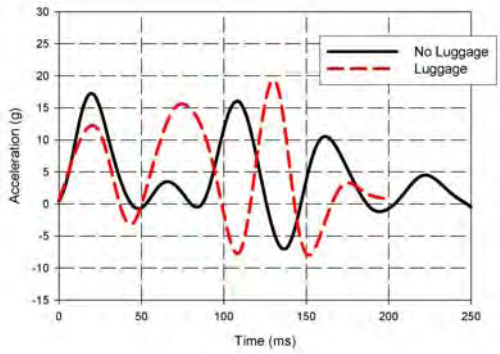

Figure 358. Floor Track Acceleration Luggage Study, FS 484—Right Outside Floor Track

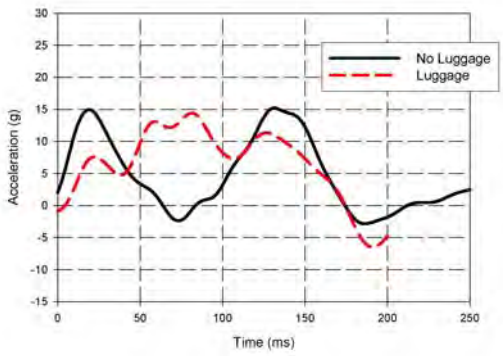

Figure 359. Floor Track Acceleration Luggage Study, FS 484—Left Inside Floor Track

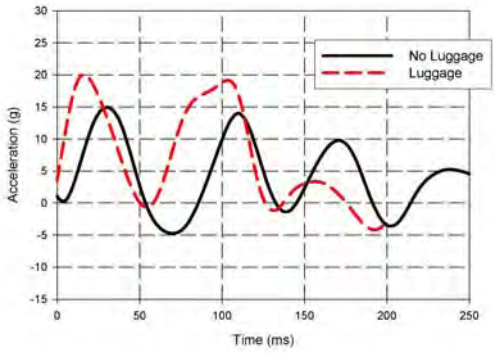

Figure 360. Floor Track Acceleration Luggage Study, FS 484—Right Inside Floor Track

8.5.4 Sidewalls.

The sidewall acceleration results are presented in figures 361 through 372. Overall, the sidewall accelerations were higher for the no luggage condition.

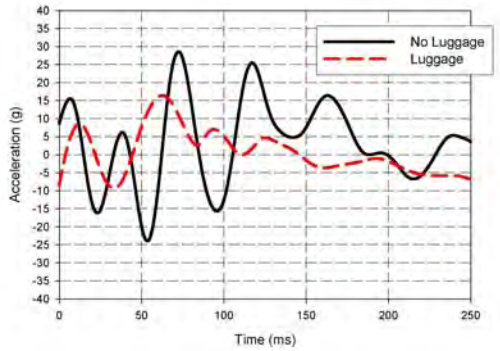

Figure 361. Upper Sidewall Acceleration Luggage Study, FS 400—Left Sidewall

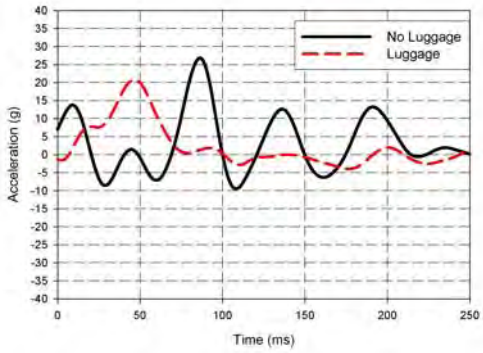

Figure 362. Upper Sidewall Acceleration Luggage Study, FS 400—Right Sidewall

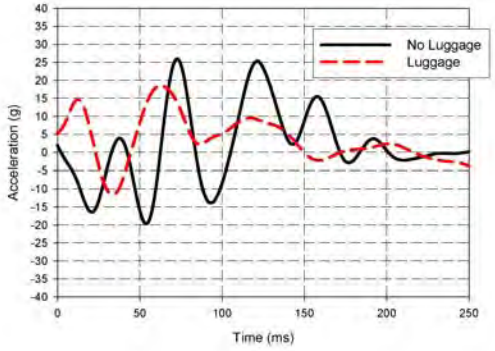

Figure 363. Upper Sidewall Acceleration Luggage Study, FS 440—Left Sidewall

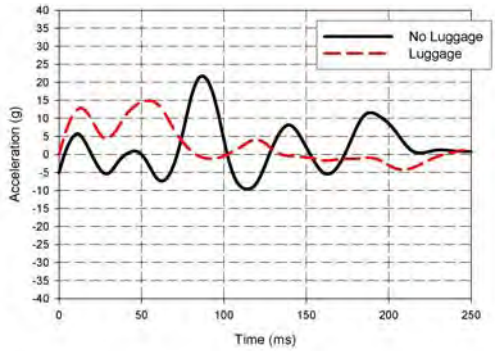

Figure 364. Upper Sidewall Acceleration Luggage Study, FS 440—Right Sidewall

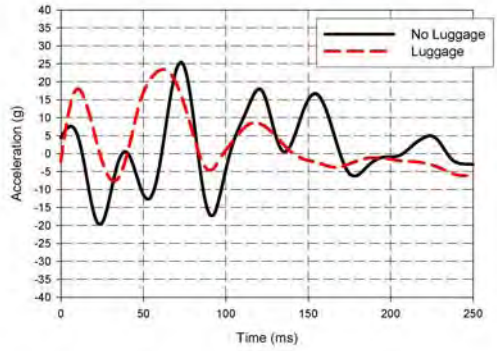

Figure 365. Upper Sidewall Acceleration Luggage Study, FS 480—Left Sidewall

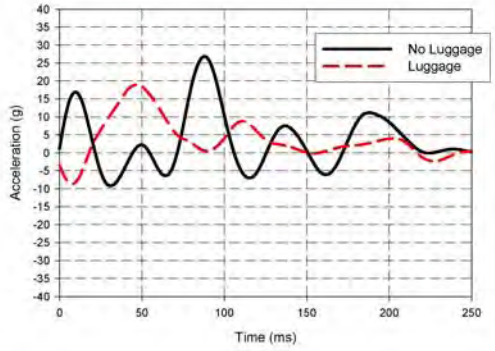

Figure 366. Upper Sidewall Acceleration Luggage Study, FS 480—Right Sidewall

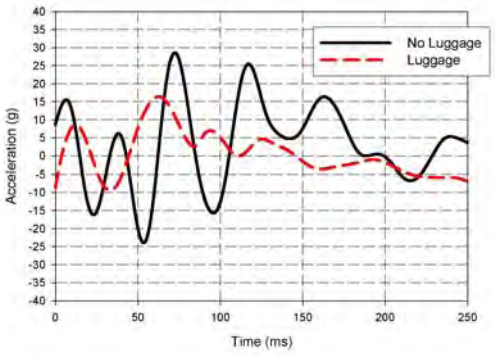

Figure 367. Lower Sidewall Acceleration Luggage Study, FS 400—Left Sidewall

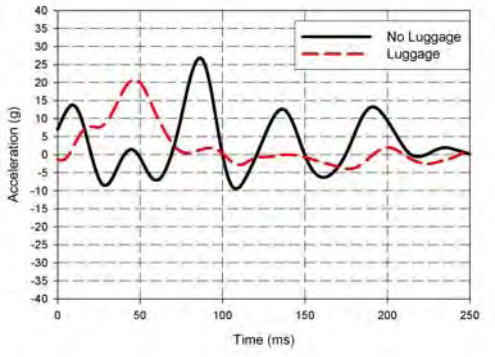

Figure 368. Lower Sidewall Acceleration Luggage Study, FS 400—Right Sidewall

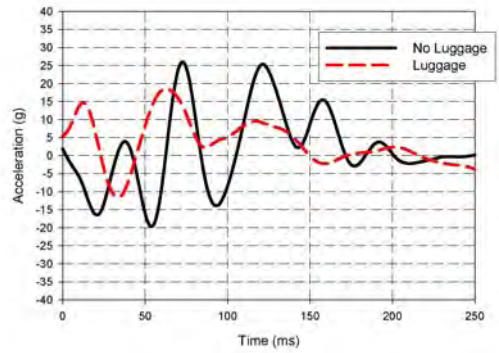

Figure 369. Lower Sidewall Acceleration Luggage Study, FS 440—Left Sidewall

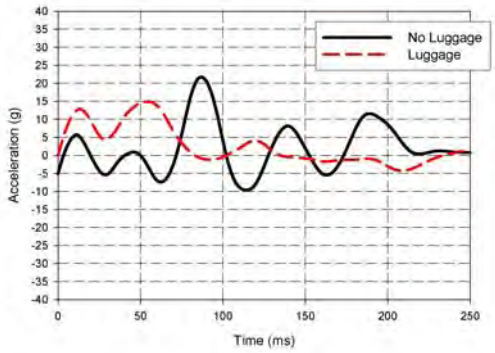

Figure 370. Lower Sidewall Acceleration Luggage Study, FS 440—Right Sidewall

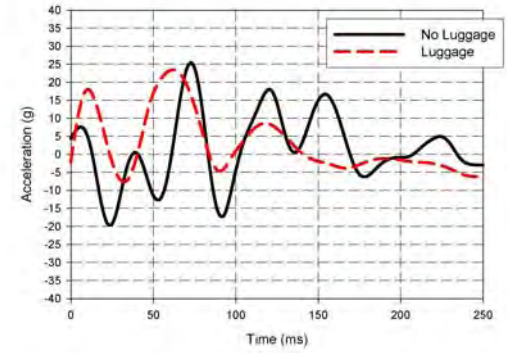

Figure 371. Lower Sidewall Acceleration Luggage Study, FS 480—Left Sidewall

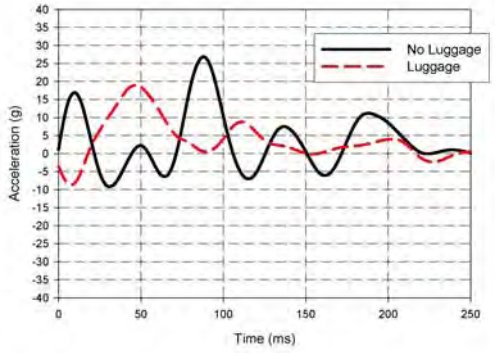

Figure 372. Lower Sidewall Acceleration Luggage Study, FS 480—Right Sidewall

8.6 COMBINED VERTICAL AND LONGITUDINAL IMPACT LOADING.

Currently, separate experimental tests are conducted to study vertical and longitudinal impacts, with each component being independently evaluated. Vertical tests employ an initial impact velocity, and then the acceleration response of the fuselage section and cabin items are assessed. Longitudinal impact tests, however, cannot follow this procedure. Unlike automobile impacts,

an aircraft impact will cover an extended area and will vary significantly, depending on the terrain, pitch angle, and other complex factors, such as separation of wings or complete fractures in the fuselage section. For longitudinal testing, a typical acceleration pulse was provided. The selected pulse was based on an analysis of actual aircraft accidents.

Fortunately, a triangular acceleration pulse with a peak at 100 ms provides a very good approximation of an actual impact event. Peak values may be in the range of 6 to 16 g's, as in the case of a recent FAA study with a B-737 fuselage section. This acceleration pulse represents the initial, and most critical, moment of impact. After this initial pulse, friction associated with sliding slowly reduces the longitudinal velocity to zero.

The experimental procedure was to accelerate the fuselage test section in the opposite direction, that is, in the aft direction. The acceleration pulse was controlled by a pneumatically operated piston inside a closed cylinder. The magnitude of acceleration was then controlled by a metering pin. The instrumented response of the overhead stowage bins and the under-floor conformal was recorded. The actual tests were conducted in 1997 at the Transportation Research Center Inc.'s Impact Simulator Facility in East Liberty, Ohio.

The three peak acceleration values studied experimentally by the FAA were 6, 9, and 16 g's. The 16-g impact resulted in substantial damage to the frames and failures where the overhead stowage bins were supported. The 6-g case resulted in no observable damage to the bins, but resulted in failure of the fuel cell supporting brackets. After removal of the fuel cell, the 9-g test case resulted in no significant damage to the overhead bins or frames. The 9-g acceleration case was selected for simulation, in combination with the previous 30-ft/sec vertical impact. The longitudinal acceleration profile that was used in the simulation is shown in figure 373.

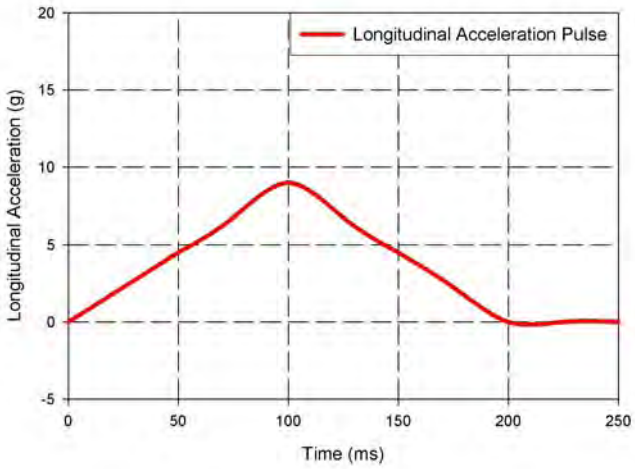

Figure 373. Acceleration Pulse for Longitudinal Impact Condition

This acceleration pulse leads to an experimentally determined velocity change of approximately 32 ft/sec, again with the applied acceleration being in the aft (positive X) direction, with respect to the occupants.

Figure 374 shows the change in velocity during the simulation for a point located on the cabin floor. This velocity profile accurately matches the profile resulting from the experimental 9-g acceleration pulse.

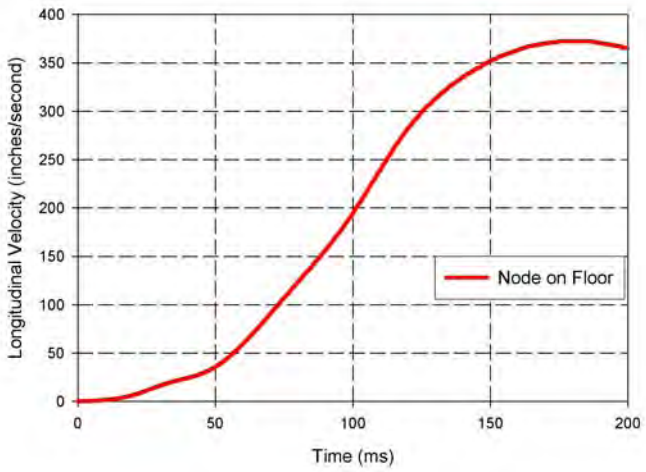

Figure 374. Velocity Change Resulting From Longitudinal Acceleration Pulse

As previously noted, a key advantage of using numerical simulations in crashworthiness studies is the ability to examine multiple impact conditions in combinations that are either not feasible or are simply too expensive to study with empirical testing. While experimental tests provide valuable data, their results are valid only for the single test condition under consideration. The simulation, in this case, is well suited to studying the combined effects of vertical and longitudinal impacts.

8.6.1 Fuselage.

The following results (figure 375) are for the 9-g longitudinal acceleration pulse condition, combined with a 30-ft/sec vertical impact. For the side view case, the skin panels were removed to show the seat response during impact more clearly.

(a) Front and Left Views, Combined Impact at t = 20 ms

Figure 375. Combined Vertical and Longitudinal Impact Loading

(b) Front and Left Views, Combined Impact at t = 40 ms

(c) Front and Left Views, Combined Impact at t = 60 ms

(d) Front and Left Views, Combined Impact at t = 80 ms

(e) Front and Left Views, Combined Impact at t = 100 ms

Figure 375. Combined Vertical and Longitudinal Impact Loading (Continued)

(f) Front and Left Views, Combined Impact at t = 120 ms

(g) Front and Left Views, Combined Impact at t = 140 ms

(h) Front and Left Views, Combined Impact at t = 160 ms

Figure 375. Combined Vertical and Longitudinal Impact Loading (Continued)

8.6.2 Overhead Stowage Bins.

8.6.2.1 Heath Tecna Bin.

The acceleration responses of the Heath Tecna bins are shown in figures 376 to 379. The results showed little effect on the peak vertical acceleration (figure 379). The obvious difference is the number of pronounced peaks occurring during the test.

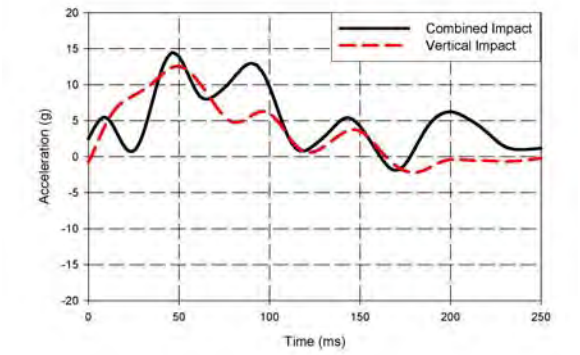

Figure 376. Heath Tecna Acceleration Longitudinal Impact Study, Forward Location

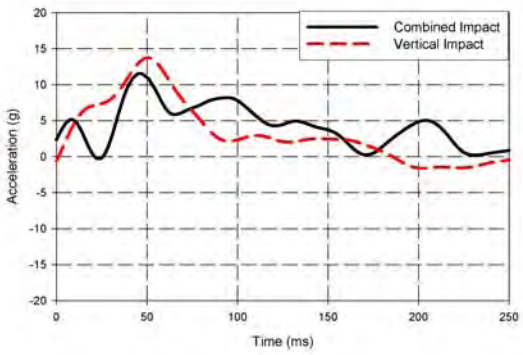

Figure 377. Heath Tecna Acceleration Longitudinal Impact Study, Aft Location

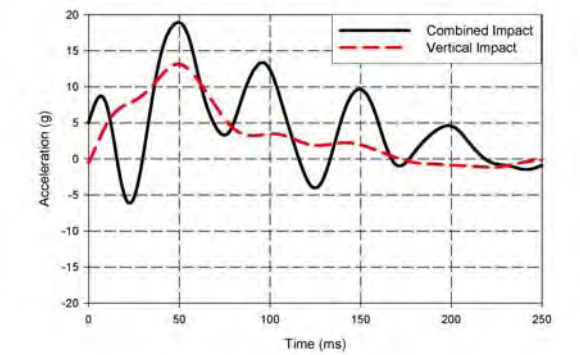

Figure 378. Heath Tecna Acceleration Longitudinal Impact Study, Center Location

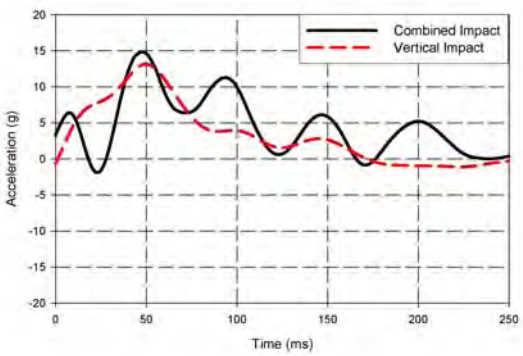

Figure 379. Heath Tecna Acceleration Longitudinal Impact Study, Average All Locations

Figures 380 through 389 present the load time histories of the supports. There was generally good agreement between the peak values of the two test conditions. Some delay was noted between the combined impact and the vertical impact cases.

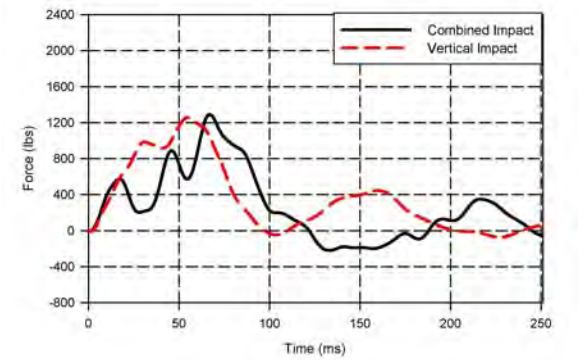

Figure 380. Heath Tecna Acceleration Longitudinal Impact Study, Forward Strut

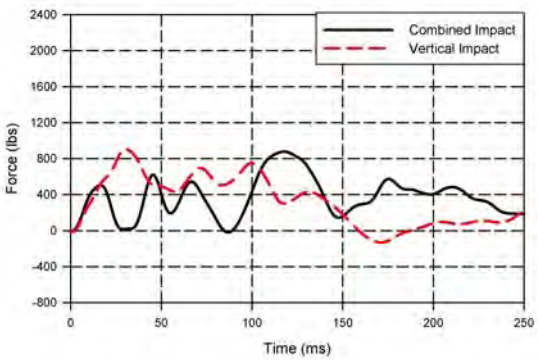

Figure 381. Heath Tecna Acceleration Longitudinal Impact Study, Aft Strut

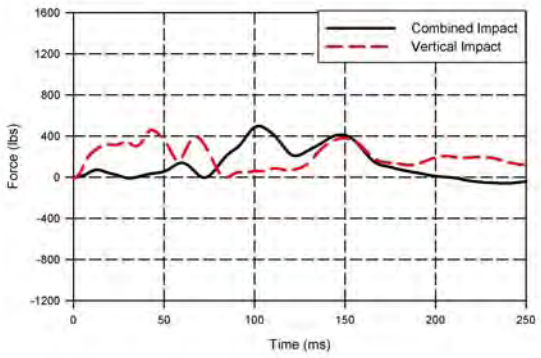

Figure 382. Heath Tecna Acceleration Longitudinal Impact Study, FS 400—A Leg of Bracket

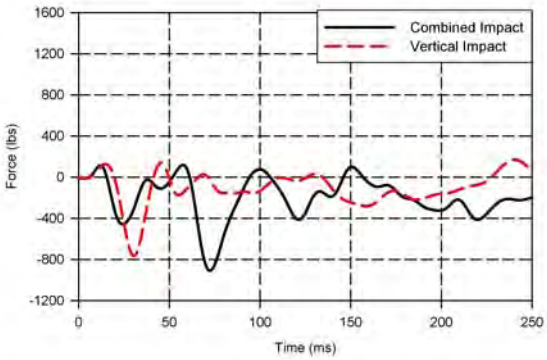

Figure 383. Heath Tecna Acceleration Longitudinal Impact Study, FS 400—B Leg of Bracket

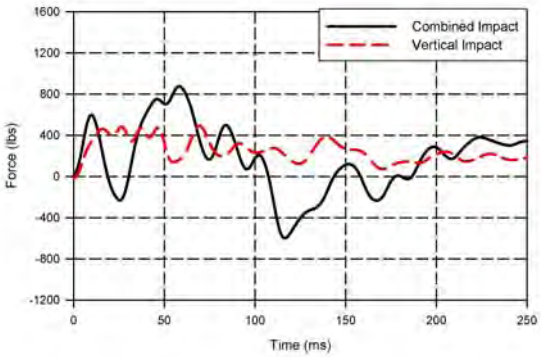

Figure 384. Heath Tecna Acceleration Longitudinal Impact Study, FS 420—A Leg of Bracket

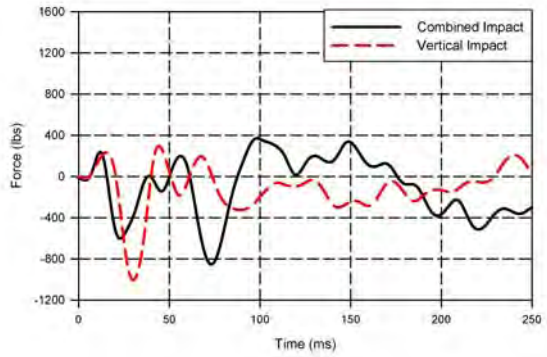

Figure 385. Heath Tecna Acceleration Longitudinal Impact Study, FS 420—B Leg of Bracket

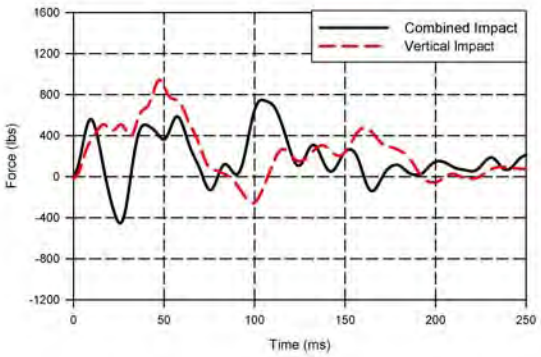

Figure 386. Heath Tecna Acceleration Longitudinal Impact Study, FS 460—A Leg of Bracket

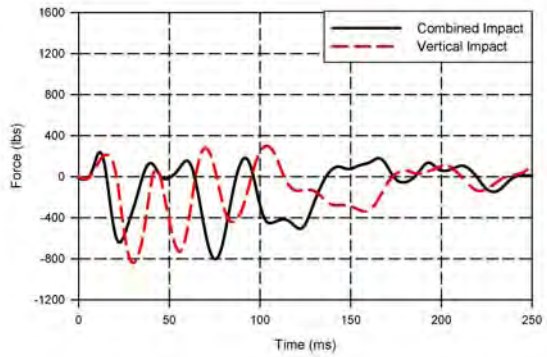

Figure 387. Heath Tecna Acceleration Longitudinal Impact Study, FS 460—B Leg of Bracket

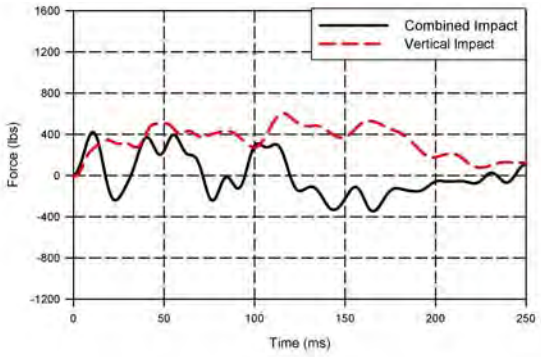

Figure 388. Heath Tecna Acceleration Longitudinal Impact Study, FS 480—A Leg of Bracket

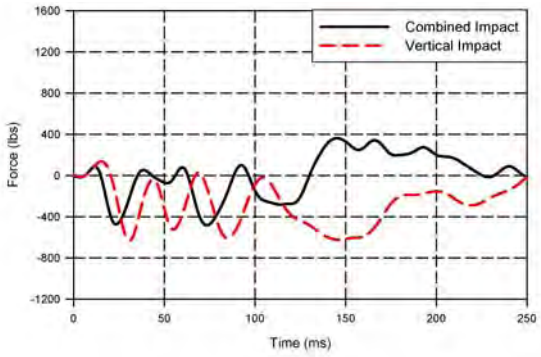

Figure 389. Heath Tecna Acceleration Longitudinal Impact Study, FS 480—B Leg of Bracket

8.6.2.2 Hitco Bin.

The Hitco bin results are presented in figures 390 through 393. Peak acceleration results were similar for both the vertical and combined impact cases. However, the combined peak pulses were delayed compared to the vertical impact case.

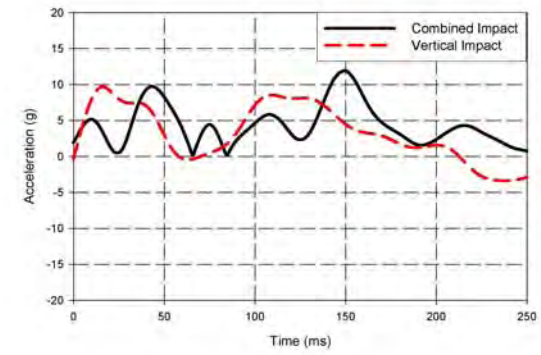

Figure 390. Hitco Acceleration Longitudinal Impact Study, Forward Location

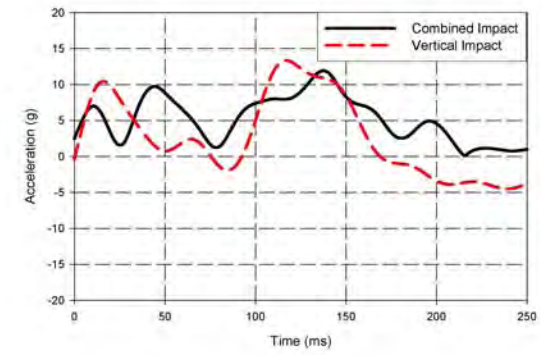

Figure 391. Hitco Acceleration Longitudinal Impact Study, Aft Location

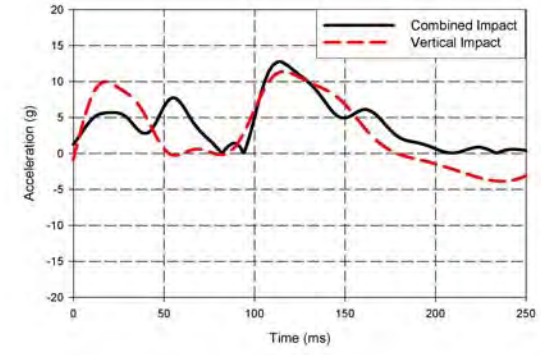

Figure 392. Hitco Acceleration Longitudinal Impact Study, Center Location

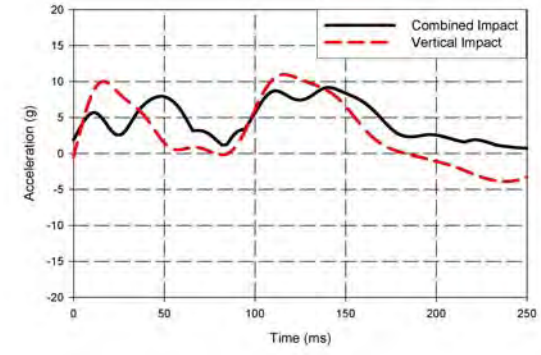

Figure 393. Hitco Acceleration Longitudinal Impact Study, Average All Locations

Figures 394 to 403 show the load histories of the supports. The forward and aft struts show a significant impulse occurring at approximately 135 ms. Figure 394 shows that the peak values were similar for the forward strut and the combined impact results in the delayed peaks. Figure 395 shows that the combined impact resulted in a higher peak load of approximately 600 lb at 135 ms and resulted in delayed peaks.

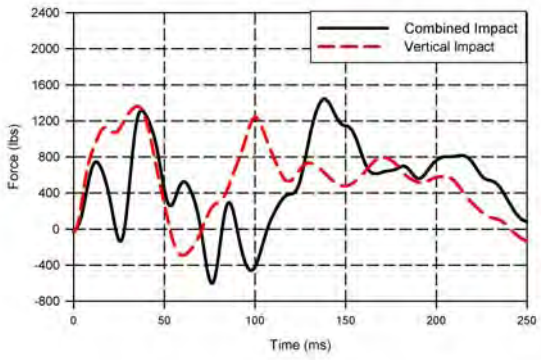

Figure 394. Hitco Bin Load Longitudinal Impact Study, Forward Strut

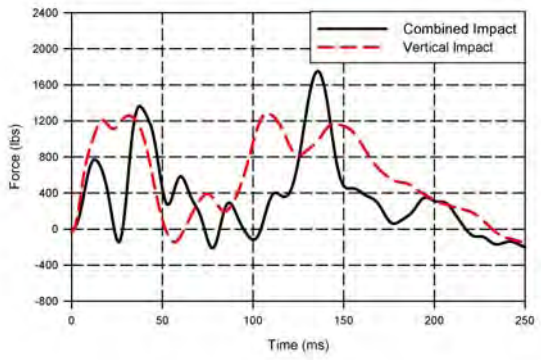

Figure 395. Hitco Bin Load Longitudinal Impact Study, Aft Strut

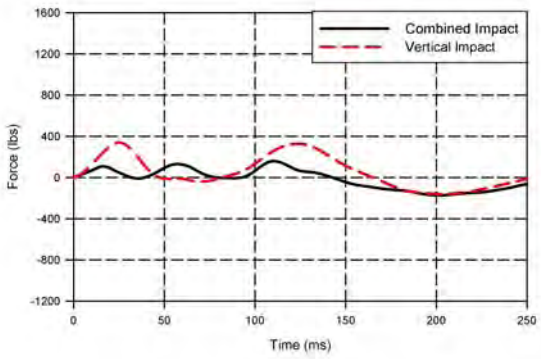

Figure 396. Hitco Bin Load Longitudinal Impact Study, FS 400 Vertical Link

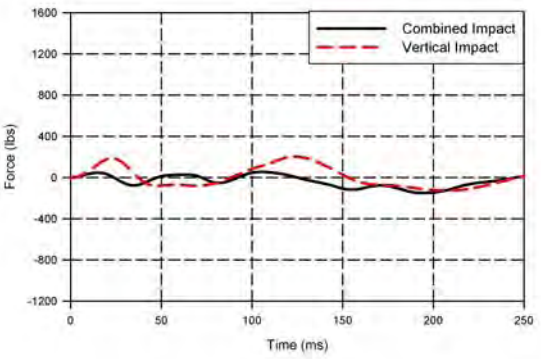

Figure 397. Hitco Bin Load Longitudinal Impact Study, FS 400 Horizontal Link

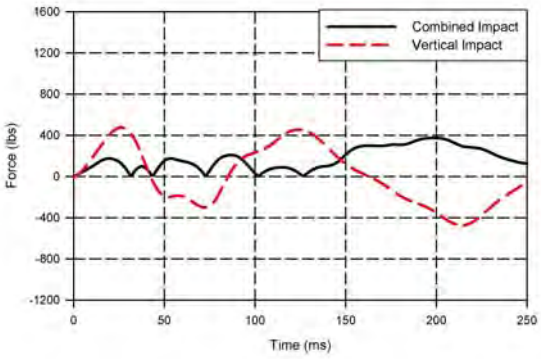

Figure 398. Hitco Bin Load Longitudinal Impact Study, FS 420 Vertical Link

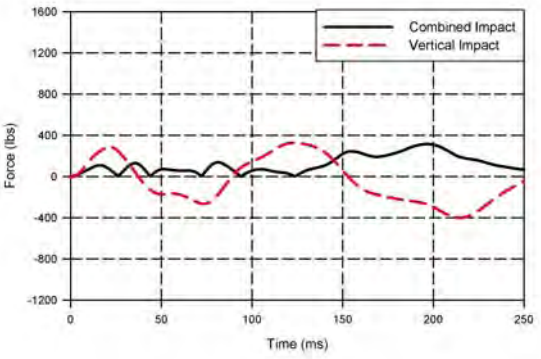

Figure 399. Hitco Bin Load Longitudinal Impact Study, FS 420 Horizontal Link

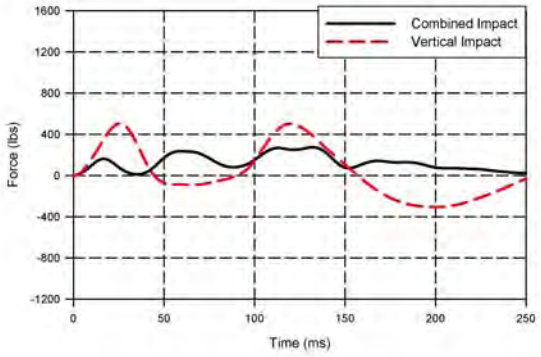

Figure 400. Hitco Bin Load Longitudinal Impact Study, FS 460 Vertical Link

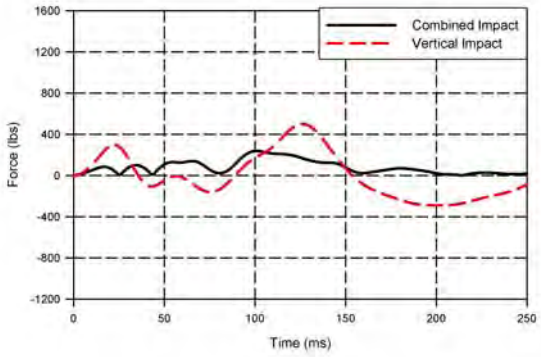

Figure 401. Hitco Bin Load Longitudinal Impact Study, FS 460 Horizontal Link

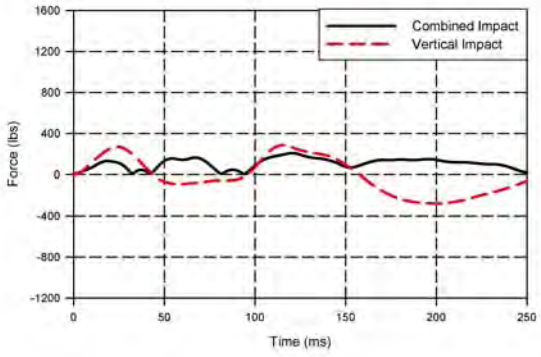

Figure 402. Hitco Bin Load Longitudinal Impact Study, FS 480 Vertical Link

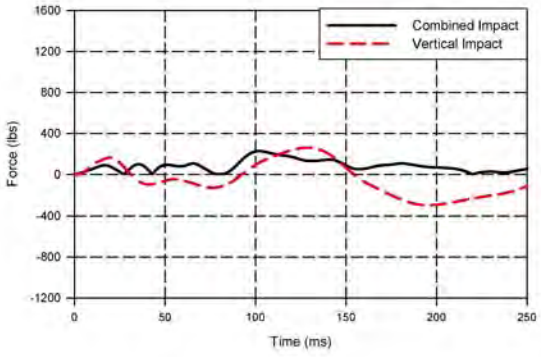

Figure 403. Hitco Bin Load Longitudinal Impact Study, FS 480 Horizontal Link

8.6.3 Floor Tracks.

Figures 404 through 417 show the results of the floor track accelerations. The right side was generally higher than the left, with a larger combined impact in the forward locations and a higher vertical impact in the aft locations. The peak values on the left side were slightly higher for the vertical impact.

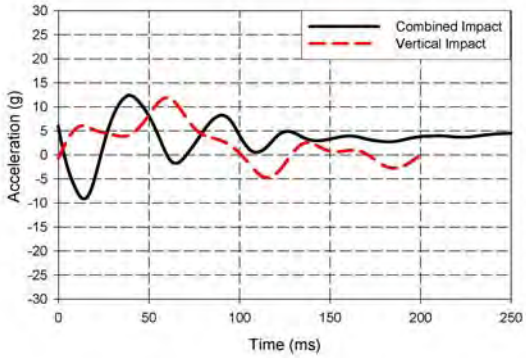

Figure 404. Floor Track Acceleration Longitudinal Impact Study, FS 380—Left Inside Floor Track

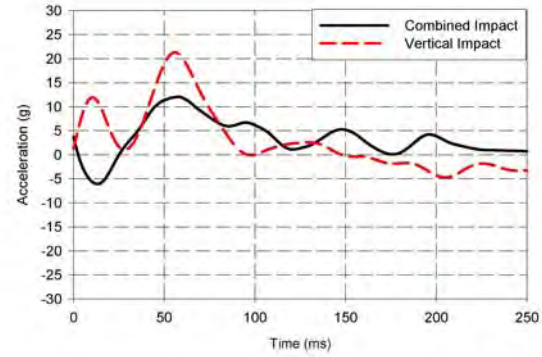

Figure 405. Floor Track Acceleration Longitudinal Impact Study, FS 380—Right Inside Floor Track

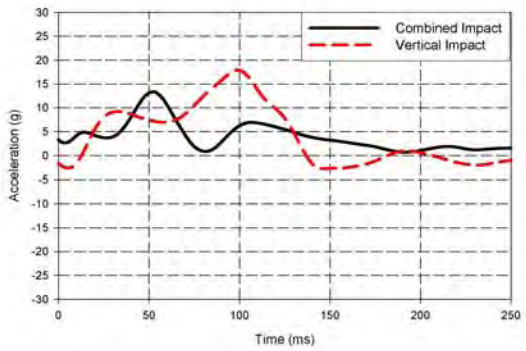

Figure 406. Floor Track Acceleration Longitudinal Impact Study, FS 418—Left Outside Floor Track

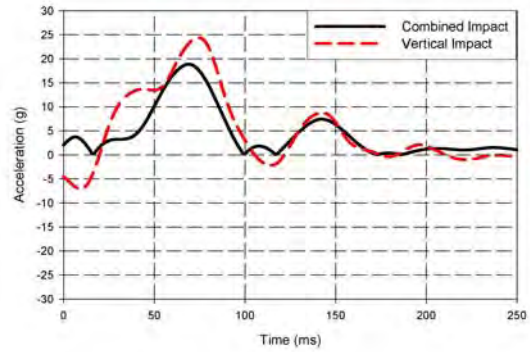

Figure 407. Floor Track Acceleration Longitudinal Impact Study, FS 418—Right Outside Floor Track

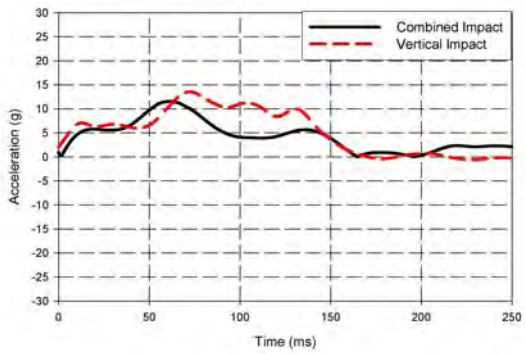

Figure 408. Floor Track Acceleration Longitudinal Impact Study, FS 418—Left Inside Floor Track

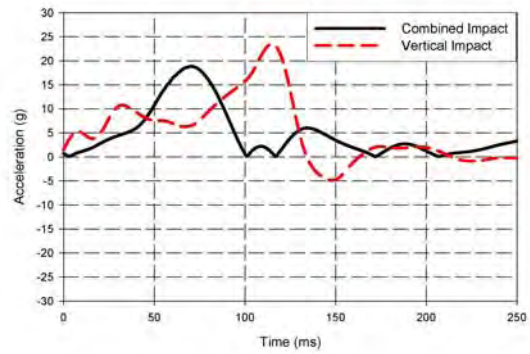

Figure 409. Floor Track Acceleration Longitudinal Impact Study, FS 418—Right Inside Floor Track

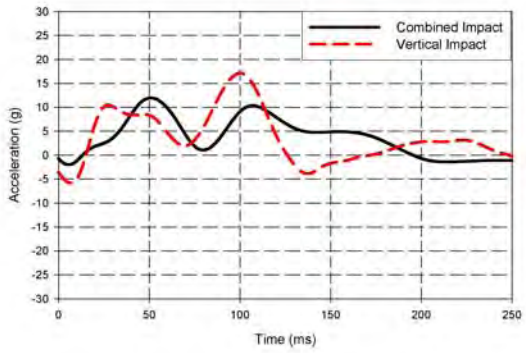

Figure 410. Floor Track Acceleration Longitudinal Impact Study, FS 452—Left Outside Floor Track

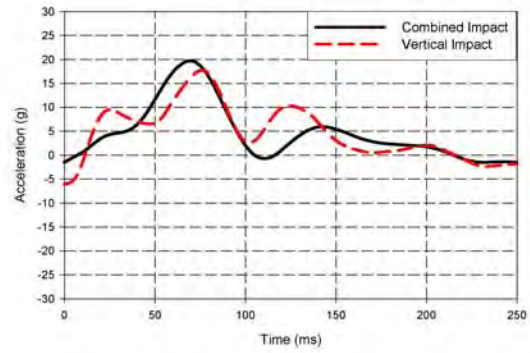

Figure 411. Floor Track Acceleration Longitudinal Impact Study, FS 452—Right Outside Floor Track

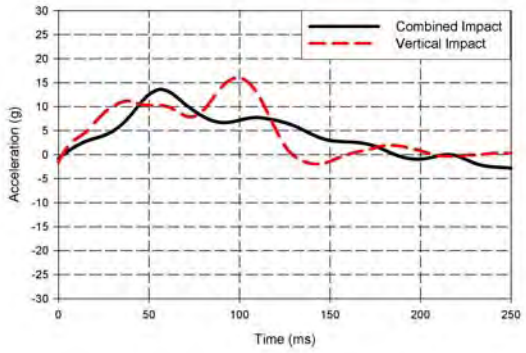

Figure 412. Floor Track Acceleration Longitudinal Impact Study, FS 452—Left Inside Floor Track

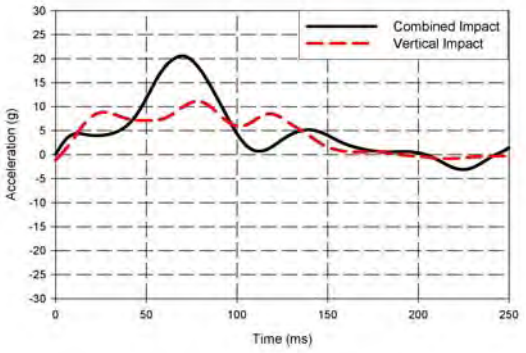

Figure 413. Floor Track Acceleration Longitudinal Impact Study, FS 452—Right Inside Floor Track

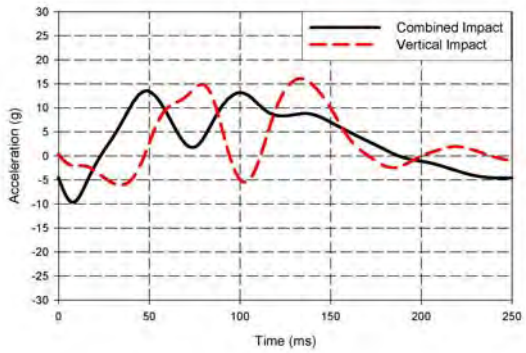

Figure 414. Floor Track Acceleration Longitudinal Impact Study, FS 484—Left Outside Floor Track

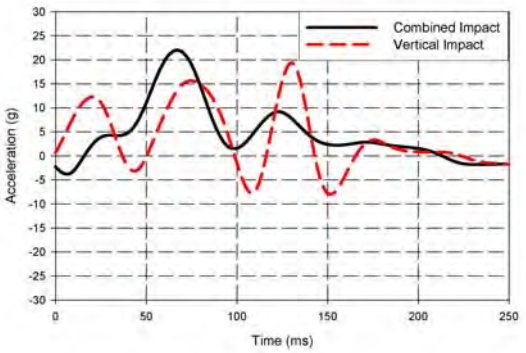

Figure 415. Floor Track Acceleration Longitudinal Impact Study, FS 484—Right Outside Floor Track

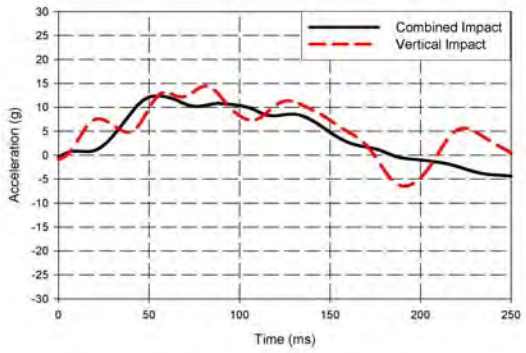

Figure 416. Floor Track Acceleration Longitudinal Impact Study, FS 484—Left Inside Floor Track

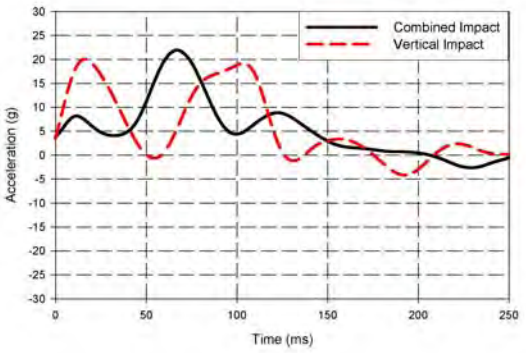

Figure 417. Floor Track Acceleration Longitudinal Impact Study, FS 484—Right Inside Floor Track

8.6.4 Sidewalls.

Figures 418 through 429 show the upper and lower sidewall accelerations. The peak values were similar for both sides.

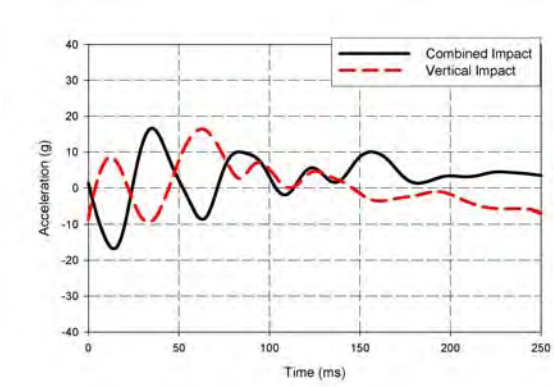

Figure 418. Upper Sidewall Acceleration Longitudinal Impact Study, FS 400—Left Sidewall

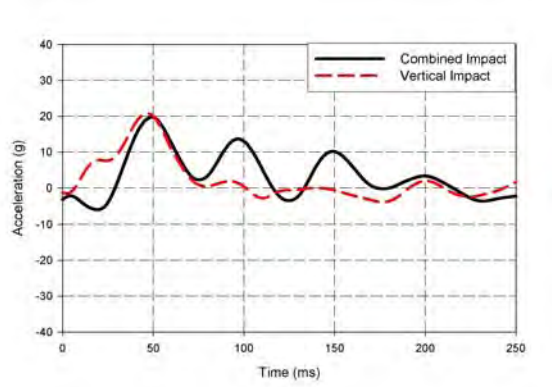

Figure 419. Upper Sidewall Acceleration Longitudinal Impact Study, FS 400—Right Sidewall

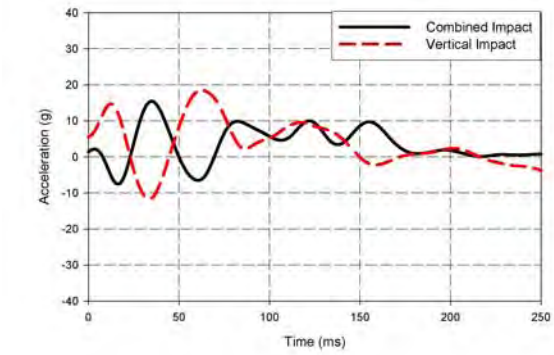

Figure 420. Upper Sidewall Acceleration Longitudinal Impact Study, FS 440—Left Sidewall

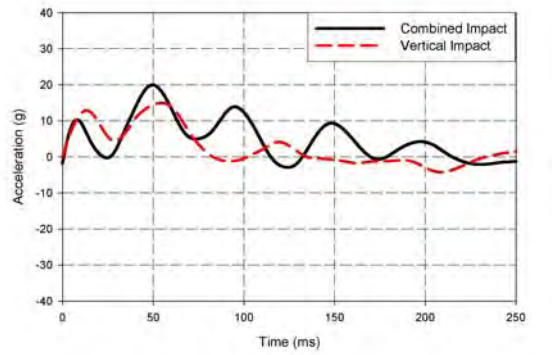

Figure 421. Upper Sidewall Acceleration Longitudinal Impact Study, FS 440—Right Sidewall

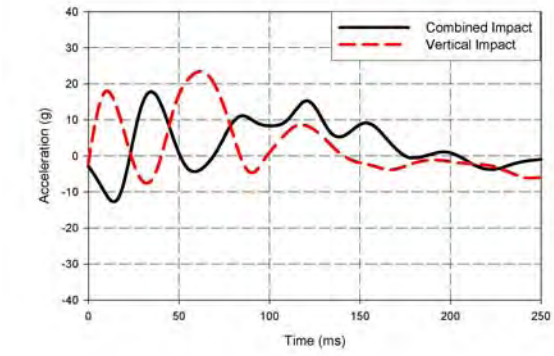

Figure 422. Upper Sidewall Acceleration Longitudinal Impact Study, FS 480—Left Sidewall

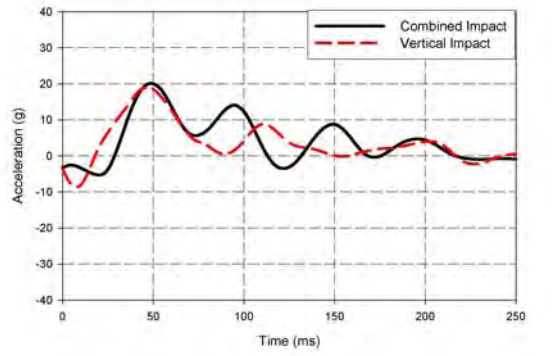

Figure 423. Upper Sidewall Acceleration Longitudinal Impact Study, FS 480—Right Sidewall

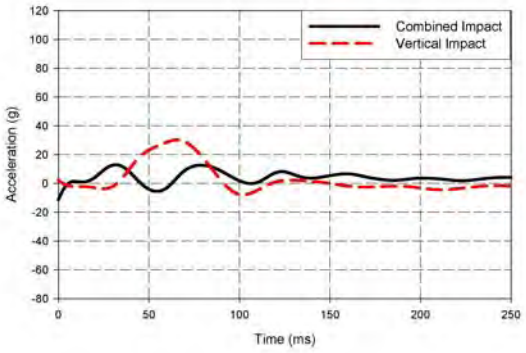

Figure 424. Lower Sidewall Acceleration Longitudinal Impact Study, FS 400—Left Sidewall

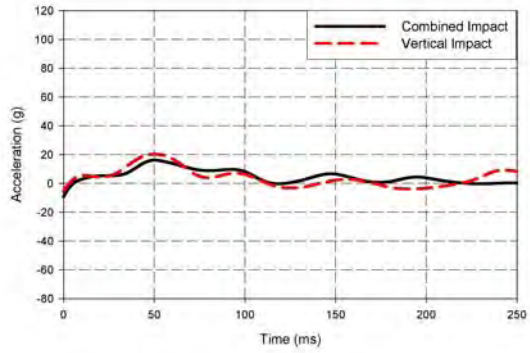

Figure 425. Lower Sidewall Acceleration Longitudinal Impact Study, FS 400—Right Sidewall

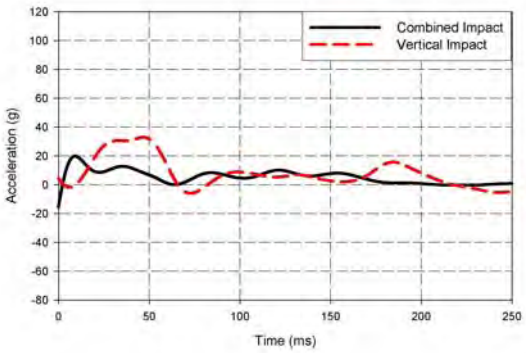

Figure 426. Lower Sidewall Acceleration Longitudinal Impact Study, FS 440—Left Sidewall

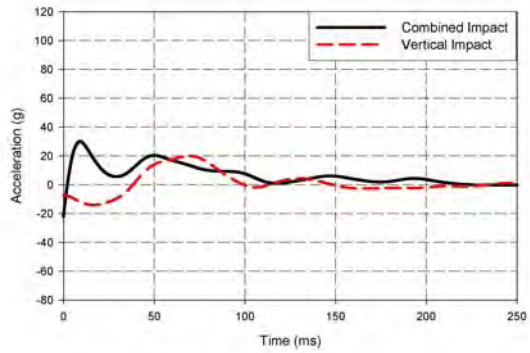

Figure 427. Lower Sidewall Acceleration Longitudinal Impact Study, FS 440—Right Sidewall

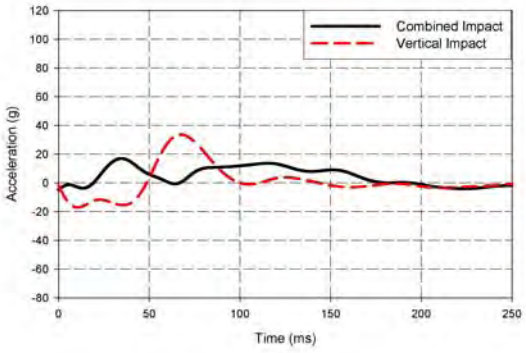

Figure 428. Lower Sidewall Acceleration Longitudinal Impact Study, FS 480—Left Sidewall

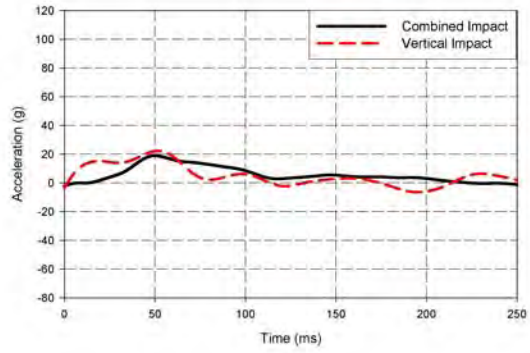

Figure 429. Lower Sidewall Acceleration Longitudinal Impact Study, FS 480—Right Sidewall

9. DISCUSSION.

The primary goals of this simulation were to assess the dynamic response of the overhead stowage bins during impact, to compare these results with experimental data, and to provide an appropriate interpretation of the experimental and simulation results. To accomplish this, the FE model had to calculate the dissipation and transfer of energy in the fuselage structure with reasonable accuracy, thus insuring that the bins experienced the correct acceleration pulse due to impact.

The simulation results showed that the combination of frames and luggage are responsible for approximately 68% of the energy dissipation during the impact. A careful examination of the responses of all structural components also indicated that a detailed and accurate representation of the frames and luggage are the two most significant factors influencing overall structural impact response.

The global pattern of deformation of the simulation is closely comparable to that observed in the experiment, with more extensive crushing on the left side of the test article in both cases. The simulation was also able to explain, as previously noted in table 2, the basic pattern of acceleration pulses experienced during impact. The two right-side pulses are separated by an interval in which the lower right-side frames were buckling. During buckling, little energy was transferred up through the frames. Once the point of maximum buckling is reached, the section becomes stiffer. This results in an acceleration pulse moving through the frames.

A similar pattern was observed on the left side, except that there were three left-side acceleration pulses. The small initial acceleration pulse was followed by buckling and the formation of a plastic hinge. When the plastic hinge impacted the ground, it set off a second pulse, followed by additional crushing on the left side. The final, smaller pulse occurred when crushing on the left side was complete, leading to a final transfer of energy up through the frames.

While the global behavior of the test structure can be understood through the buckling history of the lower frames, a detailed comparison of acceleration time histories shows some discrepancies between the simulation and experimental results. With the Hitco bin, the timing of acceleration pulses matched well between the simulation and experimental results, though the initial peak pulse was higher than expected in the simulation. The magnitude of the second pulse in the simulation matched very closely with experimental data. With the Heath Tecna bin, the magnitude of the peak acceleration response matched reasonably well with experimental data, but occurred earlier than expected. There are several possible explanations for the acceleration pulses in the simulation occurring earlier than expected or showing values higher than expected.

First, the cargo door and/or reinforcing cargo door frame may have been modeled too rigidly in the simulation. It is possible that a more detailed model of the door may be required. This is a difficult issue not only due to the complexity of the geometry but also due to the nature of the connection between the cargo door and the surrounding frame. The door was not directly fixed to the frame, but was essentially pressed onto the frame from inside. While such an attachment could be simulated, there are many unknowns, such as the exact degree of contact pressure

exerted by the door on the frame and the percentage of load transferred through the pins. This will influence the amount of load that is transferred through the door and the degree to which the door itself might buckle. The current model assumes the cargo door is rigidly attached to the surrounding frame. This assumption leads to a more rigid structure and may affect the timing, if not the peak value, of acceleration responses on the right side.

Second, all joints were modeled as if the structural elements were directly connected to each other, rather than joined with rivets. In the test article, such joints have some degree of compliance. Connections exhibit local yielding, as rivets bear out against the flanges or webs, and imperfect fits result in some delay in picking up loads. All of these factors tend to make the test article more compliant than the simulation. This could easily explain the higher initial acceleration peaks observed in the simulation. One method of addressing this is to model selected joints or rivets in greater detail with either spring connections or explicitly modeled rivets. This will increase the fidelity of the simulation, though at an increased cost in time and complexity.

Third, the test article is suspended from a cable, and thus, deforms under its own weight prior to release. At release, the test article vibrates as it moves towards equilibrium. This could influence the simulation results in a random manner, depending on what phase the frames are in when impact occurs. Though this effect could be small, accelerometer data are highly sensitive and could be influenced by such initial fluctuations. The simulation assumed that the initial condition was that of the fuselage section when sitting on the ground under 1 g of gravity.

The fourth is the effect of material properties for both the aluminum structure and the luggage. With the effects of corrosion and fatigue, it is possible that the test article could have had a lower yield strength than was initially assumed. However, the sensitivity of the simulation to material yield strength was found to be moderate rather than decisive. A reduction in yield strength of 20% led to small changes in the peak acceleration responses of the overhead stowage bins. The reduced yield strength led to an increase in crushing of approximately 4 inches on the right and left sides. The reduced yield strength improved the correlation with the experimental data at some points. Based on this comparison, a reduced yield strength of approximately 10% appears to offer the best description of material properties for this simulation.

For the luggage properties, an initial estimate was made using the material parameters of the foam covering the ribs on the EuroSID side-impact dummy. This estimate was found to be basically reasonable; however, though the initial luggage stiffness was subsequently reduced because the stiffer luggage appeared to limit crushing compared to the experimental data. While the final degree of crushing in the simulation matched well with the experimental data, the luggage material properties could be improved.

Although a static load deflection curve was obtained by Jackson and Fasanella [29] for typical luggage with strains up to 35%, the region of primary interest is 40% to 60% strain. At the fuselage center, for example, the distance from the lower edge of the under-floor beam to the bottom frame was approximately 36.5 inches initially, and 16 inches after crushing, for a crushing stroke of 56%, using data from simulation results. Experimental results showed a

slightly higher crushing stroke. Furthermore, the data reported by Jackson and Fasanella show significant nonlinear drops, making estimates of luggage properties difficult. Also, luggage in compression may behave similarly to an open-celled foam; in which case, the dynamic load deflection properties will differ from those under static conditions.

The general complexity of the impact event is illustrated by the degree of fracture in the left and right sides of the upper frames. The right side experienced a more significant acceleration pulse due to the reinforced cargo door structure. This led to the failure of the right-side seats, while the left-side seats remained upright. On the upper frames of the test article, however, the left side showed larger fractures, as measured by the degree to which the failure extended through the frame. The left-side failure occurred as a result of the acceleration pulse, but also because of the downward tilt on the left side, which changed the magnitude and location of the peak bending stresses on the upper frames. This effect was also captured in the simulation, which showed higher plastic strains on the upper left-hand-side frames compared to the upper right-hand-side frames.

The most convincing accelerometer data, in terms of validating the simulation, is the comparison of peak overhead bin accelerations and the acceleration response at the seat cushions. To accurately capture the acceleration response for such secondary structures, the simulation must correctly describe the basic buckling, crushing, and energy dissipation that are critical in crashworthiness studies.

However, as noted by Bisagni [19], the focus should not be entirely on detailed validation of acceleration results. The goal, instead, should be to replicate the basic behavior of the test article during impact and to obtain meaningful and physically reasonable results. While correlation with experimental data is important and validation of the dynamic simulation is vital, the experimental data itself is subject to a certain degree of variability. This is observed in automobile impact studies, where repeated identical tests yield noticeably different acceleration pulses in some cases. This may be due to slight variations in manufacturing, slight differences in placement of the accelerometers, or noise and other errors involved in the data acquisition process. While comparisons of accelerometer data are important, the most critical validation is a comparison of the observed pattern and the timing of crushing during impact. In this regard, the simulation showed a high level of fidelity to the actual impact event.

Once the baseline simulation was validated, it was possible to employ the model in studying alternate impact conditions. The ability to evaluate the impact response for other test cases is a major advantage of using numerical methods in conjunction with experimental testing. A wide range of possible impact conditions could be studied, such as roll angles, angle of pitch, impact into soft soil or water, angle of terrain, and combined longitudinal and vertical impact loading. It is also possible to study a variety of configurations, such as the amount of luggage loaded in the under-floor compartment or in bins, partial passenger loading, changing overhead bin supports, or loading more rigid cargo in the under-floor compartment.

10. CONCLUSIONS.

A simulation of the experimental drop test was completed, and a comparison of peak acceleration results between the simulation and experiment showed reasonable agreement. The Heath Tecna bin sustained a 14-g experimental vertical load factor, while the simulation peak acceleration value was 15 g's. The Hitco bin sustained a 13-g experimental vertical load factor, while the simulation showed a peak load of 12 g's. Peak loads in the tie rods and struts also showed reasonable correlation between the simulation and experiment. These results are very significant, as they indicate the simulation may be used to study other impact conditions and to determine conditions in which the overhead stowage bins might detach. The simulation also calculated the dynamic load distribution between the various overhead stowage bin structural supports with very reasonable accuracy. Further, the simulation accurately calculated the acceleration peak value and pulse duration for the seat rails and seats, accounting for the fact that the right-hand-side seats collapsed during testing. Also, the final deformed shape and time history of deformation of the simulation also agreed well with the experimental results. In sum, the simulation was validated through detailed comparisons with experimental data.

Three parameters in the simulation were studied to determine the degree to which they affect analytical results. Friction between the platform and test article significantly affected the observed pattern of deformation and led to different buckling patterns in the frames. Even for a vertical drop test condition, friction should be included. This also indicates that characterization of the impact surface in cases with a longitudinal impact velocity is quite important. Thus, the surface type, such as concrete, soft soil, or sand, will clearly affect the impact response of the airframe.

Material yield strength had a moderate effect on simulation results, with a lower yield strength leading to a greater degree of crushing, as expected. The peak acceleration responses showed only minor changes for this case. In general, a reduction in yield strength of 10% to 15% in the simulation is recommended to account for degradation of material properties due to corrosion and fatigue.

Inclusion of a material failure criterion did not improve the simulation results, and in fact, led to buckling behavior that was contrary to that observed in the experiment. While failure modeling is highly desirable, current uncertainties in dynamic failure criteria make implementation hazardous. It is possible that a significantly finer mesh is needed to correctly implement a failure criterion, as the removal of relatively large elements does not accurately describe the observed fractures in the test article.

The validated model was used to study the effect of luggage, roll angle, and combined vertical and longitudinal loading. Luggage plays a significant role in energy absorption, and the absence of luggage increases the peak accelerations throughout the fuselage. Even more significantly, the simulated impact without luggage resulted in the almost total collapse of the upper frame section. The collapse led to the intrusion of the bins into the occupant space, a clear violation of the desired impact response, in which the occupant space should remain intact. Thus, for a commercial transport, crashworthiness depends in large part on the type and amount of luggage in the under-floor compartment.

One of the issues addressed in the experimental test is the question of whether static testing is an appropriate method of determining loads in the overhead stowage bin supporting structures. For the purely vertical drop condition, this was found to be largely reasonable. While the load distribution between supports can change greatly under dynamic conditions, the difference in peak loading depends on the bin support configuration. The most significant change in loading occurred with the Heath Tecna bin. In static conditions, the combined struts react 66% of the vertical load. In 13-g dynamic loading conditions, the struts react 92% of the vertical load, based on experimental results. The expected loading of the struts, based on static assumptions, was 1661 lb, while the actual loading was 2314 lb. The simulation results agree, showing approximately 90% of the vertical load is reacted by the struts under dynamic loading conditions.

For the dynamic roll angle impact condition, however, it was found that the load in the vertical bin supports changed significantly with a roll angel of 10°. The 10° roll condition resulted in an increase of approximately 90% in peak tie rod loads in the Hitco bin. The 15° roll angle condition resulted in peak tie rod loads that were 80% higher than the 0° roll condition. While the 10° roll represents the worst-case condition for roll angle, in both cases, the bins would be expected to separate from the frames.

Another issue that has received attention is the separate testing of vertical and longitudinal impacts. A combined test case was simulated, with a 9-g longitudinal pulse combined with the 30-ft/sec vertical impact. It was found that these two impact modes are largely independent, because of the differences in timing for the acceleration pulses and subsequent loading. In general terms, the effect of the vertical impact tends to occur relatively early in the impact event, while the effects of the longitudinal impact occur somewhat later.

Peak loads in the overhead stowage bin supports were not significantly affected by the combined impact condition. The drag struts for the Hitco Bin and the longitudinal beam in the Heath Tecna bin experienced increased loading, as expected, due to the 9-g deceleration pulse.

Several detailed observations can be made concerning the simulation.

- The frames are the single most important structure in determining overall dynamic response and should be modeled with as much detail and accuracy as possible.

- The luggage plays a critical role in absorbing and dissipating impact energy in this event and must be included in the simulation. As previously noted, the luggage and frames combined dissipate 68% of the impact energy, with the luggage dissipating 35% of the energy. The luggage was modeled successfully as viscous foam.

- While simulation results are dependent on accurate material properties, a 20% change in yield strength had only a moderate effect on the resulting impact response of the test article. However, in the absence of manufacturer's data, coupon testing would ideally provide guidance in determining appropriate properties. The best results for the current simulation were obtained with a 10% reduction in yield strength.

- Using material failure criteria to simulate fracture in the frames led to differences in the pattern of buckling in the frames, but it did not improve the quality of the simulation results. A finer mesh should be used with failure criteria.

- Including friction between the test article and the platform had a clear qualitative effect, though the impact on final peak acceleration results was not decisive. Without friction, the test article tended to slide to the left and rotate counterclockwise, as viewed from the front. Also, omitting friction tended to reduce the initial spike in acceleration that is sometimes found in simulation results for frame locations. This reduction in the early peak value occurs because the frame section was allowed to slide inward, rather than staying fixed at or near its impact point.

- The cargo door and reinforced frame had a dominant effect on the response of the test article, both in the simulation and experimental results. Increased modeling accuracy in this region may also improve the correspondence in timing between simulation and experimental results.

- Seat structure and seat failures have a significant effect on the acceleration response of points along the floor tracks. To accurately assess floor track acceleration responses, it is important to include seats and preferable to simulate the time delay during which occupants apply loading to the seat structure.

- The level of detail in the current model was sufficient to accurately simulate the peak acceleration values for the overhead stowage bins and floor tracks and provided seat acceleration data that may be used as input in calculating occupant injury.

In more general terms, four points summarize the overall accomplishments of this crashworthiness study.

First, a simulation of a vertical drop test was successfully validated. This validation provides practical guidance concerning the level of detail required to capture the buckling and crushing behavior of the fuselage section. It also provides guidance for the parameters and material properties used in this simulation. Validation of transient dynamic simulations, particularly given the relatively small number of existing aircraft-focused simulations, remains an important concern and contributes to the level of confidence in using such simulations in a predictive manner.

Second, the luggage was found to play a significant roll in crashworthiness. With regard to simulation parameters, a viscous foam model was successfully used to simulate the luggage behavior. More broadly, the type of luggage, the amount of luggage, and the inclusion of rigid structures in the under-floor compartment are critical items in determining the impact response of the frames, seats, and overhead stowage bins. The luggage itself dissipates a significant degree of impact energy and must be considered in future crashworthiness designs.

Third, other impact conditions were found to be critical in determining failure occurrences in the overhead stowage bin supporting structures and seats. A 10° roll angle resulted in a 90% increase in peak loads in critical bin supports, and the lower stowage bin would likely have detached under such conditions. The lower seats also experienced a significant increase in loading, which again, could influence their possible failure or contribute to an increased level of occupant injuries. This finding is potentially significant, as it relates to the static qualification testing currently being conducted for overhead bins. Tests are currently only performed with a 0° roll condition. Dynamic seat testing for certification includes pitch and yaw angles, but not roll angles.

Fourth, it was found that the use of independent vertical and longitudinal impact testing is largely justified, as limited nonlinear effects were found in combining the two impact conditions. While testing is often employed based on this assumption, the exact effect of combining the two load cases has not been previously studied. This question is frequently raised, and the present study shows that the independent use of vertical and longitudinal testing yields valid results.

In sum, this report represents a significant step toward conducting an aircraft crashworthiness simulation. It has accurately captured the acceleration response of the lower seat cushions under occupant loading, indicating that the simulation may be used to assess occupant injury, as well as structural impact responses. With approximately 60,000 elements, this simulation could be readily adapted to model a full fuselage section, including a small number of finite element dummies, and still remain within the current practical limit of 500,000 elements. As computational capabilities continue to expand, it is likely that complete crashworthiness simulations, including fuselage structure, cabin items, seats, and occupants, will become routine for use in evaluating and improving crashworthy air vehicle designs.

11. REFERENCES.

1. Laananen, D.H. and Winkelman, K.L., "Analysis of Energy-Absorbing Seat Configurations for Aircraft," I*nternational Journal of Crashworthiness*, Vol. 1, No. 4, 1996.

2. Kindervater, C.M., Kohlgruber, D., and Johnson, A., "Composite Vehicle Structural Crashworthiness—A Status of Design Methodology and Numerical Simulation Techniques," *International Journal of Crashworthiness*, Vol. 4, No. 2, 1999.

3. Waldock, W.D., "A Brief History of Crashworthiness," *SAFE Association Symposium*, Phoenix, Arizona, September 20, 1997.

4. Webb, D.C., Webster, J., and Kormi, K., "Finite Element Simulation of Energy Absorption Devices Under Axial Static Compressive and Impact Loading," *International Journal of Crashworthiness*, Vol. 6, No. 3, 2001.

5. Hillmann, J., Konig, C., and Wang, X., "10 Years of Crash Simulation at Volkswagen," *Second International LS-DYNA3D Conference*, San Francisco, California, September 20 and 21, 1994.

6. Marzenmiller, A., Schweizerhof, K., and Rust, W., "Joint Failure Modeling in Crashworthiness Analysis," *Second International LS-DYNA3D Conference*, San Francisco, California, September 20 and 21, 1994.

7. Hanssen, A.G., Hopperstad, O.S., and Langseth, M., "Design of Aluminium Foam-Filled Crash Boxes of Square and Circular Cross-Sections," *International Journal of Crashworthiness*, Vol. 6, No. 2, 2001.

8. Jones, N., "Dynamic Material Properties and Inelastic Failure in Structural Crashworthiness," *International Journal of Crashworthiness*, Vol. 6, No. 1, 2001.

9. Johnson, G.R. and Beissel, S.R., "Damping Algorithms and Effects for Explicit Dynamics Computations," *International Journal of Impact Engineering*, Vol. 25, 2001, pp. 911-925.

10. Alves, M. and Jones, N., "Impact Failure of Beams Using Damage Mechanics: Part I—Analytical Model," *International Journal of Impact Engineering*, Vol. 27, 2002, pp. 837-861.

11. Kenny, S., Pegg, N., and Taheri, F., "Finite Element Investigations of the Dynamic Plastic Buckling of a Slender Beam Subject to Axial Impact," *International Journal of Impact Engineering*, Vol. 27, 2002, pp. 179-195.

12. Cui, S., Hao, H., and Cheong, H.K., "Numerical Analysis of Dynamic Buckling of Rectangular Plates Subjected to Intermediate-Velocity Impact," *International Journal of Impact Engineering*, Vol. 25, 2001, pp. 147-167.

13. Ahmed, T.U., Ramachandra, L.S., and Bhattacharyya, S.K, "Elasto-Plastic Response of Free-Free Beams Subjected to Impact Loads," *International Journal of Impact Engineering*, Vol. 25, 2001, pp. 661-681.

14. Jackson, K.E., "Impact Testing and Simulation of a Crashworthy Composite Fuselage Concept," *International Journal of Crashworthiness*, Vol. 6, No. 1, 2001.

15. Jackson, K.E. and Fasanella, E.L., "Crashworthy Evaluation of a 1/5-Scale Model Composite Fuselage Concept," U.S. Army Research Laboratory Vehicle Technology Center, Langley Research Center, Report No. NASA/TM-1999-209132 ARL-MR-441, 1999.

16. Fasanella, E.L., Boitnott, R.L., Lyle, K.H., and Jackson, K.E., "Full-Scale Crash Test and Simulation of a Composite Helicopter," *International Journal of Crashworthiness*, Vol. 6, No. 4, 2001.

17. Fasanella, E.L. and Jackson, K.E., "Crash Simulation of a Boeing 737 Fuselage Section Vertical Drop Test," U.S. Army Research Laboratory, Vehicle Technology Center, Langley Research Center, 2004.

18. Lawver, D., Nikodym, L., Tennant, D., and Levine, H., "Non-Linear Numerical Modeling of Aircraft Impact," *International Journal of Crashworthiness*, Vol. 6, No. 4, 2001.

19. Bisagni, C., "Crashworthiness of Helicopter Under-Floor Structures," *International Journal of Impact Engineering*, Vol. 27, 2002, pp. 1067-1082.

20. Vignjevic, R. and Meo, M., "Simulation of Helicopter Under-Floor Structure Impact on Water," *International Journal of Crashworthiness*, Vol. 6, No. 3, 2001.

21. Reid, J.D., "Tracking the Energy in an Energy Absorbing Guardrail Terminal," *International Journal of Crashworthiness*, Vol. 3, No. 2, 1998.

22. Altenhof, W., Saverio, P., Zamani, N., and Gaspar, R., "An Experimental and Finite Element Investigation Into the Energy Absorption Characteristics of a Steering Wheel Armature in an Impact," *International Journal of Impact Engineering*, Vol. 27, 2002, pp. 9197-212.

23. Cheng, Z.Q., Pilkey, W.D., Balandin, D.V., Bolotnik, N.N., Crandall, J.R., and Shaw, C.G., "Optimal Control of Helicopter Seat Cushions for the Reduction of Spinal Injuries," *International Journal of Crashworthiness*, Vol. 6, No. 3, 2001.

24. Nicholson, C.R. and Turnour, S.R., "Toward Simplified Methodologies for Seat Design to FAR Part 23.562," Society of Automotive Engineers, Inc., Paper No. 2002-01-1551, 2002.

25. Nicholson, C.R., Turnour, S.R., and Chapman, H., "The Design and Testing of Buckling Monocoque Seating Structures for Aircraft," Society of Automotive Engineers, Inc., Paper No. 1999-01-1599, 1998.

26. Hooper, S.J. and Ellis, D.R., "Aviation Safety and Crashworthy Seat Design," *International Journal of Crashworthiness*, Vol. 2, No. 1, 1997.

27. Teulings, A.M.G.L., Gowdy, V., Wismans, J.S.H.M., and Aljundi, B., "MADYMO Validation of Side Facing Sofa Sled Tests," North Atlantic Treaty Organization, Research and Technology Organization, Paper Number AC/323(HFM)TP/7, RTO Human Factors and Medicine Panel, Wright-Patterson Air Force Base, Ohio, August 1999.

28. Abramowitz, A., Smith, T.G., Vu, T., and Zvanya, J., "Vertical Drop Test of a Narrow-Body Transport Fuselage Section With Overhead Stowage Bins," FAA report DOT/FAA/AR-01/100, September 2002.

29. Jackson, K.E. and Fasanella, E.L., "Crash Simulation of Vertical Drop Tests of Two Boeing 737 Fuselage Sections," FAA report DOT/FAA/AR-02/62, August 2002.

30. Vignjevic, R. and Cavalcanti, M.J., "Numerical Simulation of the Lynx Helicopter Main Lift-Frame Component Collapse," *International Journal of Crashworthiness*, Vol. 2, No. 1, 1997.